



Universitat de les
Illes Balears

Departament de Física

Damping of Magnetohydrodynamic Waves in Solar Prominence Fine Structures

Tesi Doctoral

Roberto Soler Juan

*Tesi presentada per optar al Grau de Doctor en Física
per la Universitat de les Illes Balears*

Dirigida pels Profs. R. Oliver & J. L. Ballester

Palma de Mallorca, 12 d'abril de 2010

Programa Oficial de Postgrau de Ciències
Experimentals i Tecnologies (Física)

Universitat de les Illes Balears

Per Maria del Mar

Summary	7
Acknowledgments	9
I The Sun, Solar Prominences, and the MHD Theory	11
1 Introduction	13
1.1 General aspects about the Sun	13
1.2 The solar corona	15
1.3 Prominences and filaments	16
1.3.1 The prominence fine structure	18
1.4 Prominence oscillations: Observational evidence	20
1.4.1 Large-amplitude oscillations	20
1.4.2 Small-amplitude oscillations	20
1.5 Prominence oscillations: Theoretical modeling	23
1.5.1 Global oscillations	23
1.5.2 Fine-structure oscillations	24
1.5.3 Damping of the oscillations	25
2 Magnetohydrodynamic Theory	29
2.1 Plasma definition and collective behavior	29
2.2 Magnetohydrodynamic equations	32
2.2.1 Assumptions of the magnetohydrodynamic approximation	32
2.2.2 Fluid equations	33
2.2.3 Generalized induction equation for a partially ionized plasma	36
2.2.4 Non-adiabatic energy equation	41
2.2.5 Summary of the basic equations	45
2.3 Linear ideal magnetohydrodynamic waves	45
2.3.1 Linearized ideal magnetohydrodynamic equations	45
2.3.2 Dispersion relation of magnetohydrodynamic waves in uniform medium with straight magnetic field	46
II Individual Oscillations of Filament Threads	49
3 Ideal MHD Waves in a Magnetic Flux Tube	51
3.1 Model and basic equations	51
3.1.1 Equilibrium configuration	51
3.1.2 Dispersion relation	53
3.1.3 The thin tube approximation	55
3.2 Dispersion diagrams and eigenfunctions	55
3.2.1 Transverse modes	56
3.2.2 Longitudinal slow modes	58

CONTENTS

3.3	Oscillatory periods	59
3.4	Seismological application to thread oscillations	60
3.4.1	Observations	60
3.4.2	Theoretical interpretation	61
3.4.3	Estimation of the Alfvén speed and the magnetic field strength	63
3.5	Conclusion	64
4	Non-adiabatic MHD Waves in a Thread with Flow	65
4.1	Model and basic equations	66
4.1.1	Equilibrium configuration	66
4.1.2	Dispersion relation	66
4.1.3	The non-adiabatic sound speed	68
4.1.4	Analytical approximations	69
4.2	Results in the absence of flow	74
4.2.1	Dispersion diagrams	74
4.2.2	Damping times	75
4.3	Effect of mass flow	80
4.4	Conclusion	84
5	MHD Waves in a Partially Ionized Thread	85
5.1	Model and method	85
5.1.1	Equilibrium configuration	85
5.1.2	Basic equations and numerical procedure	86
5.1.3	Dimensional analysis of the induction equation	88
5.2	Analytical expressions	90
5.2.1	Alfvén modes	90
5.2.2	Kink modes	94
5.2.3	Slow modes	96
5.3	Numerical results	98
5.3.1	Alfvén modes	98
5.3.2	Kink modes	100
5.3.3	Slow modes	102
5.4	Conclusion	104
6	Resonantly Damped Kink MHD Waves	107
6.1	Resonant absorption in the Alfvén and slow continua	108
6.1.1	Model configuration	108
6.1.2	Analytical investigation	109
6.1.3	Numerical procedure	113
6.1.4	Results	114
6.2	Resonant absorption in a partially ionized thread	117
6.2.1	Equilibrium	117
6.2.2	Analytical expressions	120
6.2.3	Numerical computations	122
6.2.4	Results	122
6.3	Conclusions	125

7	Kink Modes in an Inhomogeneous Fine Structure	127
7.1	Model and basic equations	127
7.1.1	Equilibrium configuration	127
7.1.2	Mathematical method	128
7.2	Dispersion relation and analytical approximations	135
7.2.1	Damping by Cowling's diffusion	136
7.2.2	Damping by resonant absorption	137
7.3	Results	137
7.3.1	Case without transverse transitional layer ($l/a = 0$)	138
7.3.2	Case with transverse transitional layer ($l/a \neq 0$)	140
7.3.3	Effect of the position of the dense part within the flux tube	142
7.4	Conclusion	143
III Collective Oscillations of Filament Threads		147
8	Collective MHD Waves in Two Flowing Threads	149
8.1	Model and theory	149
8.1.1	Equilibrium configuration	149
8.1.2	Mathematical method	150
8.2	Collective modes in two identical filament threads	153
8.2.1	Results in the absence of flows	153
8.2.2	Effect of mass flows	159
8.3	Collective modes in two non-identical filament threads	162
8.3.1	Conditions for collective motions	162
8.3.2	Application to a particular configuration	163
8.4	Conclusion	164
9	Damping of MHD Waves in Two Cylindrical Threads	167
9.1	Model and method	167
9.1.1	Equilibrium	167
9.1.2	Basic equations	168
9.2	Damping by non-adiabatic effects	170
9.3	Damping by resonant absorption	170
9.3.1	Identical threads	172
9.3.2	Non-identical threads	177
9.4	Conclusions	179
Concluding Remarks and Future Work		183
References		185

Summary

High-resolution observations of solar filaments and prominences reveal that these large-scale coronal structures are formed by a myriad of long and thin ribbons, here called threads, which are piled up to form the prominence body. Evidences suggest that these fine structures are magnetic flux tubes anchored in the solar photosphere, which are partially filled with the cool and dense prominence material.

Individual and collective oscillations of prominence and filament fine structures are frequently reported by means of oscillatory variations in Doppler signals and spectral line intensity. Common features of these observations are that the reported oscillatory periods are usually in a narrow range between 2 and 10 minutes, that the velocity amplitudes are smaller than $\sim 3 \text{ km s}^{-1}$, and that the oscillations seem to be strongly damped after a few periods. Typically, the ratio of the damping time, τ_D , to the period, P , is $\tau_D/P < 10$. While the oscillations have been interpreted in the context of the magnetohydrodynamic (MHD) theory, i.e., in terms of the MHD normal modes supported by the filament thread body and/or propagating MHD waves, the mechanism or mechanisms responsible for the damping are not well-known and a comparative study between different damping mechanisms is needed.

In this Thesis, we study the efficiency of several physical mechanisms for the damping of MHD oscillations in prominence fine structures. Both individual and collective oscillations of threads are analyzed. We model a filament thread as a straight cylindrical magnetic flux tube with prominence conditions, embedded in a magnetized environment representing the solar coronal medium. The basic MHD equations are applied to the model and contain non-ideal terms accounting for effects as, e.g., non-adiabatic mechanisms, magnetic diffusion, ion-neutral collisions, etc., that may be of relevance in prominence plasmas and whose role on the damping of the oscillations is assessed. Our method combines analytical treatments along with numerical computations to obtain the frequency and the perturbations of the linear MHD modes.

Among the studied mechanisms, we find that the most efficient one for the damping of transverse thread oscillations, interpreted as kink MHD modes, is the process of resonant absorption in the Alfvén continuum. The efficiency of resonant absorption is independent of the plasma ionization degree and is consistent with the reported values of τ_D/P . Thermal effects, as well as magnetic diffusion, are irrelevant for the damping of transverse oscillations. Regarding longitudinal oscillations, i.e., slow MHD modes, radiative losses from the prominence plasma and ion-neutral collisions are the processes that provide the smallest damping times. Their combined effect causes an efficient attenuation of slow modes in filament threads, with τ_D/P compatible with the observed values. Finally, Alfvén waves are also investigated, and we obtain that they are damped by ion-neutral collisions. However, the damping of Alfvén waves is not very efficient because the theoretical damping times are between one and two orders of magnitude larger than the corresponding periods. All these conclusions apply for both individual and collective oscillations of threads.

Our conclusions shed some light on the problem of the attenuation of prominence oscillations, since we identify some candidates which may be responsible for the damping. The present results allow subsequent studies of MHD waves in prominences to neglect some irrelevant mechanisms. On the contrary, those important effects pointed out here should be investigated in more detail, and more complicated models representing prominence fine structures should be considered in the near future.

Resum en català

Observacions de protuberàncies i filaments solars en alta resolució mostren que aquests fenòmens coronals de gran escala estan formats per un conjunt d'estructures fines, llargues i primes, que aquí anomenem fibres, les quals s'apil·len per tal de formar el cos de la protuberància. Les evidències suggereixen que aquestes fibres són tubs de flux magnètic arrelats a la fotosfera solar, els quals estan parcialment plens amb el material fred i dens de la protuberància.

Les oscil·lacions individuals i col·lectives d'estructures fines de filaments i protuberàncies solars són freqüentment detectades mitjançant variacions oscil·latòries en senyals Doppler i en la intensitat de línies espectrals. Característiques comunes d'aquestes observacions són que els períodes d'oscil·lació obtinguts estan normalment dins un interval estret d'entre 2 i 10 minuts, que les amplituds de les velocitats són menors de $\sim 3 \text{ km s}^{-1}$ i que les oscil·lacions pareixen estar fortament esmorteïdes després de pocs períodes. Típicament, el quocient entre el temps d'esmorteïment, τ_D , i el període, P , és $\tau_D/P < 10$. Mentre que les oscil·lacions s'han interpretat dins el context de la Teoria Magnetohidrodinàmica (MHD), és a dir, en termes dels modes normals MHD suportats per la fibra de filament i/o ones MHD que es propaguen, el mecanisme o els mecanismes responsables de l'esmorteïment no són ben coneguts i encara estan sent investigats. És necessari un estudi comparatiu entre mecanismes d'esmorteïment diferents.

En aquesta Tesi, estudiem l'eficiència de varis mecanismes físics per a l'esmorteïment d'oscil·lacions MHD en estructures fines de protuberància. S'analitzen tant oscil·lacions de fibres individuals com col·lectives. Modelam una fibra de filament com un tub de flux magnètic, recte i cilíndric, amb plasma amb condicions de protuberància, immers en un entorn magnetitzat que representa el medi de la corona solar. Les equacions bàsiques de la MHD s'apliquen al model i contenen termes no ideals que tenen en compte efectes com, per exemple, mecanismes no adiabàtics, difusió magnètica, col·lisions entre ions i neutres, etc., que podrien ser rellevants en plasmes de protuberàncies i el paper dels quals sobre l'esmorteïment de les oscil·lacions es determina. El nostre mètode combina tractaments analítics juntament amb càlculs numèrics per a obtenir la freqüència i les pertorbacions dels modes MHD lineals.

D'entre els mecanismes estudiats, trobam que el més eficient per a l'esmorteïment de les oscil·lacions transversals de fibres, interpretades com modes *kink* (de doblec) MHD, és el procés d'absorció ressonant en el continu d'Alfvén. L'eficiència de l'absorció ressonant és independent del grau d'ionització del plasma i és consistent amb els valors observacionals de τ_D/P . Els efectes tèrmics, així com la difusió magnètica, són irrellevants per a l'esmorteïment de les oscil·lacions transversals. Pel que fa a les oscil·lacions longitudinals, és a dir, els modes lents MHD, les pèrdues per radiació del plasma de la protuberància i les col·lisions entre els ions i els neutres són els processos que proporcionen els menors temps d'esmorteïment. El seu efecte combinat provoca un esmorteïment eficient dels modes lents en fibres de filament, amb valors de τ_D/P compatibles amb els que s'observen. Finalment, les ones d'Alfvén també s'investiguen i obtenim que estan esmorteïdes per les col·lisions entre els ions i els neutres. No obstant això, l'esmorteïment de les ones d'Alfvén no és molt eficient perquè els temps d'esmorteïment teòrics són entre un i dos ordres de magnitud més grans que els períodes corresponents. Totes aquestes conclusions són vàlides tant per oscil·lacions de fibres individuals com col·lectives.

Les nostres conclusions contribueixen a entendre el problema de l'esmorteïment de les oscil·lacions de protuberàncies, ja que identifiquem alguns candidats que podrien ser responsables de l'esmorteïment. Els nostres resultats permeten que els següents estudis d'ones MHD en protuberàncies puguin menysprear alguns mecanismes irrellevants. Per altra banda, aquells efectes importants aquí senyalats s'haurien d'investigar amb més detall, i models d'estructures fines de protuberància més complicats s'haurien de considerar en el futur proper.

Acknowledgments

First of all, I would like to thank my supervisors, Moncho and Josep Lluís, for introducing me to the fascinating field of magnetohydrodynamic waves in the solar atmosphere, and for giving me the opportunity to be a PhD student at the Solar Physics Group of the UIB. Without their advice, guidance, and experience, it would have been impossible to write this Thesis. I am also grateful to them for allowing me to travel and to attend to a number of scientific meetings and conferences, which is very important for the training of a young researcher.

I would like to thank the rest of present and former members of the Solar Physics Group of the UIB, Jaume, Íñigo, Toni, Marc, Pep, Manuel, and Samuel, for their help and for the nice work environment at UIB. I really had a great time these last years with all of you.

I am very grateful to Oddbjørn Engvold and Yong Lin from the Universitetet i Oslo, Bernie Roberts from the University of St Andrews, and Marcel Goossens from the Katholieke Universiteit Leuven, for inviting me to visit their respective institutes and for their warm hospitality during my stays.

I acknowledge the financial support received from the *Conselleria d'Innovació, Interior i Justícia* of the *Govern de les Illes Balears* by means of a predoctoral fellowship and three grants for travel expenses to visit Norway, Scotland, and Belgium.

This Thesis has been written using a L^AT_EX style created by Jamie Brett Stevens from the University of Tasmania, who made his style available at his website.

My last acknowledgment, but maybe the most important one, is for my girlfriend, Maria del Mar, and for my parents, whose constant support and encouragement allowed me to find the motivation to finish my PhD and to write this Thesis.

Thanks to all of you!

Part I

The Sun, Solar Prominences, and the Magnetohydrodynamic Theory

1.1 General aspects about the Sun

The Sun is the closest star to Earth and the main body of the Solar System, accounting for about 99.8% of its mass. The Sun is a common main sequence star of spectral class G2, which implies a surface temperature of approximately 5,500 K. There are more than 100 million G2 class stars in our galaxy, so the Sun is not peculiar from the astronomical point of view. However, the Sun is essential for us since its energy supports almost all life on Earth and drives the Earth's climate and weather. Some physical parameters of the Sun are given in Table 1.1.

Parameter	Value
Radius (R_{\odot})	6.96×10^8 m
Mass (M_{\odot})	1.99×10^{30} kg
Average density	1.408 kg m $^{-3}$
Surface gravity	273.95 m s $^{-2}$
Luminosity (L_{\odot})	3.827×10^{26} W
Equatorial rotation period	25.38 days
Mean distance from Earth (1 AU)	1.496×10^{11} m

Table 1.1: Some values of the Sun's physical parameters.

The Sun is a near-perfect sphere roughly composed of 74% hydrogen, 25% helium, and trace quantities of other elements. Due to the high temperatures, the Sun's material is in plasma state. In addition, the plasma is in hydrostatic balance since gas pressure is balanced by the gravity force. The Sun's energy is generated by nuclear fusion of hydrogen nuclei into helium. Nuclear fusion reactions only take place at the Sun's deepest part, the core, which extends from the center to about $0.2 R_{\odot}$ ($1 R_{\odot} = 1$ solar radius). The core has a density of up to 1.5×10^5 kg m $^{-3}$ and a temperature close to 15×10^6 K. The energy generated at the Sun's core during one second is enough to meet human needs for 50,000 years. This intense heat is transferred from the core to the Sun's surface through two layers. The first layer, from $0.2 R_{\odot}$ to $0.7 R_{\odot}$, is called the radiation zone since thermal radiation is the mechanism responsible for the heat transfer in this layer. Photons are emitted, absorbed, and reemitted continuously by protons and helium nuclei until they reach the boundary with the upper layer. In this layer, energy makes its way very slowly since photons take 10^6 years for the journey. The next layer, the convection zone, extends from $0.7 R_{\odot}$ to the surface. Here, the material is not dense or hot enough to transfer the heat energy via radiation. Moreover,

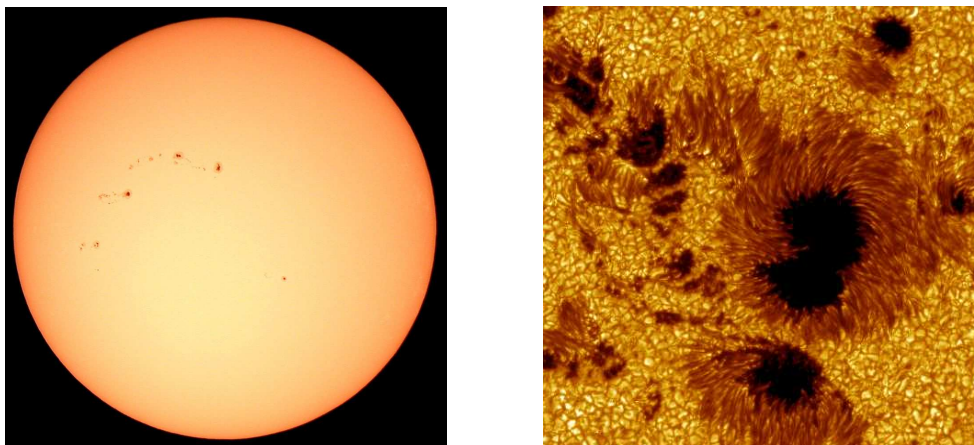


Figure 1.1: The solar photosphere. On the left: an image of the complete solar disc (Credits: *NASA/ESA/SOHO*). On the right: a closer image of a sunspot group, where granulation is also visible (Credits: *Royal Swedish Academy of Sciences*).

the temperature gradient is too large for the material to remain in static equilibrium. As a result, thermal convection becomes the dominant energy transfer mechanism. By means of convective motions, large hot plasma volumes rise and carry heat toward the Sun's surface. Eventually, these plasma volumes cool down by releasing some heat before falling and beginning the process again.

The visible surface of the Sun, the photosphere, is often considered as the first layer of the solar atmosphere (see left-hand image in Fig. 1.1). The photosphere is an extremely thin layer of about 550 km thick and with a temperature of 5,500 K, below which the Sun becomes opaque to visible light. The bulk of the emitted solar radiation comes from this thin layer. In high resolution images, the photosphere appears covered with irregularly shaped granules which are in continual motion. These granules are actually the tops of the convective cells that are overshooting the upper convection zone. Besides granulation, one can find some dark features known as sunspots (see right-hand image in Fig. 1.1), which have a temperature of about 4,000 K, being cooler than the rest of the photosphere. Sunspots are magnetic phenomena caused by the emergence of magnetic flux from the solar interior. At the center of a sunspot, the magnetic field strength can be larger than 1,000 G.

Above the photosphere lies a temperature minimum region with a temperature of about 4,000 K, followed by the less dense and more transparent chromosphere about 2,000 km thick, in which the temperature increases gradually with altitude, ranging up to around 10,000 K near the top of the chromosphere. Then, above the chromosphere there is the chromosphere-corona transition region (CCTR) in which the temperature rises rapidly, by means of a still unknown mechanism, from around 10,000 K to temperatures closer to 10^6 K. There, the external atmospheric layer, i.e., the corona, begins (see Fig. 1.2).

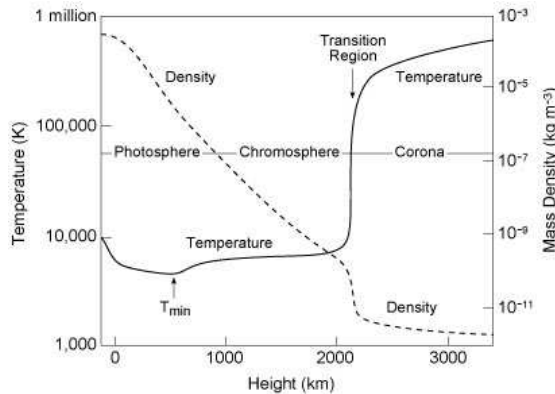


Figure 1.2: Temperature and mass density in the solar atmosphere as function to the distance above the top of the convection zone given by the VALC model of [Vernazza et al. \(1981\)](#).

1.2 The solar corona

The dazzling light of the photosphere prevents the much less bright solar corona from being normally seen in white light. Only at the times of an eclipse, or by means of a coronagraph, it is possible to see the corona with the naked eye (see left-hand image in [Fig. 1.3](#)). By a brief observation during an eclipse, one can see that the corona appears highly structured. In the quiet inner corona, the average electron density is about 10^{14} m^{-3} , but this is enhanced by factors of 5 to 20 in many of the visible structures during eclipses. The density rapidly falls off with distance from the solar surface, being less than 10^{10} m^{-3} at $10 R_{\odot}$.

With the help of spectroscopy, spectral lines corresponding to highly ionized iron (Fe XIV) and other highly ionized nuclei have been observed in the coronal spectrum, which indicates a plasma temperature in excess of 10^6 K . Parts of the corona can even reach 10^7 K . Hence, the coronal plasma is almost fully ionized. Due to its high temperature, the corona emits in abundance in the ultraviolet and extreme-ultraviolet (EUV) parts of the spectrum (see right-hand image in [Fig. 1.3](#)). In these wavelengths, a new corona appears, full of features and details. The fact that the corona is much hotter than the photosphere leads to the so-called *coronal heating problem*, as the mechanism responsible for the coronal heating remains unknown. Although some processes related to wave heating and/or magnetic reconnection are candidates, the discovery of the actual heating mechanism is one of the challenges of solar physics nowadays.

The coronal magnetic field is responsible for all the coronal behavior, structure, and dynamics, caused by the interaction between the magnetic field and the plasma. The bright zones observed in EUV images are called *active regions*. There, the magnetic field strength reaches values of more than 100 G, and correspond to the parts of the corona above the photospheric sunspots. The magnetic field causes a rich collection of phenomena inside and near active regions, like, e.g., coronal loops, flares, or coronal mass ejections. It is beyond the purpose of this work to perform a complete description of all these phenomena, but we refer the reader to [Aschwanden \(2004\)](#) for a detailed explanation.

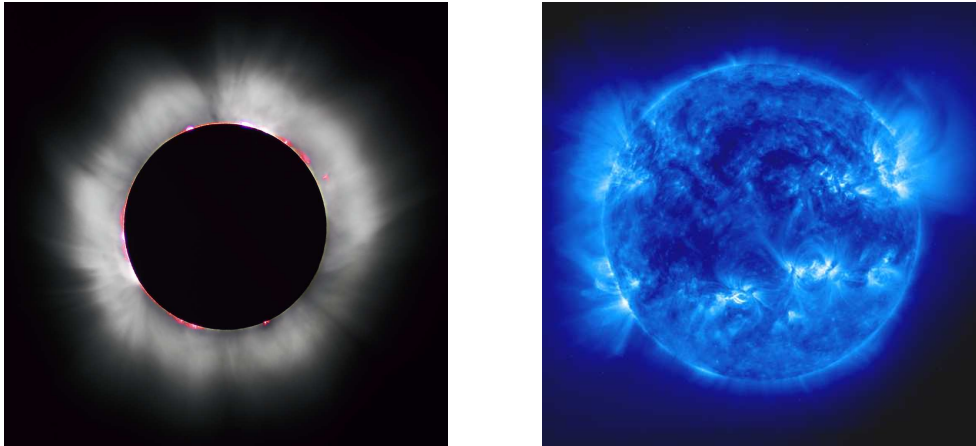


Figure 1.3: The solar corona. On the left: an image in white light during a solar eclipse. The upper part of the chromosphere and some prominences are also visible in red color (Credits: *Luc Viatour*). On the right: an image in EUV (171 Å) from the SOHO spacecraft, where active regions can be distinguished as bright zones.

1.3 Prominences and filaments

Prominences and filaments are large-scale coronal magnetic structures which are the subject of the present investigation. In this Section, we give a brief introduction to prominences and their properties. Recent reviews by [Patsourakos & Vial \(2002\)](#), [Labrosse et al. \(2010\)](#), and [Mackay et al. \(2010\)](#) provide a more detailed information about the physics of solar prominences. Although prominences are located in the corona, they possess temperatures a hundred times lower and densities a hundred or a thousand times larger than typical coronal values. The fact that their physical conditions are akin to those in the chromosphere suggests one possible scenario for prominence formation, in which prominences are made of chromospheric material which has been lifted up into the corona. Although the processes that lead to prominence formation are still under investigation, another proposed scenario to explain how prominences acquire their mass is condensation and cooling of plasma from the surrounding corona. In eclipse or coronagraph pictures, prominences appear as bright (in emission) structures at the limb, but in $H\alpha$ -images of the disc they show up as dark (in absorption) ribbons, which are called filaments (see images in Figs. 1.4 and 1.5). One must bear in mind that both structures, prominences and filaments, are the same phenomenon observed from two different points of view, the two names remaining because of historical reasons. In this work, we indistinctly use both names to refer to such magnetic structures.

Some basic questions about the nature of prominences are still unsolved, e.g., how is the denser prominence material supported against gravity in the much less dense corona, and how is the cooler prominence plasma thermally isolated from the much hotter external medium. There is no doubt that the magnetic field is responsible for keeping up the prominence plasma and maintaining it thermally shielded, but the precise structure and orientation of the magnetic field lines, especially in the surrounding corona, is still enigmatic and not well-known.

A prominence forms over time-scales of about a day. The so-called *quiescent* promi-

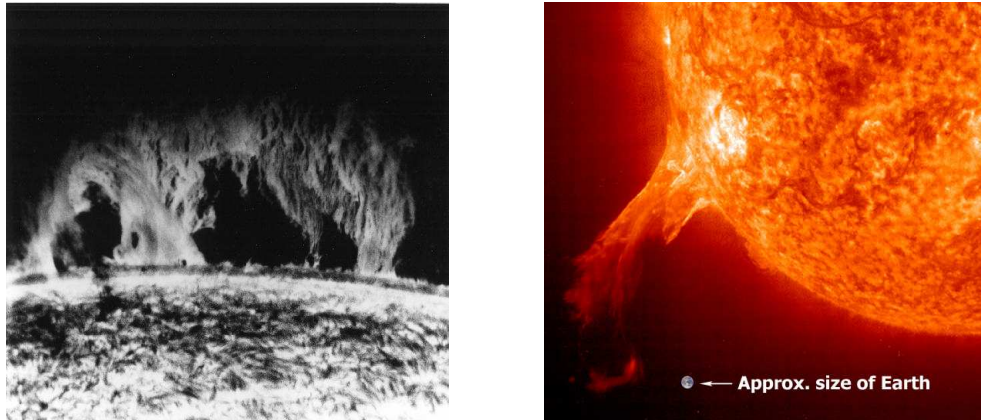


Figure 1.4: On the left: a classic $H\alpha$ (6563 \AA , $T \sim 10,000 \text{ K}$) image of a prominence at the solar limb from the Big Bear Observatory (1970). On the right: an image in EUV (304 \AA , $T \sim 60,000 - 80,000 \text{ K}$) from the SOHO spacecraft, where an erupting prominence is compared to the size of Earth.

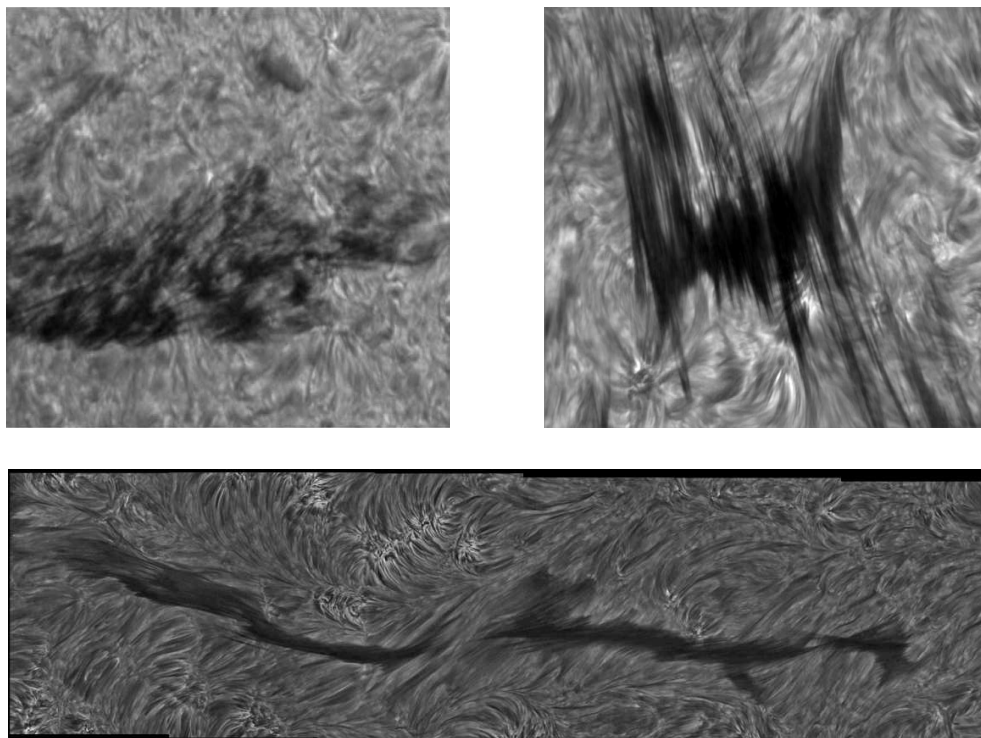


Figure 1.5: Top figures: two high-resolution $H\alpha$ images of quiescent solar filaments in which the fine-structure is clearly seen. The top left- and right-hand side images are adapted from [Lin et al. \(2003\)](#) and [Lin et al. \(2007\)](#), respectively, and were both taken by the Swedish Solar Telescope on La Palma. Bottom figure: the whole body of a filament in $H\alpha$ from the Dutch Open Telescope (2004).

Parameter	Value
Density	$2 \times 10^{-12} - 5 \times 10^{-10}$ kg m ⁻³
Temperature	5,000 – 15,000 K
Gas pressure	0.003 – 0.038 Pa
Magnetic field strength	4 – 20 G
Prominence Length	60,000 – 600,000 km
Prominence Height	10,000 – 100,000 km
Prominence Width	4,000 – 30,000 km
Fine Structure Length	3,000 – 15,000 km
Fine Structure Width	100 – 500 km

Table 1.2: Typical physical parameters of solar quiescent prominences and their fine structures. Adapted from [Patsourakos & Vial \(2002\)](#), [Aschwanden \(2004\)](#), and [Lin \(2004\)](#).

nences may persist in the corona for several months, whereas *active* prominences (i.e., those located in active regions) have life-times of only minutes or hours. At the end of their life, some prominences may suffer an instability with a subsequent eruption. Such eruptions are sometimes accompanied by a flare or coronal mass ejection. Due to their longer life-time, quiescent prominences have been more studied than the active ones. As the rest of the solar atmosphere, prominences are roughly composed by 90% hydrogen and 10% helium. The prominence plasma is only partially ionized for typical filament temperatures. The hydrogen ionization degree could probably vary in different filaments or even in different regions within the same filament ([Patsourakos & Vial 2002](#)). Regarding helium, recent studies by [Gouttebroze & Labrosse \(2009\)](#) indicate that for central prominence temperatures, the ratio of the number densities of He II to He I is around 10%, whereas the presence of He III is negligible. Typical parameters of quiescent prominence plasmas are shown in [Table 1.2](#).

1.3.1 The prominence fine structure

The fine structure of solar prominences and filaments is clearly seen in high-resolution observations (see [Fig. 1.5](#)). These fine structures, usually called *threads* or *fibrils*, appear as a myriad of long (5'' – 20'') and thin (0''.2 – 0''.6) dark ribbons in H α images of filaments on the solar disk (e.g., [Lin 2004](#); [Lin et al. 2005, 2007, 2008, 2009](#)), as well as in observations of prominences in the solar limb from the Solar Optical Telescope (SOT) aboard the Hinode satellite (e.g., [Okamoto et al. 2007](#); [Berger et al. 2008](#); [Chae et al. 2008](#); [Ning et al. 2009a](#); [Schmieder et al. 2010](#)). Although a mean value of 20 degrees has been reported, statistical studies show that the orientation of threads with respect to the filament long axis can significantly vary within the same filament ([Lin 2004](#)). Vertical threads are more commonly seen in quiescent prominences (e.g., [Berger et al. 2008](#); [Chae et al. 2008](#)) whereas horizontal threads are usually observed in active region prominences (e.g., [Okamoto et al. 2007](#)). However, [Schmieder et al. \(2010\)](#) pointed out that vertical threads might actually be a pile up of horizontal threads which seem vertical structures when projected in the plane of the sky. Since threads are observed in both the spines and barbs of filaments and prominences, it is believed that they are the prominence basic sub-structures.

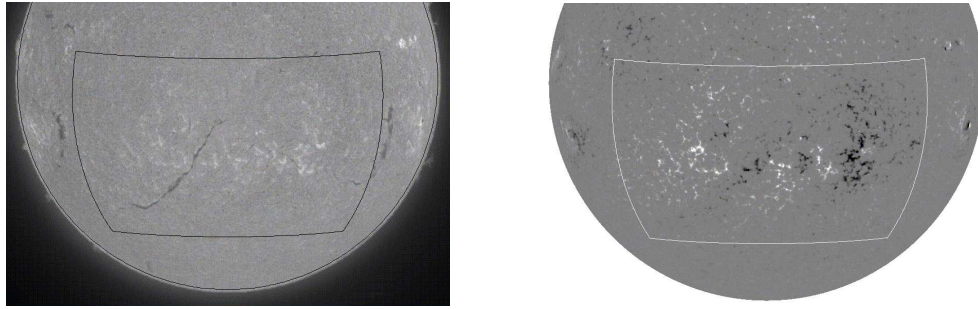


Figure 1.6: On the left: an $H\alpha$ image of a region of the solar disc where a filament is seen. On the right: a photospheric magnetogram of the same region, in which white and black colors represent opposite magnetic polarities. One can see that the filament is located between two regions of opposite polarity.

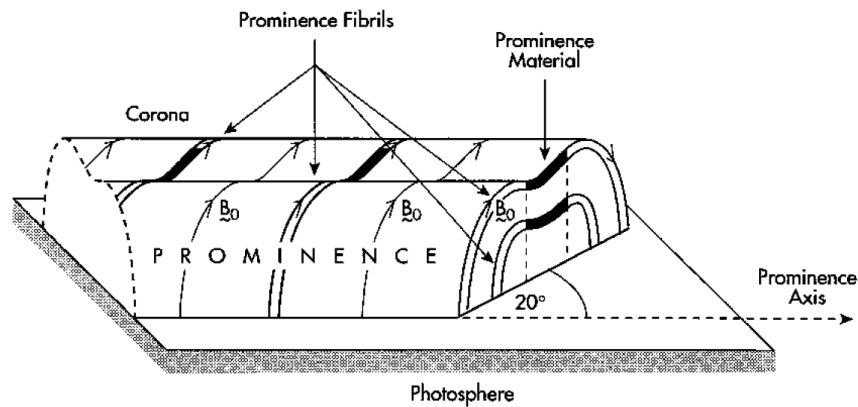


Figure 1.7: A cartoon representation of a prominence composed by several partially filled magnetic flux tubes. The dense part of the flux tubes would correspond to the observed threads in the $H\alpha$ images. From Joarder et al. (1997).

From the theoretical point of view, filament threads have been modeled as magnetic flux tubes anchored in the solar photosphere (e.g., Ballester & Priest 1989; Rempel et al. 1999), which are piled up to form the prominence body. In this interpretation, only part of the flux tubes would be filled with the cool ($\sim 10^4$ K) filament material, which would correspond to the observed threads. This is conceptually in agreement with prominence models similar to the Kippenhahn & Schlüter (1957) configuration, or its generalization by, e.g., Poland & Anzer (1971) or Hood & Anzer (1990), where the prominence material is trapped in dips near the apex of a magnetic arcade connecting two photospheric regions of opposite magnetic polarity (see Fig. 1.6). A schematic representation of a prominence formed by several fine structures is displayed in Figure 1.7. It has also been suggested from differential emission measure studies that each thread might be surrounded by its own prominence-corona transition region (PCTR) where the plasma physical properties would abruptly vary from filament to coronal conditions (Cirigliano et al. 2004). Alternatively, all threads might be embedded in a common and extensive medium with PCTR properties.

Mass flows along threads have been frequently reported (e.g., Zirker et al. 1994,

1998; Lin et al. 2003, 2005; Chae et al. 2008; Schmieder et al. 2010), with typical flow velocities of less than 30 km s^{-1} in quiescent prominences, although larger values have been detected in active region prominences (Okamoto et al. 2007). Therefore, some of the observed flow velocities may reach or be larger than the local sound speed of the prominence plasma. Regarding the presence of flows, a phenomenon which deserves special attention is the existence of the so-called counter-streaming flows, i.e., opposite flows within adjacent threads (see Zirker et al. 1998; Lin et al. 2003, for details).

1.4 Prominence oscillations: Observational evidence

The observational evidence of oscillations in prominences goes back to more than 40 years ago (Ramsey & Smith 1966). According to the amplitude of motions, prominence oscillations are usually classified in large- and small-amplitude oscillations.

1.4.1 Large-amplitude oscillations

They were the first type of oscillations observed in prominences. Since we do not study large-amplitude oscillations in the present work, their features are briefly commented here. The amplitude of these oscillations is of the order of 20 km s^{-1} or higher. They arise when a disturbance, e.g., a Moreton wave (Moreton 1960), impacts on a prominence side and shakes its whole body. As a consequence of this large-scale perturbation, the whole prominence vibrates during several periods until the oscillation is damped. Such phenomenon is also called *winking filament*, a term that comes from the optical effect caused by the oscillations on $H\alpha$ images. During the oscillations, the filament becomes visible in $H\alpha$ when it is at rest, but when its line-of-sight velocity is sufficiently large, the emission from the material falls outside the bandpass of the filter and the filament becomes invisible in $H\alpha$. Hence, the prominence alternatively shows up in and disappears from the images, causing a flickering effect. Recently, Tripathi et al. (2009) have reviewed both observational aspects and modeling efforts of large-amplitude prominence oscillations.

1.4.2 Small-amplitude oscillations

They were first detected in quiescent solar prominences 40 years ago (Harvey 1969). Their amplitude typically goes from less than 0.1 km s^{-1} to $2\text{--}3 \text{ km s}^{-1}$. The analysis of time series of line width, line intensity, and Doppler velocity reveals the local nature of the oscillations. They have been historically classified, according to their periods, in short- ($P < 10 \text{ min}$), intermediate- ($10 \text{ min} < P < 40 \text{ min}$) and long-period oscillations ($P > 40 \text{ min}$), although very short-periods of less than 1 min (e.g., Balthasar et al. 1993) and extreme ultra-long-periods of more than 8 hours (e.g., Foullon et al. 2004) have been reported. Nevertheless, the value of the period seems not to be related with the nature or the source of the trigger and is probably linked to the prominence eigenmode that is excited. Although most of the observations only reported periods, there are also a few determinations of the wavelength, λ , and phase speed, v_{ph} , of standing oscillations and propagating waves in prominences. For example, Molowny-Horas et al. (1997) reported maximum values of such quantities ($\lambda \leq 20,000 \text{ km}$ and $v_{\text{ph}} \leq 44 \text{ km s}^{-1}$) in a polar crown prominence, whereas Terradas et al. (2002) detected

1.4. PROMINENCE OSCILLATIONS: OBSERVATIONAL EVIDENCE

two propagating waves in the same prominence with $\lambda \approx 67,500$ km, $v_{\text{ph}} \approx 15$ km s⁻¹ and $\lambda \approx 50,000$ km, $v_{\text{ph}} \approx 12$ km s⁻¹, respectively. Moreover, [Terradas et al. \(2002\)](#) also found a standing wave with $\lambda \approx 44,000$ km and $v_{\text{ph}} \approx 12$ km s⁻¹ (see Fig. 1.8). The reader is referred to some recent reviews for a comprehensive information about the observational background of small-amplitude prominence oscillations (e.g., [Oliver & Ballester 2002](#); [Wiehr 2004](#); [Engvold 2008](#)).

Fine structure oscillations

Individual oscillations of prominence and filament fine structures have been frequently reported since telescopes with a high time and spatial resolution became available. Early works by [Yi et al. \(1991\)](#) and [Yi & Engvold \(1991\)](#), with a relatively low spatial resolution ($\sim 1''$), detected oscillatory variations in Doppler signals and He I line intensity from threads in quiescent filaments. Later, H α and Doppler observations with a much better spatial resolution ($\sim 0.''2$) found evidence of oscillations and propagating waves along quiescent filament threads ([Lin 2004](#); [Lin et al. 2007, 2009](#)), while observations from the Hinode spacecraft showed transverse oscillations of thread-like structures in both active region ([Okamoto et al. 2007](#)) and quiescent ([Ning et al. 2009a](#); [Schmieder et al. 2010](#)) prominences. Common features of these observations are that the reported periods are usually in a narrow range between 2 and 10 minutes, and that the velocity amplitudes are smaller than ~ 3 km s⁻¹. Therefore, the properties of thread oscillations are consistent with those of short-period oscillations reported with lower spatial resolutions, while intermediate- and long-period oscillations might be related to global oscillations of the whole prominence body. On the other hand, [Yi et al. \(1991\)](#), [Lin et al. \(2007\)](#), and [Schmieder et al. \(2010\)](#) suggested the presence of groups of neighboring threads that moved in phase, which may be a signature of collective interactions and oscillations. The large number of observations of oscillations and propagating waves in filament threads suggests that these phenomena are very frequent and ubiquitous in prominences. Since waves and mass flows have been simultaneously observed, it is likely that the presence of flows affects wave propagation in filament threads.

Damping of the oscillations

Another interesting characteristic of small-amplitude prominence oscillations is that they seem to be damped after a few periods. This behavior was previously suggested by some observations (e.g., [Landman et al. 1977](#); [Tsubaki & Takeuchi 1986](#)), but it was first extensively investigated by [Molowny-Horas et al. \(1999\)](#) and [Terradas et al. \(2002\)](#). These authors studied two-dimensional Doppler time-series from a quiescent prominence and found that oscillations detected in large areas of the prominence were typically damped after 2–3 periods (see left-hand side panel of Fig. 1.9), meaning that the oscillations were strongly attenuated. Similar results were obtained in a more recent work by [Mashnich et al. \(2009\)](#). Although the spatial resolution of the works by [Molowny-Horas et al. \(1999\)](#) and [Terradas et al. \(2002\)](#) was not enough to distinguish individual threads, one could assume that, as for large-scale oscillations, the individual and/or collective thread motions are also damped in time. This statement was recently confirmed by some high-resolution observations, which were able to resolve damped fine structure oscillations. For example, a damping pattern is seen in several high-resolution

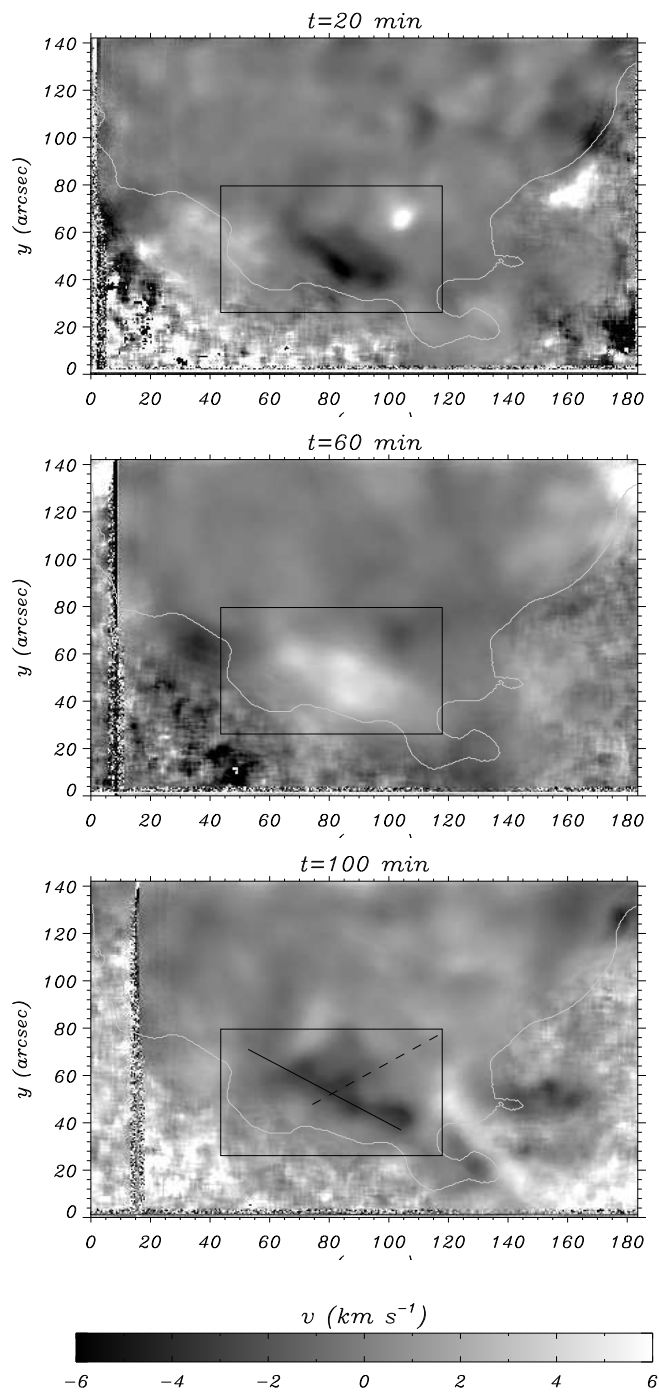


Figure 1.8: Two-dimensional Doppler velocity field at three different times in a quiescent solar prominence. The alternation of white (positive) and black (negative) velocities inside the black rectangle is a clear manifestation of an oscillatory phenomenon. The grey line represents the edge of the prominence body. From [Terradas et al. \(2002\)](#).

1.5. PROMINENCE OSCILLATIONS: THEORETICAL MODELING

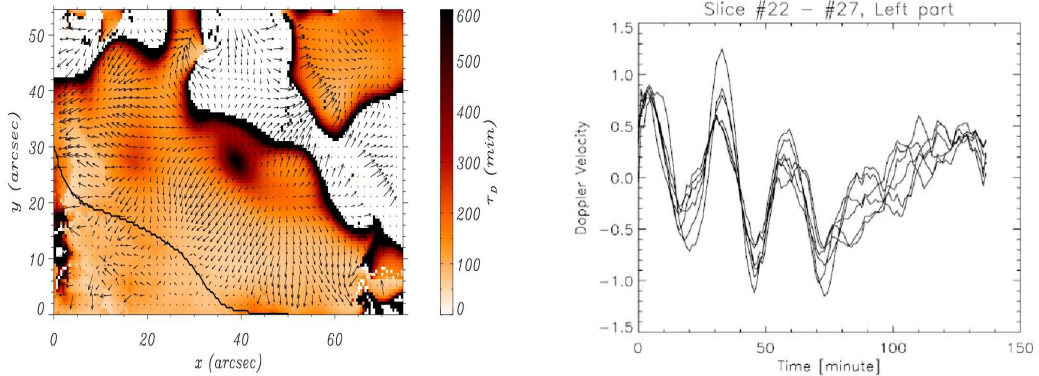


Figure 1.9: On the left: contour plot of the damping time, τ_D , obtained by [Terradas et al. \(2002\)](#) after fitting a sinusoidal function multiplied by a factor $\exp(-t/\tau_D)$ to their Doppler series. The damping times correspond to a few oscillatory periods. The arrows represent the wavevector and the continuous black line is the prominence edge. On the right: several Doppler velocity signals from different positions in an oscillating filament thread. The amplitude falls to the noise level after 3 periods, approximately. From [Lin \(2004\)](#).

Doppler time-series from individual filament threads by [Lin \(2004\)](#), see right-hand side panel of Fig. 1.9, as well as in the Hinode/SOT observations by [Ning et al. \(2009a\)](#), who reported a maximum number of 8 periods before the oscillations completely disappeared. It is expected that future observations will report more useful information concerning this damping phenomenon.

1.5 Prominence oscillations: Theoretical modeling

Here, we briefly discuss those works that have broached the theoretical investigation of prominence oscillations. As mentioned before, we restrict ourselves to studies concerning small-amplitude oscillations. From the theoretical point of view, small-amplitude prominence oscillations have been interpreted in the context of the magnetohydrodynamic (MHD) theory, more precisely, in terms of linear MHD waves. One can distinguish between works that considered models representing the whole prominence body, and so they studied global oscillations, to those investigations that focused on fine structure oscillations. While the former usually considered slab models, the latter typically adopted cylindrical configurations as a more realistic representation of prominence threads. Again, recent reviews on these issues are also available (e.g., [Ballester 2006](#); [Banerjee et al. 2007](#); [Oliver 2009](#); [Arregui & Ballester 2010](#))

1.5.1 Global oscillations

The whole prominence is modeled as a plasma slab of finite width. The slab can be isolated or, on the contrary, embedded into a hotter environment representing the solar corona. Some works have investigated the ideal, adiabatic, slow and fast MHD eigenmodes in slab-like configurations with a specific orientation of the magnetic field

(parallel, transverse, or skewed) with respect to the slab axis. Examples of such studies are [Joarder & Roberts \(1992a,b, 1993b\)](#), in which the effect of gravity is neglected and so straight magnetic field lines are considered. On the other hand, [Oliver et al. \(1992, 1993\)](#) took gravity into account and assumed curved field lines based on the [Kippenhahn & Schlüter \(1957\)](#) model modified to include the surrounding coronal plasma ([Poland & Anzer 1971](#)), whereas [Joarder & Roberts \(1993a\)](#) performed a similar study by considering the [Menzel \(1951\)](#) model. Despite this difference in the modeling, the studies by [Joarder & Roberts \(1992a,b, 1993a,b\)](#) and [Oliver et al. \(1992, 1993\)](#) agree in establishing a distinction between different normal modes depending on the dominant medium supporting the oscillation. Hence, internal modes are essentially supported by the prominence slab whereas external modes arise from the presence of the corona. In addition, hybrid (or string) modes appear due to the combined effect of both media. Hybrid and internal modes are reasonable candidates to explain the oscillations observed in large areas of a prominence (e.g., [Pouget et al. 2006](#)). In the context of this interpretation, slow and fast modes would be related to long- and intermediate-period oscillations, respectively.

It is worth mentioning that a few works, as [Oliver & Ballester \(1995, 1996\)](#) for the transverse magnetic field case, and [Soler et al. \(2007a\)](#) for the longitudinal magnetic field case, also considered the presence of a prominence-corona transition region (PCTR). While the oscillatory modes of the transverse case are similar to those without PCTR, a new class of modes, labeled as PCTR slow modes by [Soler et al. \(2007a\)](#), appear in the longitudinal case. These PCTR slow modes have been suggested by [Foullon et al. \(2009\)](#) as responsible for the very long-period oscillatory motions detected in a prominence with the SOHO/EIT instrument.

1.5.2 Fine-structure oscillations

A number of theoretical works have also attempted to explain the observed individual fine structure oscillations in terms of linear MHD waves supported by the thread body. First, investigations focused on the study of transverse oscillations supported by individual threads, taking into account the inhomogeneity of the plasma in the longitudinal direction (based on the model by [Ballester & Priest 1989](#)). To do so, the $\beta = 0$ approximation and Cartesian geometry were adopted for simplicity. [Joarder et al. \(1997\)](#) and [Díaz et al. \(2001\)](#) considered a longitudinally inhomogeneous Cartesian thread surrounded by the coronal medium. These authors found that only the low-frequency oscillatory modes are confined within the dense, central region of the thread, and that perturbations can achieve large amplitudes in the corona at long distances from the thread. Later, [Díaz et al. \(2003\)](#) assumed the same geometry, but took longitudinal propagation into account, and obtained a better confinement for the perturbations. Considering the more realistic and representative cylindrical geometry, [Díaz et al. \(2002\)](#) found that a longitudinally inhomogeneous cylindrical thread supports an even smaller number of trapped oscillations and that perturbations are much more efficiently confined within the cylinder in comparison with the Cartesian case. Later on, [Dymova & Ruderman \(2005\)](#) studied the same cylindrical configuration but assuming the thin tube approximation. Both [Díaz et al. \(2002\)](#) and [Dymova & Ruderman \(2005\)](#) concluded that the so-called kink MHD mode (see, e.g., [Edwin & Roberts 1983](#); [Goossens et al. 2009](#)) is the best candidate to explain the observed transverse, non-axisymmetric thread

1.5. PROMINENCE OSCILLATIONS: THEORETICAL MODELING

oscillations, and is also consistent with the reported short periods when realistic physical conditions of prominences are considered in the model¹.

An example of this interpretation in terms of kink modes is the work by [Terradas et al. \(2008\)](#), who performed the first application of the coronal seismology technique to prominence oscillations. [Terradas et al. \(2008\)](#) made use of the model by [Dymova & Ruderman \(2005\)](#) and the observations by [Okamoto et al. \(2007\)](#) to obtain lower limits of the prominence Alfvén speed. An interpretation of the observations by [Okamoto et al. \(2007\)](#) in terms of kink modes was also suggested by [Erdélyi & Fedun \(2007\)](#). Similarly, [Lin et al. \(2009\)](#) interpreted their observations of swaying threads in H α sequences as propagating kink waves and gave an estimation of the Alfvén speed².

Subsequently, the attention of authors turned to the study of collective oscillations of groups of threads. Cartesian geometry and the $\beta = 0$ approximation were adopted again for simplicity. Hence, [Díaz et al. \(2005\)](#) investigated the collective fast modes of systems of non-identical threads and found that the only non-leaky mode corresponds to that in which all threads oscillate in spatial phase. Later, [Díaz & Roberts \(2006\)](#) considered the limit of a periodic array of threads and obtained a similar conclusion. Therefore, these results seem to indicate that neighboring threads within the prominence should oscillate coherently, even if they have different physical properties. However, we have to point out that the Cartesian geometry provides quite an unrealistic confinement of perturbations, and so systems of more realistic cylindrical threads might not show such a clear collective behavior. This statement was confirmed by [Luna et al. \(2009\)](#), who made use of the T -matrix theory of scattering to study the collective oscillations of arbitrary systems of non-identical cylinders. Although [Luna et al. \(2009\)](#) applied their method to coronal loops, most of their results are also applicable to prominence threads. [Luna et al. \(2009\)](#) concluded that, contrary to the Cartesian case of [Díaz et al. \(2005\)](#), the collective behavior of the oscillations diminishes when cylinders with non-identical densities are considered, the oscillatory modes behaving in practice like individual modes of the cylinders if mildly different densities within the cylinders are assumed³.

1.5.3 Damping of the oscillations

Turning to the damping of oscillations, its theoretical investigation has been undertaken by a number of recent papers. Several non-ideal damping mechanisms have been proposed to explain the observed attenuation (e.g., [Ballai 2003](#)). In order to understand better these non-ideal effect and assess their efficiency as damping mechanisms, the complexity of the models has been improved step by step from very simple configurations, e.g., homogeneous media, to more realistic models representing prominence fine structures. Review papers focusing on the damping phenomenon are, e.g., [Oliver \(2009\)](#), [Mackay et al. \(2010\)](#), and [Arregui & Ballester \(2010\)](#).

¹Chapter 3 contains a comprehensive study of the kink mode and other MHD modes supported by a magnetic flux tube.

²More extensive details regarding the work by [Lin et al. \(2009\)](#) are given in Section 3.4.

³Chapter 8 contains an application of the technique developed by [Luna et al. \(2009\)](#) to the context of thread oscillations.

Homogeneous medium

By removing the ideal assumption and including dissipative terms in the basic MHD equations, several works studied the attenuation of propagating waves in a homogeneous and unbounded medium with prominence conditions. Following a treatment similar to than of [Porter et al. \(1994\)](#), the time and spatial damping by non-adiabatic effects (optically thin radiation losses, thermal conduction, and plasma heating) in a static medium was investigated by [Carbonell et al. \(2004, 2006\)](#), while the effect of a background mass flow was subsequently analyzed by [Carbonell et al. \(2009\)](#). The common conclusion of these investigations is that only slow and thermal waves are efficiently damped by non-adiabatic effects, radiative losses being the dominant mechanism, while fast waves are very slightly damped and Alfvén waves are completely unaffected.

On the other hand, the influence of partial ionization on the time damping of MHD waves has been also investigated in an unbounded medium. [Forteza et al. \(2007\)](#) followed the treatment by [Braginskii \(1965\)](#) and derived the full set of MHD equations along with the dispersion relation of linear waves in a partially ionized, single-fluid plasma (see also [Pinto et al. 2008](#)). The presence of electrons, protons, and neutral hydrogen atoms was taken into account, whereas helium and other species were not considered. In subsequent works, they extended their previous analysis by considering radiative losses and thermal conduction by electrons and neutrals ([Forteza et al. 2008](#)), and by studying the spatial damping in an equilibrium with mass flow ([Carbonell et al. 2010](#)). Their main results with respect to the fully ionized case were, first of all, that ion-neutral collisions (by means of the so-called Cowling's diffusion) can damp both Alfvén and fast waves but non-adiabatic effects remain only important for the damping of slow and thermal waves, and second, that there exist critical values of the wavenumber which constrain the wave behavior, since propagation for larger wavenumbers is forbidden. Later on, the effect of the presence of neutral and singly ionized helium on the time damping was assessed by [Soler et al. \(2010a\)](#), who found that due to the small abundance of helium in prominences ($\sim 10\%$), these species can be safely neglected.

Slab models

The efficiency of several mechanisms for the damping of prominence slab eigenmodes has also been studied. Regarding works that neglected the presence of the coronal medium, [Terradas et al. \(2001\)](#) studied the attenuation of oscillations by radiative losses based on the Newtonian law of cooling with a constant relaxation time in both the [Kippenhahn & Schlüter \(1957\)](#) and [Menzel \(1951\)](#) prominence models, whereas [Terradas et al. \(2005\)](#) performed a more complete treatment of non-adiabatic effects by assuming optically thin radiation, heating, and thermal conduction in a homogeneous slab model. The main conclusion of these studies is similar to that of studies in homogeneous media, i.e., that only slow waves are efficiently attenuated by thermal effects, radiation being the dominant damping mechanism in the range of typically observed wavelengths in prominences (from 5×10^3 km to 10^5 km according to [Oliver & Ballester 2002](#)), but fast waves remain practically undamped.

Later on, [Soler et al. \(2007b\)](#) and [Soler et al. \(2009a\)](#) considered a prominence slab embedded in the solar corona, with the magnetic field parallel and perpendicular to the slab axis, respectively, and performed a treatment of the non-adiabatic effects as in

1.5. PROMINENCE OSCILLATIONS: THEORETICAL MODELING

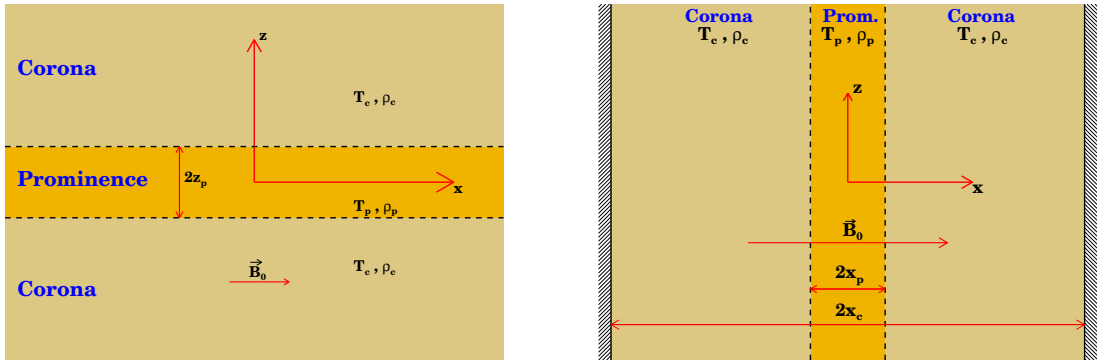


Figure 1.10: On the left: model of a prominence slab with a longitudinal magnetic field considered by Soler et al. (2007b). On the right: the equivalent model but with a transverse magnetic field adopted by Soler et al. (2009a).

Terradas et al. (2005). Schematic representations of the models considered by Soler et al. (2007b, 2009a) are displayed in Figure 1.10. Regarding the parallel magnetic field case, Soler et al. (2007b) obtained that the presence of the coronal medium can reduce the damping time of fast modes due to the influence of coronal thermal conduction, although this effect is not enough to obtain fast mode damping times compatible with those observed. In the perpendicular case, Soler et al. (2009a) showed that fast modes may be thermally unstable for some values of the wavelength due to the heat transfer from the corona to the prominence slab along magnetic field lines.

It is also worth mentioning the works by Schutgens (1997a,b) and Schutgens & Tóth (1999). These works do not specifically use slab models, but it seems appropriate to include them here because they are concerned with global prominence oscillations. Schutgens (1997a,b) modeled a filament as an infinitely thin line current surrounded by a magnetic arcade and suspended above a perfectly conducting plane representing the solar photosphere (Kuperus & Raadu 1974). They found a quite efficient attenuation of the oscillations supported by the configuration, with damping times corresponding to a few oscillatory periods. Schutgens (1997a,b) claimed that the damping is caused by time delays in the communication of disturbances between the filament and the photosphere, although an alternative interpretation in terms of wave leakage was suggested by Oliver (2009). Finally, Schutgens & Tóth (1999) performed an investigation similar to that of Schutgens (1997a,b) but considered a current-carrying filament of finite width and used the isothermal MHD equations. Schutgens & Tóth (1999) also obtained an efficient damping of the oscillations and interpreted their results in terms of emission of waves (leakage) by the filament. Although the works by Schutgens (1997a,b) and Schutgens & Tóth (1999) are relevant because they are the only investigations to date that include the effect of the photospheric surface current and a complex magnetic structure, one must be aware of the quite strong simplifications of their models.

Cylindrical models

The next obvious step is to extend these previous investigations by considering cylindrical models, thus the damping of fine structure oscillations can be studied. Arregui et al. (2008) considered a transverse inhomogeneous transitional layer between a cylindrical

filament thread and the corona, and investigated the kink mode damping by resonant absorption in the Alfvén continuum. They obtained a damping time of approximately 3 periods for typical wavelengths of prominence oscillations and a typical density contrast between the filament and the coronal plasma, meaning that resonant absorption is a good candidate to be the damping mechanism of transverse thread oscillations. Subsequently, other mechanisms have been studied in a number of papers included in the present thesis, so we do not give here more details but refer the reader to the following Chapters of the Thesis.

In Chapter 4, which is based on Soler et al. (2008), we investigate the effect of non-adiabatic mechanisms and mass flows on the damping of oscillations in homogeneous filament threads. Next, the wave propagation and damping in a partially ionized thread is studied in Chapter 5, which contains results from Soler et al. (2009d). Later on, the investigation on the damping by resonant absorption in a transverse inhomogeneous filament thread performed by Arregui et al. (2008) is extended by considering also resonant absorption in the slow continuum (Soler et al. 2009c), and the joint effect of resonant absorption and partial ionization (Soler et al. 2009e), both works included in Chapter 6. Subsequently, Chapter 7 extends the results of Chapter 6 by taking into account the longitudinal inhomogeneity of the plasma in the fine structure (Soler et al. 2010b). Finally, in Chapters 8 and 9 we investigate the damping of collective oscillations of cylindrical threads by non-adiabatic effects (Soler et al. 2009b) and resonant absorption (Soler et al. 2010c).

2

Magnetohydrodynamic Theory

2.1 Plasma definition and collective behavior

Plasma is often called the fourth state of matter. Some estimates suggest that up to 99% of matter in the entire visible universe is plasma. According to [Chen \(1984\)](#), *a plasma is a quasi-neutral gas of charged particles and neutral particles which exhibits collective behaviour*. Since a plasma is macroscopically quasi-neutral, the basic difference with a fully neutral gas (when no magnetic fields are present) is the long-range, collective interaction that a plasma presents. In solar physics, it is assumed that the coronal medium is in plasma state. This is also commonly assumed for the prominence material. Hence, to test this assertion one must prove that both media at least are ionised and show collective behavior. The first condition can be easily verified through Saha's Equation, which gives the ratio of the number density of ions, n_i , to neutrals, n_n , at a temperature T , assuming optically thin hydrogen lines,

$$\frac{n_i}{n_n} = \left(\frac{2\pi m_e k_B}{h^2} \right)^{3/2} \frac{T^{3/2}}{n_e} \exp\left(-\frac{U_i}{k_B T}\right), \quad (2.1)$$

where n_e is the number density of electrons, $k_B = 1.38 \times 10^{-23} \text{ m}^2 \text{ kg s}^{-2} \text{ K}^{-1}$ is Boltzmann's constant, $m_e = 9.1 \times 10^{-31} \text{ kg}$ is the electron mass, $h = 6.63 \times 10^{-34} \text{ m}^2 \text{ kg s}^{-1}$ is Planck's constant, and U_i is the ionization energy ($U_i = 13.6 \text{ eV}$ for hydrogen). Equation (2.1) gives $n_i/n_n \approx 2.4 \times 10^8$ for coronal conditions, and $n_i/n_n \approx 4.7 \times 10^2$ for prominence parameters. Thus, the condition of partial ionization is well-satisfied in both media.

On the other hand, the following conditions should be satisfied for a collective plasma behavior:

1. The long-range Coulomb interaction between charged particles should dominate over the short-range binary collisions with neutrals. Considering τ_0 as the typical time-scale for collective motions and τ_n as the mean time between collisions of charged particles with neutrals, this condition reduces to

$$\tau_0 \ll \tau_n. \quad (2.2)$$

The time-scale τ_0 can be related to the frequency of the global oscillatory motions of the plasma, ν , as $\tau_0 \sim \nu^{-1}$. On the other hand, a simplified expression for τ_n can be obtained as the ratio of the mean free path of particles, $\lambda_{\text{mfp}} = (n_n \sigma)^{-1}$, where σ is the collisions cross-section, to the thermal speed, $v_{\text{th}} \approx (k_B T / m_p)^{1/2} \approx 100 T^{1/2}$,

where m_p is the proton mass. Hence, assuming $\sigma \approx 10^{-19} \text{ m}^2$ for neutral hydrogen-proton collisions (Goedbloed & Poedts 2004), one has

$$\tau_n \approx \frac{10^{17}}{n_n \sqrt{T}}. \quad (2.3)$$

Considering that for a typical coronal plasma $n_n \sim 4 \times 10^{-7} \text{ m}^{-3}$, Equation (2.3) gives $\tau_n \approx 2 \times 10^{20} \text{ s}$. So, one has that for a coronal plasma $\nu \gg 5 \times 10^{-21} \text{ Hz}$, meaning that Equation (2.2) is not a “hard” restriction on the time-scales for plasma behavior in the solar corona. On the other hand, we need the value of the neutral number density in prominence conditions to give an estimation of τ_n . We must note here that n_n is not well-known for prominence plasmas. Although some authors have provided different estimations for n_n , the estimated values differ by several orders of magnitude (Patsourakos & Vial 2002; Labrosse et al. 2010), and a reliable estimation of n_n is needed in order to compute the value of τ_n for prominence conditions. Nevertheless, τ_n must definitely be several orders of magnitude smaller in prominences than in the corona. Thus, the condition given by Equation (2.2) is more restrictive in the case of prominences, meaning that that ion-neutral collisions could have a relevant role in the behavior of prominence plasmas.

2. There should be frequent enough collisions between electrons and ions to establish fluid behavior. The mean time between electron-ion collisions, τ_e , can be estimated from the mean frequency of electron-ion collisions, ν_{ei} , as $\tau_e \sim \nu_{ei}^{-1}$. Expressions for ν_{ei} are provided by, e.g., De Pontieu et al. (2001) and Goossens (2003). Therefore, τ_e can be written as

$$\tau_e \approx \frac{12\pi^{3/2}\varepsilon^2 m_e^{1/2}}{\sqrt{2}e^4 n_i \ln \Lambda} (k_B T)^{3/2}, \quad (2.4)$$

where $e = 1.6 \times 10^{-19} \text{ C}$ is the electron charge, ε is the electric permittivity ($\varepsilon = 8.854 \times 10^{-12} \text{ F m}^{-1}$ in vacuum), and $\ln \Lambda$ the Coulomb logarithm, whose value is generally between 5 and 20 and has a weak dependence on temperature and density (Priest 1982). According to Equation (2.4), the numerical value of τ_e in coronal conditions is $\tau_e \approx 1.5 \times 10^{-1} \text{ s}$, while for a prominence plasma $\tau_e \approx 2 \times 10^{-6} \text{ s}$. Taking into account this restriction along with that for ion-neutral collisions (Eq. [2.3]), we see that the typical time-scale for collective plasma interactions, τ_0 , should satisfy $\tau_e \ll \tau_0 \ll \tau_n$. Such a condition is easily fulfilled in both coronal and prominence media.

3. The length-scale of plasma dynamics should be much larger than the minimum size over which the condition of quasi-neutrality is satisfied. Thermal fluctuations can produce local charge imbalances and create huge electric fields. These electric fields cause the acceleration of particles, and the charge imbalance is neutralized almost instantaneously. These charge imbalances can occur when the thermal energy of particles, $k_B T$, is comparable with their electrostatic energy, $e\phi$. Defining the Debye length, λ_D , as the typical size of the region where the condition $k_B T \approx e\phi$ is fulfilled, then the length-scales of plasma dynamics should be much larger than

2.1. PLASMA DEFINITION AND COLLECTIVE BEHAVIOR

the Debye length. The Debye length can be estimated through Poisson's law as

$$\frac{d^2\phi}{dx^2} = \frac{1}{\varepsilon}en_e, \quad \frac{\phi}{\lambda_D^2} \sim \frac{en_e}{\varepsilon}, \quad e\phi \sim \frac{e^2n_e\lambda_D^2}{\varepsilon}, \quad (2.5)$$

where ϕ is the electrostatic potential. By imposing $k_B T \approx e\phi$, one obtains

$$\lambda_D \approx \sqrt{\frac{\varepsilon_0 k_B T}{e^2 n_e}}. \quad (2.6)$$

For coronal conditions $\lambda_D \approx 7$ cm, while for prominence conditions $\lambda_D \approx 0.006$ cm. Both values are much smaller than typical coronal and prominence spatial scales (see Table 1.2).

4. For statistical considerations, the number of particles N_D inside a Debye sphere, i.e., a sphere of radius λ_D , should be big enough. This means $N_D \gg 1$. The expression for N_D is

$$N_D = \frac{4}{3}\pi\lambda_D^3 n_e \approx 1.4 \times 10^6 \sqrt{\frac{T^3}{n_e}}, \quad (2.7)$$

which for coronal conditions gives $N_D \approx 1.4 \times 10^9$, and for prominence conditions $N_D \approx 10^4$. Again, the statistical condition is easily satisfied in both media.

One must bear in mind that coronal and prominence plasmas are permeated by magnetic fields. Hence, in addition to the microscopic or small-scale conditions involving thermodynamic quantities, more global and macroscopic conditions involving the magnetic field should be considered and incorporated to the plasma description. These additional conditions are listed below.

1. The macroscopic time-scale of the plasma processes should be much larger than the inverse of the cyclotron frequency of electrons and ions, namely $\Omega_{e,i}^{-1}$, where subscripts e and i stand for electrons and ions, respectively. According to [Goedbloed & Poedts \(2004\)](#), $\Omega_{e,i}^{-1}$ is related to the magnetic field strength B as

$$\Omega_{e,i}^{-1} = \frac{m_{e,i}}{eB}. \quad (2.8)$$

Assuming $B = 10$ G as a typical magnetic field strength in quiescent prominences and the corona, Equation (2.8) gives $\Omega_e^{-1} \approx 5.7 \times 10^{-9}$ s for electrons and $\Omega_i^{-1} \approx 10^{-5}$ s for ions. We see that ions provide with the most limiting condition due to their greater mass, although the above restriction is well-satisfied in prominence and coronal plasmas.

2. The macroscopic length-scale of plasma processes should be much larger than the cyclotron radii, $r_{e,i}$, of electrons and ions. Again, following [Goedbloed & Poedts \(2004\)](#), this quantity is inversely proportional to the magnetic field strength,

$$r_{e,i} = \frac{m_{e,i} v_{\perp e,i}}{eB}, \quad (2.9)$$

where $v_{\perp e,i}$ is the perpendicular particle velocity to the magnetic field. Considering for simplicity $v_{\perp e,i} \approx v_{th e,i} \approx (k_B T/m_{e,i})^{1/2}$ and $B = 10$ G, one can obtain

$r_e \approx 0.02$ m for electrons and $r_i \approx 1$ m for ions under coronal conditions, and $r_e \approx 0.002$ m, $r_i \approx 0.09$ m in a prominence medium. As before, ions provide with the most limiting condition but the estimated value of r_i is much smaller than the typical size of prominences and coronal magnetic structures.

We have proved that all these microscopic and macroscopic restrictions are well-satisfied under coronal and prominence conditions. Therefore, one can safely assume that both media are in plasma state. Now, in order to describe prominence and coronal phenomena, we need a physical theory which tells us how a magnetized plasma behaves. The bases of such theory are presented next.

2.2 Magnetohydrodynamic equations

2.2.1 Assumptions of the magnetohydrodynamic approximation

The most extended physical theory that describes the macroscopic behavior of a medium in a plasma state and in the presence of a magnetic field is known as magnetohydrodynamics (MHD). In the literature, the main equations of this theory are usually introduced from two different points of view. The first one starts from Boltzmann's kinetic theory and combines it with Maxwell's equations of electromagnetism in order to obtain the basic MHD equations through several approximations and assumptions. This derivation, which requires a long mathematical handling, can be followed in, e.g., [Goossens \(2003\)](#). On the other hand, the second method considers from the beginning the well-known fundamental equations of fluid dynamics together with Maxwell's equations, on the basis that a plasma is assumed a fluid made of charged and neutral particles, and permeated by electric and magnetic fields. The second approach is mathematically simpler and shorter, and one can find it in, e.g., [Priest \(1982\)](#).

In this work we choose an intermediate way. We derive the basic MHD equations starting from the fundamental equations of fluid dynamics and electromagnetism as in [Priest \(1982\)](#), but incorporate the general description of [Braginskii \(1965\)](#) for a partially ionized plasma composed by different species. When the equations of particular species are combined to obtain the single-fluid equations, our analysis follows closely that of [Goossens \(2003\)](#). Next, we briefly summarize the fundamental assumptions which lead us from the general equations to the final MHD expressions:

1. The plasma is treated as a continuum. As mentioned in Section 2.1, this assumption is valid when the length-scale of plasma processes is much larger than the species cyclotron radius.
2. The plasma is assumed to be in thermodynamic equilibrium. This means that the typical time-scales and length-scales are much larger than the collision time and the mean free path of particles, respectively.
3. Due to the presence of magnetic fields, some of the plasma properties are highly anisotropic. For example, the coefficient of thermal conductivity takes values across and along the direction of the magnetic field which differ by several orders of magnitude (see Sec. 2.2.4).

2.2. MAGNETOHYDRODYNAMIC EQUATIONS

4. The plasma is treated as a single fluid. Global plasma magnitudes are considered, which are computed as the sum of the magnitudes of each species (i.e., ions, electrons, and neutrals). In the derivation of global plasma magnitudes, all remaining terms related with a single species are neglected based on several physical arguments.
5. The equations are written in an inertial frame and relativistic effects are neglected because typical plasma velocities in the solar corona are much smaller than the speed of light.
6. A single-fluid Ohm's Law is adopted rather than the general multifluid version. This Ohm's Law, however, can be generalized to contain diffusion terms representing collisions between different species when the plasma is partially ionized (see details in Sec. 2.2.3).

Finally, note that all the following expressions are written in MKS units.

2.2.2 Fluid equations

In the single-fluid approach (see, e.g., [Braginskii 1965](#)) and assuming a hydrogen plasma composed by ions (protons), electrons, and neutrals, we define the total plasma velocity, \vec{v} , as

$$\vec{v} = \xi_e \vec{v}_e + \xi_i \vec{v}_i + \xi_n \vec{v}_n, \quad (2.10)$$

with ξ_β the relative density of species β , and \vec{v}_β the corresponding species velocity, where subscripts e, i, and n explicitly denote electron, ion, and neutral species, respectively. Due to the small electron mass, the electron contribution can be neglected from Equation (2.10), so

$$\vec{v} \approx \xi_i \vec{v}_i + \xi_n \vec{v}_n. \quad (2.11)$$

Equivalently, the fluid total density, ρ , and gas pressure, p , are

$$\rho = \rho_e + \rho_i + \rho_n \approx \rho_i + \rho_n, \quad (2.12)$$

$$p = p_e + p_i + p_n, \quad (2.13)$$

where $\rho_\beta = n_\beta m_\beta$ and $p_\beta = n_\beta k_B T_\beta$, with n_β , m_β , and T_β the number density, mass particle, and temperature of species β , respectively. Since $\rho_\beta = \xi_\beta \rho$, we get the relation $\xi_i + \xi_n \approx 1$. In addition, the macroscopic neutrality of the plasma imposes $n_e = n_i$.

Equation of state

We assume a strong thermal coupling between species, so it is possible to define a single temperature, T , representing the whole fluid. Then, the total density, gas pressure, and temperature are related as

$$p = \rho R \frac{T}{\tilde{\mu}}, \quad (2.14)$$

where $R = 8.3 \times 10^3 \text{ m}^2 \text{ s}^{-2} \text{ K}^{-1}$ is the ideal gas constant and $\tilde{\mu}$ is the mean atomic weight, i.e., the average mass per particle in units of the proton mass, defined as

$$\tilde{\mu} = \frac{1}{1 + \xi_i}. \quad (2.15)$$

CHAPTER 2. MAGNETOHYDRODYNAMIC THEORY

For fully ionized plasmas $\xi_i = 1$ and $\tilde{\mu} = 0.5$, whereas for a neutral gas $\xi_i = 0$ and $\tilde{\mu} = 1$. Therefore, the quantity $\tilde{\mu}$ can be used to indicate the plasma ionization degree. In some cases, an effective temperature enclosing the contribution of both the temperature and the mean atomic weight, namely \tilde{T} , is defined as

$$\tilde{T} = \frac{T}{\tilde{\mu}}. \quad (2.16)$$

Mass conservation

A plasma, as a continuous medium, must satisfy the equation of mass conservation. This equation can be easily obtained by adding the mass conservation equations of each species, resulting in

$$\frac{D\rho}{Dt} + \rho \nabla \cdot \vec{v} = 0, \quad (2.17)$$

where $\frac{D}{Dt} \equiv \frac{\partial}{\partial t} + \vec{v} \cdot \nabla$ is the material (or total) derivative for time variations following the plasma motion.

Momentum equation

The momentum equation (or equation of motion) establishes the force balance to which a unit volume of plasma is submitted. As for the mass conservation equation, a simple way to obtain it is to add the momentum equations of each particular species. Since this procedure is not so obvious as for the mass conservation equation, we give more details next.

In an inertial frame, the momentum equation of species β takes the following form (Braginskii 1965),

$$m_\beta n_\beta \frac{D\vec{v}_\beta}{Dt} = -\nabla p_\beta + Z_\beta n_\beta e \left(\vec{E} + \vec{v}_\beta \times \vec{B} \right) + m_\beta n_\beta \vec{g} - \nabla \cdot \mathbf{\Pi}_\beta - \sum_{\beta' \neq \beta} \vec{\mathcal{R}}_{\beta\beta'}. \quad (2.18)$$

The terms on the right-hand side of Equation (2.18) correspond to, from left to right, the gas pressure gradient force, the Lorentz force, the gravity force, the viscous force, and a term that accounts for the transfer of momentum due to collisions between different species. In Equation (2.18), \vec{E} and \vec{B} are the electric and magnetic fields, respectively, \vec{g} is the acceleration of gravity, $\mathbf{\Pi}$ is the viscosity tensor, and $\vec{\mathcal{R}}_{\beta\beta'}$ is the collision term between species β and β' , namely

$$\vec{\mathcal{R}}_{\beta\beta'} = \alpha_{\beta\beta'} (\vec{v}_\beta - \vec{v}_{\beta'}), \quad (2.19)$$

with $\alpha_{\beta\beta'}$ the friction coefficient of species β and β' (see details in Sec. 2.2.3). The factor Z_β in Equation (2.18) is $Z_i = 1$, $Z_e = -1$, and $Z_n = 0$ for ions, electrons, and neutrals, respectively. Next, we simply add the corresponding equations of ions, electrons, and neutrals, and see that the collisional terms cancel each other because we assume elastic collisions. In addition, we define the density current, \vec{j} , in terms of the difference of electron and ion velocities as

$$\vec{j} = e (n_i \vec{v}_i - n_e \vec{v}_e) = en_e (\vec{v}_i - \vec{v}_e). \quad (2.20)$$

2.2. MAGNETOHYDRODYNAMIC EQUATIONS

Hence, the total momentum equation is

$$\rho \frac{D\vec{v}}{Dt} = -\nabla p + \vec{j} \times \vec{B} + \vec{F}_g + \vec{F}_\nu, \quad (2.21)$$

where \vec{F}_g and \vec{F}_ν are the total gravity and viscous forces, respectively. The Lorentz force is usually rewritten by using the non-relativistic version of Ampere's Law, namely

$$\vec{j} = \frac{1}{\mu} \nabla \times \vec{B}, \quad (2.22)$$

giving the following more common expression for the magnetic force,

$$\vec{j} \times \vec{B} = \frac{1}{\mu} (\nabla \times \vec{B}) \times \vec{B}, \quad (2.23)$$

where μ is the magnetic permeability ($\mu = 4\pi \times 10^{-7} \text{ N A}^{-2}$ in vacuum). Furthermore, by means of the vector identity $(\nabla \times \vec{B}) \times \vec{B} = (\vec{B} \cdot \nabla) \vec{B} - \frac{1}{2} \nabla (\vec{B} \cdot \vec{B})$, Equation (2.23) reduces to

$$\vec{j} \times \vec{B} = \frac{1}{\mu} \left[(\vec{B} \cdot \nabla) \vec{B} - \frac{1}{2} \nabla (\vec{B} \cdot \vec{B}) \right]. \quad (2.24)$$

The first term on the right-hand side of Equation (2.24) represents the magnetic tension, that appears when magnetic field lines are curved. The second term is the gradient of an scalar quantity called the magnetic pressure force, namely

$$-\frac{1}{2\mu} \nabla (\vec{B} \cdot \vec{B}) = -\nabla \left(\frac{B^2}{2\mu} \right) \equiv -\nabla p_m. \quad (2.25)$$

Due to the presence of the magnetic field, an element of plasma is affected by two kinds of pressure: the gas pressure, p , and the magnetic pressure, p_m . The sum of both quantities gives us the total pressure, p_T , namely

$$p_T = p + p_m = p + \frac{B^2}{2\mu}. \quad (2.26)$$

The ratio of the gas pressure to the magnetic pressure is the plasma β parameter,

$$\beta = \frac{p}{p_m}, \quad (2.27)$$

which quantifies the importance of the former with respect to the latter. For some coronal applications, such as waves in coronal loops, the $\beta = 0$ approximation (by which gas pressure is neglected) is assumed.

On the other hand, a simplified expression for the viscous force in the case of weak magnetic field is

$$\vec{F}_\nu = -\nabla \cdot \mathbf{\Pi} \approx \rho\nu \left[\nabla^2 \vec{v} + \frac{1}{3} \nabla (\nabla \cdot \vec{v}) \right], \quad (2.28)$$

where ν is the coefficient of kinematic viscosity (see [Braginskii 1965](#), for the general expression of the viscous force). In the incompressible case, i.e., $\nabla \cdot \vec{v} = 0$, Equation (2.28) simplifies to

$$\vec{F}_\nu \approx \rho\nu \nabla^2 \vec{v}. \quad (2.29)$$

The Reynolds number, R_e , is a dimensionless quantity that gives the importance of the viscous force with respect to the inertial term in the equation of motion, and is defined as

$$R_e = \frac{|\rho \vec{v} \cdot \nabla \vec{v}|}{|\rho \nu \nabla^2 \vec{v}|} \sim \frac{\lambda_0 v_0}{\nu}, \quad (2.30)$$

with λ_0 and v_0 typical length- and velocity-scales. For coronal and prominence parameters, $R_e \gg 1$ and therefore the viscous force is usually neglected.

Finally, the total gravity force, \vec{F}_g , is

$$\vec{F}_g = -\rho g \hat{u}, \quad (2.31)$$

where \hat{u} is the unitary vector in the vertical direction, and g is the local gravitational acceleration. The effect of the gravity force is often neglected in comparison with the Lorentz and pressure forces. If both gravity and viscous forces are neglected, the ideal version of the momentum equation is

$$\rho \frac{D\vec{v}}{Dt} = -\nabla p + \frac{1}{\mu} (\nabla \times \vec{B}) \times \vec{B}. \quad (2.32)$$

2.2.3 Generalized induction equation for a partially ionized plasma

The induction equation is a relation that tells us how magnetic fields are created and destroyed. To deduce it, we must combine Maxwell's equations with an appropriate expression of Ohm's Law for a partially ionized plasma. Maxwell's equations are

$$\nabla \times \vec{B} = \mu \vec{j} + \frac{1}{c^2} \frac{\partial \vec{E}}{\partial t}, \quad (2.33)$$

$$\nabla \cdot \vec{B} = 0, \quad (2.34)$$

$$\nabla \times \vec{E} = -\frac{\partial \vec{B}}{\partial t}, \quad (2.35)$$

$$\nabla \cdot \vec{E} = \frac{\rho^*}{\varepsilon}, \quad (2.36)$$

where ρ^* is the density charge and c is the speed of light ($c = 2.998 \times 10^8$ m s⁻¹ in vacuum). The second term on the right-hand side of Equation (2.33) is neglected in non-relativistic MHD, which is justified by comparing the size of this term with the size of the left-hand side term. From Equation (2.35),

$$\frac{E_0}{\lambda_0} \sim \frac{B_0}{\tau_0}, \quad (2.37)$$

where λ_0 and τ_0 are typical length- and time-scales. Thus, the size of the second term on the right-hand side of Equation (2.33) is

$$\frac{E_0}{c^2 \tau_0} \sim \frac{B_0 \lambda_0}{c^2 \tau_0^2} \sim \frac{v_0^2 B_0}{c^2 \lambda_0} \sim \frac{v_0^2}{c^2} |\nabla \times \vec{B}| \ll |\nabla \times \vec{B}|, \quad (2.38)$$

since $v_0^2/c^2 \ll 1$, v_0 being a typical plasma velocity.

The process that leads us to obtain a valid Ohm's Law for a partially ionized plasma is long and arduous. For this reason, we refer the reader to [Forteza et al. \(2007\)](#) and

2.2. MAGNETOHYDRODYNAMIC EQUATIONS

Pinto et al. (2008) for extensive details, while we give here a summary of the method. First, we define $\vec{w} \equiv \vec{v}_i - \vec{v}_n$, and combine the momentum equations of electron, ions, and neutrals (Eq. [2.18]) to obtain the following expression after neglecting the electron inertia,

$$\vec{w} \approx \frac{1}{\alpha_n} \left(\xi_n \vec{j} \times \vec{B} + \frac{\alpha_{en}}{en_e} \vec{j} - \vec{G} \right), \quad (2.39)$$

where $\alpha_n = \alpha_{en} + \alpha_{in}$ is the neutral friction coefficient, with α_{en} and α_{in} the particular electron-neutral and ion-neutral friction coefficients, respectively, and \vec{G} is the pressure function defined as

$$\vec{G} = \xi_n \nabla (p_e + p_i) - \xi_i \nabla p_n = 2\xi_n \nabla p_i - \xi_i \nabla p_n. \quad (2.40)$$

Next, we express the electron velocity as

$$\vec{v}_e = \vec{v} - \frac{1}{en_e} \vec{j} + \xi_n \vec{w}, \quad (2.41)$$

and use Equations (2.20) and (2.39) to finally obtain the expression of the effective electric field, \vec{E}^* , from the electron momentum equation, namely

$$\begin{aligned} \vec{E}^* = \vec{E} + \vec{v} \times \vec{B} &= \frac{1}{e^2 n_e^2} \left(\alpha_e - \frac{\alpha_{en}^2}{\alpha_n} \right) \vec{j} + \frac{1}{en_e} \left(1 - 2\xi_n \frac{\alpha_{en}}{\alpha_n} \right) \vec{j} \times \vec{B} \\ &- \frac{\xi_n^2}{\alpha_n} \left(\vec{j} \times \vec{B} \right) \times \vec{B} + \frac{\xi_n}{\alpha_n} \vec{G} \times \vec{B} + \frac{1}{en_e} \left(\frac{\alpha_{en}}{\alpha_n} \vec{G} - \nabla p_e \right), \end{aligned} \quad (2.42)$$

with $\alpha_e = \alpha_{ei} + \alpha_{en}$ the total electron friction coefficient. Equation (2.42) provides us with the relation between \vec{E} , \vec{j} , and \vec{B} that we are looking for, i.e., the generalized Ohm's Law. The last step is to use Equations (2.22) and (2.35) to eliminate \vec{E} and \vec{j} in favor of \vec{B} , so the general form of the induction equation for a partially ionized plasma is

$$\begin{aligned} \frac{\partial \vec{B}}{\partial t} &= \nabla \times \left(\vec{v} \times \vec{B} \right) - \nabla \times \left[\frac{1}{\mu e^2 n_e^2} \left(\alpha_e - \frac{\alpha_{en}^2}{\alpha_n} \right) \nabla \times \vec{B} \right] \\ &- \nabla \times \left\{ \frac{1}{\mu en_e} \left[1 - 2\xi_n \frac{\alpha_{en}}{\alpha_n} \right] \left(\nabla \times \vec{B} \right) \times \vec{B} \right\} \\ &+ \nabla \times \left\{ \frac{\xi_n^2}{\mu \alpha_n} \left[\left(\nabla \times \vec{B} \right) \times \vec{B} \right] \times \vec{B} \right\} \\ &- \nabla \times \left[\frac{\xi_n}{\alpha_n} \vec{G} \times \vec{B} \right] - \nabla \times \left[\frac{1}{en_e} \left(\frac{\alpha_{en}}{\alpha_n} \vec{G} - \nabla p_e \right) \right]. \end{aligned} \quad (2.43)$$

Equation (2.43) together with the condition upon the divergence of \vec{B} given by Equation (2.34), govern the magnetic field evolution. The terms on the right-hand side of Equation (2.43) usually receive the following names in the literature: the convective term, Ohm's diffusion, Hall's diffusion, the ambipolar diffusion, the diamagnetic current term, and Biermann's battery, respectively. Among these terms, Biermann's battery is the less important in solar atmospheric plasmas, since it is only relevant when large pressure gradients are present, a situation more representative of stellar interiors, whereas Biermann's battery term is identically zero in a homogeneous plasma. For these reasons, we hereafter neglect this term. The other non-ideal terms appear due to different effects.

CHAPTER 2. MAGNETOHYDRODYNAMIC THEORY

For example, Ohm's diffusion is mainly governed by electron-ion collisions and ambipolar diffusion is mostly caused by ion-neutral collisions. On the other hand, Hall's effect is also present in the fully ionized case, but this mechanism is enhanced by ion-neutral collisions since they tend to decouple ions from the magnetic field while electrons remain able to drift with the magnetic field (Pandey & Wardle 2008). On the contrary, the diamagnetic current term couples the magnetic field evolution with pressure gradients, and since \vec{G} vanishes in both the fully ionized and fully neutrals limits (see Eq. [2.40]), the effect of the diamagnetic term is larger for intermediate values of the ionization fraction.

Equation (2.43) can be written in a more compact form by defining Ohm's, η , Hall's, η_H , and ambipolar, η_A , magnetic diffusivities, along with the diamagnetic current coefficient, $\tilde{\Xi}$. Thus,

$$\begin{aligned} \frac{\partial \vec{B}}{\partial t} &= \nabla \times (\vec{v} \times \vec{B}) - \nabla \times (\eta \nabla \times \vec{B}) - \nabla \times [\eta_H (\nabla \times \vec{B}) \times \vec{B}] \\ &+ \nabla \times \left\{ \eta_A [(\nabla \times \vec{B}) \times \vec{B}] \times \vec{B} \right\} - \nabla \times [\tilde{\Xi} \vec{G} \times \vec{B}], \end{aligned} \quad (2.44)$$

with

$$\eta = \frac{1}{\mu e^2 n_e^2} \left(\alpha_e - \frac{\alpha_{en}^2}{\alpha_n} \right), \quad (2.45)$$

$$\eta_H = \frac{1}{\mu e n_e} \left(1 - 2\xi_n \frac{\alpha_{en}}{\alpha_n} \right), \quad (2.46)$$

$$\eta_A = \frac{\xi_n^2}{\mu \alpha_n}, \quad (2.47)$$

$$\tilde{\Xi} = \frac{\xi_n}{\alpha_n}. \quad (2.48)$$

The ambipolar diffusivity, η_A , is commonly expressed in terms of the Cowling's coefficient, η_C , as

$$\eta_A = \frac{\eta_C - \eta}{|\vec{B}|^2}. \quad (2.49)$$

It is also appropriate to define Ohm's, σ , and Cowling's, σ_C , conductivities, namely

$$\sigma = \frac{1}{\mu \eta}, \quad \sigma_C = \frac{1}{\mu \eta_C}. \quad (2.50)$$

With the help of these last definitions, we can express the sum of the corresponding Ohm's and ambipolar terms in Equation (2.42) as

$$\mu \eta \vec{j} - \mu \eta_A (\vec{j} \times \vec{B}) \times \vec{B} = \frac{1}{\sigma} \vec{j}_{\parallel} + \frac{1}{\sigma_C} \vec{j}_{\perp}, \quad (2.51)$$

where \vec{j}_{\parallel} and \vec{j}_{\perp} are the components of the density current parallel and perpendicular to the background magnetic field, respectively, whose expressions given by Arber et al. (2007) are

$$\vec{j}_{\parallel} = \frac{(\vec{j} \cdot \vec{B}) \vec{B}}{|\vec{B}|^2}, \quad \vec{j}_{\perp} = \frac{\vec{B} \times (\vec{j} \times \vec{B})}{|\vec{B}|^2}. \quad (2.52)$$

2.2. MAGNETOHYDRODYNAMIC EQUATIONS

Hence, we see that the parameters η and η_C correspond to the coefficients of magnetic diffusion parallel and perpendicular to magnetic field lines, respectively. Due to the presence of neutrals $\eta_C \gg \eta$, meaning that perpendicular magnetic diffusion is much more efficient than longitudinal magnetic diffusion in a partially ionized plasma. In a fully ionized plasma $\eta_C = \eta$, so magnetic diffusion is then isotropic. As an example, the ratio η_C/η in the solar chromosphere can be computed with the physical parameters provided by the VALC model (Vernazza et al. 1981). According to the VALC model (see Fig. 2.1), the ratio η_C/η is maximum at 2000 km above the photosphere, approximately, and tends to $\eta_C/\eta \approx 1$ in both the almost neutral photosphere and the fully ionized corona. Since the temperature and density of prominence material are similar to those in the chromosphere, it is expected that the ratio η_C/η has also a large value in prominence plasmas.

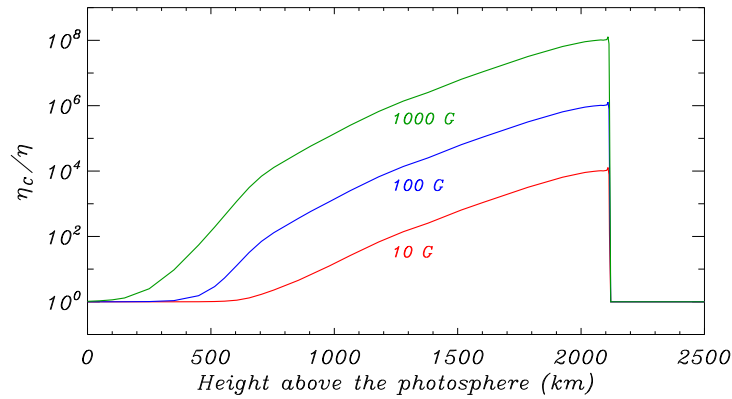


Figure 2.1: Ratio η_C/η in the solar chromosphere according to the VALC model by Vernazza et al. (1981) for different values of the magnetic field strength. The abrupt decrease around 2100 km above the photosphere, approximately, is present because the plasma becomes fully ionized when transition region temperatures are reached.

Expressions for the friction coefficients

We give here expressions for the friction coefficients between species. These expressions are needed to compute Equations (2.45)–(2.48). Each particular friction coefficient, $\alpha_{\beta\beta'}$, is computed as

$$\alpha_{\beta\beta'} = n_{\beta} m_{\beta\beta'} \nu_{\beta\beta'}, \quad (2.53)$$

with $\nu_{\beta\beta'}$ the collisional frequency between species β and β' , and

$$m_{\beta\beta'} = \frac{m_{\beta} m_{\beta'}}{m_{\beta} + m_{\beta'}}. \quad (2.54)$$

From Equation (2.53), we see that $\alpha_{\beta\beta'} = \alpha_{\beta'\beta}$. As given by De Pontieu et al. (2001), see also Equation (2.4), the collisional frequency between electrons and ions is

$$\nu_{ei} = 3.7 \times 10^{-6} \frac{n_i \ln \Lambda}{T^{3/2}}. \quad (2.55)$$

The collisional frequencies between electrons or ions and neutral species are

$$\nu_{\text{en}} = n_{\text{n}} \sqrt{\frac{8k_{\text{B}}T}{\pi m_{\text{en}}}} \Sigma_{\text{en}}, \quad \nu_{\text{in}} = n_{\text{n}} \sqrt{\frac{8k_{\text{B}}T}{\pi m_{\text{in}}}} \Sigma_{\text{in}}, \quad (2.56)$$

where $\Sigma_{\text{en}} = 10^{-19} \text{ m}^2$ and $\Sigma_{\text{in}} = 5 \times 10^{-19} \text{ m}^2$ are the electron-neutral and ion-neutral collisional cross-sections, respectively. For a hydrogen plasma, $m_{\text{i}} \approx m_{\text{n}}$, so a simplified expression for the neutral friction coefficient, α_{n} , can be provided by neglecting the contribution of electron-neutral collisions. Thus,

$$\alpha_{\text{n}} \approx \frac{1}{2} \xi_{\text{n}} (1 - \xi_{\text{n}}) \frac{\rho^2}{m_{\text{n}}} \sqrt{\frac{16k_{\text{B}}T}{\pi m_{\text{i}}}} \Sigma_{\text{in}}. \quad (2.57)$$

Fully ionized case

Let us consider the fully ionized case. In such a situation, $\xi_{\text{n}} = 0$ and therefore $\eta_{\text{A}} = \tilde{\Xi} = 0$, $\eta = \alpha_{\text{ei}}/\mu e^2 n_{\text{e}}^2$, and $\eta_{\text{H}} = 1/\mu e n_{\text{e}}$. Equation (2.44) becomes

$$\frac{\partial \vec{B}}{\partial t} = \nabla \times (\vec{v} \times \vec{B}) - \nabla \times (\eta \nabla \times \vec{B}) - \nabla \times [\eta_{\text{H}} (\nabla \times \vec{B}) \times \vec{B}]. \quad (2.58)$$

The importance of Ohm's diffusion can be estimated though the dimensionless parameter R_{m} , known as the magnetic Reynolds number, which is defined as the ratio of the magnitudes of the convective to Ohm's terms, namely

$$R_{\text{m}} = \frac{|\nabla \times (\vec{v} \times \vec{B})|}{|\nabla \times (\eta \nabla \times \vec{B})|} \sim \frac{\lambda_0 v_0}{\eta},$$

with λ_0 and v_0 typical length- and velocity-scales. For solar coronal conditions, one has $R_{\text{m}} \sim 10^{12}$, while for prominence conditions $R_{\text{m}} \sim 10^7$, meaning that Ohm's diffusion can be neglected for many applications unless very small length-scales are involved. Similarly, one can define the dimensionless parameter R_{H} , accounting for importance of Hall's diffusion term with respect to the convective term, as

$$R_{\text{H}} = \frac{|\nabla \times (\vec{v} \times \vec{B})|}{|\nabla \times [\eta_{\text{H}} (\nabla \times \vec{B}) \times \vec{B}]|} \sim \frac{\lambda_0 v_0}{\eta_{\text{H}} B_0} \sim \frac{\eta}{\eta_{\text{H}} B_0} R_{\text{m}} \sim \frac{\nu_{\text{ei}}}{\Omega_{\text{e}}} R_{\text{m}}, \quad (2.59)$$

where B_0 is a typical value of the magnetic field strength and Ω_{e} is the electron cyclotron frequency (Eq. [2.8]). Since R_{H} is proportional to R_{m} , the only possibility for Hall's term to become relevant is that $\nu_{\text{ei}}/\Omega_{\text{e}} \ll 1$. Such a situation occurs for extremely rare and hot plasmas, meaning that Hall's effect can be of relevance in solar wind conditions (e.g., Zhelyazkov et al. 1996; Miteva et al. 2003) but plays a minor role in the solar corona and prominences. In a partially ionized plasma, the relative importance of Hall's effect grows with the density of neutrals, but in coronal/prominence conditions it can be still safely neglected (Pandey & Wardle 2008; Krishan & Varghese 2008).

Finally, by neglecting both Ohm's and Hall's terms, we arrive at the induction equation for an ideal plasma, namely

$$\frac{\partial \vec{B}}{\partial t} = \nabla \times (\vec{v} \times \vec{B}). \quad (2.60)$$

2.2.4 Non-adiabatic energy equation

The energy equation governs the variation of the plasma entropy per unit mass, \mathcal{S} , as

$$\rho T \frac{D\mathcal{S}}{Dt} = -\mathcal{L}, \quad (2.61)$$

where \mathcal{L} represents the net effect of all the sources and sinks of energy. In the adiabatic case, in which the plasma is thermally isolated, i.e., there is no exchange of heat, $\mathcal{L} = 0$ and so the entropy is conserved.

Equation (2.61) is often written in terms of the thermodynamic variables pressure p and density ρ . In order to obtain this alternative expression, we use the internal energy, e , instead of the entropy, so

$$\rho \frac{De}{Dt} - \frac{p}{\rho} \frac{D\rho}{Dt} = -\mathcal{L}. \quad (2.62)$$

Now, considering that for an ideal polytropic gas

$$e = \frac{1}{\gamma - 1} \frac{p}{\rho}, \quad (2.63)$$

where γ is the adiabatic index, we obtain

$$\frac{\rho^\gamma}{\gamma - 1} \frac{D}{Dt} \left(\frac{p}{\rho^\gamma} \right) = -\mathcal{L}, \quad (2.64)$$

or, in a more common form,

$$\frac{Dp}{Dt} - \frac{\gamma p}{\rho} \frac{D\rho}{Dt} + (\gamma - 1) \mathcal{L} = 0. \quad (2.65)$$

From Equation (2.64) we see that $p\rho^{-\gamma}$ remains constant in the adiabatic case ($\mathcal{L} = 0$). In such a situation, Equation (2.65) becomes

$$\frac{Dp}{Dt} - \frac{\gamma p}{\rho} \frac{D\rho}{Dt} = 0, \quad (2.66)$$

which is the energy equation adopted in ideal MHD.

In this study we go a step forward from the ideal, adiabatic MHD and consider a more complete energy equation which includes several non-adiabatic mechanisms enclosed in the term \mathcal{L} of Equation (2.65). The general form of the energy loss function \mathcal{L} can be written as

$$\mathcal{L} = \nabla \cdot \vec{q} + \rho L - \vec{j} \cdot \vec{E}^* - Q_\nu, \quad (2.67)$$

where \vec{q} is the heat flux due to particle thermal conduction, L is the heat-loss function which balances radiative losses with an arbitrary external heating input, $\vec{j} \cdot \vec{E}^*$ is the generalized Joule heating, and Q_ν is the viscous heating.

Thermal conduction

The conductive heat vector is expressed as

$$\vec{q} = -\kappa \nabla T, \quad (2.68)$$

CHAPTER 2. MAGNETOHYDRODYNAMIC THEORY

where κ is the thermal conductivity tensor. For convenience, we split the divergence of the heat flux into the components parallel (∇_{\parallel}) and perpendicular (∇_{\perp}) to the magnetic field lines as

$$-\nabla \cdot \vec{q} = \nabla_{\parallel} \cdot (\kappa_{\parallel} \nabla_{\parallel} T) + \nabla_{\perp} \cdot (\kappa_{\perp} \nabla_{\perp} T),$$

where κ_{\parallel} and κ_{\perp} are the scalar components of the thermal conductivity tensor parallel and perpendicular to the magnetic field, respectively. In a fully ionized medium, κ_{\parallel} is governed by electrons, whereas κ_{\perp} is caused mainly by the ions. In the partially ionized case, one has to add the contribution of neutrals, κ_{n} , to both scalar conductivities, since the thermal conduction by neutrals is isotropic. Thus,

$$\kappa_{\parallel} = \kappa_{\parallel\text{e}} + \kappa_{\text{n}}, \quad (2.69)$$

$$\kappa_{\perp} = \kappa_{\perp\text{i}} + \kappa_{\text{n}}. \quad (2.70)$$

In terms of the plasma parameters (e.g., Spitzer 1962; Braginskii 1965), the expression for the parallel conductivity of electrons is

$$\kappa_{\parallel\text{e}} = 1.8 \times 10^{-10} \frac{\xi_{\text{i}} T^{5/2}}{\ln \Lambda} \text{ W m}^{-1} \text{ K}^{-1}. \quad (2.71)$$

For applications in the solar atmosphere, $\kappa_{\parallel\text{e}} \approx 10^{-11} T^{5/2} \text{ W m}^{-1} \text{ K}^{-1}$. On the other hand, the perpendicular conductivity due to ions is

$$\kappa_{\perp\text{i}} = 8.2 \times 10^{-33} \frac{(\ln \Lambda)^2 n_{\text{i}}^2}{|\vec{B}|^2 T^3} \kappa_{\parallel\text{e}} = 1.48 \times 10^{-42} \frac{\ln \Lambda \xi_{\text{i}}^3 \rho^2}{m_{\text{i}}^2 |\vec{B}|^2 T^{1/2}} \text{ W m}^{-1} \text{ K}^{-1}. \quad (2.72)$$

Finally, Parker (1953) provides with an expression for the conductivity of neutrals, namely

$$\kappa_{\text{n}} = 2.44 \times 10^{-2} \xi_{\text{n}} T^{1/2} \text{ W m}^{-1} \text{ K}^{-1}. \quad (2.73)$$

In the fully ionized case, i.e., $\kappa_{\text{n}} = 0$, the perpendicular conductivity can be neglected for prominence and coronal applications since $\kappa_{\perp}/\kappa_{\parallel} \approx 10^{-13}$, so only the parallel component is usually considered. In such a case, the heat flux is approximated by its parallel component to the magnetic field and can be written in the following form

$$-\nabla \cdot \vec{q} \approx \nabla_{\parallel} \cdot (\kappa_{\parallel} \nabla_{\parallel} T) = (\vec{B} \cdot \nabla) \left[\frac{\kappa_{\parallel}}{|\vec{B}|^2} (\vec{B} \cdot \nabla T) \right]. \quad (2.74)$$

Radiation losses and external heating

The difference between the heat input, $H(T, \rho)$, and radiative losses, $C(T, \rho)$, is often evaluated through the heat-loss function as

$$L(T, \rho) = C(T, \rho) - H(T, \rho), \quad (2.75)$$

which depends on the local plasma parameters. The determination of an analytical function of the temperature and density that describes the radiative losses of the atmospheric solar plasma is a very difficult work that has been broached by several authors, whose calculations show significant discrepancies. Rosner et al. (1978) pointed out that

2.2. MAGNETOHYDRODYNAMIC EQUATIONS

the differences arise from three basic concerns: the nature of the atomic processes involved in radiative emission, the accuracy of the atomic physical parameters considered in the calculations, and the values of the relative elemental abundances.

One reasonable semi-empirical approximation to an expression for the radiative loss function is to consider a fit which lies within the estimated error bounds of the best detailed calculations. This approach was taken into account by [Hildner \(1974\)](#), assuming an optically thin plasma (e.g., [Cox & Tucker 1969](#)), who performed a piecewise fit for the radiative losses as a function of temperature (see [Fig. 2.2](#)). The functional expression for the fit by [Hildner \(1974\)](#) is

$$C(T, \rho) = \xi_i \rho \chi^* T^\alpha, \quad (2.76)$$

where χ^* and α are piecewise functions depending on the temperature. The assumption of an optically thin plasma seems a reasonable approach for coronal conditions, whereas prominence plasmas may be considered optically thick. Some authors (e.g., [Rosner et al. 1978](#); [Milne et al. 1979](#)) have proposed corrections to the values of χ^* and α in the range of typical prominence temperatures in order to represent radiation losses in optically thick plasmas. The values of the parameters χ^* and α for various temperature ranges are given in [Table 2.1](#).

On the other hand, the processes involved in the solar atmospheric heating are still not well-known and, nowadays, it is one of the most important unsolved problems of solar physics. Several possible heating mechanisms or scenarios have been proposed as, e.g., wave heating or nanoflare heating. In some works (e.g., [Rosner et al. 1978](#); [Dahlburg & Mariska 1988](#)), the heating function is written in the following form

$$H(T, \rho) = h \rho^{a^*} T^{b^*}, \quad (2.77)$$

where the exponents a^* and b^* can be chosen to assume different heating scenarios, and h is a constant parameter whose value is chosen to satisfy the energy balance condition. Some parametrizations found in the literature are:

- constant heating per unit volume ($a^* = b^* = 0$),
- constant heating per unit mass ($a^* = 1, b^* = 0$),
- heating by coronal current dissipation ($a^* = b^* = 1$),
- heating by Alfvén mode/mode conversion ($a^* = b^* = 7/6$),
- heating by Alfvén mode/anomalous conduction damping ($a^* = 1/2, b^* = -1/2$).

Hence, the general expression for the heat-loss function in terms of the plasma conditions is

$$L(T, \rho) = \xi_i \rho \chi^* T^\alpha - h \rho^{a^*} T^{b^*}. \quad (2.78)$$

Joule heating

The expression of the generalized Joule heating in a partially ionized plasma is easily obtained by combining [Equations \(2.42\) and \(2.51\)](#), so

$$\vec{j} \cdot \vec{E}^* \approx \frac{1}{\sigma} |\vec{j}_{\parallel}|^2 + \frac{1}{\sigma_C} |\vec{j}_{\perp}|^2, \quad (2.79)$$

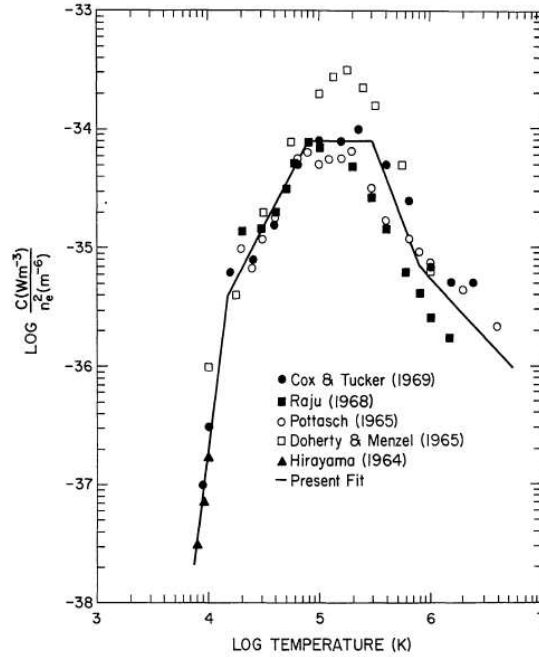


Figure 2.2: Radiative energy loss from an optically thin solar atmospheric plasma as a function of the temperature. The solid line represents the piecewise fit by [Hildner \(1974\)](#) and the symbols correspond to previous calculations made by several authors. From [Hildner \(1974\)](#).

Regime	Temperature range	χ^*	α
Prominence (1)	$T < 15 \times 10^3$ K	1.76×10^{-13}	7.4
Prominence (2)	$T < 15 \times 10^3$ K	1.76×10^{-53}	17.4
Prominence (3)	$T < 15 \times 10^3$ K	7.01×10^{-104}	30
PCTR (1)	15×10^3 K $< T < 80 \times 10^3$ K	4.29×10^{10}	1.8
PCTR (2)	80×10^3 K $< T < 300 \times 10^3$ K	2.86×10^{19}	0.0
PCTR (3)	300×10^3 K $< T < 800 \times 10^3$ K	1.41×10^{33}	-2.5
Corona	$T > 800 \times 10^3$ K	1.97×10^{24}	-1.0

Table 2.1: Values in MKS units of the parameters in the radiative loss function (Eq. [2.76]) corresponding to several temperature regimes. The three prominence regimes represent different plasma optical thicknesses, Prominence (1) corresponding to optically thin plasma, while Prominence (2) and (3) are for optically thick and very thick plasmas, respectively. Optically thin plasma is assumed for the other regimes. Prominence (2) and (3) regimes are parametrizations from [Milne et al. \(1979\)](#) and [Rosner et al. \(1978\)](#), respectively, while the rest of regimes are given by [Hildner \(1974\)](#).

2.3. LINEAR IDEAL MAGNETOHYDRODYNAMIC WAVES

where we have dropped both Biermann's battery and diamagnetic current terms because their contribution is negligible in comparison to Ohm's and Cowling's heating, whereas Hall's term does not contribute at all since $(\vec{j} \times \vec{B})$ is perpendicular to \vec{j} .

Viscous heating

The general expression for the viscous heating in terms of the complete viscosity tensor is (Braginskii 1965)

$$Q_\nu = \sum_{m,n} \mathbf{\Pi}_{mn} \frac{\partial v_m}{\partial x_n}, \quad (2.80)$$

where v_m is the m -th component of the velocity vector, and x_n is the n -th coordinate. Priest (1982) provides a simpler expression in the case of weak magnetic fields, namely

$$Q_\nu \approx \rho\nu \left(\frac{1}{2} \sum_{m,n} e_{mn} e_{mn} - \frac{2}{3} (\nabla \cdot \vec{v})^2 \right), \quad (2.81)$$

where $e_{mn} = \frac{\partial v_m}{\partial x_n} + \frac{\partial v_n}{\partial x_m}$ is the rate of strain tensor.

2.2.5 Summary of the basic equations

We summarize here the basic MHD equations derived in the last Sections, namely

$$\frac{D\rho}{Dt} = -\rho \nabla \cdot \vec{v}, \quad (2.82)$$

$$\rho \frac{D\vec{v}}{Dt} = -\nabla p + \frac{1}{\mu} (\nabla \times \vec{B}) \times \vec{B} - \rho \vec{g} - \nabla \cdot \mathbf{\Pi}, \quad (2.83)$$

$$\begin{aligned} \frac{\partial \vec{B}}{\partial t} &= \nabla \times (\vec{v} \times \vec{B}) - \nabla \times (\eta \nabla \times \vec{B}) - \nabla \times [\eta_{\text{H}} (\nabla \times \vec{B}) \times \vec{B}] \\ &+ \nabla \times \left\{ \frac{\eta_{\text{C}} - \eta}{|\vec{B}|^2} [(\nabla \times \vec{B}) \times \vec{B}] \times \vec{B} \right\} - \nabla \times [\tilde{\Xi} \vec{G} \times \vec{B}], \end{aligned} \quad (2.84)$$

$$\begin{aligned} \frac{Dp}{Dt} - \frac{\gamma p}{\rho} \frac{D\rho}{Dt} &= (\gamma - 1) [\nabla \cdot (\kappa \nabla T) - \rho L(T, \rho)] \\ &+ (\gamma - 1) \left[\frac{1}{\sigma} |\vec{j}_{\parallel}|^2 + \frac{1}{\sigma_{\text{C}}} |\vec{j}_{\perp}|^2 + \sum_{m,n} \mathbf{\Pi}_{mn} \frac{\partial v_m}{\partial x_n} \right], \end{aligned} \quad (2.85)$$

$$p = \rho R \frac{T}{\tilde{\mu}}, \quad (2.86)$$

along with the condition $\nabla \cdot \vec{B} = 0$.

2.3 Linear ideal magnetohydrodynamic waves

2.3.1 Linearized ideal magnetohydrodynamic equations

One of the typical applications of the MHD theory is the study of MHD waves in a magnetized plasma (Alfvén 1942). However, since Equations (2.82)–(2.86) form a

collection of coupled non-linear differential equations, their solution, even numerically, is extremely complicated. The first approximation one can perform is to consider the ideal case, i.e., to neglect all dissipative effects. Thus, Equations (2.82)–(2.86) become

$$\frac{D\rho}{Dt} = -\rho\nabla \cdot \vec{v}, \quad (2.87)$$

$$\rho \frac{D\vec{v}}{Dt} = -\nabla p + \frac{1}{\mu} (\nabla \times \vec{B}) \times \vec{B}, \quad (2.88)$$

$$\frac{\partial \vec{B}}{\partial t} = \nabla \times (\vec{v} \times \vec{B}), \quad (2.89)$$

$$\frac{Dp}{Dt} - \frac{\gamma p}{\rho} \frac{D\rho}{Dt} = 0, \quad (2.90)$$

$$p = \rho R \frac{T}{\bar{\mu}}, \quad (2.91)$$

where the gravity force has also been dropped from the momentum equation. We can go even further by restricting ourselves to waves with a small velocity amplitude in comparison to the sound and Alfvén speeds. In such a case, it is enough to consider the linear regime. After linearization, Equations (2.87)–(2.91) reduce to a more simplified form, and it is possible to obtain analytical solutions in some simple situations.

We assume that each physical quantity, f , can be written as the sum of an equilibrium value, f_0 , and a perturbation, f_1 . Thus, $\vec{B}(t, \vec{r}) = \vec{B}_0 + \vec{B}_1(t, \vec{r})$, $p(t, \vec{r}) = p_0 + p_1(t, \vec{r})$, $\rho(t, \vec{r}) = \rho_0 + \rho_1(t, \vec{r})$, $T(t, \vec{r}) = T_0 + T_1(t, \vec{r})$, and $\vec{v}(t, \vec{r}) = \vec{v}_1(t, \vec{r})$, where subscripts 0 and 1 denote equilibrium and perturbed quantities, respectively, and \vec{r} is the position vector. Hereafter, the equilibrium values are taken homogeneous and constant in time. Next, we replace these expressions into Equations (2.87)–(2.91) and assume small perturbations, so we neglect all non-linear terms in the perturbed quantities. The resultant linear equations are

$$\frac{\partial \rho_1}{\partial t} = -\rho_0 \nabla \cdot \vec{v}_1, \quad (2.92)$$

$$\rho_0 \frac{\partial \vec{v}_1}{\partial t} = -\nabla p_1 + \frac{1}{\mu} (\nabla \times \vec{B}_1) \times \vec{B}_0, \quad (2.93)$$

$$\frac{\partial \vec{B}_1}{\partial t} = \nabla \times (\vec{v}_1 \times \vec{B}_0), \quad (2.94)$$

$$\frac{\partial p_1}{\partial t} - c_s^2 \frac{\partial \rho_1}{\partial t} = 0, \quad (2.95)$$

$$\frac{p_1}{p_0} = \frac{\rho_1}{\rho_0} + \frac{T_1}{T_0}, \quad (2.96)$$

along with $\nabla \cdot \vec{B}_1 = 0$, where $c_s^2 = \frac{\gamma p_0}{\rho_0}$ is the adiabatic sound speed squared.

2.3.2 Dispersion relation of magnetohydrodynamic waves in uniform medium with straight magnetic field

It is well-known that perturbations from the equilibrium state in a gas propagate at the sound speed of the medium, c_s , as variations in pressure and the other thermodynamic quantities. On the other hand, due to the presence of a magnetic field, waves in

2.3. LINEAR IDEAL MAGNETOHYDRODYNAMIC WAVES

a plasma are also driven by the Lorentz force besides the pressure force. In the absence of gravity, two kinds of waves can occur in a magnetized, ideal plasma: Alfvén waves and magnetoacoustic (or magnetosonic) waves. Linear Alfvén waves are driven exclusively by the magnetic tension and propagate non-dispersively along the field lines at a fixed velocity, i.e., the Alfvén speed v_A (defined below). However, magnetoacoustic waves arise from the combined effect of the pressure gradient and the Lorentz force. Two types of magnetoacoustic waves are possible, called slow and fast magnetoacoustic waves.

We assume a uniform and unbounded medium with density ρ_0 , pressure p_0 , and temperature T_0 , permeated by a homogeneous magnetic field, \vec{B}_0 . The propagation of small perturbations from the equilibrium state is governed by Equations (2.92)–(2.96), which, following Lighthill (1960), can be combined to arrive at the next expressions

$$\frac{\partial^2}{\partial t^2} \left[\frac{\partial^2}{\partial t^2} - (c_s^2 + v_A^2) \nabla^2 \right] \Delta + \frac{c_s^2 v_A^2}{|\vec{B}_0|^2} (\vec{B}_0 \cdot \nabla)^2 \nabla^2 \Delta = 0, \quad (2.97)$$

$$\left[\frac{\partial^2}{\partial t^2} - \frac{v_A^2}{|\vec{B}_0|^2} (\vec{B}_0 \cdot \nabla)^2 \right] \Psi = 0, \quad (2.98)$$

where $v_A^2 = \frac{|\vec{B}_0|^2}{\mu \rho_0}$ is the Alfvén speed squared, and Δ and Ψ are the divergence and the component of the rotational of the velocity perturbation along magnetic field lines, respectively, defined as

$$\Delta = \nabla \cdot \vec{v}_1, \quad (2.99)$$

$$\Psi = \frac{(\nabla \times \vec{v}_1) \cdot \vec{B}_0}{|\vec{B}_0|}. \quad (2.100)$$

Equation (2.97) governs magnetoacoustic waves, whereas Equation (2.98) stands for Alfvén waves (Alfvén 1942). Now, we take the x -axis orientated along the magnetic field direction, $\vec{B}_0 = B_0 \hat{e}_x$, and consider perturbations in the form of plane waves, so they are written proportional to $\exp(i\vec{k} \cdot \vec{r} - i\omega t)$, where ω is the frequency and \vec{k} the wave vector. With no loss of generality, we choose the z -axis so that the wave vector is in the xz -plane, so $\vec{k} = k_x \hat{e}_x + k_z \hat{e}_z$. For arbitrary Δ and Ψ , Equations (2.97) and (2.98) provide us with the dispersion relation for magnetoacoustic waves, namely

$$\omega^4 - (v_A^2 + c_s^2) k^2 \omega^2 + v_A^2 c_s^2 k^4 \cos^2 \theta = 0, \quad (2.101)$$

and for Alfvén waves, namely

$$\omega^2 - k_x^2 v_A^2 = 0, \quad (2.102)$$

with $k^2 = k_x^2 + k_z^2$ and $\theta = \arctan(k_z/k_x)$. From Equation (2.102), we see that Alfvén waves propagate with a constant phase speed, $\omega/k_x = v_A$. In addition, Alfvén waves have no associated density, temperature, or gas pressure changes. Regarding magnetoacoustic waves, the analytical solution of Equation (2.101) is

$$\omega^2 = \frac{k^2}{2} \left[(v_A^2 + c_s^2) \pm \sqrt{(v_A^2 + c_s^2)^2 - 4v_A^2 c_s^2 \cos^2 \theta} \right], \quad (2.103)$$

where the $-$ sign corresponds to the slow wave and the $+$ sign to the fast wave, whose properties depend on the relation between c_s and v_A . For typical physical conditions in

CHAPTER 2. MAGNETOHYDRODYNAMIC THEORY

the solar corona and prominences, $c_s < v_A$, so the slow wave is essentially an acoustic wave modified by the magnetic field and the fast wave is a magnetic wave which is driven by magnetic pressure and weakly affected by acoustic effects. This behavior is the contrary when $c_s > v_A$ (see, e.g., [Goossens 2003](#)). Figure (2.3) displays a polar plot of the phase velocity, ω/k , of Alfvén, fast, and slow waves for both $c_s < v_A$ and $c_s > v_A$ cases. The limit values of the phase speed for propagation parallel and perpendicular to magnetic field lines are labeled in Figure (2.3). Note that neither Alfvén nor slow waves can propagate perpendicularly to the magnetic field.

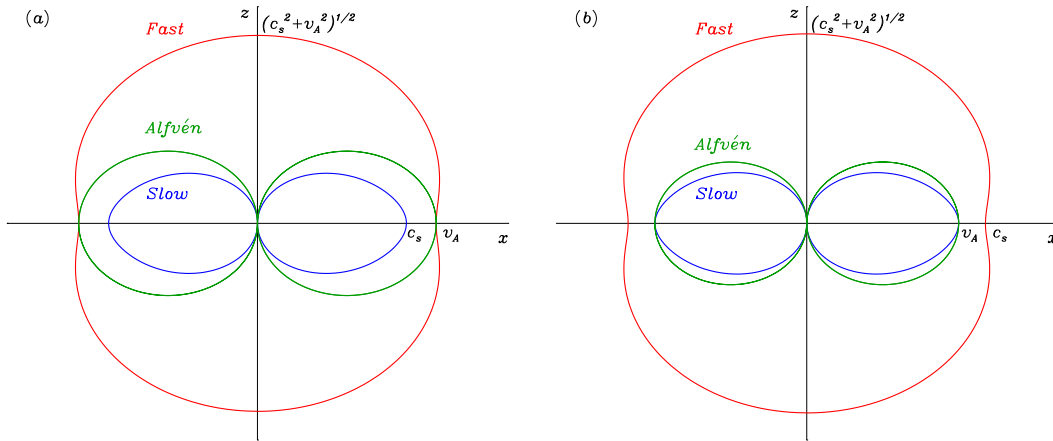


Figure 2.3: Polar plot of the phase speed of Alfvén and magnetoacoustic waves. (a) Case $c_s < v_A$. (b) Case $c_s > v_A$. In both cases, the horizontal and vertical axes correspond to propagation parallel and perpendicular to magnetic field lines, respectively.

In the limit $c_s \ll v_A$, Equation (2.103) simplifies to

$$\omega^2 \approx k_x^2 c_s^2, \quad (2.104)$$

for the slow wave, and

$$\omega^2 \approx k^2 v_A^2, \quad (2.105)$$

for the fast wave. One must bear in mind that the distinction between Alfvén, fast, and slow waves can be more ambiguous in a different equilibrium, since these three modes are in general coupled (for a discussion on this issue in cylindrical geometry see [Goossens et al. 2009](#)). The case of a uniform, unbounded medium represents a unique situation in which the properties of the three modes are well-determined.

Part II

**Individual Oscillations of
Filament Threads**

3

Ideal Magnetohydrodynamic Waves in a Cylindrical Magnetic Flux Tube

The purpose of this thesis is to study the efficiency of several mechanisms for the damping of MHD waves in filament threads. Here, we study the ideal MHD wave modes supported by a model representing a filament thread. In subsequent Chapters, we analyze how the ideal solutions are affected by the presence of non-ideal effects. We find the dispersion relation of the fast and slow magnetoacoustic modes (Sec. 3.1.2) and obtain an approximation to the frequency in the thin tube limit (Sec. 3.1.3). Later, we numerically solve the full dispersion relation and perform a parametric study of the solutions (Sec. 3.2 and 3.3). Finally, we perform a seismological application by comparing the theoretical predictions of the model with the observed oscillatory behavior of several threads in a solar filament, allowing us to estimate the Alfvén speed and the magnetic field strength of the filament (Sec. 3.4).

3.1 Model and basic equations

3.1.1 Equilibrium configuration

The model configuration considered here to represent a filament thread (Fig. 3.1) is composed of a straight and homogeneous plasma cylinder of radius a with filament

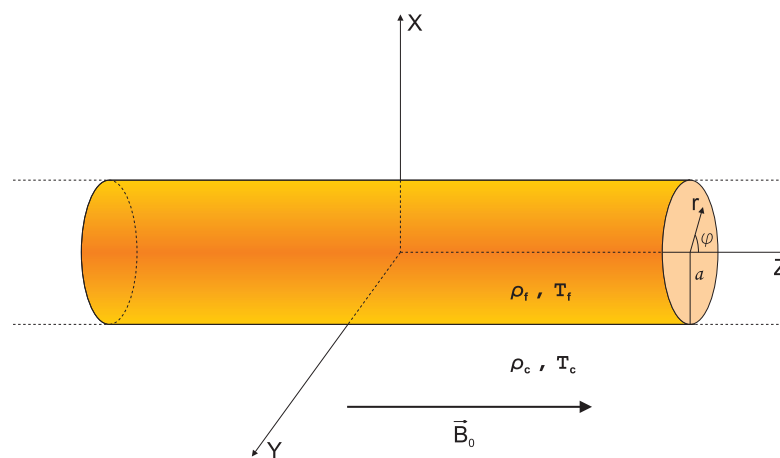


Figure 3.1: Sketch of the cylindrical flux tube model considered in this Chapter.

conditions (density ρ_f and temperature T_f) embedded in an unbounded and homogeneous corona (density ρ_c and temperature T_c). We use a subscript 0 to refer to the equilibrium quantities when the medium is not specified, and subscripts f and c to explicitly denote filament and coronal values, respectively. The cylinder is unlimited in the longitudinal direction, which is along the z -axis. The magnetic field is uniform and orientated along the cylinder axis, $\vec{B}_0 = B_0 \hat{e}_z$, B_0 being the same constant in the thread and in the coronal medium. This model does not take into account the longitudinal inhomogeneity of the plasma, as was considered in, e.g., [Díaz et al. \(2002\)](#) and [Dymova & Ruderman \(2005\)](#). See Chapter 7 for an estimation of the effect of the longitudinal plasma inhomogeneity.

The theory of ideal MHD waves supported by homogeneous, straight, and untwisted cylindrical magnetic flux tubes has been developed in a number of papers, most of them applied to the context of coronal loop oscillations (see the review by [Ruderman & Erdélyi 2009](#)), during the last 30 years. Hydromagnetic surface waves propagating in cylindrical tubes were studied by [Wilson \(1979\)](#) and [Wentzel \(1979\)](#), while the general dispersion relation of MHD normal modes in a magnetic cylinder was derived by [Wilson \(1980, 1981\)](#) for a non-magnetized environment, and [Spruit \(1982\)](#) for a magnetized external plasma. These referred works focused their study on the mathematical properties of the dispersion relation and did not provide a complete account of the oscillatory modes supported by the flux tube. In the case of trapped modes, a general investigation was performed by [Edwin & Roberts \(1983\)](#), who plotted phase speed diagrams under photospheric and coronal conditions, and obtained approximated expressions for the frequency in the thin tube (TT) limit (see also [Roberts et al. 1984](#)). Regarding leaky modes, i.e., wave solutions that are radiated away from the flux tube and therefore are damped in time, they were briefly discussed by [Spruit \(1982\)](#), but more comprehensive studies were performed by [Cally \(1986, 2003\)](#) and [Ruderman & Roberts \(2006a\)](#). Subsequent investigations that have contributed to the field are, e.g., [Abdelatif \(1988\)](#), [Díaz et al. \(2004\)](#), and [Goossens et al. \(2009\)](#). Further studies have included additional effects in the model such as, e.g., stratification, magnetic twist, curvature, or non-circular cross-sections. The reader is referred to [Ruderman & Erdélyi \(2009\)](#), and references therein, for a detailed explanation of how these additional ingredients affect the oscillatory modes.

By means of time-dependent simulations of the excitation of oscillations in cylindrical flux tubes, [Terradas et al. \(2007\)](#) showed that the stationary state of the tube oscillation is governed by the trapped normal modes ([Edwin & Roberts 1983](#)), whereas the transient behavior between the initial excitation and the stationary state is dominated by high-frequency leaky modes ([Cally 1986, 2003](#)). Since the time-scale of the transient phase is much smaller than the period of the oscillations, it seems reasonable to restrict ourselves to trapped modes in order to theoretically study the observed oscillations of filament threads. It is worth mentioning here a very peculiar solution found by [Cally \(2003\)](#), called the *principal leaky kink* (PLK) mode, which could be of relevance. According to [Cally \(2003\)](#), the PLK mode has a frequency very similar to that of the trapped kink mode for long wavelengths. However, the PLK mode is damped in time due to leakage in the external medium, which makes it a possible candidate to explain the observed damped transverse oscillations of coronal loops (and filament threads). Nevertheless, [Ruderman & Roberts \(2006a\)](#) argued that the PLK mode is a physically meaningless solution, although this issue is still under debate ([Cally 2006; Ruderman & Roberts 2006b](#)). We also discard the PLK mode in our investigation.

3.1.2 Dispersion relation

The linear, ideal MHD magnetosonic modes supported by our flux tube model are governed by Equation (2.97). By using cylindrical coordinates, namely r , φ , and z for the radial, azimuthal, and longitudinal coordinates, respectively, Equation (2.97) becomes

$$\frac{\partial^2}{\partial t^2} \left[\frac{\partial^2}{\partial t^2} - (c_s^2 + v_A^2) \nabla^2 \right] \Delta + c_s^2 v_A^2 \frac{\partial^2}{\partial z^2} \nabla^2 \Delta = 0, \quad (3.1)$$

with $\Delta = \nabla \cdot \vec{v}_1$, where \vec{v}_1 is the velocity perturbation vector. Next, since φ and z are ignorable directions, we write

$$\Delta = R(r) \exp(im\varphi + ik_z z - i\omega t), \quad (3.2)$$

where m is an integer that plays the role of the azimuthal wavenumber, k_z is the longitudinal wavenumber, ω is the frequency, and $R(r)$ is a function accounting for the radial dependence. In the absence of magnetic twist, solutions are degenerate with respect to positive and negative values of m , so we only consider positive values of this parameter. Now, applying this last expression to Equation (3.1), one finds that $R(r)$ satisfies the well-known Bessel equation of order m , namely

$$\frac{d^2 R(r)}{dr^2} + \frac{1}{r} \frac{dR(r)}{dr} + \left(m_0^2 - \frac{m^2}{r^2} \right) R(r) = 0, \quad (3.3)$$

with

$$m_0^2 = \frac{(\omega^2 - k_z^2 v_A^2) (\omega^2 - k_z^2 c_s^2)}{(v_A^2 + c_s^2) (\omega^2 - k_z^2 c_T^2)}, \quad (3.4)$$

$$c_T^2 = \frac{v_A^2 c_s^2}{v_A^2 + c_s^2}, \quad (3.5)$$

where c_T is the so-called cusp (or tube) speed. The character of the solutions depends on the sign of m_0^2 . Thus, oscillations are body-like if $m_0^2 > 0$ and solutions of Equation (3.3) are Bessel functions. On the contrary, if $m_0^2 < 0$ oscillations are surface-like (or evanescent) and solutions of Equation (3.3) are modified Bessel functions. The quantity m_0^2 has to be evaluated both in the filament thread, m_f^2 , and the coronal medium, m_c^2 . Since we restrict ourselves to non-leaky modes, the evanescent condition in the corona is imposed on the perturbations, namely $m_c^2 < 0$. On the other hand, for typical prominence and coronal conditions, the ordering of sound and Alfvén speeds is $c_{sf} < v_{Af} < c_{sc} < v_{Ac}$, which does not permit the existence of surface waves within the thread, so $m_f^2 > 0$. Then, $R(r)$ is a piecewise function as follows

$$R(r) = \begin{cases} A_1 J_m(m_f r) + A_2 Y_m(m_f r) & \text{if } r \leq a, \\ A_3 I_m(n_c r) + A_4 K_m(n_c r) & \text{if } r > a, \end{cases} \quad (3.6)$$

with $n_c^2 = -m_c^2$, A_1 , A_2 , A_3 , and A_4 being complex constants. J_m and Y_m are the Bessel functions of the first and second kind, and I_m and K_m are the modified Bessel functions of the first and second kind, respectively, of order m (Abramowitz & Stegun 1972). We

seek for regular solutions at $r = 0$ and vanishing at infinity, so we set $A_2 = A_3 = 0$. Expressions for the perturbed quantities as a function of Δ and its radial derivative are

$$v_r = -\frac{(\omega^2 - k_z^2 c_s^2)}{\omega^2 m_0^2} \frac{\partial \Delta}{\partial r}, \quad (3.7)$$

$$v_\varphi = -i \frac{(\omega^2 - k_z^2 c_s^2)}{\omega^2 m_0^2} \frac{m}{r} \Delta, \quad (3.8)$$

$$v_z = i \frac{c_s^2 k_z}{\omega^2} \Delta, \quad (3.9)$$

$$\rho_1 = -i \frac{\rho_0}{\omega} \Delta, \quad (3.10)$$

$$p_1 = -i \frac{\rho_0 c_s^2}{\omega} \Delta, \quad (3.11)$$

$$T_1 = -i \frac{T_0}{\omega} (\gamma - 1) \Delta, \quad (3.12)$$

$$B_r = -B_0 k_z \frac{(\omega^2 - k_z^2 c_s^2)}{\omega^3 m_0^2} \frac{\partial \Delta}{\partial r}, \quad (3.13)$$

$$B_\varphi = -i B_0 k_z \frac{(\omega^2 - k_z^2 c_s^2)}{\omega^3 m_0^2} \frac{m}{r} \Delta, \quad (3.14)$$

$$B_z = -i B_0 \frac{(\omega^2 - k_z^2 c_s^2)}{\omega^3} \Delta, \quad (3.15)$$

$$p_{m1} = \frac{B_0}{\mu} B_z = -i \rho_0 v_A^2 \frac{(\omega^2 - k_z^2 c_s^2)}{\omega^3} \Delta, \quad (3.16)$$

$$p_{T1} = p_1 + p_{m1} = -i \rho_0 \frac{(\omega^2 - k_z^2 c_s^2) (\omega^2 - k_z^2 v_A^2)}{\omega^3 m_0^2} \Delta, \quad (3.17)$$

where v_r , v_φ , and v_z are the velocity perturbations, B_r , B_φ , and B_z are the magnetic field perturbations, ρ_1 , p_1 , and T_1 are the density, gas pressure, and temperature perturbations, and p_{m1} and p_{T1} are the magnetic pressure and total pressure perturbations, respectively.

In order to obtain the dispersion relation that governs the behavior of wave modes, we impose the continuity of the Lagrangian radial displacement, $\xi_r = i v_r / \omega$, and the total pressure perturbation, p_{T1} , at the cylinder edge, $r = a$. After some algebra, the following expression is obtained,

$$\frac{n_c}{\rho_c (\omega^2 - k_z^2 v_{Ac}^2)} \frac{K'_m(n_c a)}{K_m(n_c a)} - \frac{m_f}{\rho_f (\omega^2 - k_z^2 v_{Af}^2)} \frac{J'_m(m_f a)}{J_m(m_f a)} = 0, \quad (3.18)$$

where the prime denotes the derivative with respect to r . Equation (3.18) corresponds to the well-known dispersion relation obtained by [Edwin & Roberts \(1983\)](#). The solutions of Equation (3.18) can be classified according to several criteria. Considering the value of the azimuthal wavenumber, solutions with $m = 0$ are called sausage modes, solutions with $m = 1$ are kink modes, and solutions with $m \geq 2$ are fluting modes. Considering their magnetoacoustic properties, wave modes with a phase velocity, ω/k_z , in the range $c_{Tf} < \omega/k_z < c_{sf}$ and whose dominant velocity component is along magnetic field lines are identified as internal slow modes. These slow modes are not very sensitive

3.2. DISPERSION DIAGRAMS AND EIGENFUNCTIONS

to the value of m . On the other hand, the modes with $v_{\text{Af}} < \omega/k_z < v_{\text{Ac}}$, which are mainly polarized transversely to magnetic field lines, are usually denoted as fast modes. However, [Goossens et al. \(2009\)](#) pointed out that the mode with $m = 1$, the so-called kink mode, has mixed alfvénic and fast properties, the magnetic tension being the dominant restoring force. For this reason, we use the more general expression *transverse modes*, based on their displacement polarization, to refer to solutions with $v_{\text{Af}} < \omega/k_z < v_{\text{Ac}}$.

3.1.3 The thin tube approximation

Equation (3.18) is a transcendental equation that has to be solved numerically. It is possible to go further analytically by considering the thin tube (TT) approximation, i.e., $k_z a \ll 1$. In terms of the wavelength, λ_z , the TT approximation applies for $\lambda_z/a \gg 1$. We perform a first order, asymptotic expansion for small arguments of the Bessel functions in Equation (3.18) for $m \neq 0$. The dispersion relation then becomes

$$\rho_f (\omega^2 - k_z^2 v_{\text{Af}}^2) + \rho_c (\omega^2 - k_z^2 v_{\text{Ac}}^2) = 0, \quad (3.19)$$

whose analytical solution is

$$\omega^2 = \frac{\rho_f v_{\text{Af}}^2 + \rho_c v_{\text{Ac}}^2}{\rho_f + \rho_c} k_z^2 \equiv \omega_k^2, \quad (3.20)$$

where ω_k is the so-called kink frequency. Note that Equation (3.20) is only valid for transverse modes with $m \neq 0$, so neither fast sausage nor slow modes are described.

3.2 Dispersion diagrams and eigenfunctions

Here, we compute phase velocity diagrams of the solutions of Equation (3.18) as a function of the dimensionless longitudinal wavenumber, $k_z a$. As mentioned in the Introduction (Chap. 1), the observed width of filament threads is in the range $0''.2 - 0''.6$ ([Lin 2004](#)), and therefore a ranges from 75 km to 375 km, approximately. On the other hand, the detected wavelengths of prominence oscillations are between 5×10^3 km and 10^5 km ([Oliver & Ballester 2002](#)). One can combine both quantities (the wavelength and the thread width) into the dimensionless quantity $k_z a$, and compute its upper and lower limits. So, for $a = 75$ km, $5 \times 10^{-3} \lesssim k_z a \lesssim 9 \times 10^{-2}$, while for $a = 375$ km, $2 \times 10^{-2} \lesssim k_z a \lesssim 4 \times 10^{-1}$. Thus, taking into account both intervals and considering that thinner threads than those resolved by present-day telescopes might exist, the relevant range of $k_z a$ of prominence oscillations covers two orders of magnitude and corresponds to $10^{-3} \lesssim k_z a \lesssim 10^{-1}$. This range of $k_z a$ contains all realistic values of the wavelength and the thread width. Thus, the results within this range of $k_z a$ will deserve special attention.

The following equilibrium parameters are considered in all computations: $\tilde{T}_f = 10^4$ K, $\rho_f = 5 \times 10^{-11}$ kg m $^{-3}$, $\tilde{T}_c = 2 \times 10^6$ K, $\rho_c = 2.5 \times 10^{-13}$ kg m $^{-3}$, $B_0 = 5$ G, and $a = 100$ km. The gas pressure is $p_0 = 4.15 \times 10^{-3}$ Pa, which is uniform everywhere in the equilibrium, and $\beta \approx 0.05$. Hence, the density contrast between the internal and external plasmas is $\rho_f/\rho_c = 200$, while their characteristic speeds are: $c_{\text{Tf}} = 11.56$ km s $^{-1}$, $c_{\text{sf}} = 11.76$ km s $^{-1}$, $v_{\text{Af}} = 63.08$ km s $^{-1}$, $c_{\text{Tc}} = 163.51$ km s $^{-1}$, $c_{\text{sc}} = 166.33$ km s $^{-1}$, and $v_{\text{Ac}} = 892.06$ km s $^{-1}$.

3.2.1 Transverse modes

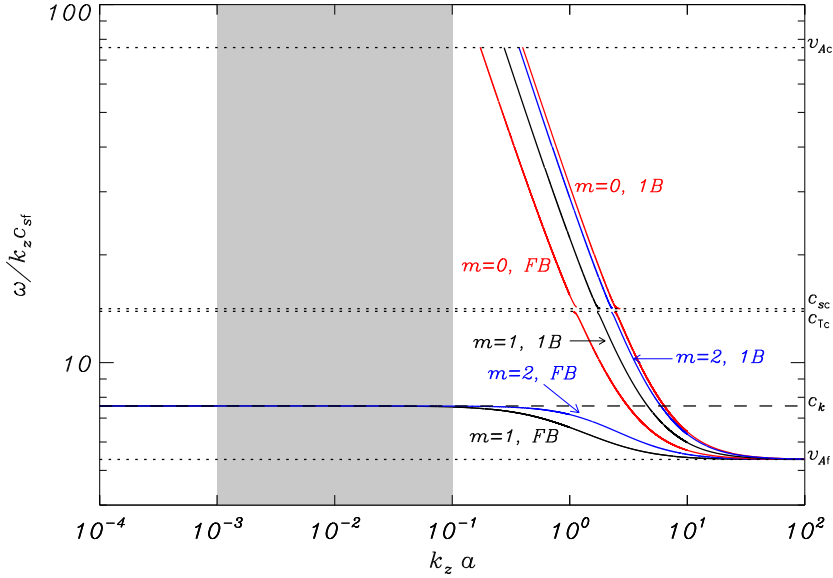


Figure 3.2: Normalized phase velocity, $\omega/k_z c_{sf}$, as a function of $k_z a$ corresponding to transverse modes with $m = 0$ (sausage), $m = 1$ (kink), and $m = 2$ (first fluting). FB and 1B denote fundamental and first branch, respectively. Note the forbidden region $c_{Tc} < \omega/k_z < c_{sc}$ where evanescent waves in the corona are not possible. The shaded zone corresponds to the relevant range of $k_z a$ of prominence oscillations. Note that both axes are in logarithmic scale.

First, we start with transverse modes. Figure 3.2 displays the phase velocity of modes with $m = 0, 1$, and 2 . The phase velocity of the trapped solutions is in the range $v_{Af} < \omega/k_z < v_{Ac}$, although it is worth mentioning the existence of a forbidden region at $c_{Tc} < \omega/k_z < c_{sc}$, where the evanescent condition is not fulfilled because $m_c^2 > 0$. Solutions have frequency cut-offs when the forbidden region is reached. The region $c_{Tc} < \omega/k_z < c_{sc}$ is inhabited by a collection of leaky modes with slow-like properties, whose behavior is dominated by coronal conditions, and whose amplitude within the flux tube is negligible (see Soler et al. 2007a, for a discussion of these modes in Cartesian geometry). We do not study these leaky coronal slow modes here.

For a fixed m , solutions can be classified according to the number of zeros of the total pressure perturbation in the radial direction (for $r \neq 0$). Thus, the solution without zeroes is the radially fundamental mode, the solution with one zero is the first radial harmonic, and so on. These radial harmonics are here called *branches*. We only have considered the fundamental and first branches in Figure 3.2. The behavior of all modes for $k_z a \gg 1$ is similar. The phase velocity of all of them tends toward the internal Alfvén speed as $k_z a$ increases. On the contrary, the behavior for $k_z a \ll 1$ is substantially different. The only solutions that exist as non-leaky waves for $k_z a \ll 1$ are the fundamental branches of modes with $m \neq 0$. Note that the rest of solutions are leaky, i.e., $\omega/k_z > v_{Ac}$, in the relevant range of $k_z a$ and for smaller values. Therefore,

3.2. DISPERSION DIAGRAMS AND EIGENFUNCTIONS

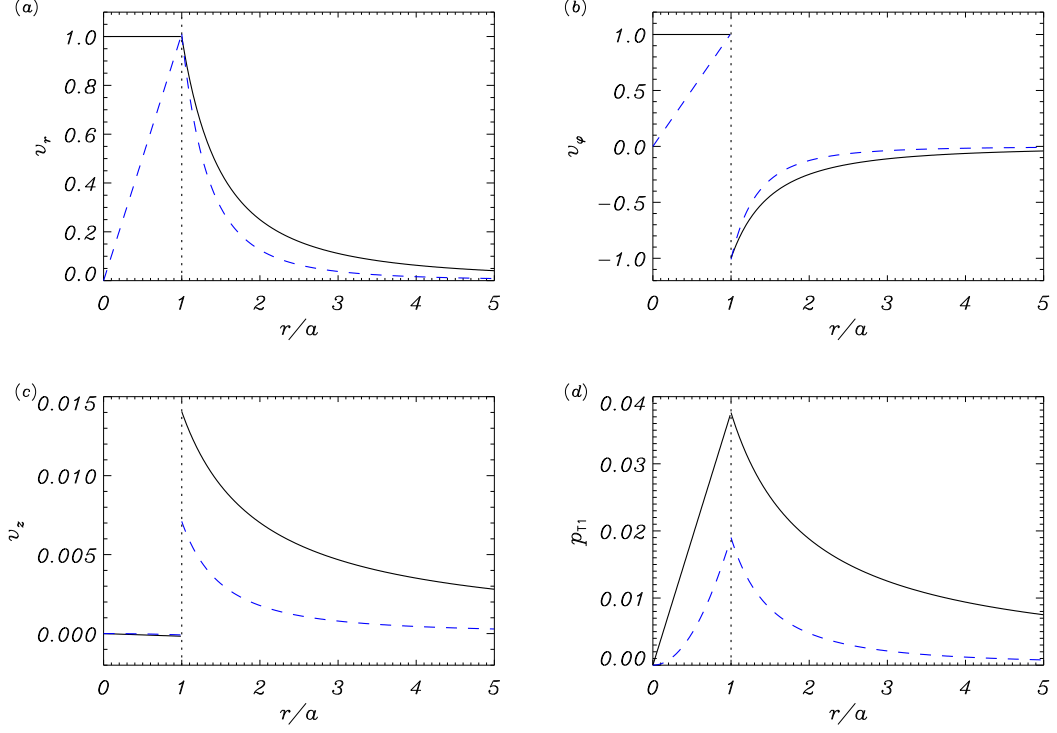


Figure 3.3: Eigenfunctions of perturbations (a) v_r , (b) v_φ , (c) v_z , and (d) p_{T_1} of the transverse modes for $k_z a = 10^{-2}$. The solid black line corresponds to the kink mode and the dashed blue line is for the first fluting mode. The vertical dotted line represents the edge of the cylinder. Arbitrary units have been used.

we discard sausage ($m = 0$) modes, and all the harmonic branches, from our subsequent analysis. For the sake of simplicity, we hereafter refer to the fundamental branches of the transverse modes with $m = 1$ and $m = 2$ as the kink and first fluting modes, respectively.

The phase velocity of all the fundamental branches with $m \neq 0$ for $k_z a \ll 1$ agrees with the value obtained in the TT case from Equation (3.20), namely

$$c_k \equiv \frac{\omega_k}{k_z} = \sqrt{\frac{(\rho_f v_{Af}^2 + \rho_c v_{Ac}^2)}{(\rho_f + \rho_c)}}, \quad (3.21)$$

where c_k is the so-called kink speed. For a uniform magnetic field, Equation (3.21) can be rewritten as

$$c_k = v_{Af} \sqrt{\frac{2}{1 + \rho_c/\rho_f}}. \quad (3.22)$$

In the case of filament threads, $\rho_f \gg \rho_c$, so the kink speed approximately is $c_k \approx \sqrt{2}v_{Af}$. For the considered parameters, one has that $c_k \approx 89.2 \text{ km s}^{-1}$.

Next, we study the eigenfunctions. Figure 3.3 shows the perturbations v_r , v_φ , v_z , and p_{T_1} of both the kink and first fluting modes for $k_z a = 10^{-2}$. The other perturbations are proportional to the plotted ones (see Eqs. [3.7]–[3.17]). Regarding the kink mode,

the amplitudes of both v_r and v_φ are almost uniform within the cylinder, meaning that the flux tube moves almost like a solid block. On the contrary, the amplitudes of v_r and v_φ of the first fluting mode are zero at the cylinder axis and maximum at the cylinder boundary, so this mode behaves in practice like a surface wave, although we recall that this solution satisfies $m_f^2 > 0$. This result for the first fluting mode stands for other fluting modes with larger m . In addition, $v_z \ll v_r$ and $v_z \ll v_\varphi$ for both the kink and fluting modes, meaning that they are mainly transversely polarized. We can see that the kink mode is the only solution that significantly displaces the cylinder axis, then being a good candidate to be related to the transverse oscillations of filament threads. Finally, note that both v_φ and v_z are discontinuous at the cylinder boundary.

3.2.2 Longitudinal slow modes

We turn our attention to slow modes. Figure 3.4 shows the phase velocity diagram of slow modes with $m = 0, 1$, and 2 , where only the fundamental branches are considered. The slow mode phase velocities are enclosed in the narrow range $c_{Tf} < \omega/k_z < c_{sf}$. The behavior of all solutions is very similar. Their phase velocity tends toward c_{sf} for $k_z a \gg 1$, and toward c_{Tf} for $k_z a \ll 1$. Note that the slow mode spectrum is anti-sturmian, with the fundamental branches having a larger frequency than their corresponding radial harmonics. In the relevant range of $k_z a$, one finds that $\omega/k_z \approx c_{Tf}$, but since $c_{Tf}/c_{sf} \approx 0.983$ for the present equilibrium parameters, a good approximation for the slow mode frequency is also $\omega/k_z \approx c_{sf}$ for any value of k_z and m .

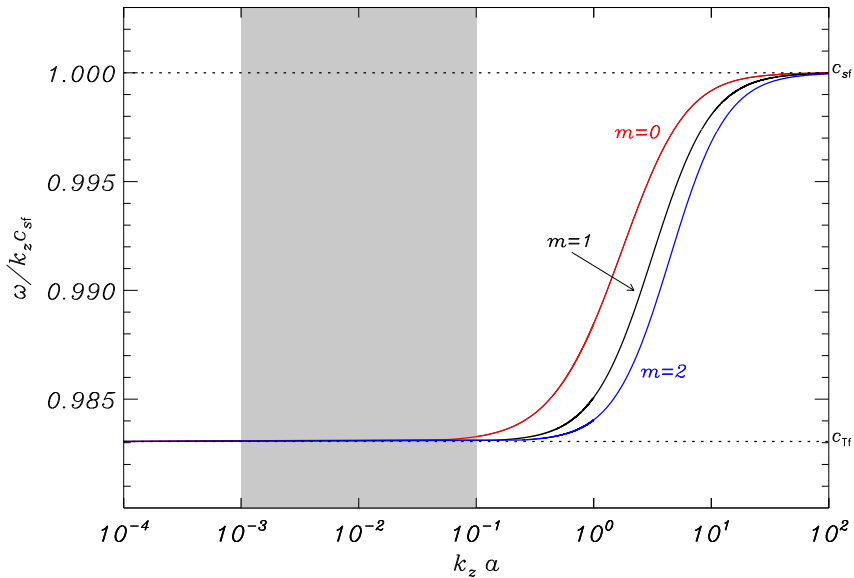


Figure 3.4: Normalized phase velocity, $\omega/k_z c_{sf}$, as a function of $k_z a$ corresponding to slow modes with $m = 0, 1$, and 2 . Only the fundamental branches are plotted. The shaded zone corresponds to the relevant range of $k_z a$ of prominence oscillations. Note that the horizontal axis is in logarithmic scale.

The eigenfunctions of the slow modes with $m = 0, 1$, and 2 are displayed in Fig-

ure 3.5. As expected, we clearly see that the dominant velocity perturbation is v_z , which is along magnetic field lines. In addition, we obtain that $v_z \approx 0$ in the coronal medium, meaning that slow modes are essentially confined within the cylinder and are almost insensitive to the physical conditions of the corona. By comparing Figures 3.3d and 3.5d, we see that, for similar velocity amplitudes, the total pressure perturbation is much larger for the slow modes than for the kink modes, obtaining the well-known conclusion that kink modes are almost incompressible disturbances while slow modes are compressible waves.

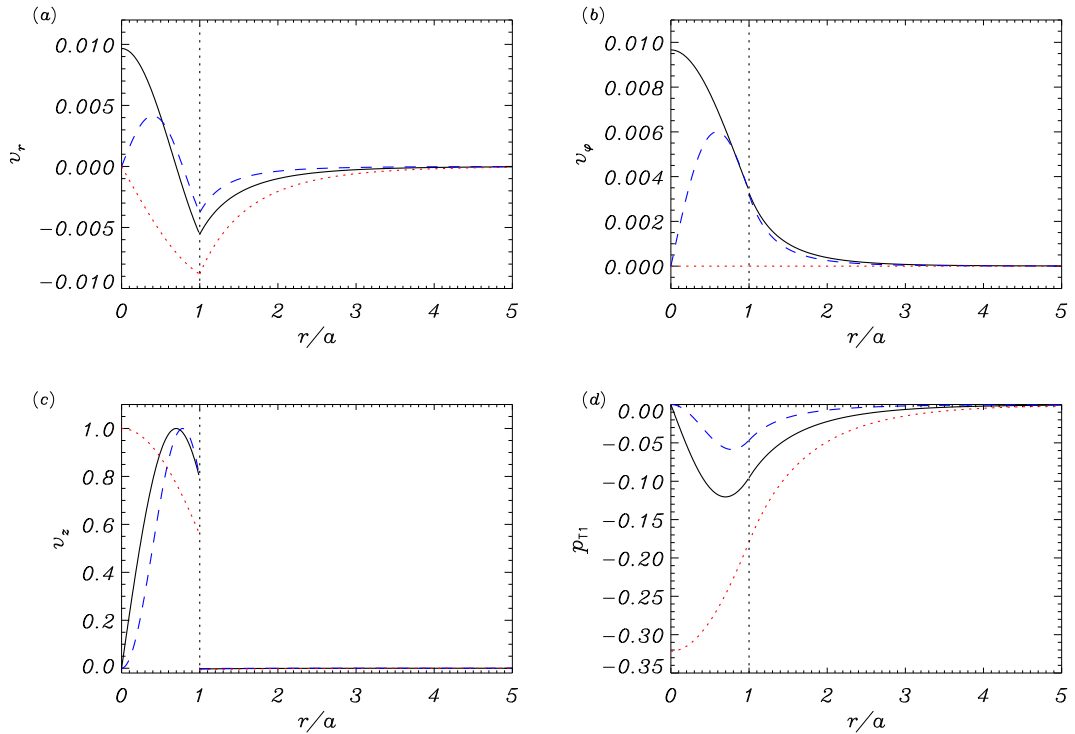


Figure 3.5: Eigenfunctions of perturbations (a) v_r , (b) v_ϕ , (c) v_z , and (d) p_{T1} of the slow modes. The line styles represent $m = 0$ (red dotted), $m = 1$ (solid black), and $m = 2$ (dashed blue). The vertical dotted line represents the edge of the cylinder. Arbitrary units have been used.

3.3 Oscillatory periods

Apart from the phase velocity and the polarization of motions, the oscillatory periods related to the different eigenmodes of the flux tube allow us to compare the theoretical predictions with the periods reported by the observers (see Sec. 1.4.2). The period, P , is computed from the frequency as

$$P = \frac{2\pi}{\omega}. \quad (3.23)$$

We must note that the precise value of the period depends on the physical properties considered in the model. Here, we consider the same physical conditions used in previous

Sections. We compute the periods of the kink mode and the slow mode with $m = 1$ (Fig. 3.6). Since there are very few determinations of the wavelength in the case of thread oscillations, we plot the period for the whole range of detected wavelengths of small-amplitude prominence oscillations. For comparative purposes, the different ranges of periods usually detected in prominence oscillations are indicated in Figure 3.6.

We see that the kink mode period is consistent with the typical periods of transverse thread oscillations (2 – 10 min), which are in the range of short periods usually reported in low-resolution observations of prominence oscillations. Again, we conclude that the kink mode is a good candidate to be responsible of the observed transverse thread oscillations.

On the contrary, the period related to the slow mode is larger. Although the slow mode period is compatible with the intermediate and long periods of small amplitude prominence oscillations, these intermediate- and long-period oscillations detected with low spatial resolutions have not been related yet to fine structure motions. It is likely that these intermediate- and long-period oscillations are related to global eigenmodes of the whole prominence instead of local oscillations of fine structures.

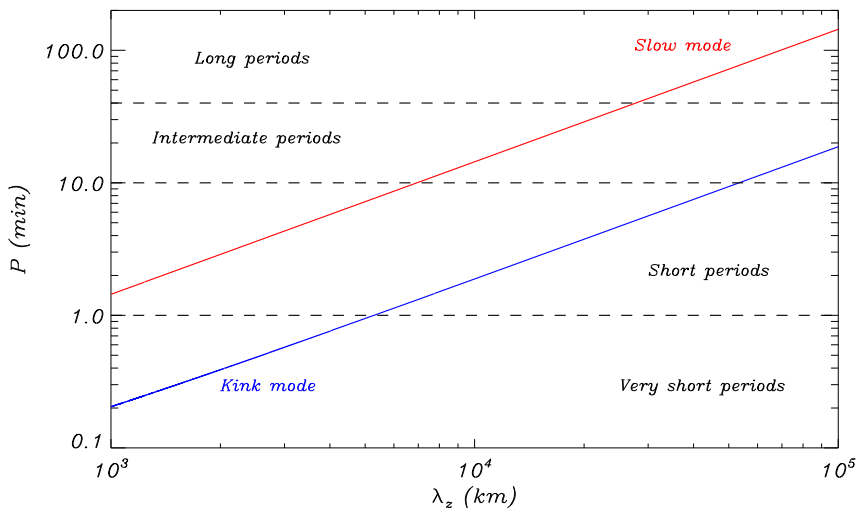


Figure 3.6: Period of the kink and slow ($m = 1$) modes in the range of typically observed wavelengths of prominence oscillations, λ_z . The horizontal dashed lines separate the period values according to the typical classification of short-, intermediate-, and long-period oscillations.

3.4 Seismological application to transverse thread oscillations¹

3.4.1 Observations

From recent high-resolution observations of a quiescent filament obtained with the Swedish 1m Solar Telescope in La Palma, Lin et al. (2009) detected swaying motions of

¹This Section is based on the results of Y. Lin, R. Soler, O. Engvold, J. L. Ballester, Ø. Langangen, R. Oliver, & L. H. M. Rouppe van der Voort 2009, *Swaying threads of a solar filament*, ApJ, 704, 870.

3.4. SEISMOLOGICAL APPLICATION TO THREAD OSCILLATIONS

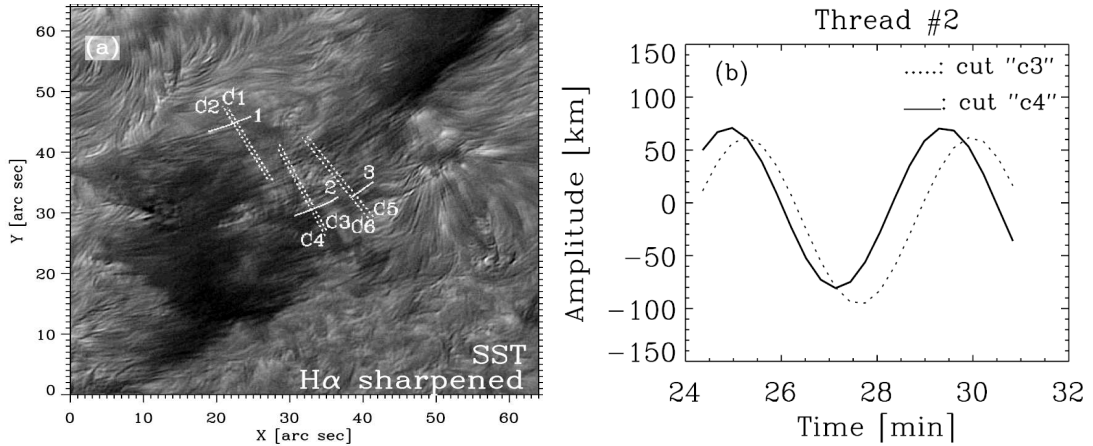


Figure 3.7: (a) Sharpened H α image of the target filament. Three of the ten studied threads are marked by solid white lines, whereas the dashed lines denote the location of the cuts. (b) Fitted sinusoidal curves of the temporal variation of the position of the thread at both cuts of thread # 2. Adapted from Figures 1 and 2 of Lin et al. (2009).

individual filament threads in the plane of the sky. While extensive details regarding the observational technique are given by Lin et al. (2009), we focus here on the interpretation of their observations. By means of H α filtergrams, many thin threads in the filament were resolved (see Fig. 3.7a). Sequences of H α images showed that some threads swayed back and forth in the plane of the sky. Ten of such swaying threads were selected for a more in-depth investigation. For each selected thread, two or three perpendicular cuts were made to measure the properties of possible propagating waves. The temporal variations of the positions of the threads within the cuts were fitted by sinusoidal curves (see Fig. 3.7b), from which the period, P , and the amplitude, A , of the wave were both derived (see the second and fourth columns of Table 3.1). The oscillatory character of these motions was checked by means of Doppler signals simultaneously obtained from the same filament threads, which revealed oscillatory periods similar to those computed from the H α sequences (further details are given by Lin et al. 2009). Assuming that the wave is propagating along the thread, the phase difference between two fitted curves at different cuts represents the time interval, T , the wave needs to travel between the two cuts. Given the distance, L , between the two cuts, the wave phase velocity was computed as $v_{\text{ph}} = L/T$ (see the third column of Table 3.1). From the results of Table 3.1, it is noticeable that the amplitude of motions at the two cuts of some threads, e.g., threads # 3 and 10, are significantly different. As suggested by Lin et al. (2009), it is likely that the change of the amplitude is caused by the spatial damping of the wave as it propagates along the thread, but unfortunately this issue was not studied in detail.

3.4.2 Theoretical interpretation

Such as shown in the last Sections, the kink mode is among the possible wave modes the only one that can produce a significant transverse displacement of the cylinder axis. Hence, the kink mode is the best candidate for an interpretation of the present observations. Moreover, the kink mode produces short-period oscillations of the order

CHAPTER 3. IDEAL MHD WAVES IN A MAGNETIC FLUX TUBE

Thread-Cut	P (min)	v_{ph} (km s ⁻¹)	A (km)	v_{Af} (km s ⁻¹)	B_0 (G)
1-c1	3.5 ± 0.1	16 ± 3	79 ± 6	12 ± 2	0.9 ± 0.3
1-c2	3.9 ± 0.1		70 ± 7		
2-c3	4.72 ± 0.05	20 ± 6	79 ± 7	14 ± 4	1.1 ± 0.5
2-c4	4.50 ± 0.03		76 ± 6		
3-c5	3.9 ± 0.1	24 ± 6	67 ± 10	17 ± 4	1.3 ± 0.5
3-c6	4.4 ± 0.1		110 ± 9		
4-c7	3.66 ± 0.04	36 ± 6	88 ± 4	26 ± 4	2.0 ± 0.4
4-c8	3.69 ± 0.04		86 ± 4		
5-c9	3.76 ± 0.02	57 ± 9	96 ± 3	41 ± 6	3.2 ± 0.7
5-c10	3.78 ± 0.03		81 ± 3		
6-c11	2.7 ± 0.1	28 ± 12	57 ± 4	20 ± 8	1.6 ± 0.9
6-c12	4.0 ± 0.1		73 ± 5		
7-c13	2.0 ± 0.1	62 ± 10	52 ± 3	44 ± 7	3.5 ± 0.8
7-c14	1.9 ± 0.1		59 ± 3		
7-c15	2.0 ± 0.1		52 ± 4		
8-c16	3.1 ± 0.1	40 ± 6	56 ± 4	29 ± 4	2.3 ± 0.5
8-c17	3.0 ± 0.1		34 ± 2		
9-c18	2.8 ± 0.1	20 ± 3	34 ± 3	14 ± 2	1.1 ± 0.2
9-c19	2.6 ± 0.1		57 ± 4		
10-c20	5.4 ± 0.1	28 ± 9	88 ± 3	20 ± 6	1.6 ± 0.7
10-c21	5.0 ± 0.2		58 ± 3		

Table 3.1: For the 10 selected H α swaying threads, the period (P), phase velocity (v_{ph}), and amplitude (A) of the detected propagating waves, along with estimations of the Alfvén speed (v_{Af}) by considering Equation (3.24), and the magnetic field strength (B_0) by assuming $\rho_f = 5 \times 10^{-11}$ kg m⁻³. Adapted from Tables 1 and 2 of Lin et al. (2009).

of minutes for typical filament plasma conditions (see Fig. 3.6), which is also compatible with the measured periods. Since the observed threads appear to be very thin and long structures, it seems reasonable to consider the thin tube approximation. According to Equation (3.22) the kink mode phase velocity is $c_k = v_{\text{Af}} [2 / (1 + \rho_c / \rho_f)]^{1/2}$. Now, assuming that the thread oscillations observed from the H α sequences are the result of a propagating kink mode, the measured phase velocity, v_{ph} , can be related to the kink speed, so $c_k = v_{\text{ph}}$. However, since v_{Af} and the ratio ρ_f / ρ_c are both unknown, we cannot obtain a unique solution from the last Equation. Nevertheless, we have to bear in mind that the ratio ρ_f / ρ_c is large in the case of filament threads. A value typically considered is $\rho_f / \rho_c \approx 200$. Figure 3.8a displays the ratio c_k^2 / v_{Af}^2 as a function of ρ_f / ρ_c . We see that for a large and realistic density contrast, the curve becomes flat and so the ratio c_k^2 / v_{Af}^2 is then almost independent of the density contrast. In such a situation, the factor $[2 / (1 + \rho_c / \rho_f)]^{1/2} \approx \sqrt{2}$ and so the kink speed directly depends on the filament Alfvén speed, $c_k \approx \sqrt{2} v_{\text{Af}}$. Therefore, it is possible to give a direct seismological estimation of the thread Alfvén speed from the measured phase velocity as

$$v_{\text{Af}} \approx v_{\text{ph}} / \sqrt{2}. \quad (3.24)$$

3.4. SEISMOLOGICAL APPLICATION TO THREAD OSCILLATIONS

The technique of MHD seismology has been applied by some authors to obtain information of the plasma physical conditions in the context of coronal loop oscillations (e.g., Nakariakov & Ofman 2001; Arregui et al. 2007a, 2008; Goossens et al. 2008) and prominence oscillations (Terradas et al. 2008). Since the density contrast in the case of coronal loops typically has a small value, the factor with the density ratio cannot be dropped from Equation (3.22) and it is not possible to give a direct estimation of the Alfvén speed from the observed kink speed. However, the much larger density of filament threads allows us to provide a more accurate determination of the Alfvén speed.

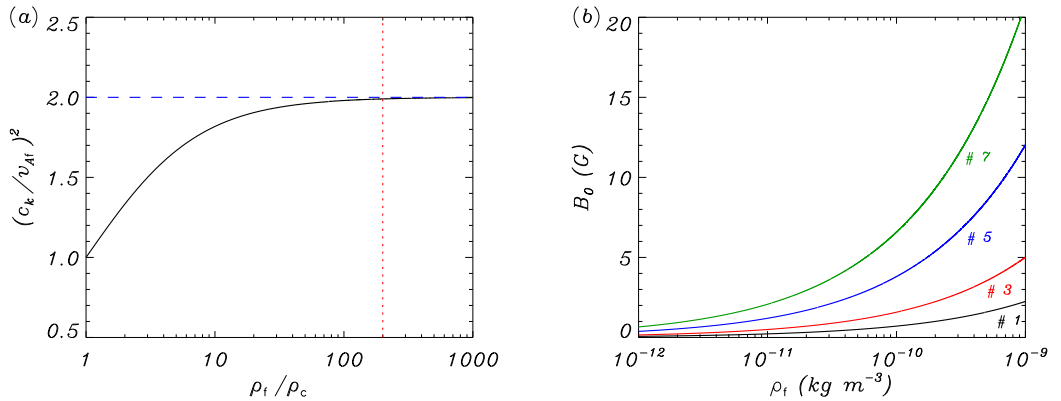


Figure 3.8: (a) Ratio c_k^2/v_{Af}^2 as a function of the density contrast, ρ_f/ρ_c . The horizontal dashed line corresponds to the value of the ratio c_k^2/v_A^2 for $\rho_f/\rho_c \rightarrow \infty$ and the vertical dotted line represents $\rho_f/\rho_c = 200$. (b) Magnetic field strength, B_0 , as a function of the filament thread density, ρ_f , corresponding to threads # 1, 3, 5, and 7.

3.4.3 Estimation of the Alfvén speed and the magnetic field strength

The fifth column of Table 3.1 contains an estimation of the Alfvén speed of each swaying thread observed in the H α sequences by taking Equation (3.24) into account. We see that the Alfvén speed varies in a wide range, which suggests that the physical properties, i.e., density, magnetic field strength, etc., significantly change in different threads of the filament. Once the Alfvén speed is determined, we have a relation between the magnetic field strength and the thread density, i.e., $B_0 = v_{Af}\sqrt{\mu\rho_f}$. Since the thread density is an unknown parameter, we cannot uniquely determine the magnetic field strength or vice versa. Figure 3.8b shows the dependence of B_0 with ρ_f corresponding to four selected threads. The density is allowed to vary in a wide range, $10^{-12} \text{ kg m}^{-3} < \rho_f < 10^{-9} \text{ kg m}^{-3}$, and subsequently the magnetic field strength is in the range $0.1 \text{ G} \lesssim B_0 \lesssim 20 \text{ G}$. This range agrees with the usually reported values of the magnetic field strength in quiescent prominences and filaments (e.g., Patsourakos & Vial 2002). By assuming a typical value of $\rho_f = 5 \times 10^{-11} \text{ kg m}^{-3}$ for the thread density and considering the results for the ten studied threads, one obtains a magnetic field strength which varies in the range $0.5 \text{ G} \lesssim B_0 \lesssim 5 \text{ G}$ (see the sixth column of Table 3.1). Although we have to be cautious with the values obtained in this very rough estimation, the present results suggest that the magnetic field in the filament is not homogeneous and could largely vary between threads. Also, this could happen for the density, but the results

are more sensible to magnetic field strength variations than to density variations. In addition, high-resolution observations suggest that the plasma parameters may vary along individual threads, which may affect the derived Alfvén speed and magnetic field strength.

3.5 Conclusion

In this Chapter, we have studied the properties of ideal MHD waves in a cylindrical magnetic flux tube representing a prominence fine-structure. By comparing the theoretical properties of these waves with the observations, i.e., periods, polarization of motions, etc., we conclude that the kink MHD mode is the best candidate to be responsible for the observed short-period, transverse oscillations of filament threads. On the other hand, slow-like modes have larger periods than those typically observed in thread oscillations. In the context of this interpretation, we related the observations of swaying motions of filament threads by [Lin et al. \(2009\)](#) to propagating kink modes, and gave a seismological estimation of the Alfvén speed by considering the values of the phase velocity reported by [Lin et al. \(2009\)](#). The obtained values of the Alfvén speed and the magnetic field strength are consistent with previous determinations of Alfvén speeds in prominences.

The next Chapters focus on the study of the damping phenomenon by taking different mechanisms into account and by assessing their efficiency for the damping of MHD waves in cylindrical filament threads.

4

Non-adiabatic Magnetohydrodynamic Waves in a Filament Thread with Mass Flow*

The aim of the present Chapter is to describe the effect of both mass flow and non-adiabatic effects on the oscillations supported by an individual prominence thread. Non-adiabatic effects are sometimes neglected when MHD waves are investigated in theoretical works. The adiabatic assumption is suitable when time-scales associated with non-adiabatic mechanisms are much larger than the typical oscillation time-scale. Nevertheless, depending on the medium physical properties, this condition is not always satisfied and the consideration of non-adiabatic effects is important to perform a realistic description of the wave behavior. For example, the importance of radiative losses and thermal conduction can be roughly estimated through two dimensionless parameters introduced by [De Moortel & Hood \(2004\)](#), called the thermal ratio, d , and the radiation ratio, r , which are essentially the ratio of the sound travel time ($\tau_s = \lambda_0/c_s$) to the conduction time-scale ($\tau_c = \lambda_0^2 p_0 / [(\gamma - 1)\kappa_{\parallel} T_0]$) and to the radiation time-scale ($\tau_r = \gamma p_0 / [(\gamma - 1)\rho_0^2 \chi^* T_0^\alpha]$), respectively, and where λ_0 is a typical length-scale and the rest of parameters are defined in [Chapter 2](#). Then,

$$d = \frac{(\gamma - 1)\kappa_{\parallel} T_0 \rho_0}{\gamma^2 p_0^2 \tau_s} = \frac{1}{\gamma} \frac{\tau_s}{\tau_c}, \quad (4.1)$$

$$r = \frac{(\gamma - 1)\tau_s \rho_0^2 \chi^* T_0^\alpha}{\gamma p_0} = \frac{\tau_s}{\tau_r}. \quad (4.2)$$

For typical physical conditions of the solar corona, $d \approx 4.83$ and $r \approx 6 \times 10^{-5}$, while for prominence conditions, $d \approx 10^{-6}$ and $r \approx 0.82$. These values suggest that thermal conduction can have an important role in coronal conditions, whereas radiation should be taken into account in prominence plasmas.

Here, we study the non-adiabatic magnetoacoustic wave modes supported by the same cylindrical filament thread model adopted in [Chapter 3](#). We obtain an analytical dispersion relation describing slow, fast, and thermal modes ([Sec. 4.1.2](#)). We perform several approximations and obtain analytical expressions for the ratio of the damping time to the period of the three solutions ([Sec. 4.1.4](#)). Later, we numerically solve the dispersion relation and compare the numerical results with the approximations. The efficiency of non-adiabatic effects on the damping of the oscillations is assessed by comparing the theoretical damping ratios with those reported in observations ([Sec. 4.2](#)). In addition, the effect of mass flows along the filament thread is also studied ([Sec. 4.3](#)).

*This Chapter is based on the results of [R. Soler, R. Oliver, & J. L. Ballester 2008](#), *Nonadiabatic Magnetohydrodynamic Waves in a Cylindrical Prominence Thread with Mass Flow*, *ApJ*, 685, 725.

4.1 Model and basic equations

4.1.1 Equilibrium configuration

The model configuration is that considered in Chapter 3, i.e., a homogeneous and infinite cylinder of radius a with density ρ_f and temperature T_f , embedded in an unbounded and also homogeneous corona with density ρ_c and temperature T_c . The magnetic field is uniform and orientated along the cylinder axis, $\vec{B}_0 = B_0 \hat{e}_z$. Here, a steady mass flow is assumed along the z -direction, whose flow velocity can be different in the thread and in the corona. Thus, $\vec{v}_f = v_f \hat{e}_z$ and $\vec{v}_c = v_c \hat{e}_z$ correspond to the steady flow in the flux tube and in the corona, respectively, with v_f and v_c constants. A subscript 0 is used when there is no need to specify the medium.

The effect of steady mass flows on the oscillatory modes of magnetic structures has been theoretically investigated by a number of authors (e.g., Goossens et al. 1992; Nakariakov & Roberts 1995; Erdélyi et al. 1995; Terra-Homem et al. 2003; Terradas et al. 2010, among other works). The most relevant studies for the present investigation are Nakariakov & Roberts (1995), who studied the effect of a steady flow on waves in coronal and photospheric slabs, and Terra-Homem et al. (2003), who extended the former study to cylindrical geometry. In addition to producing a shift of the oscillatory frequency, both papers show that the main effect of the flow is to break the symmetry between forward (parallel) and backward (anti-parallel) wave propagation to the flow direction and, for sufficiently strong flows, to forbid anti-parallel propagation of slow modes.

Carbonell et al. (2009) performed the first attempt to study the combined effect of both non-adiabatic mechanisms and steady flows on the time damping of slow and thermal waves in a homogeneous, unbounded prominence plasma. These authors found that the mass flow does not modify the damping time of both slow and thermal waves with respect to the case without flow, but the period of the slow wave increases dramatically for flow velocities close to the sound speed. Moreover, the thermal disturbance behaves as a propagating mode in the presence of flow. The present work goes a step forward with respect to Carbonell et al. (2009) since a more complex geometry is assumed here.

4.1.2 Dispersion relation

The non-adiabatic version of the energy equation (Eq. [2.85]) is considered. We assume that the plasma is fully ionized, and so the cross-field or perpendicular thermal conduction is absolutely negligible. Since we restrict ourselves to the linear regime, the terms corresponding to Joule and viscous heating are not present in the linearized energy equation, namely

$$\begin{aligned} & \frac{\partial p_1}{\partial t} + \rho_0 v_0 \frac{\partial p_1}{\partial z} - c_s^2 \left(\frac{\partial \rho_1}{\partial t} + \rho_0 v_0 \frac{\partial \rho_1}{\partial z} \right) \\ & + (\gamma - 1) \left[\rho_0 L_\rho \rho_1 + \rho_0 L_T T_1 - \kappa_{\parallel} \frac{\partial^2 T_1}{\partial z^2} \right] = 0, \end{aligned} \quad (4.3)$$

where all symbols have the same meaning as in Chapter 3, and L_ρ and L_T are the partial derivatives of the heat-loss function with respect to density and temperature,

respectively, namely

$$L_\rho = \left(\frac{\partial L}{\partial \rho} \right)_T, \quad L_T = \left(\frac{\partial L}{\partial T} \right)_\rho. \quad (4.4)$$

Therefore, parallel thermal conduction to the magnetic field, radiative losses, and heating are considered as non-adiabatic effects. Since the results for different heating scenarios do not show significant differences for prominence conditions (Carbonell et al. 2004; Terradas et al. 2005), here we restrict ourselves to a constant heating per unit volume ($a^* = b^* = 0$).

Assuming perturbations proportional to $\exp(ik_z z + im\varphi - i\omega t)$, one can combine Equation (4.3) with the Equation of state (Eq. [2.86]) to obtain the following relation between the pressure and density perturbations

$$p_1 = \Lambda_0^2 \rho_1, \quad (4.5)$$

with

$$\Lambda_0^2 = \frac{\tilde{\gamma} p_0}{\rho_0}, \quad \tilde{\gamma} = \left[\frac{(\gamma - 1)(\tilde{\kappa}_\parallel k_z^2 + \omega_T - \omega_\rho) - i\gamma\Omega_0}{(\gamma - 1)(\tilde{\kappa}_\parallel k_z^2 + \omega_T) - i\Omega_0} \right], \quad (4.6)$$

where $\Omega_0 = \omega - v_0 k_z$ is the Doppler-shifted frequency (Terra-Homem et al. 2003), $\tilde{\gamma}$ is here called the non-adiabatic index, and $\tilde{\kappa}_\parallel$, ω_ρ , and ω_T are defined as

$$\tilde{\kappa}_\parallel \equiv \frac{T_0}{p_0} \kappa_\parallel, \quad \omega_\rho \equiv \frac{\rho_0}{p_0} \rho_0 L_\rho, \quad \omega_T \equiv \frac{\rho_0}{p_0} T_0 L_T. \quad (4.7)$$

The complex quantity Λ_0 is here called the non-adiabatic sound speed. The real part of Λ_0 plays the role of the sound speed when non-adiabatic effects are present. By means of this definition, one can see that the effect of non-adiabatic terms is to modify the medium sound speed. Hence, it is expected that non-adiabatic effects most probably affect slow modes since they are mainly governed by acoustic effects. For the same reason, linear Alfvén waves are not damped by non-adiabatic mechanisms and are not considered in the present investigation. If non-adiabatic terms are neglected, $\tilde{\gamma} = \gamma$ and $\Lambda_0 = c_s$. With the help of Equation (4.6), we can follow again the treatment by Lighthill (1960) as in Chapter 3, and arrive at the governing equation of magnetoacoustic waves, namely

$$\Upsilon^2 [\Upsilon^2 - (\Lambda_0^2 + v_A^2) \nabla^2] \Delta + \Lambda_0^2 v_A^2 \frac{\partial^2}{\partial z^2} \nabla^2 \Delta = 0, \quad (4.8)$$

where $\Delta = \nabla \cdot \vec{v}_1$ and Υ is a linear operator defined as

$$\Upsilon = \frac{\partial}{\partial t} + v_0 \frac{\partial}{\partial z}. \quad (4.9)$$

Note that Equation (4.8) reduces to Equation (3.1) when both the effect of the flow and the non-adiabatic effects are dropped, i.e., $v_0 = 0$ and $\Lambda_0 = c_s$. The rest of perturbations depend on Δ according to Equations (3.7)–(3.17) if the replacements $\omega \rightarrow \Omega_0$ and $c_s \rightarrow \Lambda_0$ are performed. Thus, by writing $\Delta = R(r) \exp(ik_z z + im\varphi - i\omega t)$, we see that $R(r)$ satisfies again the Bessel Equation (Eq. [3.3]), with the radial wavenumber m_0 defined now as

$$m_0^2 = \frac{(\Omega_0^2 - k_z^2 v_A^2)(\Omega_0^2 - k_z^2 \Lambda_0^2)}{(v_A^2 + \Lambda_0^2)(\Omega_0^2 - k_z^2 c_T^2)}, \quad (4.10)$$

where \tilde{c}_T is the non-adiabatic cusp speed defined as

$$\tilde{c}_T^2 = \frac{v_A^2 \Lambda_0^2}{v_A^2 + \Lambda_0^2}. \quad (4.11)$$

Due to the presence of non-adiabatic effects, the radial wavenumber squared, m_0^2 , is now a complex quantity. Hence, no pure body-like or surface-like waves are possible in non-adiabatic magnetohydrodynamics. If one assumes that $|\Re(m_0^2)| > |\Im(m_0^2)|$ provided that non-adiabatic effects produce a small correction to the adiabatic wave modes, the dominant wave character depends on the sign of $\Re(m_0^2)$. Within the cylinder, oscillations are *mainly* body-like if $\Re(m_f^2) > 0$, whereas if $\Re(m_f^2) < 0$ oscillations are *mainly* surface-like. Note that, as for ideal waves, the situation $\Re(m_f^2) < 0$ is not possible for prominence conditions, meaning that perturbations are mainly body-like within the filament thread. On the other hand, the condition of outgoing waves whose amplitude is evanescent in the corona requires $\Re(m_c^2) < 0$ and $\Re(m_c/\Omega_c) > 0$. Then, $R(r)$ can be expressed as the following piecewise function

$$R(r) = \begin{cases} A_1 J_m(m_f r), & \text{if } r \leq a, \\ A_2 K_m(n_c r), & \text{if } r > a, \end{cases} \quad (4.12)$$

with $n_c^2 = -m_c^2$, A_1 and A_2 being complex constants. The dispersion relation is finally obtained by imposing the continuity of the Lagrangian radial displacement, $\xi_r = iv_r/\Omega_0$, and the total pressure perturbation, p_{T1} , at the cylinder edge, $r = a$. Thus,

$$\frac{n_c}{\rho_c (\Omega_c^2 - k_z^2 v_{Ac}^2)} \frac{K'_m(n_c a)}{K_m(n_c a)} - \frac{m_f}{\rho_f (\Omega_f^2 - k_z^2 v_{Af}^2)} \frac{J'_m(m_f a)}{J_m(m_f a)} = 0, \quad (4.13)$$

where the prime denotes derivative with respect to r . If the effect of the flow is dropped, i.e., $\Omega_f^2 = \Omega_c^2 = \omega^2$, Equation (4.13) is formally identical to the dispersion relation in the ideal case (Eq. [3.18]) because all the terms related to non-adiabatic effects are enclosed in the present definitions of m_f and n_c . The solution of Equation (4.13) for real k_z and m is a complex frequency, $\omega = \omega_R + i\omega_I$, damped solutions corresponding to $\omega_I < 0$. The oscillatory period, P , damping time, τ_D , and the ratio of both quantities are computed as

$$P = \frac{2\pi}{|\omega_R|}, \quad \tau_D = \frac{1}{|\omega_I|}, \quad \frac{\tau_D}{P} = \frac{1}{2\pi} \frac{|\omega_R|}{|\omega_I|}. \quad (4.14)$$

In the absence of flow, the complex oscillatory frequencies obtained by solving Equation (4.13) appear in pairs, $\omega_1 = \omega_R + i\omega_I$ and $\omega_2 = -\omega_R + i\omega_I$. The solution ω_1 corresponds to a wave propagating toward the positive z -direction (parallel to magnetic field lines), whereas ω_2 corresponds to a wave that propagates toward the negative z -direction (anti-parallel to magnetic field lines). For short, we call them forward and backward waves, respectively. Both forward and backward wave modes are equivalent and show exactly the same physical properties in the absence of flow. However, the symmetry between waves whose propagation is parallel or anti-parallel with respect to the flow direction is broken by the presence of flows.

4.1.3 The non-adiabatic sound speed

The non-adiabatic sound speed, $\Lambda_0 = (\tilde{\gamma} p_0 / \rho_0)^{1/2}$, plays an important role in the present investigation. Its value depends on the non-adiabatic mechanisms through the

quantity $\tilde{\gamma}$ given by Equation (4.6). In the absence of flow, one must replace Ω_0 by ω in Equation (4.6). We have that $\tilde{\gamma}$ depends on the frequency, so each eigenmode *feels* a different value of the non-adiabatic sound speed. Since the precise value of the sound speed is only relevant for slow modes, let us consider $\omega \approx c_s k_z$ in Equation (4.6). Then,

$$\tilde{\gamma} \approx \left[\frac{(\gamma - 1) (\tilde{\kappa}_{\parallel} k_z^2 + \omega_T - \omega_{\rho}) - i\gamma c_s k_z}{(\gamma - 1) (\tilde{\kappa}_{\parallel} k_z^2 + \omega_T) - i c_s k_z} \right]. \quad (4.15)$$

We can evaluate $\tilde{\gamma}$ in different limits. For $k_z a \ll 1$, the terms with k_z^2 and k_z can be neglected in Equation (4.15), which can be rewritten by taking into account that ω_T and ω_{ρ} are related through the exponent of the radiative losses function, α , as $\omega_T = \alpha \omega_{\rho}$. Hence,

$$\tilde{\gamma} \approx \frac{\alpha - 1}{\alpha}. \quad (4.16)$$

On the other hand, for $k_z a \gg 1$ the terms with k_z^2 are the dominant ones in Equation (4.15), so $\tilde{\gamma}$ becomes

$$\tilde{\gamma} \approx 1. \quad (4.17)$$

Therefore, the non-adiabatic sound speed is $\Lambda_0 \approx [(\frac{\alpha-1}{\alpha}) p_0/\rho_0]^{1/2}$ for $k_z a \ll 1$, and $\Lambda_0 \approx (p_0/\rho_0)^{1/2}$ for $k_z a \gg 1$. The value of Λ_0 for large wavenumber corresponds to the isothermal sound speed, whereas the value for small k_z depends on the radiative regime by means of the exponent α .

Now, we assume prominence conditions and numerically compute $\Re(\Lambda_f)$ as a function of $k_z a$ using Equation (4.15) (see Fig. 4.1a). The behavior of $\Re(\Lambda_f)$ in the limits of small and large $k_z a$ is consistent with our analytical estimations (Eqs. [4.16] and [4.17]), while for intermediate $k_z a$ the non-adiabatic sound speed coincides with the adiabatic sound speed. To shed light on this result, Figure 4.1b shows $\Re(\Lambda_f)$ for three different prominence radiative regimes and in the case without thermal conduction, i.e., $\kappa_{\parallel} = 0$. As expected, for small $k_z a$ and including the relevant range, the non-adiabatic sound speed is governed by radiation. On the other hand, for large $k_z a$ the dominant mechanism is thermal conduction. Note that although thermal conduction is responsible for the behavior of $\Re(\Lambda_f)$ in the case of large $k_z a$, the isothermal value of the sound speed is independent on the value of κ_{\parallel} (when $\kappa_{\parallel} \neq 0$, obviously).

4.1.4 Analytical approximations

Transverse modes

As in the ideal case, the dispersion relation (Eq. [4.13]) is a transcendental equation that has to be solved numerically. Some analytical progress is possible in the TT case. A first order, asymptotic expansion for $k_z a \ll 1$ and $m \neq 0$ of the Bessel functions of Equation (4.13) gives

$$\rho_f (\Omega_f^2 - k_z^2 v_{Af}^2) + \rho_c (\Omega_c^2 - k_z^2 v_{Ac}^2) = 0. \quad (4.18)$$

Taking into account that $\Omega_f = \omega - v_f k_z$ and $\Omega_c = \omega - v_c k_z$, the analytical solution of Equation (4.18) is

$$\omega = \frac{(\rho_f v_f + \rho_c v_c)}{(\rho_f + \rho_c)} k_z \pm \left[\frac{(\rho_f v_{Af}^2 + \rho_c v_{Ac}^2)}{(\rho_f + \rho_c)} k_z^2 - \frac{\rho_f \rho_c}{(\rho_f + \rho_c)^2} (v_f - v_c)^2 k_z^2 \right]^{1/2}, \quad (4.19)$$

CHAPTER 4. NON-ADIABATIC MHD WAVES IN A THREAD WITH FLOW

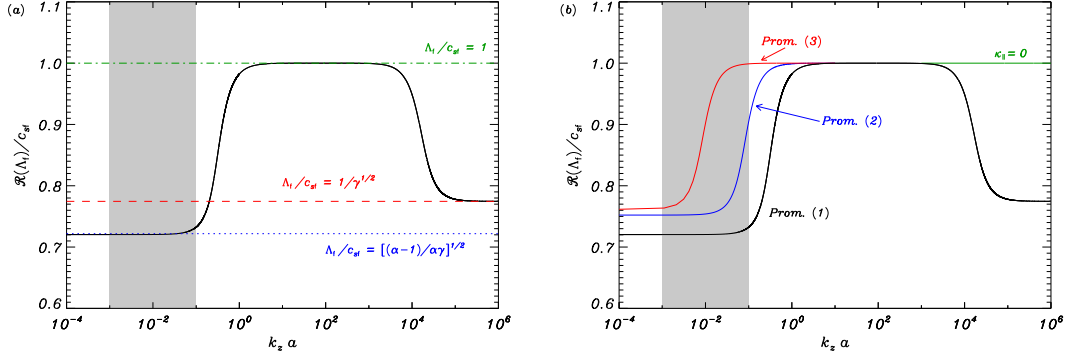


Figure 4.1: Real part of the prominence non-adiabatic sound speed as a function of $k_z a$. (a) Result considering the Prominence (1) radiative regime. The horizontal lines denote the limit values of the non-adiabatic sound speed. (b) Results for the different prominence radiative regimes. For comparative purposes, the result in the absence of thermal conduction ($\kappa_{\parallel} = 0$) is also computed for the Prominence (1) radiative regime. The shaded zone corresponds to the relevant range of $k_z a$ of prominence oscillations.

where the + and – signs correspond to forward and backward waves, respectively. When $v_f = v_c = 0$, Equation (4.19) reduces to Equation (3.20). Note that Equation (4.19) contains no terms related to non-adiabatic effects, meaning that transverse modes with $m \neq 0$ are undamped in the TT limit. This result allows us to predict that the kink mode damping by non-adiabatic mechanisms is very inefficient for realistic values of the wavenumber. It is possible to approximate Equation (4.19) in the case $v_c = 0$, $v_f \ll v_{Af}$, and $\rho_f \gg \rho_c$, namely

$$\omega \approx v_f k_z \pm \omega_k, \quad (4.20)$$

with ω_k the kink mode frequency in the absence of flow, meaning that the kink mode frequency shift is approximately linear with v_f for small values of the flow velocity.

On the other hand, it is possible to obtain from Equation (4.19) the critical value of the flow velocity that leads to the Kelvin-Helmholtz (KH) instability, namely

$$(v_f - v_c)_{\text{KH}} = \sqrt{\frac{\rho_f + \rho_c}{\rho_f \rho_c} (\rho_f v_{Af}^2 + \rho_c v_{Ac}^2)}. \quad (4.21)$$

In the absence of flow in the coronal medium, i.e., $v_c = 0$, the critical flow velocity can be expressed in terms of the internal Alfvén speed and the density contrast,

$$(v_f)_{\text{KH}} = v_{Af} \sqrt{2 \left(\frac{\rho_f}{\rho_c} + 1 \right)}. \quad (4.22)$$

These expressions agree with those derived by Holzwarth et al. (2007) and Terradas et al. (2010). For a typical density contrast of filaments, $\rho_f/\rho_c = 200$, one has $(v_f)_{\text{KH}} \approx 20v_{Af}$. Since the observed flow velocities are less than 30 km s^{-1} in quiescent prominences, which corresponds to sub-Alfvénic velocities, the KH critical velocity is much larger than the observed values.

Slow modes

To obtain an analytical expression of the slow mode frequency, let us consider its approximation in the ideal, static case, namely $\omega^2 \approx c_{\text{sf}}^2 k_z^2$. Such as happens for all the expressions described so far, we can simply perform the replacements $\omega \rightarrow \Omega_0$ and $c_s \rightarrow \Lambda_0$ to extend this approximation to the non-adiabatic case with flow, so

$$\Omega_0^2 \approx \Lambda_0^2 k_z^2. \quad (4.23)$$

By considering first the ideal case with flow, i.e., $\Omega_0^2 = c_s^2 k_z^2$, one obtains the expected result for the frequency, namely

$$\omega \approx v_0 k_z \pm c_s k_z, \quad (4.24)$$

where again the + and – signs correspond to forward and backward waves, respectively.

Provided that the main effect of the flow is to shift the real part of the frequency, let us consider the non-adiabatic case without flow, i.e., $\omega^2 \approx \Lambda_0^2 k_z^2$, to obtain an approximation for the imaginary part of the frequency. We write the frequency as $\omega = \omega_{\text{R}} + i\omega_{\text{I}}$ and neglect terms with ω_{I}^2 and ω_{I}^3 . Then, the following expression for ω_{I} is obtained

$$\omega_{\text{I}} \approx -\frac{(\gamma - 1)}{2\gamma} \left[\frac{(\gamma - 1)(\tilde{\kappa}_{\parallel} k_z^2 + \omega_{\text{T}}) + \omega_{\rho}}{c_s^2 k_z^2 + (\gamma - 1)^2 (\tilde{\kappa}_{\parallel} k_z^2 + \omega_{\text{T}})^2} \right] c_s^2 k_z^2. \quad (4.25)$$

Note that Equation (4.25) is valid for all values of k_z since so far we have only assumed $\omega_{\text{I}} \ll \omega_{\text{R}}$. Equation (4.25) is not only useful to calculate the damping time, but also provides us with a criterion for the wave thermal instability by finding the combination of parameters that causes $\omega_{\text{I}} > 0$, namely

$$(\gamma - 1)(\kappa_{\parallel} k_z^2 + \rho_0 L_T) + \frac{\rho_0^2}{T_0} L_{\rho} < 0, \quad (4.26)$$

where we have used Equation (4.7) to express $\tilde{\kappa}_{\parallel}$, ω_{T} , and ω_{ρ} in terms of the equilibrium density and temperature. Equation (4.26) turns out to be the instability criterion for near-isentropic acoustic oscillations obtained by Field (1965) in his Equation (25b). When $k_z a \ll 1$, thermal conduction can be omitted and the instability criterion is further simplified by taking the full expressions for L_T and L_{ρ} into account. Hence, Equation (4.26) becomes

$$\alpha < \frac{-1}{\gamma - 1}, \quad (4.27)$$

which gives $\alpha < -0.6$ for $\gamma = 5/3$. According to Equation (4.27), none of the three prominence radiative regimes of Table 2.1 is thermally unstable, but the PCTR (3) and coronal regimes fulfill the instability condition, as was obtained by Carbonell et al. (2004).

Let us consider now the different limits of $k_z a$ and calculate the approximate expression of τ_{D}/P in each case in the presence of flow. For $k_z a \ll 1$ and according to Equations (4.16) and (4.24), we can approximate the real part of the slow mode frequency as $\omega_{\text{R}} \approx v_0 k_z \pm \sqrt{\frac{\alpha-1}{\alpha\gamma}} c_s k_z$. Then we compute the ratio $\omega_{\text{I}}/\omega_{\text{R}}$ and neglect the terms with k_z^2 . Hence, the expression for τ_{D}/P is

$$\frac{\tau_{\text{D}}}{P} \approx \frac{\gamma}{\pi} \left[\frac{(\gamma - 1) \alpha^2 \omega_{\rho}}{(\gamma - 1) \alpha + 1} \right] \frac{v_0 \pm \sqrt{\frac{\alpha-1}{\alpha\gamma}} c_s}{c_s^2} k_z^{-1}, \quad \text{if } k_z a \ll 1, \quad (4.28)$$

CHAPTER 4. NON-ADIABATIC MHD WAVES IN A THREAD WITH FLOW

where we have used the relation $\omega_T = \alpha\omega_\rho$. From Equation (4.28) we see that $\tau_D/P \sim \mathcal{O}(k_z^{-1})$ when $k_z a \ll 1$. Note that the term related to thermal conduction is absent in Equation (4.28), which indicates that the slow mode damping in the TT limit is dominated by radiative losses. In the opposite situation, i.e., for $k_z a \gg 1$, we approximate the real part of the frequency as $\omega_R \approx v_0 k_z \pm \frac{1}{\sqrt{\gamma}} c_s k_z$ (Eqs. [4.17] and [4.24]), and the dominant terms in the ratio ω_I/ω_R are those with k_z^2 . Therefore, τ_D/P is now

$$\frac{\tau_D}{P} \approx \frac{\gamma}{\pi} \tilde{\kappa}_\parallel \frac{\left| v_0 \pm \frac{1}{\sqrt{\gamma}} c_s \right|}{c_s^2} k_z, \quad \text{if } k_z a \gg 1. \quad (4.29)$$

Thus, we see that $\tau_D/P \sim \mathcal{O}(k_z)$ when $k_z a \gg 1$, and the damping is independent of the radiation terms since the limit $k_z a \gg 1$ corresponds to the isothermal regime dominated by thermal conduction. Finally, for intermediate $k_z a$, one has that $\omega_R \approx v_0 k_z \pm c_s k_z$, but we have to use the complete expression of ω_I given by Equation (4.25). Therefore, we obtain

$$\frac{\tau_D}{P} \approx \frac{\gamma}{\pi(\gamma-1)} \left[\frac{c_s^2 k_z^2 + (\gamma-1)^2 (\tilde{\kappa}_\parallel k_z^2 + \omega_T)^2}{(\gamma-1)(\tilde{\kappa}_\parallel k_z^2 + \omega_T) + \omega_\rho} \right] \frac{|v_0 \pm c_s|}{c_s^2 k_z}, \quad \text{if } k_z a \sim 1. \quad (4.30)$$

We see that the expression of τ_D/P for intermediate $k_z a$ does not have a simple dependence with k_z .

Thermal mode

Now we turn our attention to the thermal or condensation mode. The thermal mode is a very peculiar solution that only appears in the presence of non-adiabatic effects. In the absence of flows, its frequency is purely imaginary, so the thermal mode is a non-propagating, purely damped disturbance. The temperature perturbations are more important for the thermal mode than for the magnetoacoustic modes. Because of its unstable character in some coronal conditions, the thermal mode has been investigated as a possible mechanism for the formation of prominences and their fine structures (e.g., [van der Linden 1993](#); [Ireland et al. 1998](#)). The general properties of the thermal mode have been studied in uniform, unbounded plasmas (e.g., [Field 1965](#)), in coronal slabs (e.g., [van der Linden & Goossens 1991](#)), and in coronal cylinders (e.g., [An 1984](#)).

Following a similar argument as in [van der Linden & Goossens \(1991\)](#), we check that the evanescent assumption in the corona ($m_c^2 < 0$) along with the body-wave assumption within the thread ($m_f^2 > 0$) can be both satisfied by the thermal mode. Let us express the thermal mode frequency as $\omega = is$, where s is real and here called the damping rate. The situation $s < 0$ corresponds to a damped thermal mode, whereas $s > 0$ occurs if the mode is thermally unstable. From Equation (4.10) one obtains

$$m_0^2 = -\frac{(s^2 + k_z^2 v_A^2)(s^2 + k_z^2 \Lambda_0^2)}{(v_A^2 + \Lambda_0^2)(s^2 + k_z^2 \tilde{c}_T^2)} = -(s^2 + k_z^2 v_A^2) \frac{\mathcal{A}}{\mathcal{B}}. \quad (4.31)$$

The quantities \mathcal{A} and \mathcal{B} are the following third-order polynomials in s ,

$$\mathcal{A} = s^3 + \mathcal{N}_2 s^2 + k_z^2 c_s^2 s + k_z^2 c_s^2 \mathcal{N}_2, \quad (4.32)$$

$$\mathcal{B} = s^3 + \mathcal{N}_3 s^2 + k_z^2 c_T^2 s + k_z^2 c_T^2 \mathcal{N}_1, \quad (4.33)$$

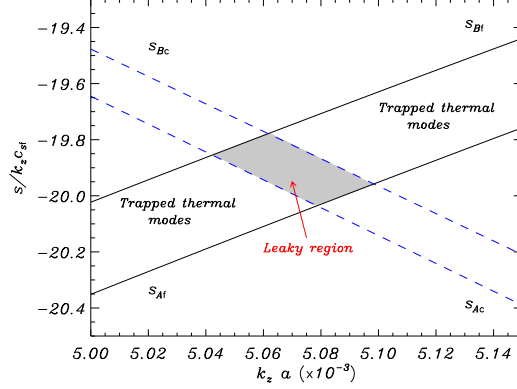


Figure 4.2: Normalized solutions of $\mathcal{A} = 0$ (Eq. [4.32]) and $\mathcal{B} = 0$ (Eq. [4.33]) for prominence (solid lines) and coronal (dashed lines) conditions. The shaded zone, i.e., the overlap of the regions where $m_f^2 > 0$ (between solid lines) and $m_c^2 > 0$ (between dashed lines), points the region where the thermal mode does not exist as an evanescent-like solution.

with

$$\mathcal{N}_1 = \frac{(\gamma - 1)}{\gamma} (\tilde{\kappa}_{\parallel} k_z^2 + \omega_T - \omega_{\rho}), \quad (4.34)$$

$$\mathcal{N}_2 = (\gamma - 1) (\tilde{\kappa}_{\parallel} k_z^2 + \omega_T), \quad (4.35)$$

$$\mathcal{N}_3 = \frac{\mathcal{N}_2 v_A^2 + \mathcal{N}_1 c_s^2}{v_A^2 + c_s^2}. \quad (4.36)$$

The condition $m_f^2 > 0$ implies that $\text{sign}(\mathcal{A}_f) \neq \text{sign}(\mathcal{B}_f)$. The solutions of $\mathcal{A} = 0$ are a pair of complex conjugate roots and a real root, while the same stands for the roots of $\mathcal{B} = 0$. Then, the condition $m_f^2 > 0$ is only verified in the region between the real roots of $\mathcal{A}_f = 0$ and $\mathcal{B}_f = 0$, namely $s_{\mathcal{A}_f}$ and $s_{\mathcal{B}_f}$, respectively, which are very close to each other. On the other hand, the external evanescent requirement ($m_c^2 < 0$) is verified outside the region between the real solutions of $\mathcal{A}_c = 0$ and $\mathcal{B}_c = 0$, namely $s_{\mathcal{A}_c}$ and $s_{\mathcal{B}_c}$ respectively. In a weak damping situation, one can neglect the terms with s^2 and s^3 , so the real roots of $\mathcal{A} = 0$ and $\mathcal{B} = 0$ are $s_{\mathcal{A}} \approx -\mathcal{N}_2$ and $s_{\mathcal{B}} \approx -\mathcal{N}_1$, respectively. By computing these real roots considering prominence and coronal conditions (Fig. 4.2), one obtains that these regions do not overlap except for $5.04 \times 10^{-3} \lesssim k_z a \lesssim 5.10 \times 10^{-3}$, where $m_f^2 > 0$ but also $m_c^2 > 0$, so the evanescent assumption is not verified. Then, the thermal mode cannot exist as a non-leaky solution in such a forbidden region. However, outside this extremely narrow overlapping region, the fundamental thermal mode and all its radial harmonics exist with an almost identical damping rate in the range $s_{\mathcal{B}_f} < s < s_{\mathcal{A}_f}$, whose value is also almost independent of the azimuthal wavenumber, m .

To obtain a simple expression of the thermal mode damping rate, let us approximate $s \approx s_{\mathcal{B}}$. This approximation is similar to the approximation $\omega \approx c_s k_z$ considered in the case of the slow mode. Then, we take $\mathcal{B} = 0$ and neglect the terms with s^2 and s^3 in

Equation (4.33), obtaining

$$s \approx -\frac{(\gamma - 1)}{\gamma} (\tilde{\kappa}_{\parallel} k_z^2 + \omega_T - \omega_{\rho}). \quad (4.37)$$

Equation (4.37) is equivalent to the approximated expression for the thermal mode frequency provided by Carbonell et al. (2009). Expressing ω_T and ω_{ρ} in terms of L_T and L_{ρ} , the following criterion should be satisfied to have a damped, stable solution

$$\kappa_{\parallel} k_z^2 + \rho_0 \left(L_T - \frac{\rho_0}{T_0} L_{\rho} \right) > 0. \quad (4.38)$$

Equation (4.38) is the same stability criterion provided by Field (1965) in his Equation (25a). Since for prominence conditions this inequality is verified for all real values of k_z , the thermal mode is always a damped solution in our case.

By defining the thermal mode damping time as $\tau_D = 1/|s|$, one obtains from Equation (4.37) that

$$\tau_D \approx \frac{\gamma}{(\gamma - 1)} (\tilde{\kappa}_{\parallel} k_z^2 + \omega_T - \omega_{\rho})^{-1}. \quad (4.39)$$

The long and short wavelength limits of Equation (4.39) are, respectively,

$$\tau_D \approx \frac{\gamma}{(\gamma-1)(\alpha-1)\omega_{\rho}} \quad \text{if} \quad k_z a \ll 1, \quad (4.40)$$

$$\tau_D \approx \frac{\gamma}{(\gamma-1)\tilde{\kappa}_{\parallel} k_z^2} \quad \text{if} \quad k_z a \gg 1, \quad (4.41)$$

thus the damping time is constant for $k_z a \ll 1$ and is $\mathcal{O}(k_z^{-2})$ for $k_z a \gg 1$.

In the presence of flow, the thermal mode frequency has a real part given by the Doppler shift as $\omega = v_0 k_z + is$. In such a case, the ratio of the damping time to the period is

$$\frac{\tau_D}{P} \approx \frac{1}{2\pi} \frac{\gamma}{(\gamma - 1)} \frac{|v_0 k_z|}{(\tilde{\kappa}_{\parallel} k_z^2 + \omega_T - \omega_{\rho})}. \quad (4.42)$$

4.2 Results in the absence of flow

We first study the case without flows, i.e., $v_f = v_c = 0$. The physical parameters used in the following computations are the same considered in Chapter 3: $\tilde{T}_f = 10^4$ K, $\rho_f = 5 \times 10^{-11}$ kg m⁻³, $\tilde{T}_c = 2 \times 10^6$ K, $\rho_c = 2.5 \times 10^{-13}$ kg m⁻³, $B_0 = 5$ G, and $a = 100$ km. Unless otherwise stated, we assume the Prominence (1) and Corona regimes of Table 2.1 to represent the prominence and coronal plasma radiative losses, respectively.

4.2.1 Dispersion diagrams

Here, we compute the phase velocity diagrams of transverse and slow modes, and compare them to the corresponding diagrams in the adiabatic case. We restrict ourselves to the fundamental branches of modes with $m = 0, 1$, and 2.

We first consider transverse modes. Figure 4.3a displays the phase velocity, ω_R/k_z , as a function of $k_z a$. Note that Figure 4.3 is a projection of the phase velocity on the real plane, since ω is now a complex quantity. Figure 4.3a can be compared with

Figure 3.2, corresponding to the ideal, adiabatic case, and we see that the phase velocity of transverse modes is barely affected by the presence of non-adiabatic mechanisms. Hence, the period of these solutions is approximately the same as in the ideal case. The main novelty with respect to the ideal case is that the ideal forbidden band inhabited by leaky coronal slow modes, i.e., $c_{\text{Tc}} < \omega/k_z < c_{\text{sc}}$, is replaced by the complex region $\tilde{c}_{\text{Tc}} < \omega/k_z < \Lambda_c$, whose projection on the plane of Figure 4.3a is indicated by dotted lines. Now, the sausage mode frequency does not cross the forbidden region in the complex space, and so there is no frequency cut-off when the sausage mode phase velocity reaches the projection of the forbidden region on the real plane, $\Re(\tilde{c}_{\text{Tc}}) < \omega_{\text{R}}/k_z < \Re(\Lambda_c)$.

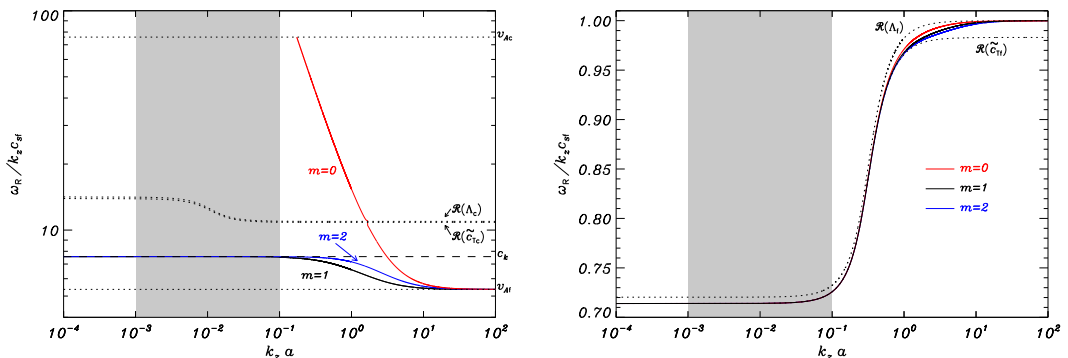


Figure 4.3: Normalized phase velocity, $\omega_{\text{R}}/k_z c_{\text{sf}}$, as a function of $k_z a$ corresponding to non-adiabatic normal modes with $m = 0, 1$, and 2 . (a) Result for transverse modes. Note that the interval $\Re(\tilde{c}_{\text{Tc}}) < \omega_{\text{R}}/k_z < \Re(\Lambda_c)$ is a projection on the plane of the figure of the complex forbidden region $\tilde{c}_{\text{Tc}} < \omega/k_z < \Lambda_c$. (b) Result for slow modes. The dotted lines denote the interval $\Re(\tilde{c}_{\text{Tf}}) < \omega_{\text{R}}/k_z < \Re(\Lambda_f)$, which is a projection on the plane of the figure of the complex region $\tilde{c}_{\text{Tf}} < \omega/k_z < \Lambda_f$. In both panels, the shaded zone corresponds to the relevant range of $k_z a$ of prominence oscillations. Note that the horizontal axes are in logarithmic scale.

Contrary to transverse modes, the phase velocity diagram of slow modes shows significant differences with respect to the adiabatic case (compare Figs. 3.4 and 4.3b). First, the adiabatic phase velocity band $c_{\text{Tf}} < \omega/k_z < c_{\text{sf}}$ is replaced by its non-adiabatic, complex counterpart $\tilde{c}_{\text{Tf}} < \omega/k_z < \Lambda_f$. Figure 4.3b displays a projection of this complex band on the real plane. The range of phase velocities of slow modes is even narrower than in the ideal case. Since both $\Re(\tilde{c}_{\text{Tf}})$ and $\Re(\Lambda_f)$ depend on $k_z a$, the range of allowed phase velocities is not constant with $k_z a$. For example, in the relevant range of $k_z a$, the allowed phase velocities are smaller than for larger $k_z a$. This causes the slow mode period in the non-adiabatic case to be larger than in the ideal case. Despite these differences with the adiabatic case, we see that the non-adiabatic slow modes are also very insensitive to the value of m .

4.2.2 Damping times

Now, we study the efficiency of the different non-adiabatic mechanisms for the damping of the eigenmodes. Here, the relevant quantity is the ratio of the damping time to the period, τ_{D}/P . Values of $\tau_{\text{D}}/P < 10$ are realistic, whereas larger values indicate that

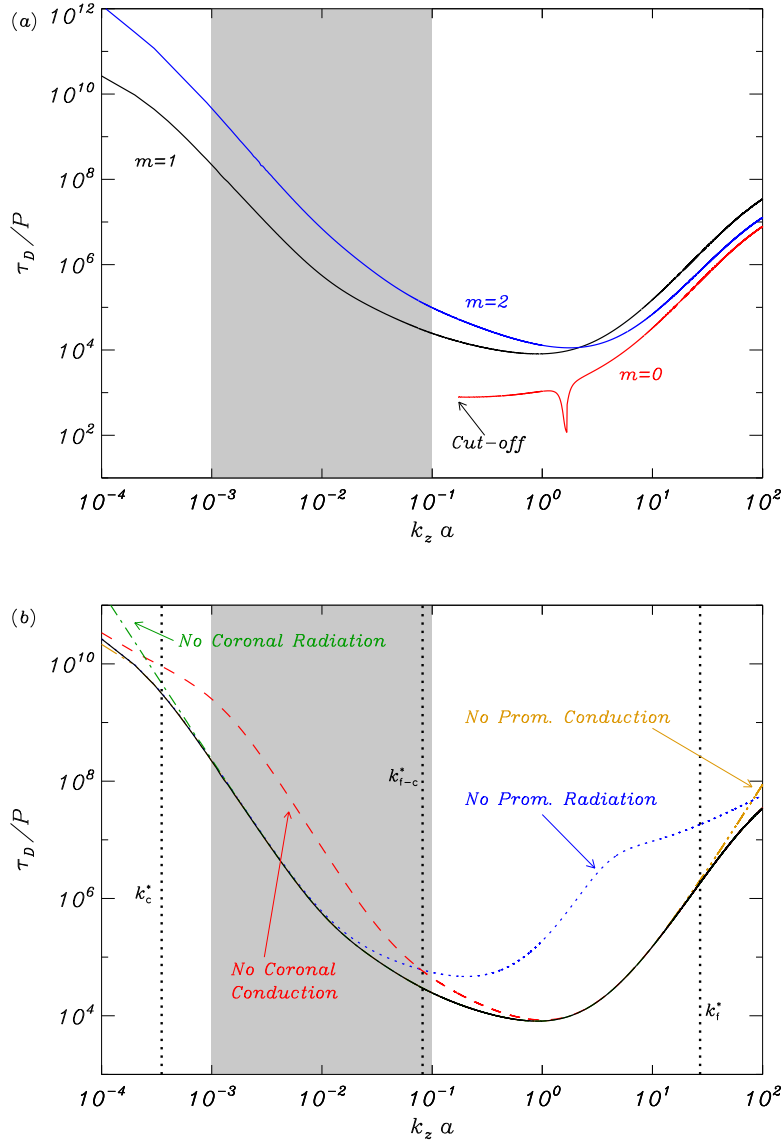


Figure 4.4: (a) Ratio of the damping time to the period, τ_D/P , as a function of $k_z a$ corresponding to the non-adiabatic sausage ($m = 0$), kink ($m = 1$), and first fluting ($m = 2$) modes. Note the sausage mode frequency cut-off. (b) τ_D/P versus $k_z a$ of the kink mode (solid line). The different discontinuous lines correspond to the solution when a specific non-adiabatic mechanism, indicated by means of labels, is removed from the energy equation. The vertical dotted lines are the approximated transitional wavenumber between the ranges of dominance of the different mechanisms given by Equations (4.43) and (4.44).

the considered mechanisms are not efficient enough to provide damping times consistent with those observed.

Transverse modes

Figure 4.4a shows τ_D/P versus $k_z a$ for the sausage, kink, and first fluting transverse modes. In all the cases, we see that $\tau_D/P \gg 10$. In particular, the values of τ_D/P of the kink mode within the observationally relevant range of $k_z a$ go from 10^4 to 10^8 , approximately, meaning that non-adiabatic effects cannot explain the observed damping of transverse thread oscillations. The sausage mode shows a peculiar behavior for $k_z a \approx 2$, where τ_D/P reaches a pronounced minimum. This minimum is caused by the coupling to leaky coronal slow modes when the sausage mode phase velocity is in the range $\Re(\tilde{c}_{Tc}) < \omega_R/k_z < \Re(\Lambda_c)$.

Figure 4.4b allows us to shed light on the kink mode behavior. In order to know which is the most dominant damping mechanism, we compare the damping time obtained when considering all non-adiabatic terms with the results obtained when a specific mechanism is removed from the energy equation. With this analysis, we are able to know where the omitted mechanism has an appreciable effect on the damping. Coronal thermal conduction turns out to be the dominant mechanism in the relevant range of $k_z a$, while prominence radiation losses and prominence thermal conduction only become important for larger $k_z a$. On the contrary, coronal radiation losses are negligible but for $k_z a$ smaller than the realistic values.

Approximate values of k_z for which the transitions between the different regimes governed by the damping mechanisms take place can be computed by considering the thermal ratio, d , and the radiation ratio, r , given by Equations (4.1) and (4.2), respectively, and following a similar process to that of Carbonell et al. (2006) and Soler et al. (2007b). We relate the typical length-scale, λ_0 , that appears in the expressions of d and r with the longitudinal wavenumber, $\lambda_0 \sim k_z^{-1}$. Then, the condition $d = r$ gives us the transitional wavenumber, k^* , between the radiation-dominated regime and the conduction-dominated regime, namely

$$k^* \approx \rho_0 \sqrt{\frac{\chi^* T_0^{\alpha-1}}{\kappa_{\parallel}}}, \quad (4.43)$$

which has to be evaluated for both prominence and coronal conditions to know the approximated values of k_z for the prominence radiation-prominence conduction transition, k_f^* , and the coronal radiation-coronal conduction transition, k_c^* , respectively. On the other hand, the approximate wavenumber for the transition from coronal conduction to prominence radiation, k_{f-c}^* , can be estimated by imposing $d_c = r_f$, where the subscripts indicate what physical conditions must be considered, thus

$$k_{f-c}^* \approx \rho_f \sqrt{\frac{\rho_f \chi_f^* T_f^{\alpha_f}}{\rho_c \kappa_{\parallel c} T_c}}. \quad (4.44)$$

These approximate transitional wavenumbers are shown by means of vertical lines in Figure 4.4b. We see a good agreement of k_{f-c}^* and k_c^* with the actual transitional wavenumbers. However, the actual value of k_f^* is larger than the approximation, although the order of magnitude of the approximation is the correct one.

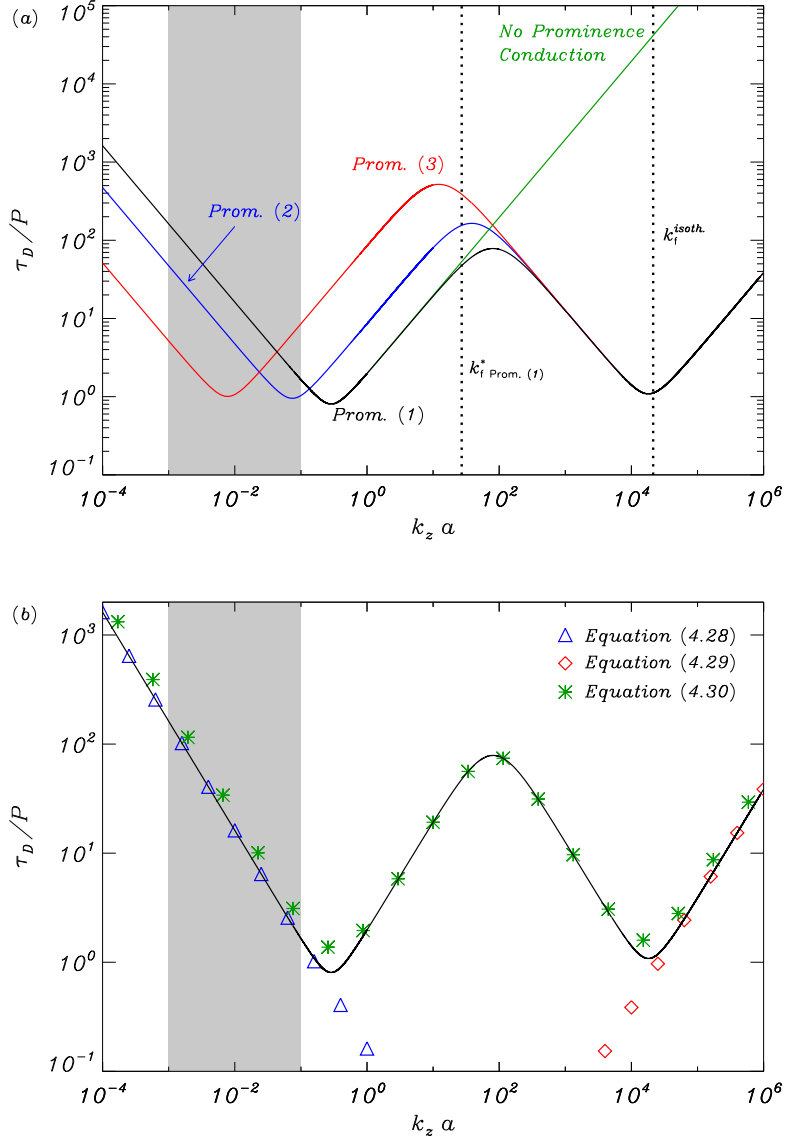


Figure 4.5: Ratio of the damping time to the period, τ_D/P , as a function of $k_z a$ corresponding to the non-adiabatic slow mode with $m = 1$. (a) Results for the different prominence radiative regimes (labeled within the Figure) and for the case without prominence thermal conduction. The result in the absence of thermal conduction is computed for the Prominence (1) regime. The vertical dotted lines are the approximate transitional wavenumbers between the radiative regime and the conductive regime, k_f^* given by Equation (4.43), and the critical wavenumber of the isothermal regime, k_f^{isoth} given by Equation (4.45). (b) The numerical solution for the Prominence (1) regime (solid line) is compared with several analytical approximations (Eqs. [4.28]–[4.30]).

Slow modes

Turning now to slow modes, we plot in Figure 4.5a τ_D/P versus $k_z a$ corresponding to the slow mode with $m = 1$. Since the other slow waves with a different m show the same properties, we restrict ourselves to this solution for the sake of simplicity. The slow mode is much more efficiently attenuated than the kink mode and its damping is entirely governed by prominence mechanisms. Neither coronal conduction nor coronal radiation are important for the slow mode damping. This result can be understood on the basis of the slow mode perturbations. As shown in Chapter 3, the dominant slow mode velocity perturbation is v_z , which is essentially confined within the thread, so slow modes are almost unaffected by the coronal physical properties. In the realistic range of $k_z a$, radiation losses from the prominence plasma is the dominant damping mechanism. The value of τ_D/P depends on the radiative regime considered, but for the three prominence radiative regimes of Table 2.1 it is possible to obtain $\tau_D/P < 10$ for relevant $k_z a$. Therefore, radiation losses offer a consistent explanation for the slow mode damping. On the other hand, the slow mode damping for large $k_z a$ is dominated by prominence thermal conduction. Again, the prominence radiation-prominence conduction transitional wavenumber is well-approximated by Equation (4.43). For a large enough $k_z a$, thermal conduction becomes so efficient that the isothermal regime is reached. Porter et al. (1994) provide an approximate expression for the critical wavenumber of the isothermal regime, k^{isoth} , which in our notation is

$$k^{\text{isoth}} \approx \frac{2}{\tilde{k}_{\parallel}} \bar{c}, \quad (4.45)$$

with $\bar{c} = c_s$ for slow modes, and $\bar{c} = v_A$ for fast modes. An excellent agreement between the actual critical wavenumber of the isothermal regime and the approximation is seen in Figure 4.5a.

Next, we compare in Figure 4.5b the numerical solution of the full dispersion relation with the approximations derived in Section 4.1.4. The approximations for $k_z a \ll 1$ (Eq. [4.28]) and $k_z a \gg 1$ (Eq. [4.29]) are plotted by means of the symbols \triangle and \diamond , respectively, while the approximation for intermediate $k_z a$ (Eq. [4.30]) is indicated with the symbols $*$. All approximations are in an almost perfect agreement with the full solution in their respective ranges. It is worth noting that the expression for intermediate $k_z a$ is also quite accurate both in the long and short wavelength limit.

Thermal mode

Finally, we study the thermal mode. Figure 4.6 displays the damping time, τ_D , of the thermal mode as a function of $k_z a$. As for the slow mode, the azimuthal wavenumber m is almost irrelevant for the thermal mode behavior, so we only present the results for $m = 1$. One can see that this mode is very quickly attenuated and that radiative losses from the prominence plasma are responsible for the damping in the realistic range of $k_z a$, whereas prominence thermal conduction is only relevant for large $k_z a$. As the prominence plasma optical thickness is increased by considering Prominence (2) and Prominence (3) regimes, the damping time grows in the relevant range of wavenumbers. Again, the similarity with slow modes is clear since coronal mechanisms have a negligible effect, the thermal mode damping being exclusively dominated by prominence mechanisms. The approximation

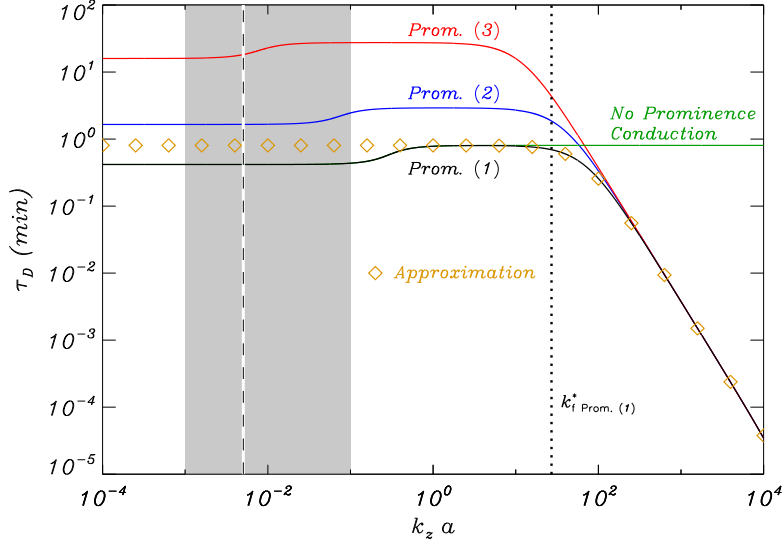


Figure 4.6: Damping time, τ_D , of the thermal mode with $m = 1$ as a function of $k_z a$. The different lines correspond to the results for the three prominence radiative regimes (labeled within the Figure) and the case without prominence thermal conduction. The symbols \diamond correspond to the analytical approximation given by Equation (4.39). The result in the absence of thermal conduction and the analytical approximation are both computed for the Prominence (1) regime. The vertical dotted line is the approximated transitional wavenumber between the radiative regime and the conductive regime, k_f^* , given by Equation (4.43). The discontinuous line within the shaded zone denotes the leaky region of thermal modes.

given by Equation (4.39) is in reasonable agreement with the full numerical solution for small $k_z a$ (see symbols in Fig 4.6), while the agreement is almost perfect for large $k_z a$.

4.3 Effect of mass flow

Hereafter, we include a longitudinal steady mass flow in the model in order to assess its influence on the previously described oscillatory modes. We assume no flow in the external medium, i.e., $v_c = 0$. Moreover, the internal flow is taken towards the positive z -direction, i.e., $v_f > 0$. Note that all other possible configurations can be obtained by means of a suitable election of the reference frame.

The reader is referred to Terra-Homem et al. (2003) for a detailed description of the modification of the phase velocity diagram due to the presence of flow. In short, the symmetry between forward ($\omega_R > 0$) and backward ($\omega_R < 0$) waves is broken by the flow. The phase velocity, ω_R/k_z , of slow modes is between $\pm \Re(\tilde{c}_{Tf}) + v_f$ and $\pm \Re(\Lambda_f) + v_f$, where the $+$ and $-$ signs stand for forward and backward waves, respectively. For a flow velocity larger than the real part of the filament non-adiabatic sound speed, the phase speed of backward slow waves is dragged to positive values, and so they become forward waves in practice (see Carbonell et al. 2009). We call these solutions *reversed*

waves. Note that the observed flow velocities range from 5 km s^{-1} to 25 km s^{-1} (Zirker et al. 1998; Lin et al. 2003, 2005), while the filament adiabatic sound speed of our model is $\approx 12 \text{ km s}^{-1}$, meaning that supersonic flows are realistic in the context of prominences. On the other hand, the phase velocity of transverse waves is in the ranges from $\pm v_{Af} + v_f$ to $\pm v_{Ac}$, where again the + and – signs stand for forward and backward waves, respectively.

Regarding thermal modes, the real part of their frequency now acquires a positive value, and their phase velocity is equal to the flow velocity. Thus, thermal modes behave as propagating forward waves with respect to the static, external reference frame. Although this result could be relevant from the observational point of view, since thermal modes might be detected as propagating waves in flowing filament threads (see a comment on this issue in Carbonell et al. 2009), their quick attenuation makes them very difficult to detect in practice.

We focus next on the effect of the flow on the ratio τ_D/P . To perform this investigation, we fix the longitudinal wavenumber to $k_z a = 10^{-2}$ and vary the flow velocity in the range $0 < v_f/c_{sf} < 3$, which approximately coincides with the observed velocities. The radiative regime of the prominence plasma is Prominence (1) in all computations. Figure 4.7 displays τ_D/P versus the flow velocity for the kink mode and the slow mode (with $m = 1$). We have checked that, as predicted by Equation (4.25), the slow mode damping time does not depend on the flow velocity, so the variation of τ_D/P is exclusively due to the variation of the period. We obtain that the slow backward mode is more attenuated than the forward wave. The value of τ_D/P for the slow backward wave reduces dramatically as the flow velocity approaches the real part of the filament non-adiabatic sound speed. For such a flow velocities, the slow backward wave period tends to infinity since the real part of the frequency goes to zero and changes sign when the direction of propagation is reversed.

On the other hand, the dependence of the kink mode τ_D/P on the flow velocity is the opposite to that of the slow mode, i.e., the kink forward mode is more efficiently damped than its corresponding backward solution. In addition, the variation of τ_D/P is mainly due to the variation of the damping time, since the kink mode period is not significantly changed for the considered flow velocities. The damping time of the kink forward wave is more affected by the presence of flow than that of the backward wave. Figure 4.8 helps us understand the behavior of the kink forward mode damping time. We see that when the kink forward wave phase velocity is in the range $\Re(\tilde{c}_{Tc}) < \omega_R/k_z < \Re(\Lambda_c)$, that corresponds to the region inhabited by leaky coronal slow modes, the ratio τ_D/P has a minimum. This minimum is caused by the coupling of the kink forward wave to the mentioned leaky coronal slow modes. This coupling phenomenon is also responsible for the minimum of the sausage mode τ_D/P observed in Figure 4.4a. Although the coupling with coronal modes reduces the value of τ_D/P by an order of magnitude for $v_f/c_{sf} \approx 3$ with respect to the case without flow, this effect is not important enough to obtain realistic values of the kink mode damping time.

Finally, Figure 4.9 shows the thermal mode τ_D/P with $k_z a = 10^{-1}$, 10^{-2} , and 10^{-3} , and the analytical approximation (Eq. [4.42]) for $k_z a = 10^{-2}$. In practice, the values of τ_D/P are so small that the amplitude of the oscillation drops to zero much before a single period is completed, which makes the thermal mode extremely difficult to detect and so not very relevant from an observational point of view. We see that the approximation gives a slightly larger τ_D/P than the numerically value.

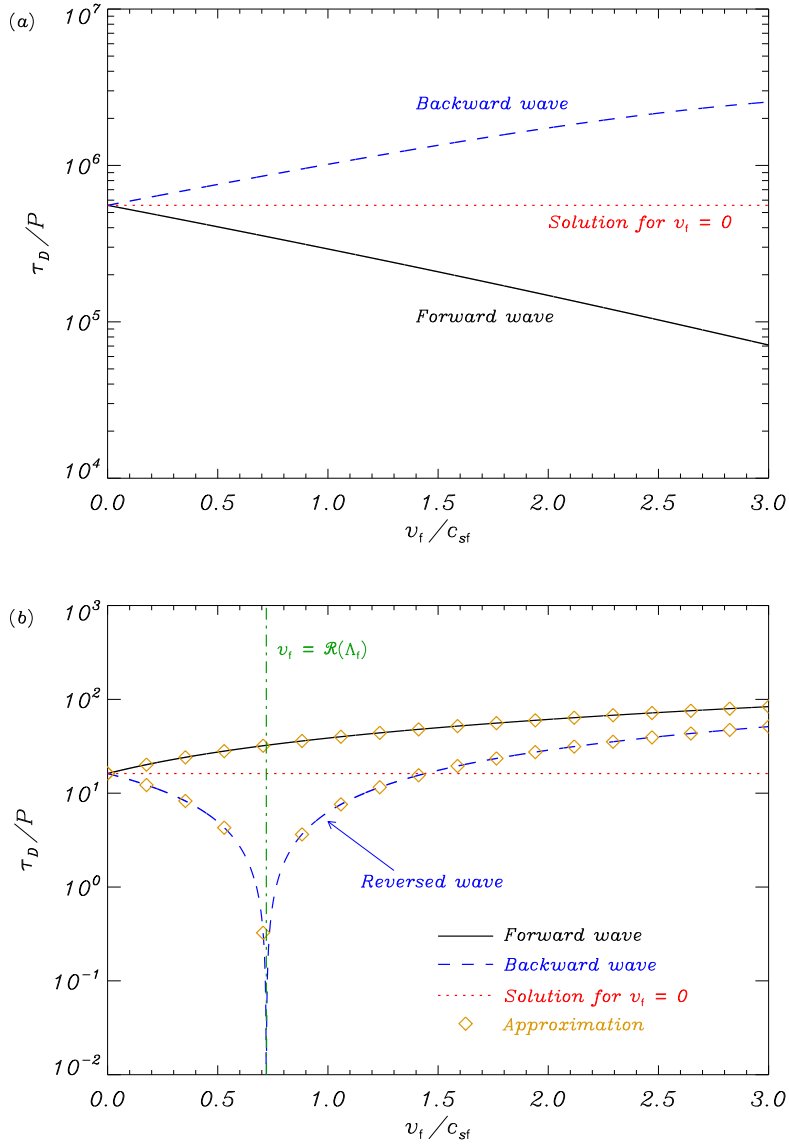


Figure 4.7: Ratio of the damping time to the period, τ_D/P , as a function of v_f/c_{sf} for $k_z a = 10^{-2}$ corresponding to (a) kink modes and (b) slow modes. The meaning of the different line styles is indicated inside the panels. The analytical approximation for the slow modes corresponds to Equation (4.28).

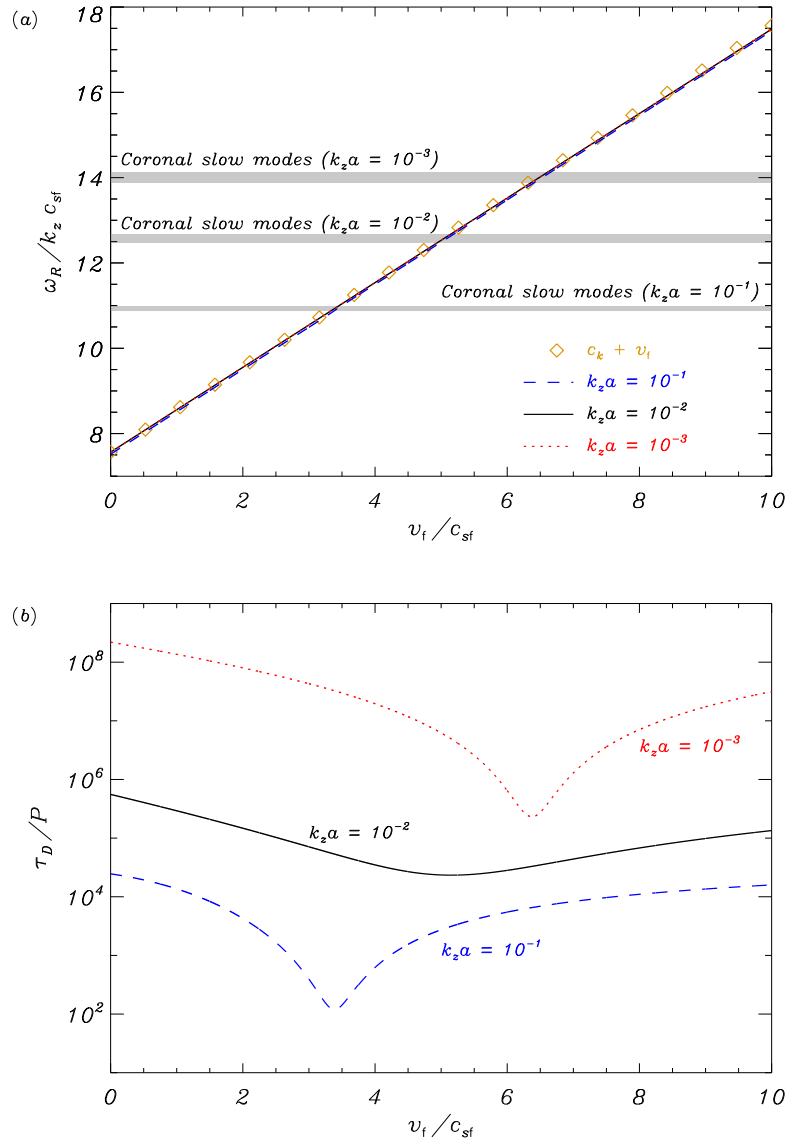


Figure 4.8: (a) Normalized phase velocity and (b) corresponding values of τ_D/P of the forward kink mode as a function of v_f/c_{sf} for $k_z a = 10^{-1}$, 10^{-2} , and 10^{-3} . The shaded regions denote the range of phase velocities of the leaky coronal slow modes. The symbols are the approximate value of the phase velocity (Eq. [4.20]).

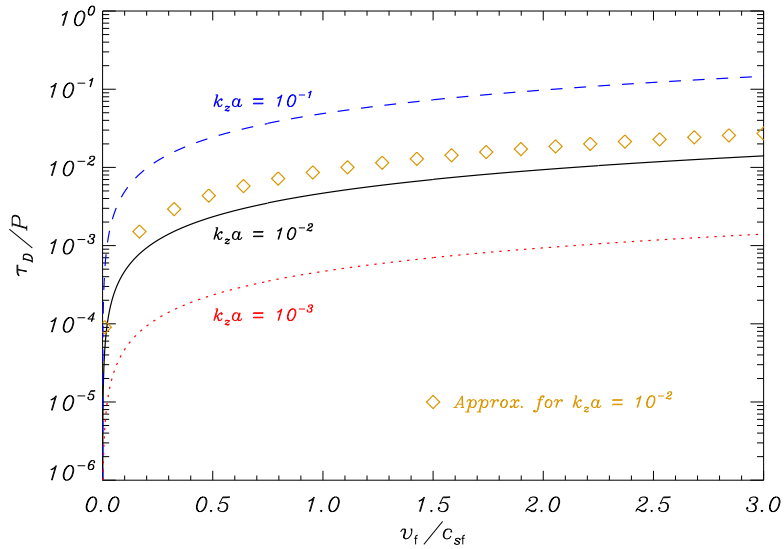


Figure 4.9: τ_D/P of the thermal mode as a function of v_f/c_{sf} for $k_z a = 10^{-1}$, 10^{-2} , and 10^{-3} . Symbols are the approximated value of τ_D/P for $k_z a = 10^{-2}$ obtained from Equation (4.42).

4.4 Conclusion

In agreement with previous studies in simpler configurations (Carbonell et al. 2006, 2009; Terradas et al. 2005; Soler et al. 2007b, 2009a), non-adiabatic mechanisms only produce damping times compatible with the observations in the case of slow modes. The main effect of the flow on these solutions is that only parallel propagation to the flow is allowed for strong enough flows. On the other hand, the damping of thermal modes is extremely efficient but, for this very reason, these waves would be impossible to observe in prominences. On the contrary, the kink mode damping in the absence of flow is negligible. When flow is present, the kink mode damping is slightly improved in the case of forward waves, the ratio τ_D/P being diminished by an order of magnitude for realistic flow velocities. However, the kink mode damping time is still several orders of magnitude larger than the reported values and even much larger than the lifetimes of filament threads, which means that neither non-adiabatic mechanisms nor mass flows provide with reasonable kink mode damping times applicable to prominences. For this reason, it is likely that other damping mechanisms, different from thermal effects, are responsible for the observed efficient attenuation of transverse thread motions.

5

Magnetohydrodynamic Waves in a Partially Ionized Filament Thread*

In previous Chapters, we have neglected the presence of neutrals and have assumed a fully ionized prominence plasma. The main motivation for the present Chapter is to assess the effect of neutrals, and in particular that of ion-neutral collisions, on the propagation and damping of MHD waves in filament threads.

Here, we consider the generalized induction equation (Eq. [2.84]), which contains diffusion terms accounting for the effect of the collisions between the different plasma species. We numerically solve the full MHD equations and obtain the period and damping time of Alfvén, slow, and fast MHD modes (Sec. 5.1.2). When possible, we find analytical approximations of the ratio of the damping time to the period (Sec. 5.2), and compare them to the numerical results (Sec. 5.3). In addition, we obtain analytical expressions for the critical wavenumbers that constrain wave propagation along the filament thread. Finally, we assess the efficiency of the non-ideal terms in the induction equation for the damping of oscillations.

5.1 Model and method

5.1.1 Equilibrium configuration

Again, our filament thread model is composed of a homogeneous and infinite magnetic flux tube of radius a with prominence conditions (density $\rho_f = 5 \times 10^{-11} \text{ kg m}^{-3}$ and temperature $T_f = 8000 \text{ K}$) surrounded by an unbounded and homogeneous coronal medium (density $\rho_c = \rho_f/200 = 2.5 \times 10^{-13} \text{ kg m}^{-3}$ and temperature T_c). The thread radius is $a = 100 \text{ km}$. The magnetic field is uniform and orientated along the cylinder axis, $\vec{B}_0 = B_0 \hat{e}_z$, with $B_0 = 5 \text{ G}$. The mean atomic weight, $\tilde{\mu}$, indicates the plasma ionization degree ($\tilde{\mu} = 0.5$ for a fully ionized plasma and $\tilde{\mu} = 1$ for a neutral gas). The coronal medium is assumed to be fully ionized, so $\tilde{\mu}_c = 0.5$, while the filament ionization degree, $\tilde{\mu}_f$, is considered a free parameter. Since the magnetic field is homogeneous, the continuity of gas pressure across the cylinder boundary selects the coronal temperature. Thus,

$$T_c = \frac{\rho_f \tilde{\mu}_c}{\rho_c \tilde{\mu}_f} T_f. \quad (5.1)$$

*This Chapter is based on the results of R. Soler, R. Oliver, & J. L. Ballester 2009, *Magnetohydrodynamic Waves in a Partially Ionized Filament Thread*, ApJ, 699, 1553.

According to the above expression, the coronal temperature varies between $T_c = 8 \times 10^5$ K for $\tilde{\mu}_f = 0.5$ and $T_c = 1.6 \times 10^6$ K for $\tilde{\mu}_f = 1$.

There is an extensive literature regarding wave propagation in a partially ionized multi-fluid plasma in the context of laboratory plasma physics (e.g., [Watanabe 1961a,b](#); [Tanenbaum 1961](#); [Tanenbaum & Mintzer 1962](#); [Woods 1962](#); [Kulsrud & Pearce 1969](#); [Watts & Hanna 2004](#)). In astrophysical plasmas, the typical frequency of MHD waves is much smaller than the collisional frequencies between species. In such a case the one-fluid approach is usually adopted. One can find examples of works studying MHD waves in an unbounded, partially ionized, one-fluid plasma applied, e.g., to molecular clouds (e.g., [Balsara 1996](#)), to protoplanetary disks (e.g., [Desch 2004](#)), and to wave damping in the solar atmosphere (e.g., [De Pontieu et al. 2001](#); [Khodachenko et al. 2004](#); [Leake et al. 2005](#)). In the context of solar prominences, works by [Forteza et al. \(2007, 2008\)](#) and [Carbonell et al. \(2010\)](#) are relevant. [Forteza et al. \(2007\)](#) followed the treatment by [Braginskii \(1965\)](#) and derived the full set of MHD equations for a partially ionized, one-fluid plasma. As showed in Chapter 2, a generalized Ohm's Law has to be considered in a partially ionized plasma, which includes the effect of the collisions between different species. As a result, some additional terms appear in the magnetic induction equation in comparison to the fully ionized case. [Forteza et al. \(2007\)](#) applied the equations to study the time damping of linear, adiabatic waves in an unlimited prominence medium. In subsequent works, this investigation was extended to the non-adiabatic case by including thermal conduction by neutrals and electrons and radiative losses ([Forteza et al. 2008](#)), and by studying the spatial damping ([Carbonell et al. 2010](#)). Here, we use the formalism of [Forteza et al. \(2007\)](#) and investigate the propagation of MHD waves in a partially ionized, cylindrical filament thread. Since we focus on the effect of the diffusive terms of the magnetic induction equation, we consider the adiabatic energy equation, so wave damping will be exclusively due to partial ionization effects. There is a previous investigation of waves affected by ion-neutral collisions in a solar magnetic structure by [Kumar & Roberts \(2003\)](#), but these authors considered the slab geometry and focused on surface waves in photospheric-like conditions. Hence, to our knowledge the present work is the first attempt to study MHD wave propagation in a partially ionized cylindrical flux tube.

5.1.2 Basic equations and numerical procedure

Our basic equations for the discussion of linear, adiabatic MHD waves in a partially ionized cylinder correspond to Equations (2.92)–(2.96), where the induction equation (Eq. [2.94]) is now replaced by the linearized version of the generalized induction equation (Eq. [2.84]), namely

$$\begin{aligned} \frac{\partial \vec{B}_1}{\partial t} &= \nabla \times (\vec{v}_1 \times \vec{B}_0) - \nabla \times (\eta \nabla \times \vec{B}_1) - \nabla \times [\eta_H (\nabla \times \vec{B}_1) \times \vec{B}_0] \\ &+ \nabla \times \left\{ \frac{\eta_C - \eta}{B_0^2} [(\nabla \times \vec{B}_1) \times \vec{B}_0] \times \vec{B}_0 \right\} - \nabla \times [\Xi \nabla p_1 \times \vec{B}_0], \end{aligned} \quad (5.2)$$

with $\Xi = \tilde{\Xi} \xi_i \xi_n$ and the rest of symbols have the same meaning as in previous Chapters. Note that since the filament thread and the coronal plasma are both assumed homogeneous, the coefficients of the diffusive terms in Equation (5.2) are constants and not affected by the spatial derivatives.

Next, perturbations are written proportional to $\exp(im\varphi + ik_z z - i\omega t)$, and the basic equations become

$$i\omega\rho_1 = \rho_0 \left(v_r' + \frac{v_r}{r} + \frac{im}{r}v_\varphi + ik_z v_z \right), \quad (5.3)$$

$$i\omega v_r = \frac{1}{\rho_0} p_1' - \frac{v_A^2}{B_0} (ik_z B_r - B_z'), \quad (5.4)$$

$$i\omega v_\varphi = \frac{im}{r} \frac{1}{\rho_0} p_1 - \frac{v_A^2}{B_0} \left(ik_z B_\varphi - \frac{im}{r} B_z \right), \quad (5.5)$$

$$i\omega v_z = \frac{ik_z}{\rho_0} p_1, \quad (5.6)$$

$$i\omega B_r = -ik_z B_0 v_r + \eta \left(\frac{m^2}{r^2} B_r + \frac{im}{r} B_\varphi' + \frac{im}{r^2} B_\varphi \right) \\ + \eta_H B_0 \left(k_z^2 B_\varphi - k_z \frac{m}{r} B_z \right) + \eta_C \left(k_z^2 B_r + ik_z B_z' \right) + ik_z \Xi B_0 p_1', \quad (5.7)$$

$$i\omega B_\varphi = -ik_z B_0 v_\varphi - \eta \left(B_\varphi'' + \frac{1}{r} B_\varphi' - \frac{1}{r^2} B_\varphi - \frac{im}{r} B_r' + \frac{im}{r^2} B_r \right) \\ - \eta_H B_0 \left(k_z^2 B_r + ik_z B_z' \right) - \eta_C \left(k_z \frac{m}{r} B_z - k_z^2 B_\varphi \right) - k_z \Xi B_0 \frac{m}{r} p_1, \quad (5.8)$$

$$i\omega B_z = B_0 \left(v_r' + \frac{1}{r} v_r + \frac{im}{r} v_\varphi \right) + \eta_H B_0 \left(ik_z B_\varphi' + ik_z \frac{1}{r} B_\varphi - ik_z \frac{m}{r} B_r \right) \\ - \eta_C \left(B_z'' + \frac{1}{r} B_z' - \frac{m^2}{r^2} B_z - ik_z B_r' - \frac{ik_z}{r} B_r + k_z \frac{m}{r} B_\varphi \right) \\ - \Xi B_0 \left(p_1'' + \frac{1}{r} p_1' - \frac{m^2}{r^2} p_1 \right), \quad (5.9)$$

$$i\omega (p_1 - c_s^2 \rho_1) = 0, \quad (5.10)$$

where the prime denotes derivative with respect to r .

Equations (5.4)–(5.10) form an eigenvalue problem. The eigenvalue is ω and the eigenvector is $(\rho_1, v_r, v_\varphi, v_z, B_r, B_\varphi, B_z, p_1)$. We numerically solve Equations (5.4)–(5.10) by means of the PDE2D code (Sewell 2005) based on finite elements (see, e.g., Terradas et al. 2005, for an explanation of the method). Since the eigenvalue ω is in general a complex quantity, Equations (5.4)–(5.10) are separated into their real and imaginary parts. Cubic Hermite elements are used, which in the present case provide an appropriate description of wave modes. The numerical integration of Equations (5.4)–(5.10) is performed from the cylinder axis, $r = 0$, to the finite edge of the numerical domain, $r = r_{\max}$. The evanescent condition is imposed in the coronal medium, so all perturbations vanish at $r = r_{\max}$. Therefore, the edge of the numerical domain is located far enough from the filament thread to obtain a good convergence of the solution and to avoid numerical errors (typically, we consider $r_{\max} = 100a$). The boundary conditions at $r = 0$ are imposed by symmetry arguments. The PDE2D program uses a collocation method and the generalized matrix eigenvalue problem is solved using the shifted inverse power method. We assume fixed, real, and positive k_z and m , so the numerical solution gives us the complex eigenvalue, $\omega = \omega_R + i\omega_I$, closest to the provided initial frequency guess, as well as the corresponding eigenfunctions of perturbations. Wave solutions appear in pairs, corresponding to forward ($\omega_R > 0$) and backward ($\omega_R < 0$) waves. Since

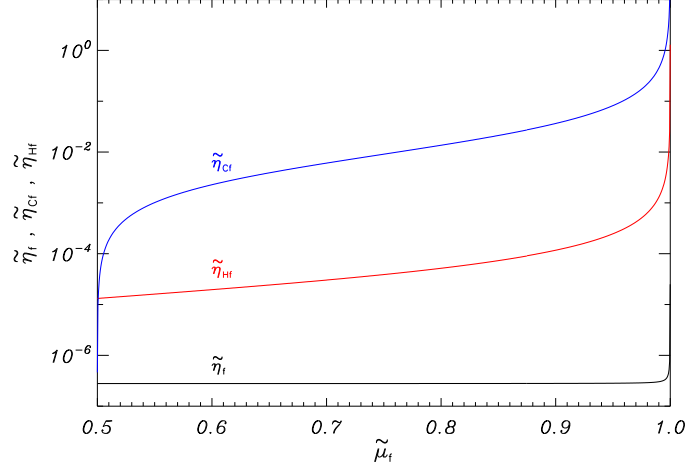


Figure 5.1: Dimensionless Ohm's, $\tilde{\eta}$, Hall's, $\tilde{\eta}_H$, and Cowling's, $\tilde{\eta}_C$, magnetic diffusivities of the filament plasma as a function of the filament ionization degree, $\tilde{\mu}_i$. For comparison purposes, the respective values in the fully ionized coronal medium ($\tilde{\mu}_c = 0.5$) are: $\tilde{\eta}_c = \tilde{\eta}_{Cc} \approx 1.4 \times 10^{-11}$ and $\tilde{\eta}_{Hc} \approx 1.8 \times 10^{-4}$.

there are no flows in the equilibrium configuration, both directions of propagation are equivalent and so we restrict ourselves to solutions with $\omega_R > 0$.

5.1.3 Dimensional analysis of the induction equation

Here, we quantify the importance of the diffusion terms of Equation (5.2) by means of a dimensional analysis. It is convenient for our following analysis to write Ohm's, Cowling's, and Hall's diffusivities in a dimensionless form as

$$\tilde{\eta} = \frac{\eta}{v_{Af}a}, \quad \tilde{\eta}_C = \frac{\eta_C}{v_{Af}a}, \quad \tilde{\eta}_H = \frac{\eta_H B_0}{v_{Af}a}, \quad (5.11)$$

where tildes denote dimensionless quantities. Figure 5.1 displays the filament plasma dimensionless diffusivities as a function of the filament ionization degree.

First, we have to assess the typical length-scale of each dissipative term because magnetic diffusion is not isotropic in a partially ionized plasma. An examination of Equations (5.8), (5.9), and (5.10) reveals that longitudinal derivatives only appear in the terms with η_C and η_H , while the terms with η only contain radial and azimuthal derivatives. Therefore, the typical length-scale of both Cowling's and Hall's terms is the longitudinal wavelength, λ_z , which can be expressed in terms of the longitudinal wavenumber, $\lambda_z = 2\pi k_z^{-1}$. On the other hand, the typical length-scale of the ohmic term is the filament thread radius, a . By taking into account these relevant length-scales, and since magnetic diffusion parallel to field lines is governed by Ohm's diffusion, we define the parallel magnetic Reynolds number, $\mathcal{R}_{m\parallel}$, as the magnitude of the convective term with respect to that of Ohm's term, namely

$$\mathcal{R}_{m\parallel} \sim \frac{|\nabla \times (\vec{v}_1 \times \vec{B}_0)|}{|\nabla \times (\eta \nabla \times \vec{B}_1)|} \sim \frac{v_{Af}a}{\eta} \sim \frac{1}{\tilde{\eta}}. \quad (5.12)$$

On the other hand, magnetic diffusion perpendicular to field lines is dominated by Cowling's diffusion. Therefore, we equivalently define the perpendicular magnetic Reynolds number, $\mathcal{R}_{m\perp}$, as the magnitude of the convective term with respect to that of Cowling's term, namely

$$\mathcal{R}_{m\perp} \sim \frac{|\nabla \times (\vec{v}_1 \times \vec{B}_0)|}{\left| \nabla \times \left\{ \frac{\eta_C - \eta}{B_0^2} \left[(\nabla \times \vec{B}_1) \times \vec{B}_0 \right] \times \vec{B}_0 \right\} \right|} \sim \frac{v_{Af} \lambda_z^2}{\eta_C a} \sim \left(\frac{2\pi}{k_z a} \right)^2 \frac{1}{\tilde{\eta}_C}. \quad (5.13)$$

Finally, the dimensionless number \mathcal{H} gives us the magnitude of the convective term with respect to that of Hall's term, namely

$$\mathcal{H} \sim \frac{|\nabla \times (\vec{v}_1 \times \vec{B}_0)|}{\left| \nabla \times \left[\eta_H (\nabla \times \vec{B}_1) \times \vec{B}_0 \right] \right|} \sim \frac{v_{Af} \lambda_z^2}{\eta_H B_0 a} \sim \left(\frac{2\pi}{k_z a} \right)^2 \frac{1}{\tilde{\eta}_H}. \quad (5.14)$$

We see that $\mathcal{R}_{m\parallel}$ is independent of the longitudinal wavenumber, while $\mathcal{R}_{m\perp}$ and \mathcal{H} are both inversely proportional to k_z^2 . This suggests that the relative importance of Cowling's and Hall's diffusion increases with k_z . To perform a simple calculation, we take $k_z a = 1$, $a = 100$ km, $\tilde{\mu}_f = 0.8$, and compute $\tilde{\eta}$, $\tilde{\eta}_C$, and $\tilde{\eta}_H$ using the filament equilibrium properties. We obtain $\mathcal{R}_{m\parallel} \approx 4 \times 10^6$, $\mathcal{R}_{m\perp} \approx 3 \times 10^3$, and $\mathcal{H} \approx 8 \times 10^5$. For the considered parameters, Cowling's diffusion is dominant, while Ohm's and Hall's diffusion have minor roles. Taking a more appropriate value of $k_z a = 10^{-2}$ into account, one obtains $\mathcal{R}_{m\parallel} \approx 4 \times 10^6$, $\mathcal{R}_{m\perp} \approx 3 \times 10^7$, and $\mathcal{H} \approx 8 \times 10^9$. Thus, in the case of thin tubes, Ohm's diffusion seems more relevant than the other mechanisms.

It is possible to obtain an estimation of the longitudinal wavenumber for which both Ohm's and Cowling's diffusion have the same importance by equaling the parallel and perpendicular magnetic Reynolds numbers, i.e., $\mathcal{R}_{m\parallel} \approx \mathcal{R}_{m\perp}$. By this procedure we obtain

$$(k_z a)_C \approx 2\pi \sqrt{\frac{\tilde{\eta}}{\tilde{\eta}_C}}, \quad (5.15)$$

which gives $(k_z a)_C \approx 2.8 \times 10^{-2}$ for the same parameters assumed before. These estimations are consistent with the results of [Forteza et al. \(2007\)](#), who obtained that the term with Cowling's diffusion was the dominant mechanism in their case since they considered quite a large value for the wavenumber component parallel to magnetic field lines, and therefore ohmic diffusion was not important in their computations. We have to bear in mind that the relevant range of $k_z a$ of prominence oscillations corresponds to $10^{-3} \lesssim k_z a \lesssim 10^{-1}$, so according to Equation (5.15), both ohmic and Cowling's diffusion could be important in such a range of $k_z a$.

Next, we compute the value of $k_z a$ for which Hall's and Ohm's terms have the same importance by setting $\mathcal{R}_{m\parallel} \approx \mathcal{H}$. We obtain

$$(k_z a)_H \approx 2\pi \sqrt{\frac{\tilde{\eta}}{\tilde{\eta}_H}}, \quad (5.16)$$

whose value is $(k_z a)_H \approx 4.6 \times 10^{-1}$, so we get $(k_z a)_C < (k_z a)_H$. One can see that this last relation is always fulfilled by comparing Equations (5.15) and (5.16) and taking

into account that $\tilde{\eta}_C > \tilde{\eta}_H$ in our equilibrium configuration (see Fig. 5.1). Therefore, Cowling's diffusion becomes dominant over Ohm's diffusion for smaller wavenumbers than those needed for Hall's term to become more relevant than Ohm's diffusion. Next, we have to know whether Cowling's diffusion or Hall's diffusion dominate for $k_z a$ beyond both transitional values. To do so, we consider the situation when both mechanisms have the same importance, i.e., $\mathcal{R}_{m\perp} \approx \mathcal{H}$, which implies $\tilde{\eta}_C \approx \tilde{\eta}_H$. However, we must point out again that in our model $\tilde{\eta}_C > \tilde{\eta}_H$, so the last condition is never satisfied, meaning that Cowling's diffusion is always more important than Hall's diffusion.

By means of this simple dimensional analysis, we conclude that Hall's diffusion is always the less relevant mechanism for all values of $k_z a$ and has a minor effect on wave modes. This result is in agreement with Pandey & Wardle (2008) and Krishan & Varghese (2008), who showed that Hall's term may be only important for frequencies larger than $\sim 10^4$ Hz, which are much larger than the observed frequencies of prominence oscillations. For this reason and for the sake of simplicity, Hall's diffusion is hereafter neglected from the present investigation.

5.2 Analytical expressions

Apart from the full numerical solution of the basic equations (Eqs. [5.4]–[5.10]), we also perform an analytical investigation, which will allow us understand better the numerical results. Unlike the non-adiabatic case studied in Chapter 4, it is not possible to obtain a simple dispersion relation describing all the eigenmodes when the generalized induction equation for a partially ionized plasma is taken into account. Hence, simplifications are required in order to proceed analytically. Next, we study separately the Alfvén, kink, and slow modes.

5.2.1 Alfvén modes

We start our analytical investigation by studying Alfvén waves. Some works have investigated Alfvén wave propagation in partially ionized plasmas (e.g., Watanabe 1961b; Tanenbaum & Mintzer 1962; Watts & Hanna 2004; Pandey & Wardle 2008; Forteza et al. 2008), but to our knowledge a detailed investigation in cylindrical geometry applied to solar plasmas remains to be done. In cylindrical geometry, Alfvén modes are coupled to magnetoacoustic modes except for $m = 0$. Thus, we assume no azimuthal dependence in order to study Alfvén waves separately from the other wave modes. We see that by setting $m = 0$ and neglecting Hall's term, Equations (5.6) and (5.9) are decoupled from the rest and become

$$i\omega v_\varphi = -ik_z \frac{v_A^2}{B_0} B_\varphi, \quad (5.17)$$

$$i\omega B_\varphi = -ik_z B_0 v_\varphi - \eta \left(B_\varphi'' + \frac{1}{r} B_\varphi' - \frac{1}{r^2} B_\varphi \right) + \eta_C k_z^2 B_\varphi. \quad (5.18)$$

These equations only involve the perturbations v_φ and B_φ , so Alfvén modes are purely torsional, incompressible waves for $m = 0$. Now, we use Equation (5.17) to express v_φ as a function of B_φ and, after substituting it in Equation (5.18), a single expression for

B_φ is obtained, namely

$$\eta B_\varphi'' + \eta \frac{1}{r} B_\varphi' + \left[\frac{i}{\omega} (\omega^2 - v_A^2 k_z^2 + i\omega\eta_C k_z^2) - \eta \frac{1}{r^2} \right] B_\varphi = 0. \quad (5.19)$$

For $\eta \neq 0$, Equation (5.19) can be rewritten as

$$B_\varphi'' + \frac{1}{r} B_\varphi' + \left(m_A^2 - \frac{1}{r^2} \right) B_\varphi = 0, \quad (5.20)$$

with

$$m_A^2 = \frac{i}{\eta\omega} (\omega^2 - k_z^2 \Gamma_A^2), \quad \Gamma_A^2 = v_A^2 - i\omega\eta_C. \quad (5.21)$$

It is straight-forward to check that the same equation applies for v_φ . Hence, the Alfvén wave is governed by a Bessel equation of order 1, where m_A plays the role of the radial wavenumber and Γ_A is equivalent to the modified (or resistive) Alfvén speed defined in Equation (29) of [Forteza et al. \(2008\)](#). We then see that when magnetic diffusion is present, Alfvén modes are not strictly confined to magnetic surfaces and become *global* eigenmodes of the flux tube (see, e.g., [Ferraro & Plumpton 1961](#); [Sy 1984](#); [Copil et al. 2008](#)).

The general solution of Equation (5.20) for regular perturbations at $r = 0$ and vanishing at infinity is

$$B_\varphi(r) = \begin{cases} A_1 J_1(m_{Af}r), & \text{if } r \leq a, \\ A_2 H_1^{(1)}(m_{Ac}r), & \text{if } r > a, \end{cases} \quad (5.22)$$

A_1 and A_2 being complex constants. J_1 and $H_1^{(1)}$ are the usual Bessel function and Hankel function of the first kind, respectively, of order 1 ([Abramowitz & Stegun 1972](#)). We have to note here that m_{Af} and m_{Ac} are both complex quantities. Even with a complex m_{Af} , the function J_1 remains as a correct description for the solutions within the cylinder. For complex arguments, the Bessel function J_1 can be expressed as a combination of functions J and I (see, e.g. [Abramowitz & Stegun 1972](#); [Yousif & Melka 1997](#)), so the resistive Alfvén mode has a mixed body and surface character. For the same reason, the solution in the coronal medium has mixed propagating and evanescent properties. This fact leads us to use the more convenient representation of the external solution in terms of a Hankel function instead of the modified Bessel function K with a real argument usually considered for evanescent waves (see [Cally 1986](#)). The condition for outgoing waves is fulfilled by selecting the appropriate branch of m_{Ac} such that $\Re(m_{Ac}/\omega) > 0$ ([Stenuit et al. 1999](#)).

In order to obtain the dispersion relation, we need to impose boundary conditions at $r = a$. [Woods \(1962\)](#) and [Tomimura \(1990\)](#) provide appropriate boundary conditions for our case, namely

$$[[B_\varphi]] = 0, \quad [[\eta B_\varphi']] = -\frac{B_\varphi}{r} [[\eta]], \quad (5.23)$$

where $[[X]] = X_c - X_f$ stands for the jump of the quantity X at $r = a$. B_φ is set continuous across the boundary because we assume no surface currents on the interface between the thread and the corona. On the contrary, the jump of the radial derivative of B_φ is determined by the difference between the internal and external ohmic diffusivities.

Applying these boundary conditions and after some algebra, the following dispersion relation is obtained,

$$\eta_c m_{Ac} \frac{H_1^{(1)}(m_{Ac}a)}{H_1^{(1)}(m_{Ac}a)} - \eta_f m_{Af} \frac{J_1'(m_{Af}a)}{J_1(m_{Af}a)} = \frac{\eta_f - \eta_c}{a}. \quad (5.24)$$

Equation (5.24) is the general dispersion relation for Alfvén waves in a partially ionized cylinder, where the effect of both Ohm’s and Cowling’s diffusion is included. However, no straight-forward conclusions can be extracted from Equation (5.24) without solving it numerically or applying some approximations. To perform a more in-depth analytical study of Alfvén wave propagation, let us go step by step and let us consider now the case in which Ohm’s diffusion can be neglected, i.e., $k_z a \gg (k_z a)_C$. By taking $\eta = 0$ in Equation (5.19) one obtains that Alfvén waves verify

$$\frac{i}{\omega} (\omega^2 - v_A^2 k_z^2 + i\omega\eta_C k_z^2) B_\varphi = 0. \quad (5.25)$$

Now, B_φ can be an arbitrary function because for $\eta = 0$ the different magnetic surfaces are no longer coupled. The dispersion relation for Alfvén modes in the regime dominated by Cowling’s diffusion is

$$\omega^2 + i\eta_C k_z^2 \omega - k_z^2 v_A^2 = 0. \quad (5.26)$$

Equation (5.26) is formally identical to Equation (49) of Pandey & Wardle (2008). Its exact solution gives us a complex frequency as

$$\omega = \pm \frac{k_z}{2} \sqrt{4v_A^2 - \eta_C^2 k_z^2} - i \frac{k_z^2}{2} \eta_C. \quad (5.27)$$

Because of the presence of an imaginary part of the frequency, we obtain the well-known result that the Alfvén wave is damped by Cowling’s diffusion, i.e., by ion-neutral collisions, in a partially ionized plasma (see, e.g., Haerendel 1992; De Pontieu & Haerendel 1998; De Pontieu 1999; De Pontieu et al. 2001; Leake et al. 2005, for studies on the damping of Alfvén waves in the solar chromosphere). Obviously, if $\eta_C = 0$ we recover the ideal, undamped Alfvén mode, i.e., $\omega = \pm k_z v_A$. From Equation (5.27) we can also see that the real part of the Alfvén frequency vanishes for a critical value of k_z given by

$$k_z^c = \frac{2v_A}{\eta_C}. \quad (5.28)$$

This critical wavenumber is equivalent to that given by Equation (38) of Forteza et al. (2008) for Alfvén waves in an unbounded medium considering parallel propagation to magnetic field lines. For $k_z > k_z^c$ the Alfvén wave becomes a non-propagating, purely damped disturbance.

Now, our aim is to take the case $\eta \neq 0$ into account but performing some approximations to the general dispersion relation (Eq. [5.24]). To do so, we take into account that $\eta_f/\eta_c \approx 3 \times 10^3$, thus we can neglect the coronal Ohm’s diffusion in front of the filament Ohm’s diffusion¹. In such a case, torsional motions of the flux tube do not

¹In the following expressions, it is important not to mistake the Ohm’s diffusivity in the corona, namely η_c , for the Cowling’s coefficient, namely η_C .

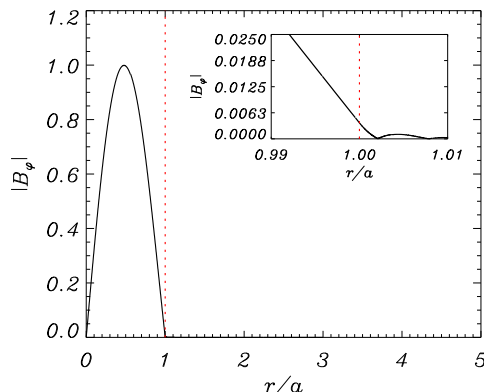


Figure 5.2: Modulus in arbitrary units of the eigenfunction B_φ as a function of r/a corresponding to the radially fundamental Alfvén mode with $m = 0$, $\tilde{\mu}_f = 0.8$, and $k_z a = 10^{-2}$. The vertical dotted line corresponds to the filament thread edge. The small panel shows a close-up of the eigenfunction close to the boundary between the thread and the corona.

disturb the coronal plasma since different magnetic surfaces in the corona are not coupled when $\eta_c = 0$. Therefore, and with no loss of generality, we set $B_\varphi = 0$ at $r = a$, meaning that we assume the Alfvén mode is strictly confined within the cylinder. To make sure that this approximation is also appropriate when $\eta_c \neq 0$, we numerically solve Equations (5.17) and (5.18) with the PDE2D code and compute the eigenfunction B_φ corresponding to the radially fundamental Alfvén mode (see Fig. 5.2). Although the eigenfunction is not strictly confined within the cylinder, we note that the amplitude of B_φ for $r > a$ is much smaller than that within the thread. On the basis of this evidence, assuming $B_\varphi \approx 0$ at $r = a$ seems a reasonable approximation. According to Equation (5.22), we have $J_1(m_{\text{Af}}a) \approx 0$, which implies that $m_{\text{Af}}a \approx j_1$, with $j_1 \approx 3.8317$ the first zero of the Bessel function J_1 . Hence, by considering the expression for m_{Af} (Eq. [5.21]), the Alfvén mode frequency is

$$\omega = \pm \frac{1}{2} \sqrt{4v_{\text{Af}}^2 k_z^2 - \left(\eta_{\text{Cf}} k_z^2 + \eta_{\text{f}} \frac{j_1^2}{a^2} \right)^2} - \frac{i}{2} \left(\eta_{\text{Cf}} k_z^2 + \eta_{\text{f}} \frac{j_1^2}{a^2} \right). \quad (5.29)$$

The above expression is consistent with previous results since for $\eta_{\text{f}} = 0$ it reduces to Equation (5.27). Note that Equation (5.29) is only valid for the radially fundamental Alfvén mode. Equivalent expressions for the radial harmonics can be simply obtained by replacing j_1 with the corresponding zero of the function J_1 that applies to each case, e.g., the first radial harmonic is described by the second zero, the second radial harmonic by the third zero, and so on.

As before, we can obtain an expression for the critical k_z at which the real part of the Alfvén frequency vanishes. Thus,

$$k_z^{c\pm} = \frac{v_{\text{Af}}}{\eta_{\text{Cf}}} \pm \frac{\sqrt{v_{\text{Af}}^2 - \eta_{\text{Cf}} \eta_{\text{f}} j_1^2 / a^2}}{\eta_{\text{Cf}}}. \quad (5.30)$$

We see that two values of k_z^c are now possible. The one given by the + sign, namely k_z^{c+} , is a correction of the previously described critical wavenumber for $\eta_f = 0$ (Eq. [5.28]). On the other hand, the one given by the – sign, namely k_z^{c-} , is a new critical value which arises because of the combination of two effects, i.e., the nonzero value of η_f and the presence of the factor j_1^2/a^2 given by the geometry. Since Forteza et al. (2008) considered an infinite medium, this geometry-related critical wavenumber is absent in their investigation. Taking into account that $\eta_{Cf}\eta_f j_1^2/a^2 v_A^2 \ll 1$, a first-order Taylor expansion of Equation (5.30) gives

$$k_z^{c+} \approx \frac{v_{Af}}{\eta_{Cf}} \left(2 - \frac{\eta_{Cf}\eta_f j_1^2/a^2}{2v_{Af}^2} \right) \approx \frac{2v_{Af}}{\eta_{Cf}}, \quad k_z^{c-} \approx \frac{\eta_f j_1^2/a^2}{2v_{Af}}, \quad (5.31)$$

whose dimensionless forms are

$$k_z^{c+} a \approx \frac{2}{\tilde{\eta}_{Cf}}, \quad k_z^{c-} a \approx \frac{\tilde{\eta}_f}{2} j_1^2. \quad (5.32)$$

One can see that $k_z^{c-} a$ does not depend on η_{Cf} and so it is not affected by the plasma ionization degree. Furthermore, since $k_z^{c-} a < k_z^{c+} a$, the Alfvén wave only exists as a propagating mode for $k_z^{c-} a < k_z a < k_z^{c+} a$.

Equation (5.29) also allows us to obtain the ratio of the damping time to the period as

$$\frac{\tau_D}{P} = \frac{\sqrt{4v_{Af}^2 k_z^2 - (\eta_{Cf} k_z^2 + \eta_f j_1^2/a^2)^2}}{2\pi (\eta_{Cf} k_z^2 + \eta_f j_1^2/a^2)}. \quad (5.33)$$

Let us evaluate τ_D/P in the different limits of $k_z a$ but far from the critical values. For $k_z^{c-} a \ll k_z a \ll (k_z a)_C$, we can neglect Cowling's diffusion, thus

$$\frac{\tau_D}{P} \approx \frac{1}{\pi} \frac{v_{Af}}{\eta_f j_1^2/a^2} k_z, \quad (5.34)$$

whereas for $(k_z a)_C \ll k_z a \ll k_z^{c+} a$, Ohm's diffusion is irrelevant, therefore

$$\frac{\tau_D}{P} \approx \frac{1}{\pi} \frac{v_{Af}}{\eta_{Cf}} k_z^{-1}. \quad (5.35)$$

The transition between both behaviors is expected to take place for $k_z a \approx (k_z a)_C$.

5.2.2 Kink modes

Here, we turn our attention to the kink mode. It is not possible to give a simple dispersion relation for this wave when both ohmic and ambipolar magnetic diffusion are considered. Some analytical progress can be performed by adopting the $\beta = 0$ case and neglecting ohmic diffusion, i.e., $\eta = 0$. In such a situation, the relevant equations are

$$\rho_0 \frac{\partial \vec{v}_1}{\partial t} = \frac{1}{\mu} (\nabla \times \vec{B}_1) \times \vec{B}_0, \quad (5.36)$$

$$\frac{\partial \vec{B}_1}{\partial t} = \nabla \times (\vec{v}_1 \times \vec{B}_0) + \nabla \times \left\{ \frac{\eta_C}{B_0^2} [(\nabla \times \vec{B}_1) \times \vec{B}_0] \times \vec{B}_0 \right\}. \quad (5.37)$$

From Equation (5.36) and assuming a time dependence of the form $\exp(-i\omega t)$, i.e., only valid for normal modes, one can write the magnetic force term in Equation (5.36) as

$$\left(\nabla \times \vec{B}_1\right) \times \vec{B}_0 = -\frac{i\omega B_0^2}{v_A^2} \vec{v}_1, \quad (5.38)$$

which can be used to rewrite Equation (5.37) in compact form as

$$\frac{\partial \vec{B}_1}{\partial t} = \frac{\Gamma_A^2}{v_A^2} \nabla \times \left(\vec{v}_1 \times \vec{B}_0\right), \quad (5.39)$$

with Γ_A^2 the resistive Alfvén speed defined in Equation (5.21). Equation (5.39) is formally identical to the ideal induction equation with the extra factor Γ_A^2/v_A^2 in the convective term. Note that $\Gamma_A^2/v_A^2 = 1$ when $\eta_C = 0$. Now, it is straight-forward to find a dispersion relation by following the same procedure as in the ideal case (see details in Chap. 3), obtaining

$$\frac{n_c}{\rho_c (\omega^2 - k_z^2 \Gamma_{Ac}^2)} \frac{K'_m(n_c a)}{K_m(n_c a)} - \frac{m_f}{\rho_f (\omega^2 - k_z^2 \Gamma_{Af}^2)} \frac{J'_m(m_f a)}{J_m(m_f a)} = 0, \quad (5.40)$$

where the quantities m_f and n_c are given by

$$m_f^2 = \frac{(\omega^2 - k_z^2 \Gamma_{Af}^2)}{\Gamma_{Af}^2}, \quad n_c^2 = \frac{(k_z^2 \Gamma_{Ac}^2 - \omega^2)}{\Gamma_{Ac}^2}. \quad (5.41)$$

Note that Equation (5.40) applies to all values of m and not only to kink modes ($m = 1$). In the case $m \neq 0$ and $k_z a \ll 1$, Equation (5.40) becomes

$$\rho_f (\omega^2 - k_z^2 \Gamma_{Af}^2) + \rho_c (\omega^2 - k_z^2 \Gamma_{Ac}^2) = 0, \quad (5.42)$$

whose solution after neglecting terms with k_z^4 is

$$\omega = \pm \sqrt{\frac{(\rho_f v_{Af}^2 + \rho_c v_{Ac}^2)}{(\rho_f + \rho_c)}} k_z - i \frac{(\rho_f \eta_{Cf} + \rho_c \eta_{Cc})}{2(\rho_f + \rho_c)} k_z^2. \quad (5.43)$$

According to Equation (5.43) the kink mode τ_D/P due to Cowling's diffusion in the thin tube case is

$$\frac{\tau_D}{P} = \frac{(\rho_f + \rho_c)^{1/2} (\rho_f v_{Af}^2 + \rho_c v_{Ac}^2)^{1/2}}{\pi (\rho_f \eta_{Cf} + \rho_c \eta_{Cc})} k_z^{-1}. \quad (5.44)$$

However, one must bear in mind that for $k_z a \ll (k_z a)_C$, Ohm's diffusion is more relevant than Cowling's diffusion. For this reason the damping ratio given by Equation (5.44) is probably much larger than that due to Ohm's diffusion. We check this last statement later with our numerical computations.

Next, we determine whether the kink mode has any critical wavenumber. To do so, we consider the different limits of the real part of the kink mode frequency, ω_R . For parallel propagation to magnetic field lines, i.e., $k_z a \gg 1$, the kink mode behaves like an internal Alfvén mode. Hence, the kink mode frequency tends to $\omega_R \approx \omega_{Af}$, with ω_{Af} the internal Alfvén frequency given by the real part of Equation (5.29). Then, $k_z^{c+} a$ given by Equation (5.28) is also a critical wavenumber of the kink mode. On the other hand, for

$k_z a \ll 1$ the kink mode frequency tends to ω_k , which for $\rho_f \gg \rho_c$ can be approximated by $\omega_k \approx \sqrt{2}\omega_{Af}$. Again, the kink mode behavior is determined by the internal Alfvén frequency for $k_z a \ll 1$, and the kink mode has also a lower critical wavenumber $k_z^{c-} a$. Nevertheless, the expression for the Alfvén mode $k_z^{c-} a$ (Eq. [5.31]) is not appropriate for the kink mode since j_1 is not a valid approximation of the kink mode radial wavenumber when $k_z a \ll 1$. A general expression, i.e., independent of the geometry, of $k_z^{c-} a$ is

$$k_z^{c-} a \approx \frac{\tilde{\eta}_f}{2} (k_{\perp} a)^2, \quad (5.45)$$

where $k_{\perp} a$ is the (dimensionless) perpendicular wavenumber to the magnetic field lines and depends on the model geometry. For our present cylindrical filament thread, this geometry-related factor can be written as $(k_{\perp} a)^2 \approx (k_r a)^2 + (k_{\varphi} a)^2$, where $k_r a$ and $k_{\varphi} a$ are the radial and azimuthal wavenumbers, respectively. We approximate $(k_r a)^2$ by its expression in the $\beta = 0$, ideal case, namely

$$(k_r a)^2 \approx \frac{\omega_R^2 a^2}{v_{Af}^2} - (k_z a)^2. \quad (5.46)$$

For $k_z a \ll 1$ and $\rho_f \gg \rho_c$, $\omega_R^2 \approx 2v_{Af}^2 k_z^2$, so $(k_r a)^2 \approx (k_z a)^2$. On the other hand, the azimuthal wavenumber can be expressed as $(k_{\varphi} a)^2 \approx m^2$. Since the critical wavenumber $k_z^{c-} a$ occurs for $k_z a \ll 1$, the azimuthal wavenumber dominates over the radial one and we get $(k_{\perp} a)^2 \approx m^2$. The lower critical wavenumber is, therefore,

$$k_z^{c-} a \approx \frac{\tilde{\eta}_f}{2} m^2, \quad (5.47)$$

with $m = 1$ in the kink mode case.

5.2.3 Slow modes

Such as for the Alfvén and kink waves, it is possible to perform some simple analytical calculations in the case of the slow modes. Here, it is crucial to take into account the common result regarding the ideal slow mode propagation in both the Cartesian slab (e.g., [Edwin & Roberts 1982](#)) and the cylinder (e.g., [Edwin & Roberts 1983](#), see also Chap. 3). It is well-known that the slow mode in a $\beta < 1$, homogeneous medium is mainly polarized along the magnetic field direction. So, if one considers a magnetic structure, say, a slab or a cylinder, the slow mode is almost insensible to the perpendicular geometry to magnetic field lines and is mostly governed by the physical conditions internal to the structure. In such a case, the slow mode frequency is well approximated by solving the dispersion relation corresponding to a homogeneous medium with the internal physical conditions, and selecting an appropriate value for the perpendicular wavenumber to the magnetic field, namely k_{\perp} . This k_{\perp} contains the effect of the geometry of the magnetic structure. To apply this technique, we consider the dispersion relation for a partially ionized, homogeneous, and infinite plasma derived by [Forteza et al. \(2007\)](#) in their Equation (24), which in our notation is

$$\begin{aligned} & \omega^4 - i(k_z^2 + k_{\perp}^2) \eta_{Cf} \omega^3 - (c_{sf}^2 + v_{Af}^2) (k_z^2 + k_{\perp}^2) \omega^2 \\ & + i c_{sf}^2 (k_z^2 + k_{\perp}^2) [(k_z^2 + k_{\perp}^2) \eta_{Cf} - k_{\perp}^2 \Xi_f \rho_f v_{Af}^2] \omega + (k_z^2 + k_{\perp}^2) k_z^2 c_{sf}^2 v_{Af}^2 = 0. \end{aligned} \quad (5.48)$$

Equation (5.48) is a fourth-order polynomial that contains both fast and slow modes, but we are here only interested in approximating the slow mode frequency. Since this quantity is smaller than that of the fast mode for the same wavenumber, we could reasonably assume that the higher order terms in ω are related to the fast mode, while the lower order terms in ω are related to the slow mode. This assumption especially applies to small values of the wavenumber, i.e., small frequencies. In such a situation, one can neglect the terms with ω^3 and ω^4 in Equation (5.48) to roughly drop the fast mode contribution. Also, we neglect the term with Ξ_f to simplify matters. So, the dispersion relation becomes a second order polynomial for the frequency that can be solved exactly, namely

$$\omega \approx \pm \sqrt{c_{\text{Tf}}^2 k_z^2 - \frac{c_{\text{Tf}}^4 \eta_{\text{Cf}}^2}{4v_{\text{Af}}^4} (k_z^2 + k_{\perp}^2)^2} - i \frac{c_{\text{Tf}}^2 \eta_{\text{Cf}}}{2v_{\text{Af}}^2} (k_z^2 + k_{\perp}^2). \quad (5.49)$$

We check the validity of this approximation by taking $\eta_{\text{Cf}} = 0$, and we get $\omega \approx \pm c_{\text{Tf}} k_z$, which is consistent with the slow mode frequency in the ideal case. A critical wavenumber, k_z^{cs} , can be derived by setting the real part of Equation (5.49) equal to zero, namely

$$k_z^{cs} = \frac{v_{\text{Af}}^2}{c_{\text{Tf}} \eta_{\text{Cf}}} \pm \sqrt{\frac{v_{\text{Af}}^4}{c_{\text{Tf}}^2 \eta_{\text{Cf}}^2} - k_{\perp}^2}. \quad (5.50)$$

In principle, we obtain two critical values from Equation (5.50). The one given by the + sign corresponds to a very large value of k_z , and we must point out that it is not a correct critical value. The reason for obtaining this spurious critical wavenumber is that Equation (5.49) fails to correctly approximate the slow mode frequency when k_z is large (in comparison with k_{\perp}), since the terms with ω^3 and ω^4 in Equation (5.48) are relevant for the slow mode in such a case and cannot be neglected. Our subsequent numerical results confirm that this critical wavenumber is not a valid solution. On the contrary, the critical wavenumber given by the – sign is a correct solution. For $k_{\perp}^2 c_{\text{Tf}}^2 \eta_{\text{Cf}}^2 / v_{\text{Af}}^4 \ll 1$ it can be approximated by

$$k_z^{cs} \approx \frac{c_{\text{Tf}} \eta_{\text{Cf}}}{2v_{\text{Af}}^2} k_{\perp}^2, \quad (5.51)$$

or in a dimensionless form as

$$k_z^{cs} a \approx \frac{c_{\text{Tf}} \tilde{\eta}_{\text{Cf}}}{2v_{\text{Af}}} (k_{\perp} a)^2. \quad (5.52)$$

Hence, the critical wavenumber is both determined by the geometry, through $k_{\perp} a$, and by the ionization degree, through $\tilde{\eta}_{\text{Cf}}$. As a consequence, the slow mode has no critical wavenumber in the unbounded medium, studied by Forteza et al. (2008). For $k_z \gg k_z^{cs}$, we can take the real part of the frequency as $\omega_{\text{R}} \approx \pm c_{\text{Tf}} k_z$ and use Equation (5.49) to obtain the ratio τ_{D}/P as

$$\frac{\tau_{\text{D}}}{P} \approx \frac{1}{\pi} \frac{v_{\text{Af}}^2}{c_{\text{Tf}} \eta_{\text{Cf}}} \frac{k_z}{(k_z^2 + k_{\perp}^2)}. \quad (5.53)$$

We have to provide an appropriate value of k_{\perp} for the slow mode. Again, let us consider two well-known results regarding the slow mode behavior in the ideal case. First, the dominant velocity perturbation for the slow mode is along magnetic field lines, i.e., v_z , and second, the corona has a negligible effect and the slow mode is mainly

governed by the internal medium. In the ideal case, the perturbation v_z of the slow mode with azimuthal wavenumber m is proportional to the Bessel function J_m . One possibility is to assume that v_z is also approximately described by the function J_m in the partially ionized case. Similarly as done for Alfvén waves in Section 5.2.1, we could take v_z fully confined within the filament thread and impose $v_z = 0$ at $r = a$. In such a situation, we approximate $(k_\perp a)^2 \approx j_m^2 + m^2$, where the term j_m is the first zero of the Bessel function J_m and accounts for the radial contribution to the perpendicular wavenumber. Thus, the slow mode critical wavenumber takes the following form

$$k_z^{cs} a \approx \frac{c_{\text{Tf}} \tilde{\eta}_{\text{Cf}}}{2v_{\text{Af}}} (j_m^2 + m^2). \quad (5.54)$$

We can now examine Figure 3.5c (corresponding to the slow mode perturbations in the ideal case) and see that actually v_z is not strictly confined within the filament thread and that $v_z \neq 0$ at $r = a$, which could make j_m slightly different from the actual radial wavenumber, and Equation (5.54) less accurate for approximating the actual critical value than the corresponding expressions for the kink and Alfvén critical wavenumbers. This point is checked later by our numerical computations.

5.3 Numerical results

5.3.1 Alfvén modes

Again, we start with Alfvén modes. We solve Equation (5.24) and plot in Figure 5.3a the Alfvén wave phase velocity as a function of $k_z a$ for several ionization degrees. As analytically predicted, the Alfvén mode only propagates between two critical wavenumbers, the first of them being independent of the ionization degree. At these critical wavenumbers, the real part of the Alfvén frequency vanishes. Note that the critical values are far from the range of $k_z a$ relevant for prominence oscillations. We see that, except near the critical wavenumbers, the Alfvén mode phase velocity is almost equal to v_{Af} . The approximate values of the critical wavenumbers (Eq. [5.31]) for the case $\tilde{\mu}_f = 0.8$ are denoted by vertical lines in Figure 5.3a.

On the other hand, Figure 5.3b displays the ratio τ_{D}/P as a function of $k_z a$. τ_{D}/P is independent of $\tilde{\mu}_f$ for small $k_z a$, while it is significantly affected by the ionization degree for large $k_z a$. The maximum of τ_{D}/P occurs within or close to the relevant range of $k_z a$. Figure 5.4 allows a better understanding of the behavior of τ_{D}/P . Here, we select $\tilde{\mu}_f = 0.8$ and display a comparison of the full value of τ_{D}/P with that obtained by neglecting one of the two possible damping mechanisms, i.e., Ohm’s diffusion (by setting $\eta = 0$) or ion-neutral collisions (by setting $\eta_{\text{C}} = \eta$). As expected, Cowling’s diffusion, i.e., ion-neutral collisions, has an important effect on the damping time for large $k_z a$, whereas Ohm’s diffusion dominates for small $k_z a$. As estimated by Equation (5.15), the transition between both regimes takes place within the relevant range of $k_z a$. The estimated transitional wavenumber (vertical line in Fig. 5.4) is close to the actual value. Computations for different values of $\tilde{\mu}_f$ show equivalent results.

Finally, the approximation given by Equation (5.29) is compared with the complete numerical solution by means of symbols in both panels of Figure 5.3. Only the case $\tilde{\mu}_f = 0.8$ is studied again for simplicity. We see that there is an excellent agreement between the full solution and the approximation.

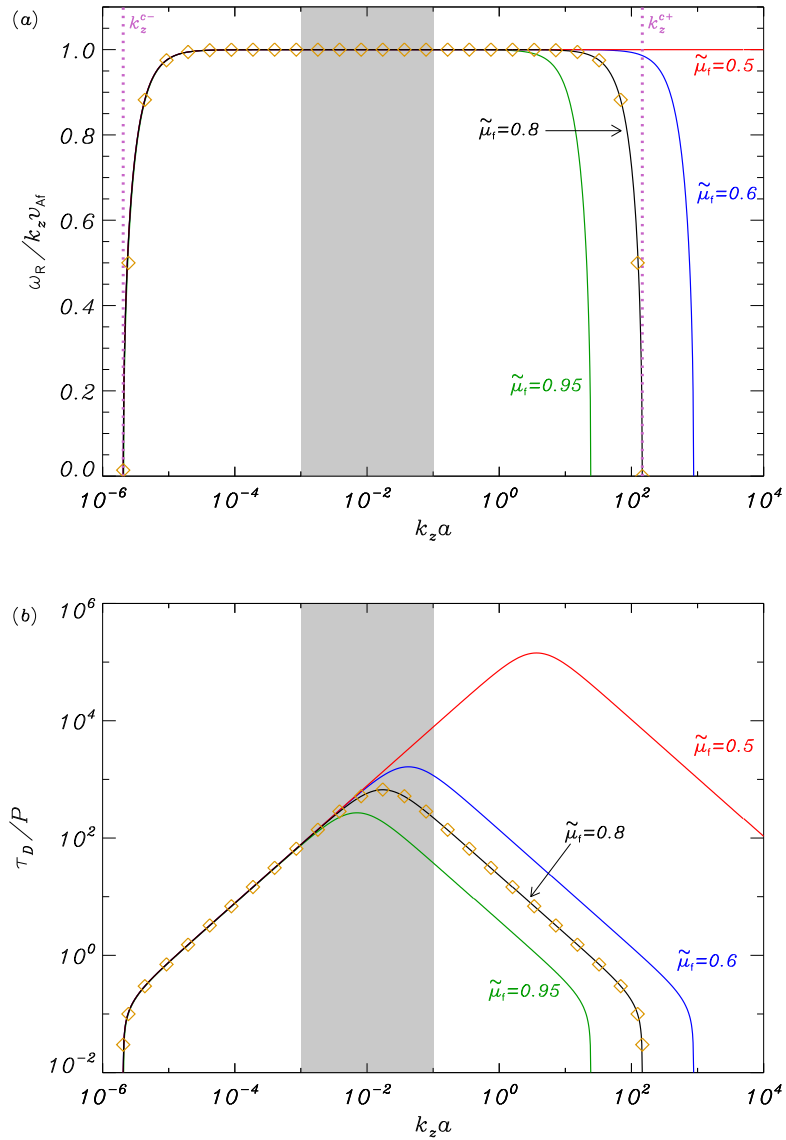


Figure 5.3: (a) Normalized phase velocity of the Alfvén mode with $m = 0$ as a function of $k_z a$ for $\tilde{\mu}_f = 0.5, 0.6, 0.8$, and 0.95 . The vertical dotted lines are the approximated critical wavenumbers given by Equation (5.31) for $\tilde{\mu}_f = 0.8$. (b) The corresponding values of τ_D / P . In both panels, symbols correspond to the approximation given by Equation (5.29) for $\tilde{\mu}_f = 0.8$.

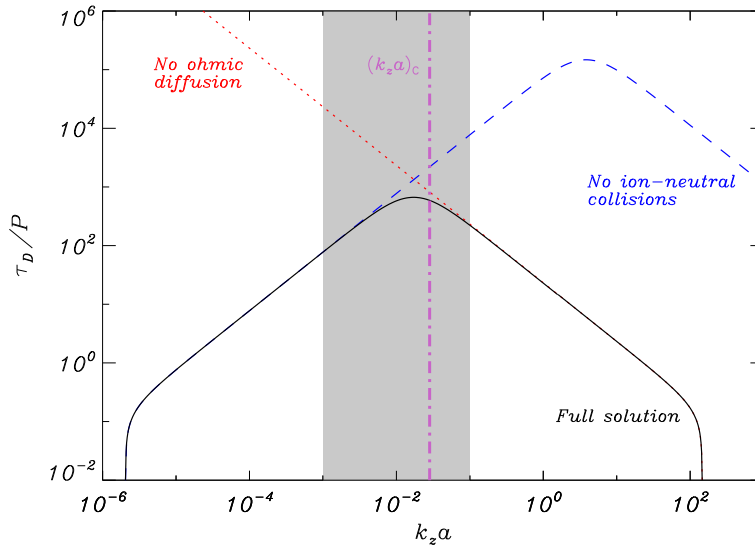


Figure 5.4: τ_D/P of the Alfvén mode with $m = 0$ as a function of $k_z a$ for $\tilde{\mu}_f = 0.8$. The different line styles represent: the full solution (solid), the solution in the absence of ion-neutral collisions, i.e., $\eta_C = \eta$ (dashed), and the solution after neglecting Ohm’s diffusion, i.e., $\eta = 0$ (dotted). The vertical dot-dashed line is the transitional wavenumber given by Equation (5.15).

5.3.2 Kink modes

Now, we turn our attention to the kink mode. Figure 5.5a displays the kink mode phase speed as a function of $k_z a$ obtained by means of the PDE2D numerical code. We see that the propagation of the kink wave is also constrained by the existence of two critical wavenumbers, correctly described by Equations (5.28) and (5.47), denoted by vertical lines. Note that since the left-hand side critical wavenumber is very small ($k_z^c a \approx 5 \times 10^{-7}$) and the horizontal axis of Figure 5.5a is in logarithmic scale, the approximation for this critical wavenumber seems less accurate than that for the right-hand side critical value, although the precision of both of them is similar. Drawing our attention to the relevant range of $k_z a$, we obtain $\omega/k_z \approx c_k$ as in the ideal case, so diffusive effects do not seem relevant to wave propagation for the observed wavelengths. The dependence of τ_D/P with $k_z a$ is shown in Figure 5.5b. This result is very similar to that obtained for the Alfvén mode, hence most of the comments of Section 5.3.1 regarding the Alfvén mode damping also apply to the kink mode case. Next, we consider the analytical dispersion relation and solve Equation (5.40) for $m = 1$ and $\tilde{\mu}_f = 0.8$, the corresponding result being plotted with symbols in Figure 5.5. The solution of the analytical dispersion relation agrees well with the numerical solution in the range of $k_z a$ dominated by Cowling’s diffusion. As expected, the numerical and analytical solutions do not agree for small $k_z a$ because the effect of ohmic diffusion is not included in the analytical dispersion relation.

We check the efficiency of the different damping mechanisms on the kink mode. Figure 5.6 shows a comparison of the value of τ_D/P of the kink wave with that obtained

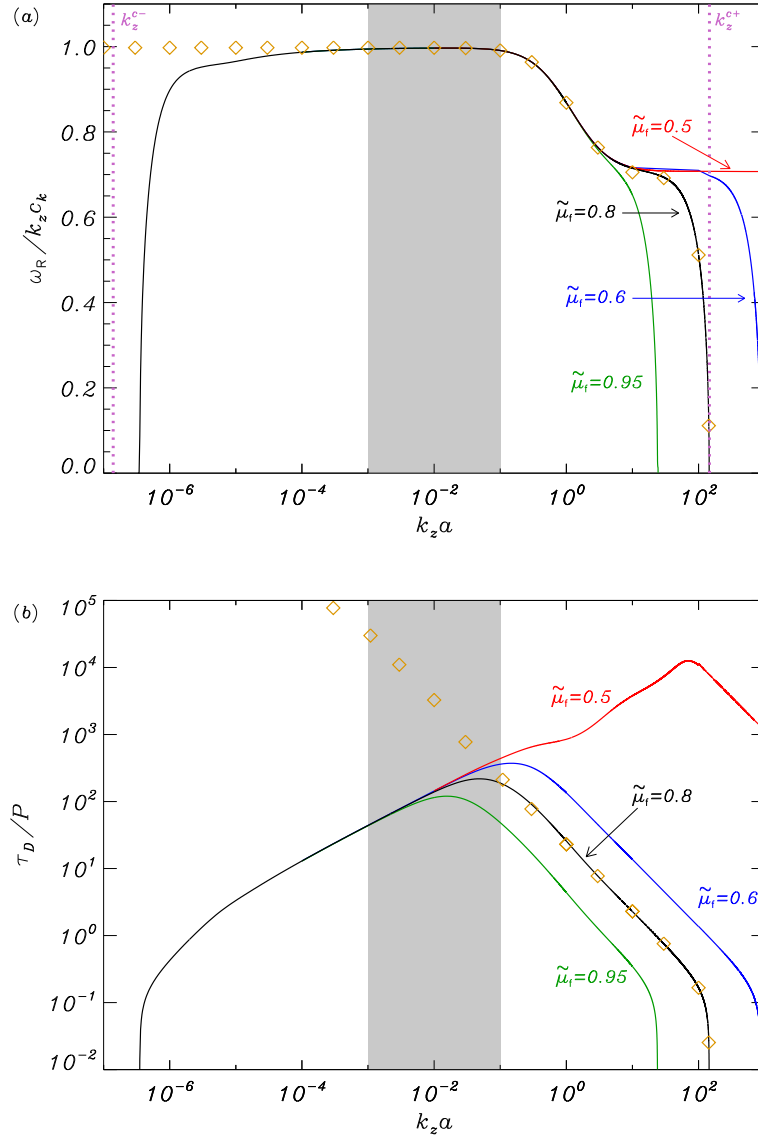


Figure 5.5: (a) Normalized phase velocity of the kink mode as a function of $k_z a$ for $\tilde{\mu}_f = 0.5, 0.6, 0.8$, and 0.95 . The vertical dotted lines are the approximated critical wavenumbers given by Equations (5.28) and (5.47) for $\tilde{\mu}_f = 0.8$. (b) The corresponding values of τ_D / P . In both panels, symbols correspond to the solution obtained by solving the analytical dispersion relation (Eq. [5.40]) for $\tilde{\mu}_f = 0.8$.

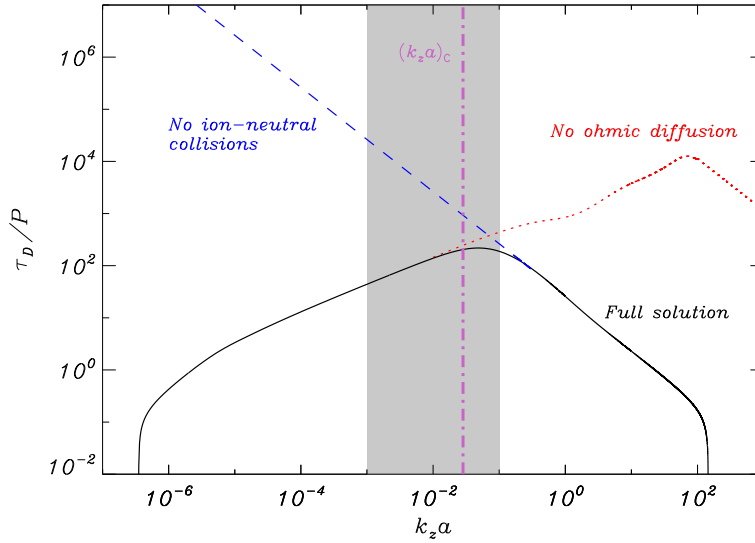


Figure 5.6: τ_D/P of the kink mode as a function of $k_z a$ for $\tilde{\mu}_f = 0.8$. The different line styles represent: the full solution (solid), the solution in the absence of ion-neutral collisions, i.e., $\eta_C = \eta$ and $\Xi = 0$ (dashed), and the solution after neglecting Ohm's diffusion, i.e., $\eta = 0$ (dotted). The vertical dot-dashed line is the transitional wavenumber given by Equation (5.15).

by neglecting Ohm's diffusion ($\eta = 0$) or ion-neutral collisions ($\eta_C = \eta$ and $\Xi = 0$). Only the solutions corresponding to $\tilde{\mu}_f = 0.8$ are displayed for the sake of simplicity. The result for the kink mode is very similar to that obtained for the Alfvén mode (see Fig. 5.4), namely that Ohm's diffusion dominates for small $k_z a$ and ion-neutral collisions are dominant for large $k_z a$. The transition between both behaviors takes place within the relevant range of $k_z a$, where $\tau_D/P \gg 10$. Therefore, neither Ohm's diffusion nor ion-neutral collisions can provide damping times compatible with those observed. By performing equivalent computations for other values of $\tilde{\mu}_f$, we conclude that, in agreement with Forteza et al. (2007), only for an almost neutral plasma ($\tilde{\mu}_f > 0.95$) and large $k_z a$, one can obtain a τ_D/P consistent with observations. Although, the efficiency of Ohm's diffusion and ion-neutral collisions is not enough to produce realistic kink mode damping times, these mechanisms are much more efficient than the non-adiabatic effects studied in Chapter 4 for the kink mode damping.

5.3.3 Slow modes

The last wave mode that we study in this investigation is the slow mode. We numerically obtain the frequency of the radially fundamental mode with $m = 1$, but we note again that the slow mode behavior is weakly affected by the value of the azimuthal wavenumber. Figure 5.7a shows the slow mode phase speed as a function of $k_z a$. The slow mode behavior is also affected by the presence of a critical wavenumber, which is highly dependent on the ionization degree. The slow mode is totally damped for k_z smaller than the critical value. The presence of the critical wavenumber is correctly

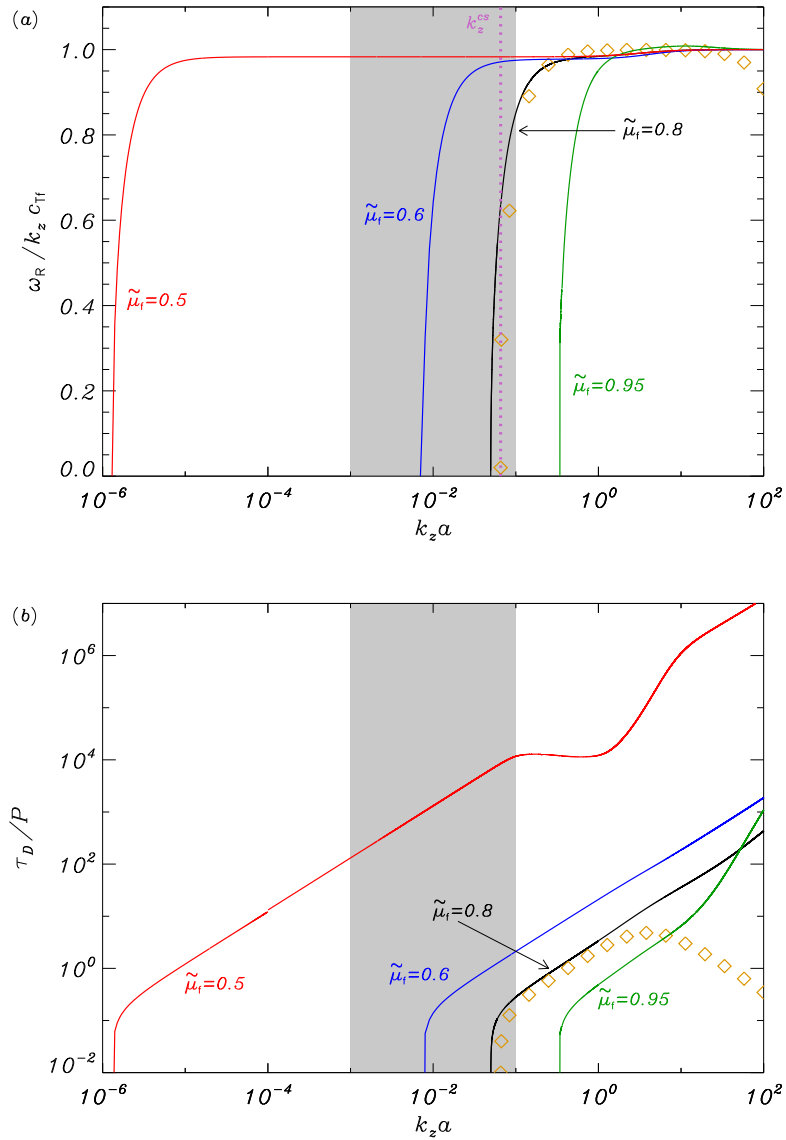


Figure 5.7: (a) Normalized phase velocity of the slow mode with $m = 1$ as a function of $k_z a$ for $\tilde{\mu}_f = 0.5, 0.6, 0.8$, and 0.95 . The vertical dotted line is the approximated critical wavenumber given by Equation (5.54) for $\tilde{\mu}_f = 0.8$. (b) The corresponding values of τ_D / P . In both panels, symbols correspond to the approximation given by Equation (5.49) for $\tilde{\mu}_f = 0.8$.

described by the approximation (Eq. [5.54]), although the approximated value is slightly larger than the actual one. We see that for large enough $\tilde{\mu}_f$, the critical $k_z a$ falls inside or is larger than the relevant values. This result has important implications from the observational point of view, since it suggests that the slow wave might not propagate in realistic, thin filament threads. For $k_z a$ larger than the critical value, the slow mode phase speed is close to the internal cusp speed, c_{Tf} .

On the other hand, Figure 5.7b displays τ_D/P again as a function of $k_z a$. The ratio τ_D/P achieves very small values close to the position of the critical wavenumber. The reason for this behavior is that the real part of the frequency tends to zero and so the period tends to infinity. Also, we see that the damping time grows rapidly when $\tilde{\mu}_f \rightarrow 0.5$, i.e., the dependence of τ_D/P on $\tilde{\mu}_f$ is more sensitive to the ionization degree for an almost fully ionized plasma than for a weakly ionized plasma.

We take now $\tilde{\mu}_f = 0.8$ and compute the approximate slow mode frequency from Equation (5.49). This result is plotted by means of symbols in both panels of Figure 5.7. We see that the approximation is reasonably good for $k_z a < 1$ and near the critical k_z . However, it diverges from the numerical result for $k_z a > 1$ because the assumptions considered for deriving Equation (5.49) are not satisfied for large $k_z a$, as commented in Section 5.2.3.

Finally, the particular effect of Ohm's diffusion and ion-neutral collisions on the slow mode damping is assessed in Figure 5.8. We obtain that the slow mode damping is entirely governed by ion-neutral collisions (Cowling's diffusion). It is worth noting that Ohm's diffusion never becomes important for the slow mode damping because the presence of the critical wavenumber does not allow the slow mode to propagate for very small $k_z a$, where Ohm's diffusion might be of relevance. In addition, Figure 5.7b indicates that when $\tilde{\mu}_f$ is large, the efficiency of ion-neutral collisions for the slow mode damping is similar to that of non-adiabatic mechanisms studied in Chapter 4. This result suggests that the joint effect of non-adiabatic mechanisms and Cowling's diffusion may produce a very efficient damping of slow waves in partially ionized filament threads.

5.4 Conclusion

In this Chapter, we have studied the propagation of Alfvén, kink, and slow MHD waves in a partially ionized, homogeneous filament thread. Contrary to the fully ionized, ideal case, we have found that wave propagation is constrained by the presence of critical values of the longitudinal wavenumber. This result is of special relevance in the case of the slow magnetoacoustic mode, since the critical wavenumber lies within the relevant range, i.e., the observed wavelengths of prominence oscillations, for typical prominence parameters. This might prevent the slow mode propagation in thin filament threads and, therefore, this mode might not be observationally detectable.

Turning our attention to the wave damping, we have obtained that for both Alfvén and kink waves, ion-neutral collisions (by means of Cowling's diffusion) dominate for large $k_z a$, i.e., short wavelengths, while Ohm's diffusion is more important for small $k_z a$, i.e., large wavelengths. On the contrary, the slow mode is totally governed by Cowling's diffusion. With the exception of the slow mode, these mechanisms cannot provide damping times compatible with those observed when typical values of the wavelength are considered. In the case of both Alfvén and kink waves, one has to consider very

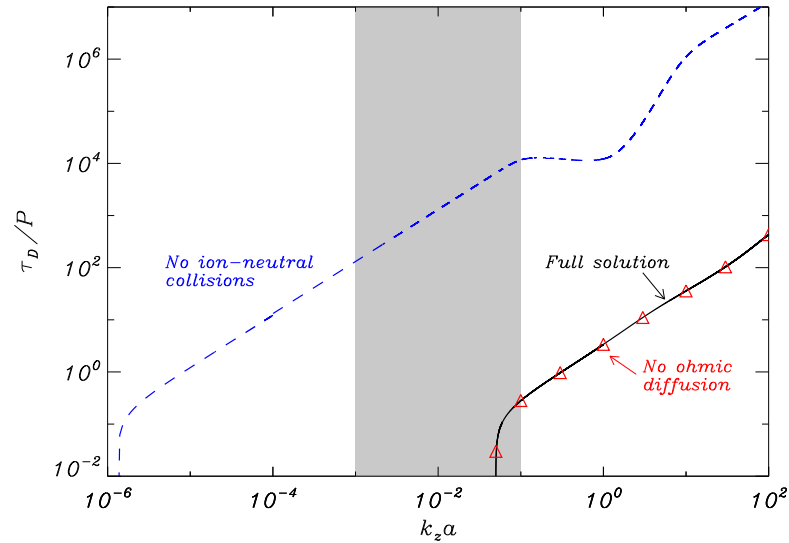


Figure 5.8: τ_D/P of the slow mode with $m = 1$ as a function of $k_z a$ for $\tilde{\mu}_f = 0.8$. The different line styles represent: the full solution (solid), the solution in the absence of ion-neutral collisions, i.e., $\eta_C = \eta$ and $\Xi = 0$ (dashed), and the solution after neglecting Ohm's diffusion, i.e., $\eta = 0$ (symbols).

short wavelengths and almost neutral plasmas to obtain realistic values of the damping time.

One must be aware that here we have considered a plasma composed only by hydrogen. It is interesting to estimate the effect of the presence of helium on the results. Soler et al. (2010a) assessed the effect of neutral and singly ionized helium on the wave time damping in a homogeneous, unbounded plasma with prominence conditions. They obtained that the efficiency of Cowling's diffusion is increased by the presence of helium, due to the additional collisions of neutral and ionized hydrogen species with helium species. However, when realistic abundances of helium in prominences are considered ($\sim 10\%$), it turns out that this effect has a very minor influence on the wave damping. We expect that similar conclusions apply in the cylindrical case and so the presence of helium can be safely neglected.

Resonantly Damped Kink Magnetohydrodynamic Waves in a Filament Thread*

Among the damping mechanisms investigated in the previous Chapters, none of them can produce kink mode damping times compatible with the observations of damped transverse thread oscillations. [Arregui et al. \(2008\)](#) studied numerically the kink mode damping by resonant absorption in the Alfvén continuum in pressure-less filament fine structures. They obtained $\tau_D/P \approx 3$ for typical wavelengths of prominence oscillations and realistic density contrasts. Resonant absorption has been previously investigated as a damping mechanism for the kink mode in coronal flux tubes by, e.g., [Ruderman & Roberts \(2002\)](#) and [Goossens et al. \(2002\)](#), who derived analytical expressions for the damping time. Recent reviews by [Goossens et al. \(2006\)](#) and [Goossens \(2008\)](#) have summarized the main results of the resonant damping of kink modes in coronal loops. If prominence conditions are considered in the analytical expressions of [Ruderman & Roberts \(2002\)](#) and [Goossens et al. \(2002\)](#), a very good agreement with the numerical results of [Arregui et al. \(2008\)](#) is obtained. On the basis of the result by [Arregui et al. \(2008\)](#), the process of resonant absorption also seems a good candidate to be responsible for the kink mode attenuation in filament threads. Here, we study the efficiency of resonant absorption for the damping of kink modes in fully ionized and partially ionized filament threads.

As in previous Chapters, we combine numerical computations and analytical approximations to obtain the period and the damping time of kink modes in transversely inhomogeneous filament threads. From an analytical point of view, the damping by resonant absorption in both the Alfvén and slow continua is investigated in fully ionized filament threads by means of the thin tube and thin boundary approximations (Sec 6.1). We assess the particular role on the kink mode damping of the coupling to Alfvén continuum modes and to slow continuum modes. Next, we consider partial ionization of the filament plasma and study its effect on the process of resonant absorption and on the damping of kink modes (Sec 6.2). In both the fully ionized and partially ionized cases, the general MHD equations are solved numerically, and the numerical results are compared with the previously obtained approximations.

*This Chapter is based on the results of R. Soler, R. Oliver, J. L. Ballester, & M. Goossens 2009, *Damping of Filament Thread Oscillations: Effect of the Slow Continuum*, ApJ, 695, L166 and R. Soler, R. Oliver, & J. L. Ballester 2009, *Resonantly Damped Kink Magnetohydrodynamic Waves in a Partially Ionized Filament Thread*, ApJ, 707, 662.

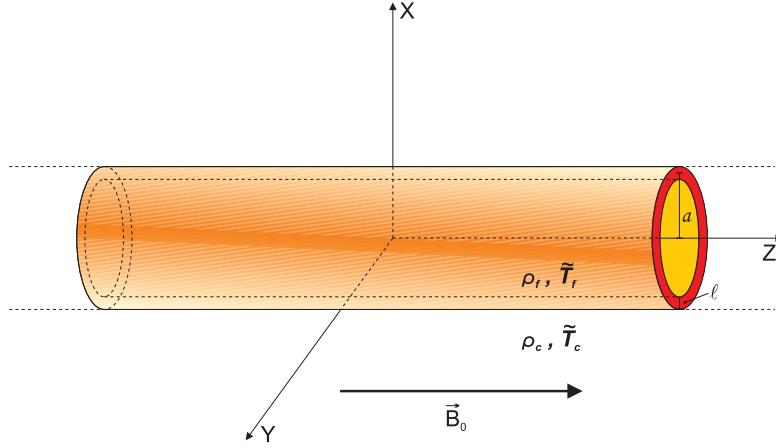


Figure 6.1: Sketch of the filament thread model considered in this Chapter.

6.1 Resonant absorption in the Alfvén and slow continua

6.1.1 Model configuration

As in previous Chapters, the model for the present equilibrium configuration is a straight cylinder with prominence-like conditions embedded in an unbounded corona. Here, we include a transversely inhomogeneous transitional layer between both regions (see Fig. 6.1). We consider that the filament plasma is fully ionized. The effect of partial ionization is assessed in Section 6.2. Therefore, our model is equivalent to that of Arregui et al. (2008), although they neglected plasma pressure and adopted the $\beta = 0$ approximation. The plasma β in solar prominences is probably small, but it is definitely nonzero. We take gas pressure into account, i.e. the $\beta \neq 0$ case, and assess the effect of the plasma β on the resonant damping of kink modes.

The density profile, $\rho_0(r)$, is adopted after Ruderman & Roberts (2002) and only depends on the radial direction as

$$\rho_0(r) = \begin{cases} \rho_f, & \text{if } r \leq a - l/2, \\ \rho_{\text{tr}}(r), & \text{if } a - l/2 < r < a + l/2, \\ \rho_c, & \text{if } r \geq a + l/2, \end{cases} \quad (6.1)$$

with

$$\rho_{\text{tr}}(r) = \frac{\rho_f}{2} \left\{ \left(1 + \frac{\rho_c}{\rho_f} \right) - \left(1 - \frac{\rho_c}{\rho_f} \right) \sin \left[\frac{\pi}{l} (r - a) \right] \right\}. \quad (6.2)$$

In these expressions, ρ_f is the filament thread density, ρ_c is the coronal density, a is the tube mean radius, and l is the transitional layer width. The limits $l/a = 0$ and $l/a = 2$ correspond to a homogeneous tube and a fully inhomogeneous tube, respectively. We use the following densities: $\rho_f = 5 \times 10^{-11} \text{ kg m}^{-3}$ and $\rho_c = 2.5 \times 10^{-13} \text{ kg m}^{-3}$. Therefore, the density contrast between the internal and external plasma is $\rho_f/\rho_c = 200$. The plasma temperature is related to the density through the usual ideal gas equation (Eq. [2.14]). The radial profile of the effective temperature, $\tilde{T}_0(r)$, is

$$\tilde{T}_0(r) = \begin{cases} \tilde{T}_f, & \text{if } r \leq a - l/2, \\ \tilde{T}_{\text{tr}}(r), & \text{if } a - l/2 < r < a + l/2, \\ \tilde{T}_c, & \text{if } r \geq a + l/2, \end{cases} \quad (6.3)$$

6.1. RESONANT ABSORPTION IN THE ALFVÉN AND SLOW CONTINUA

with

$$\tilde{T}_{\text{tr}}(r) = 2\tilde{T}_{\text{f}} \left\{ \left(1 + \frac{\tilde{T}_{\text{f}}}{\tilde{T}_{\text{c}}} \right) - \left(1 - \frac{\tilde{T}_{\text{f}}}{\tilde{T}_{\text{c}}} \right) \sin \left[\frac{\pi}{l} (r - a) \right] \right\}^{-1}. \quad (6.4)$$

We consider $\tilde{T}_{\text{f}} = 10^4$ K and $\tilde{T}_{\text{c}} = 2 \times 10^6$ K for the internal and external effective temperatures, respectively. The magnetic field is taken homogeneous and orientated along the z -direction, $\vec{B}_0 = B_0 \hat{e}_z$, with $B_0 = 5$ G everywhere. With these parameters, the total pressure is constant everywhere in the equilibrium, and $\beta \approx 0.04$.

In the presence of the transitional layer, it is well-known that the kink mode is resonantly coupled to Alfvén continuum modes. In terms of the frequency, this means that the kink frequency, ω_k , is between the internal, ω_{Af} , and external, ω_{Ac} , Alfvén frequencies, i.e., $\omega_{\text{Af}} < \omega_k < \omega_{\text{Ac}}$. This last condition can be equivalently expressed in terms of the phase velocity, so $v_{\text{Af}} < c_k < v_{\text{Ac}}$. It turns out that, for filament conditions, the kink mode phase velocity is also within the slow (or cusp) continuum that extends between the internal, c_{Tf} , and external, c_{Tc} , cusp speeds, i.e., $c_{\text{Tf}} < c_k < c_{\text{Tc}}$. In such a case, the kink mode is not only resonantly coupled to Alfvén continuum modes but also to slow continuum modes. The frequency of the kink mode is both within the Alfvén and slow continua because of the high density and low temperature of the prominence material in comparison with the coronal values. Hence, the slow continuum damping arises as an additional mechanism to damp the kink mode in filament threads, whose effect was not included in the investigation by [Arregui et al. \(2008\)](#). For coronal loops the kink frequency is outside the slow continuum. A coronal loop is presumably hotter and denser than its surrounding corona, so the ordering of cusp, Alfvén, and kink speeds is $c_{\text{Tc}} < c_{\text{Tf}} < v_{\text{Af}} < c_k < v_{\text{Ac}}$. Therefore, there is no slow resonance for the kink mode in coronal loops. Although the slow resonance has been previously investigated in the context of absorption of driven MHD waves in the solar atmosphere (e.g., [Čadež et al. 1997](#); [Erdélyi et al. 2001](#)) and sunspots (e.g., [Keppens 1996](#)), the effect of the slow resonance on the damping of the kink modes has not been investigated before.

6.1.2 Analytical investigation

We consider the linear, ideal MHD equations for the $\beta \neq 0$ case (Eqs. [2.92]–[2.96]) and adopt cylindrical coordinates. All symbols in the following expressions have the same meaning as in previous Chapters. We follow a normal mode approach and since φ and z are ignorable coordinates, the perturbed quantities are put proportional to $\exp(im\varphi + ik_z z - i\omega t)$. In the absence of a transitional layer, i.e., $l/a = 0$, the dispersion relation is obtained by imposing the continuity of the Lagrangian radial displacement, ξ_r , and the total pressure perturbation, $p_{\text{T}1}$, at $r = a$, and corresponds to Equation (3.18).

When an inhomogeneous transitional layer is present in the model, we cannot obtain an analytical expression for the dispersion relation unless some assumptions are made. The position of the Alfvén, r_{A} , and slow, r_{s} , resonance points can be computed by equating the kink frequency, ω_k , to the local Alfvén, $\omega_{\text{A}} = v_{\text{A}} k_z$, and cusp, $\omega_{\text{c}} = c_{\text{T}} k_z$, frequencies, respectively. By this procedure, we obtain

$$r_{\text{A}} = a + \frac{l}{\pi} \arcsin \left[\frac{\rho_{\text{f}} + \rho_{\text{c}}}{\rho_{\text{f}} - \rho_{\text{c}}} - \frac{2v_{\text{Af}}^2 k_z^2}{\omega_k^2} \frac{\rho_{\text{f}}}{(\rho_{\text{f}} - \rho_{\text{c}})} \right], \quad (6.5)$$

for the Alfvén resonance point, and

$$r_s = a + \frac{l}{\pi} \arcsin \left[\frac{\rho_f + \rho_c}{\rho_f - \rho_c} - \frac{2c_{Tf}^2 k_z^2}{\omega_k^2} \frac{\rho_f}{(\rho_f - \rho_c)} \right], \quad (6.6)$$

for the slow resonance point. Note that we need the value of ω_k to determine both r_A and r_s . The ideal MHD equations are singular at $r = r_A$ and $r = r_s$. The singularity is removed if dissipative effects, such as magnetic diffusion or viscosity, are considered in a region around the resonance point, i.e., the dissipative layer.

The jump conditions and the Thin Boundary approximation

A method for obtaining an analytical dispersion relation is to combine the jump conditions at the resonance points and the approximation of the thin boundary (TB). The jump conditions were derived by Sakurai et al. (1991a) and Goossens et al. (1995) for the driven problem and later by Tirry & Goossens (1996) for the eigenvalue problem. This method was used, e.g., by Sakurai et al. (1991b) for determining the absorption of sound waves in sunspots, Goossens et al. (1992) for determining surface eigenmodes in incompressible and compressible plasmas, Van Doorselaere et al. (2004) for kink eigenmodes in pressure-less coronal loops, and in a number of other papers in the context of MHD waves in the solar atmosphere (e.g., Erdélyi et al. 1995; Keppens 1996; Stenuit et al. 1998; Andries et al. 2000; Goossens et al. 2009, among other works). The assumptions behind the TB approximation and its applications have been recently reviewed by Goossens (2008). In short, the main assumption of the TB approximation is that there is a region around the dissipative layer where both ideal and dissipative MHD apply. If one takes a sufficiently thin transitional layer, i.e., $l/a \ll 1$, we can assume that the thickness of the dissipative layer, namely δ , roughly coincides with the width of the whole inhomogeneous transitional layer, i.e. $\delta \sim l$. So, we can simply use the jump conditions to connect analytically the perturbations from the homogeneous part of the tube to those of the external medium, and avoid the numerical integration of the dissipative MHD equations across the inhomogeneous region. This method is in principle only valid when the inhomogeneous length-scale and the resonant layer have similar sizes, but Van Doorselaere et al. (2004) showed numerically that the results obtained in the TB approximation are still approximately valid even when the assumption $l/a \ll 1$ is not strictly fulfilled. Apart from the Alfvén resonance, Sakurai et al. (1991a) also provided jump conditions for the slow resonance, which can be applied to the present situation. Hence, the jump conditions and the TB formalism allows us to assess the particular contribution of the slow resonance to the kink mode damping.

The jump conditions at the Alfvén resonance point, $r = r_A$, for the radial displacement and the total pressure perturbation provided by Sakurai et al. (1991a) in the case of a straight magnetic field are,

$$[[\xi_r]] = -i\pi \frac{m^2/r_A^2}{|\rho_0 \Delta_A|_{r_A}} p_T, \quad [[p_{T1}]] = 0, \quad \text{at} \quad r = r_A, \quad (6.7)$$

where $[[X]] = X_c - X_f$ stands for the jump of the quantity X , and $\Delta_A = \frac{d}{dr} [\omega^2 - \omega_A^2(r)]$. The respective jump conditions at the slow resonance point, $r = r_s$, are

$$[[\xi_r]] = -i\pi \frac{k_z^2}{|\rho_0 \Delta_c|_{r_s}} \left(\frac{c_s^2}{c_s^2 + v_A^2} \right)^2 p_{T1}, \quad [[p_{T1}]] = 0, \quad \text{at} \quad r = r_s, \quad (6.8)$$

6.1. RESONANT ABSORPTION IN THE ALFVÉN AND SLOW CONTINUA

where $\Delta_c = \frac{d}{dr} [\omega^2 - \omega_c^2(r)]$, and the factor $\frac{c_s^2}{c_s^2 + v_A^2} = \frac{\beta}{\beta + 2/\gamma} \approx 0.034$ is a constant everywhere in the equilibrium, with $\gamma = 5/3$ the adiabatic index. The Alfvén jump conditions (Eq. [6.7]) are independent of k_z , but they depend on m , so for $m = 0$ there is no Alfvén resonance. On the contrary, the slow jump conditions (Eq. [6.8]) are independent of m , but they depend on k_z , so for $k_z = 0$ there is no slow resonance.

In our model the magnetic field is straight and homogeneous so that the variations of the local Alfvén frequency and the local cusp (or slow) frequency are only due to the variation of the density. In addition, from the resonance condition we have $\omega_A(r_A) = \omega_c(r_s) = \omega_k$, thus

$$|\rho_0 \Delta_A|_{r_A} = \omega_k^2 |\partial_r \rho_0|_{r_A}, \quad (6.9)$$

and

$$|\rho_0 \Delta_c|_{r_s} = \omega_k^2 |\partial_r \rho_0|_{r_s}, \quad (6.10)$$

where $|\partial_r \rho_0|_{r_A}$ and $|\partial_r \rho_0|_{r_s}$ are the moduli of the radial derivative of the density profile evaluated at $r = r_A$ and $r = r_s$, respectively. Next, we apply the jump conditions to obtain a correction to the dispersion relation (Eq. [3.18]) due to both resonances in the TB approximation, namely

$$\begin{aligned} & \frac{n_c}{\rho_c (\omega^2 - k_z^2 v_{Ac}^2)} \frac{K'_m(n_c a)}{K_m(n_c a)} - \frac{m_f}{\rho_f (\omega^2 - k_z^2 v_{Af}^2)} \frac{J'_m(m_f a)}{J_m(m_f a)} \\ &= -i\pi \frac{m^2/r_A^2}{\omega_k^2 |\partial_r \rho_0|_{r_A}} - i\pi \left(\frac{c_s^2}{c_s^2 + v_A^2} \right)^2 \frac{k_z^2}{\omega_k^2 |\partial_r \rho_0|_{r_s}}, \end{aligned} \quad (6.11)$$

with m_f and n_c given by Equation (3.4). The first term on the right-hand side of Equation (6.11) corresponds to the effect of the Alfvén resonance, while the second term is present due to the slow resonance. If both terms are dropped, Equation (6.11) simply reduces to Equation (3.18). When only one of the two terms is present, we can assess the particular effect of the corresponding resonance. In order to solve Equation (6.11), we need the value of the kink frequency and the resonance positions. For this reason, we use a two-step procedure. First, we solve the dispersion relation for the case $l/a = 0$ (Eq. [3.18]) and obtain ω_k . Next, we assume that the real part of the frequency is approximately the same when the inhomogeneous transitional layer is included, allowing us to determine r_A and r_s from Equations (6.5) and (6.6), respectively. Subsequently, we compute $|\partial_r \rho_0|_{r_A}$ and $|\partial_r \rho_0|_{r_s}$. Finally, we solve the complete dispersion relation (Eq. [6.11]) with these parameters.

Expressions in the thin tube limit

Further analytical progress can be made by combining the thin boundary (TB) and the thin tube (TT) approximations. The combination of both the TB and TT approximations has been applied in several works (e.g., Goossens et al. 1992; Ruderman & Roberts 2002; Goossens et al. 2002, 2009). We perform an asymptotic expansion for small arguments of the Bessel functions in Equation (3.18) by considering the long-wavelength limit, i.e., $k_z a \ll 1$, and only keep the lowest order, nonzero term of the

expansion. Thus, the dispersion relation becomes

$$\rho_c \frac{m/a}{(\omega^2 - k_z^2 v_{Af}^2)} + \rho_f \frac{m/a}{(\omega^2 - k_z^2 v_{Ac}^2)} - i\pi \frac{\rho_f \rho_c}{\omega_k^2} \left[\frac{m^2/r_A^2}{|\partial_r \rho_0|_{r_A}} + \frac{k_z^2}{|\partial_r \rho_0|_{r_s}} \left(\frac{c_s^2}{c_s^2 + v_A^2} \right)^2 \right] = 0. \quad (6.12)$$

Now, we write the frequency as $\omega = \omega_k + i\omega_I$. Expressions for $|\partial_r \rho_0|_{r_A}$ and $|\partial_r \rho_0|_{r_s}$ are obtained from the density profile (Eq. [6.1]) as

$$|\partial_r \rho_0|_A = \left(\frac{\rho_f - \rho_c}{l} \right) \frac{\pi}{2} \cos \alpha_A, \quad |\partial_r \rho_0|_s = \left(\frac{\rho_f - \rho_c}{l} \right) \frac{\pi}{2} \cos \alpha_s, \quad (6.13)$$

with $\alpha_A = \pi(r_A - a)/l$ and $\alpha_s = \pi(r_s - a)/l$. We insert these expressions in Equation (6.12) and neglect terms with ω_I^2 . After some algebraic manipulations, we obtain an expression for the ratio ω_k/ω_I . It is straightforward to give an expression for τ_D/P , namely

$$\frac{\tau_D}{P} = \mathcal{F} \frac{1}{(l/a)} \left(\frac{\rho_f + \rho_c}{\rho_f - \rho_c} \right) \left[\frac{m}{\cos \alpha_A} + \frac{(k_z a)^2}{m} \left(\frac{c_s^2}{c_s^2 + v_A^2} \right)^2 \frac{1}{\cos \alpha_s} \right]^{-1}, \quad (6.14)$$

where \mathcal{F} is a numerical factor that depends on the density profile ($\mathcal{F} = 2/\pi$ in our sinusoidal case). As in previous expressions, the term with k_z corresponds to the contribution of the slow resonance. If this term is dropped, Equation (6.14) only takes the Alfvén resonance into account and, for $m = 1$ and $\cos \alpha_A = 1$, is equivalent to the expression first obtained by [Goossens et al. \(1992\)](#) in their Equation (77) or, in a form more similar to Equation (6.14), by [Ruderman & Roberts \(2002\)](#) in their Equation (56).

We approximate the kink mode frequency by its expression in the TT case (Eq. [3.20]). Thus, the resonance positions can be estimated. From Equation (6.5) we directly get $r_A \approx a$, whereas after a Taylor expansion of the arcsin function, Equation (6.6) provides

$$r_s \approx a + \frac{l}{\pi} \left(\frac{\rho_f + \rho_c}{\rho_f - \rho_c} \right) \left(1 - \frac{c_s^2}{c_s^2 + v_A^2} \right), \quad (6.15)$$

which for $\rho_f \gg \rho_c$ and $v_A^2 \gg c_s^2$ simplifies to $r_s \approx a + l/\pi$. We obtain that the resonances occur at different positions, with $r_s > r_A$. For the values of r_s and r_A in the TT case, $\cos \alpha_A \approx 1$ and $\cos \alpha_s \approx \cos(1) \approx 0.54$. Now, we take $m = 1$, $l/a = 0.2$, and $k_z a = 10^{-2}$ to make a simple calculation. Equation (6.14) gives $\tau_D/P \approx 3.21$. In agreement with [Arregui et al. \(2008\)](#), the obtained damping ratio is consistent with the observations of damped transverse thread oscillations.

Next, we assume $r_A \approx r_s \approx a$ for simplicity, so $\cos \alpha_A \approx \cos \alpha_s \approx 1$. The particular contribution of each resonance is estimated by the ratio of the two terms in Equation (6.14), namely

$$\frac{(\tau_D)_A}{(\tau_D)_s} \approx \frac{(k_z a)^2}{m^2} \left(\frac{c_s^2}{c_s^2 + v_A^2} \right)^2, \quad (6.16)$$

where $(\tau_D)_A$ and $(\tau_D)_s$ are the damping times exclusively due to the Alfvén and slow resonances, respectively. Assuming the same parameters as before, we obtain $(\tau_D)_A / (\tau_D)_s \approx$

6.1. RESONANT ABSORPTION IN THE ALFVÉN AND SLOW CONTINUA

10^{-7} , meaning that the Alfvén resonance is much more efficient than the slow resonance for damping the kink mode. We can consider the limit case of incompressible plasma, i.e., $c_s \rightarrow \infty$, so $\frac{c_s^2}{c_s^2 + v_A^2} \rightarrow 1$. Therefore, $(\tau_D)_A / (\tau_D)_s \approx (k_z a / m)^2 \ll 1$ for realistic values of $k_z a$. By means of these simple calculations, we can anticipate two important results. First of all, the kink mode damping by resonant absorption can explain the observed attenuation of transverse thread oscillations, and second, the slow resonance is irrelevant for the kink mode damping in comparison with the Alfvén resonance. Both results are checked next by our numerical computations.

6.1.3 Numerical procedure

In addition to the analytical approximations, we also numerically solve the full eigenvalue problem by means of the PDE2D code (Sewell 2005). We consider the linear MHD equations and include the effect of Ohm's diffusion in the induction equation in order to remove the singularity at the resonance positions. Thus, the equations solved with PDE2D are

$$i\omega\rho_1 = \rho_0 \left(v_r' + \frac{v_r}{r} + \frac{im}{r}v_\varphi + ik_z v_z \right) + \rho_0' v_r, \quad (6.17)$$

$$i\omega v_r = \frac{1}{\rho_0} p_1' - \frac{v_A^2}{B_0} (ik_z B_r - B_z'), \quad (6.18)$$

$$i\omega v_\varphi = \frac{im}{r} \frac{1}{\rho_0} p_1 - \frac{v_A^2}{B_0} \left(ik_z B_\varphi - \frac{im}{r} B_z \right), \quad (6.19)$$

$$i\omega v_z = \frac{ik_z}{\rho_0} p_1, \quad (6.20)$$

$$i\omega B_r = -ik_z B_0 v_r + \eta \left(k_z^2 B_r + \frac{m^2}{r^2} B_r + \frac{im}{r} B_\varphi' + \frac{im}{r^2} B_\varphi + ik_z B_z' \right), \quad (6.21)$$

$$i\omega B_\varphi = -ik_z B_0 v_\varphi - \eta \left(k_z \frac{m}{r} B_z + B_\varphi'' + \frac{1}{r} B_\varphi' - \frac{1}{r^2} B_\varphi - k_z^2 B_\varphi - \frac{im}{r} B_r' + \frac{im}{r^2} B_r \right), \quad (6.22)$$

$$i\omega B_z = B_0 \left(v_r' + \frac{1}{r} v_r + \frac{im}{r} v_\varphi \right) - \eta \left(B_z'' + \frac{1}{r} B_z' - \frac{m^2}{r^2} B_z - ik_z B_r' - \frac{ik_z}{r} B_r + k_z \frac{m}{r} B_\varphi \right), \quad (6.23)$$

$$i\omega (p_1 - c_s^2 \rho_1) = -c_s^2 \rho_0' v_r, \quad (6.24)$$

where the prime denotes derivative with respect to r .

The set-up conditions for the PDE2D code are those explained in Section 5.1.2. Here, we use a nonuniform grid with a large density of grid points within the inhomogeneous transitional layer to correctly describe the small spatial scales that develop due to both resonances. The PDE2D code has been previously used by, e.g., Terradas et al. (2006) and Arregui et al. (2008) to investigate the process of resonant absorption in coronal loops and filament threads, respectively.

We assume a constant and uniform value of Ohm's diffusivity, η , in Equations (6.17)–(6.24). It is important recalling that we do not study here the damping by magnetic

diffusion (which was done in Chap. 5) and that diffusion is only included to remove the singularity from the equations. This could be also accomplished by considering, e.g., viscosity. The actual value of η and the magnetic Reynolds number, $R_m = v_A a / \eta$, are not relevant as long as R_m is large enough for the damping by magnetic diffusion to be much less efficient than that due to resonant absorption. The magnetic Reynolds number in the corona is considered to be around 10^{12} , but using this value requires taking an enormous number of grid points in the numerical computations because of the dependence of the dissipative layer thickness with R_m . Sakurai et al. (1991a) give expressions for the thickness of the Alfvén, δ_A , and slow, δ_c , dissipative layers, namely

$$\delta_A = \left[\left| \frac{\omega}{\Delta_A} \right| \eta \right]_{r_A}^{1/3}, \quad \delta_c = \left[\left| \frac{\omega}{\Delta_c} \right| \frac{\omega_c^2}{\omega_A^2} \eta \right]_{r_s}^{1/3}. \quad (6.25)$$

We see that both δ_A and δ_c are proportional to $R_m^{-1/3}$. Also, it is straight-forward to check that $\delta_A > \delta_c$ for the same value of R_m . We therefore use a smaller value of R_m , and consequently a smaller number of grid points, but make sure that the damping time is still independent of R_m and that there are enough grid points within the dissipative layers. In the next Section, these numerical results are compared with the analytical approximations.

6.1.4 Results

Since we focus our investigation on the kink mode, we fix $m = 1$ in all computations. First, we take $k_z a = 10^{-2}$ and $l/a = 0.2$. We numerically compute (see Fig. 6.2) the kink mode eigenfunctions: the velocity perturbations, v_r , v_φ , and v_z , the magnetic field perturbations, B_r , B_φ , and B_z , the density perturbation, ρ_1 , and the gas pressure perturbation, p_1 . The behavior of B_r and B_φ is similar to that of v_r and v_φ , respectively, and hence they are not plotted in Figure 6.2. Because of the resonances, the perturbations show large peaks within the transitional layer. Figure 6.3 displays a close-up of the eigenfunctions in the inhomogeneous layer, which allows us to ascertain the position of the resonances in more detail. The peaks of the perturbations v_r , v_φ , and ρ_1 are related to the Alfvén resonance, while the perturbations v_z , B_z , and p_1 are more affected by the slow resonance and their peaks appear at a different position. In agreement with the analytical expressions for the dissipative layer thickness (Eq. [6.25]), we see that the peaks related to the Alfvén resonance are wider than those related to the slow resonance, meaning that the slow resonance produces a thinner resonant layer. Considering the numerical value of the real part of the frequency, we get $r_A/a \approx 1$ and $r_s/a \approx 1.08$ from Equations (6.5) and (6.6), respectively. Both values are in good agreement with the position of peaks in Figures 6.2 and 6.3. We have also checked that the total pressure perturbation, i.e., $p_{T1} = p_1 + B_0 B_z / \mu$, is almost constant across the transitional layer.

Next, we plot in Figure 6.4a the ratio of the damping time to the period, τ_D/P , as a function of $k_z a$ corresponding to the kink mode for $l/a = 0.2$. In this Figure, we compare the numerical results with those obtained from the analytical dispersion relation in the TB approximation (Eq. [6.11]). The individual contribution of each resonance in the TB approximation has been determined by solving Equation (6.11) and only taking into account the term on the right-hand side related to the desired resonance. At first sight, we see that the slow resonance (dashed line in Fig. 6.4a) is much less efficient than the

6.1. RESONANT ABSORPTION IN THE ALFVÉN AND SLOW CONTINUA

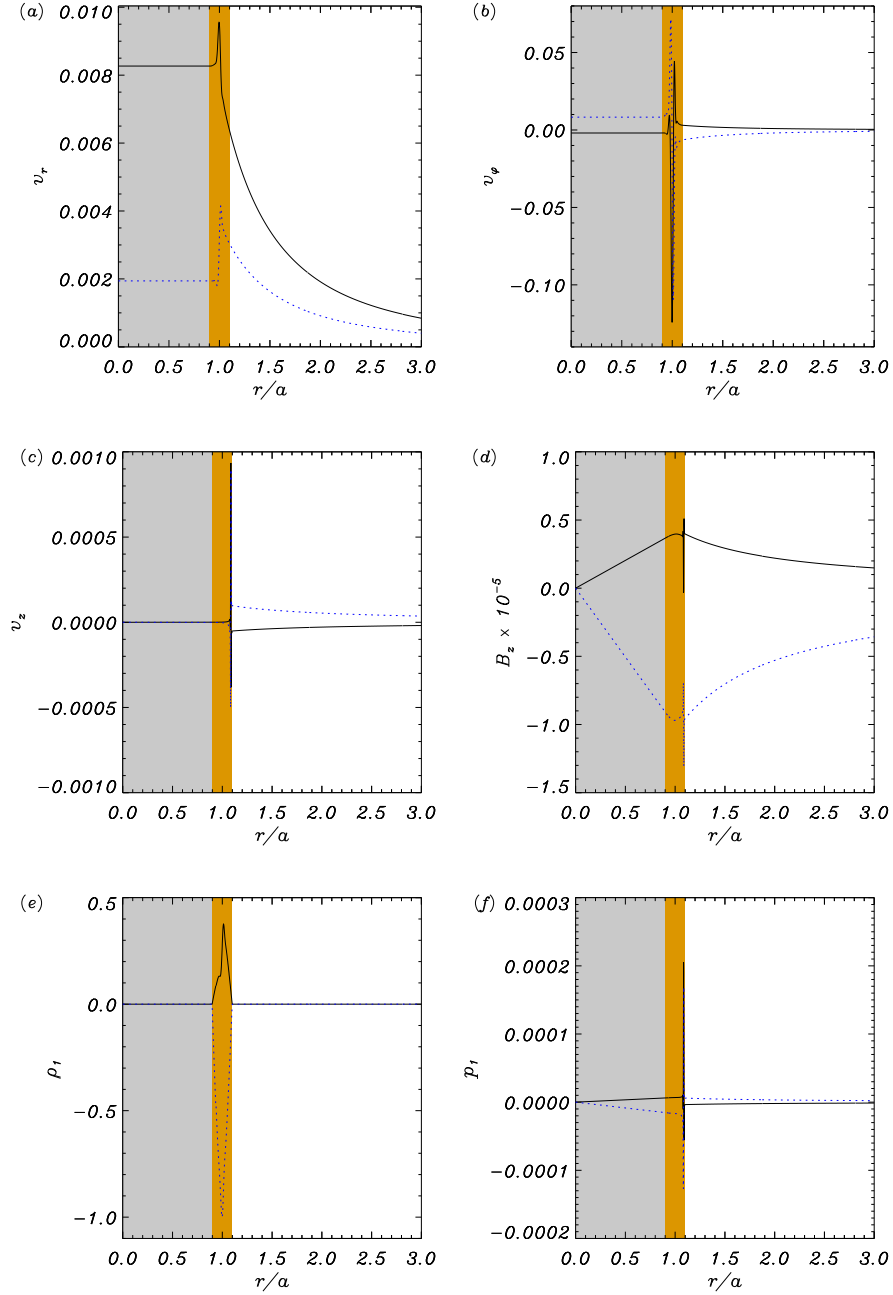


Figure 6.2: Eigenfunctions of kink mode perturbations versus r/a for $k_z a = 10^{-2}$ and $l/a = 0.2$. (a) v_r , (b) v_ϕ , (c) v_z , (d) B_z , (e) ρ_1 , and (f) p_1 . The solid line is the real part and the dotted line is the imaginary part of the corresponding eigenfunction. The grey zone denotes the homogeneous part of the tube whereas the brown region corresponds to the inhomogeneous transitional layer. Arbitrary units have been used.

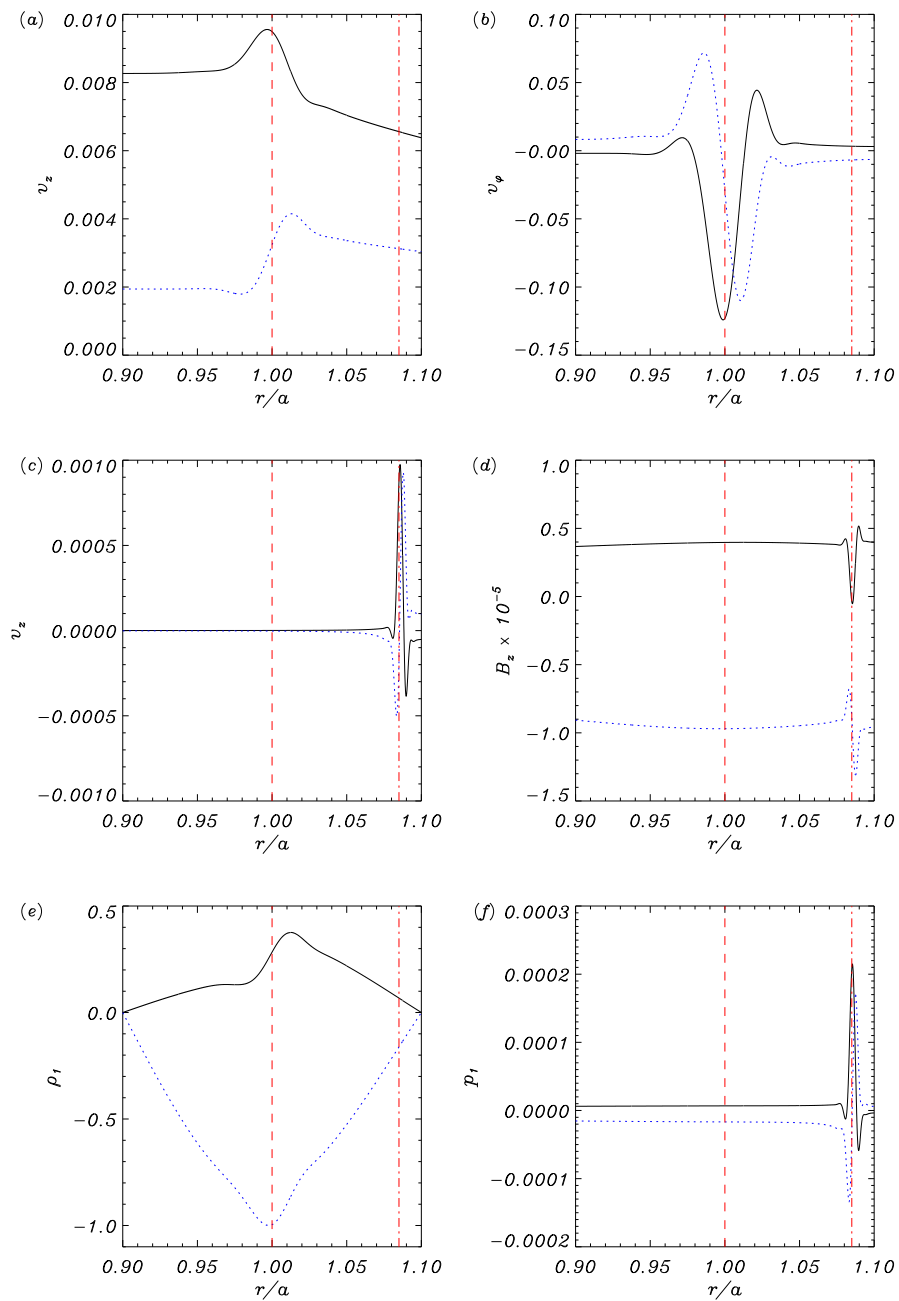


Figure 6.3: Same as Figure 6.2, but focusing on the inhomogeneous transitional layer (the brown region in Fig 6.2). The vertical dashed and dot-dashed lines correspond to the Alfvén and slow resonance positions given by Equations (6.5) and (6.6), respectively.

6.2. RESONANT ABSORPTION IN A PARTIALLY IONIZED THREAD

Alfvén resonance (symbols) in damping the kink mode. For the wavenumbers relevant to prominence oscillations, $10^{-3} < k_z a < 10^{-1}$, the value of τ_D/P related to the slow resonance is between 4 and 8 orders of magnitude larger than the ratio obtained by the Alfvén resonance. On the other hand, the complete numerical solution (solid line) is close to the result for the Alfvén resonance. In agreement with the result in the thin tube limit (Eq. [6.16]), we obtain $\tau_D/P \approx 3$ in the relevant range of $k_z a$. For larger $k_z a$, the value of τ_D/P increases and the efficiency of the Alfvén resonance as a damping mechanism decreases. For $k_z a \approx 10^2$ both the slow and the Alfvén resonances produce similar (and inefficient) damping times.

Figure 6.4b displays τ_D/P as a function of the transitional layer thickness, l/a , for $k_z a = 10^{-2}$. As stated by Arregui et al. (2008, see their Fig. 2d), the discrepancy between the numerical result and the TB approximation increases with l/a , the difference being around 20% for $l/a = 1$. However, for small, realistic values of l/a this discrepancy is less important and the TB approach is a very good approximation to the numerical result. We also see that the Alfvén resonance is always much more efficient than the slow resonance for all values of l/a .

The present result shows that, contrary to the Alfvén resonance, the slow resonance is very inefficient in damping the kink mode for typical prominence conditions. Although we have only presented the results for kink modes, this conclusion also holds for fluting modes ($m \geq 2$). The very inefficient kink mode damping due to the slow resonance is comparable to that due to non-adiabatic effects studied in Chapter 4. Therefore, we conclude that the effect of the slow resonance is not relevant to the damping of transverse thread oscillations, which is more likely governed by the Alfvén resonance.

6.2 Resonant absorption in a partially ionized filament thread

Resonant absorption seems to be the most likely explanation for the kink mode damping, since it is the only mechanism of all studied here that can produce the observed ratio of the damping time to the period. On the other hand, in Chapter 5 we saw that the effect of partial ionization could also be relevant, at least for short wavelengths and small ionization degrees. The aim of the present Section is to take both mechanisms into account and to assess their combined effect on the kink mode damping. We have found no similar work in the literature in which the phenomenon of resonant absorption is studied in a partially ionized plasma.

6.2.1 Equilibrium

We assume the same filament thread model as in Section 6.1, but since we already know that the slow resonance is irrelevant, we adopt the $\beta = 0$ approximation for the sake of simplicity. In addition, we consider here the prominence material to be partially ionized. Thus, the plasma properties are characterized by two quantities: the density, ρ_0 , and the ionization fraction, $\tilde{\mu}$, which gives us information about the plasma degree of ionization. The dependence of the density with the radial direction is again the sinusoidal profile given by Equation (6.1), where the internal and external densities take the same values. We also choose the same functional dependence for the ionization

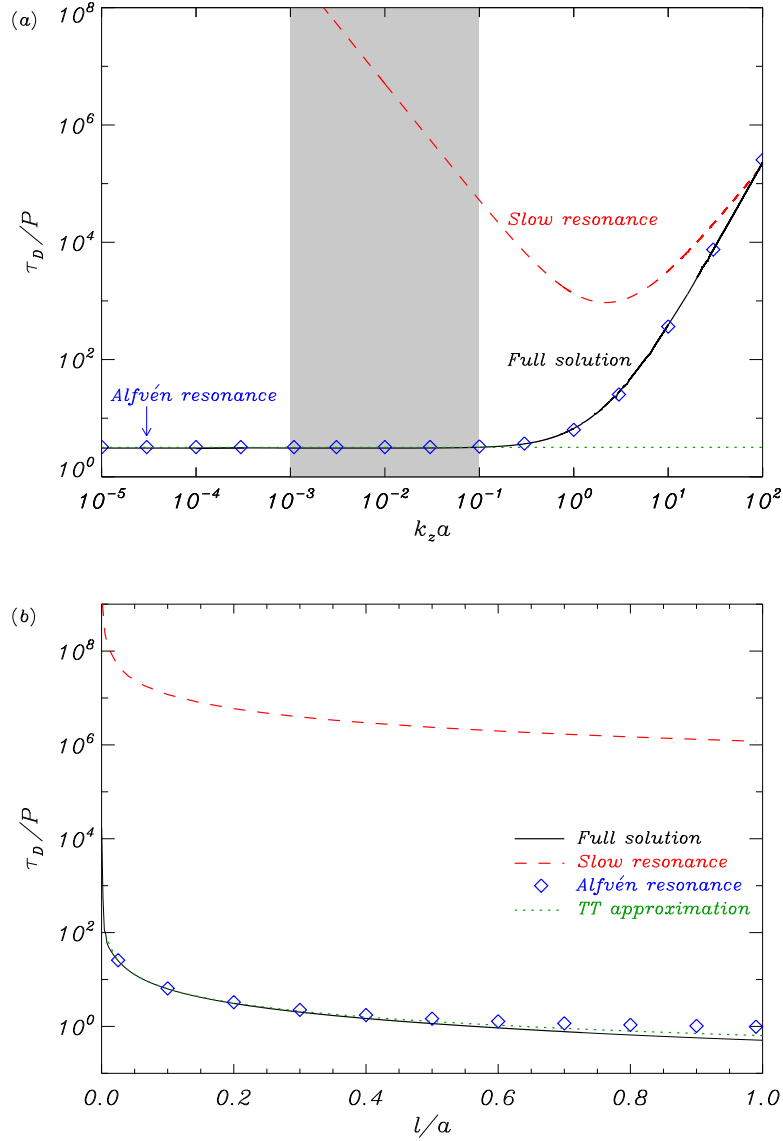


Figure 6.4: (a) τ_D/P of the kink mode as a function of $k_z a$ for $l/a = 0.2$. (b) τ_D/P of the kink mode as a function of l/a for $k_z a = 10^{-2}$. In both panels, the different line styles represent: the full numerical solution (solid), the solution exclusively due to the slow resonance in the TB approximation (dashed), and the solution exclusively due to the Alfvén resonance in the TB approximation (symbols). The dotted line is the approximation in the TT limit given by Equation (6.14).

6.2. RESONANT ABSORPTION IN A PARTIALLY IONIZED THREAD

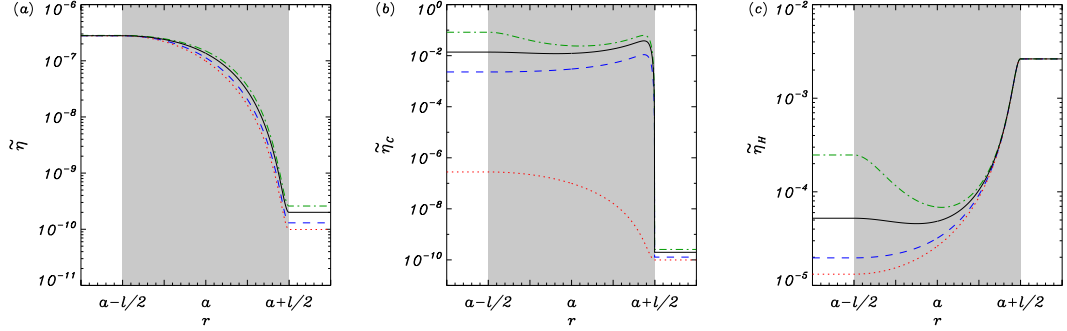


Figure 6.5: Radial profiles of (a) $\tilde{\eta}$, (b) $\tilde{\eta}_C$, and (c) $\tilde{\eta}_H$ considered in Section 6.2. The transitional layer (shaded zone) is enhanced in order to see the change from filament to coronal values. The line styles represent different ionization degrees: $\tilde{\mu}_f = 0.5$ (dotted line), $\tilde{\mu}_f = 0.6$ (dashed line), $\tilde{\mu}_f = 0.8$ (solid line), and $\tilde{\mu}_f = 0.95$ (dash-dotted line).

fraction profile,

$$\tilde{\mu}(r) = \begin{cases} \tilde{\mu}_f, & \text{if } r \leq a - l/2, \\ \tilde{\mu}_{\text{tr}}(r), & \text{if } a - l/2 < r < a + l/2, \\ \tilde{\mu}_c, & \text{if } r \geq a + l/2, \end{cases} \quad (6.26)$$

with

$$\tilde{\mu}_{\text{tr}}(r) = \frac{\tilde{\mu}_f}{2} \left\{ \left(1 + \frac{\tilde{\mu}_c}{\tilde{\mu}_f} \right) - \left(1 - \frac{\tilde{\mu}_c}{\tilde{\mu}_f} \right) \sin \left[\frac{\pi}{l} (r - a) \right] \right\}, \quad (6.27)$$

where the filament ionization fraction, $\tilde{\mu}_f$, is considered a free parameter and the corona is assumed to be fully ionized, so $\tilde{\mu}_c = 0.5$. Recent studies by Gouttebroze & Labrosse (2009) on radiative transfer in cylindrical threads suggest (see their Fig. 1b) an almost uniform ionization degree in the core of the thread surrounded by a transitional zone where the plasma ionization degree abruptly increases toward fully ionized coronal conditions. Our ionization fraction profile (Eqs. [6.26] and [6.27]) attempts to represent such a behavior.

We use the basic MHD equations for a partially ionized plasma in the one-fluid approach (Eqs. [2.82] and [2.86]). After considering linear perturbations and removing gas pressure terms by setting $\beta = 0$, the relevant equations for our investigation are the momentum equation and the induction equation, that contains the terms corresponding to Ohm's, ambipolar, and Hall's diffusion, namely

$$\begin{aligned} \frac{\partial \vec{B}_1}{\partial t} &= \nabla \times (\vec{v}_1 \times \vec{B}_0) - \nabla \times (\eta \nabla \times \vec{B}_1) - \nabla \times [\eta_H (\nabla \times \vec{B}_1) \times \vec{B}_0] \\ &+ \nabla \times \left\{ \frac{\eta_C - \eta}{B_0^2} [(\nabla \times \vec{B}_1) \times \vec{B}_0] \times \vec{B}_0 \right\}. \end{aligned} \quad (6.28)$$

Since η , η_C , and η_H are functions of the plasma physical conditions (Eq. [2.45]–[2.47]), their values in our equilibrium depend on the radial coordinate. Therefore, terms including radial derivatives of these quantities arise in Equation (6.28). Figure 6.5 displays the radial profiles of the dimensionless diffusivities $\tilde{\eta}$, $\tilde{\eta}_C$, and $\tilde{\eta}_H$ (Eq. [5.11]) according to the equilibrium properties. This Figure focuses on the transitional layer, where the

dimensionless coefficients vary by several orders of magnitude from internal to external values. In a homogeneous thread, i.e., for $l/a = 0$, Hall's diffusion is irrelevant in comparison with Ohm's and Cowling's diffusion (see Sec. 5.1.3). However, the small spatial scales that develop due to the Alfvén resonance might cause the dimensional analysis of Section 5.1.3 not to apply for the case $l/a \neq 0$. For this reason, we keep Hall's term in the following numerical computations.

6.2.2 Analytical expressions

As in Section 5.2.2, it is possible to give an analytical dispersion relation for the case $l/a = 0$ when the terms with η and η_H are dropped from the induction equation. This dispersion relation corresponds to Equation (5.40). Our aim is to extend this analytical investigation to the case $l/a \neq 0$. To do so, we use again the jump conditions for the radial displacement and the total pressure perturbation provided by Equation (6.7) in combination with the TB approach. An important result for the present investigation was obtained by Goossens et al. (1995), who proved that the jump conditions derived by Sakurai et al. (1991a) for Alfvén resonances in ideal MHD remain valid in dissipative MHD. This also allows us to apply the jump conditions derived by Sakurai et al. (1991a) to the present case. Hence, we arrive at the dispersion relation in the TB approximation, namely

$$\frac{n_c}{\rho_c (\omega^2 - k_z^2 \Gamma_{Ac}^2)} \frac{K'_m(n_c a)}{K_m(n_c a)} - \frac{m_f}{\rho_f (\omega^2 - k_z^2 \Gamma_{Af}^2)} \frac{J'_m(m_f a)}{J_m(m_f a)} = -i\pi \frac{m^2/r_A^2}{\omega_k^2 |\partial_r \rho_0|_{r_A}}, \quad (6.29)$$

with m_f and n_c defined in Equation (5.41), and Γ_A given by Equation (5.21).

As in the fully ionized case, we go further analytically and consider the TT approximation. We perform a first order, asymptotic expansion of the Bessel functions of Equation (6.29) for $k_z a \ll 1$. The dispersion relation becomes

$$\rho_f (\omega^2 - k_z^2 \Gamma_{Af}^2) + \rho_c (\omega^2 - k_z^2 \Gamma_{Ac}^2) - i\pi \left(\frac{m}{a}\right) \frac{\rho_f \rho_c}{|\partial_r \rho_0|_{r_A}} \frac{(\omega^2 - k_z^2 \Gamma_{Af}^2) (\omega^2 - k_z^2 \Gamma_{Ac}^2)}{\omega_k^2} = 0. \quad (6.30)$$

Now, we write the frequency as $\omega = \omega_k + i\omega_I$, and the modified Alfvén speed squared is approximated by $\Gamma_A^2 \approx v_A^2 - i\omega_k \eta_C$. We insert these expressions in Equation (6.30) and neglect terms with ω_I^2 and $\omega_I k_z^2$. It is straight-forward to obtain an expression for the ratio ω_I/ω_k , namely

$$\frac{\omega_I}{\omega_k} = -\frac{\pi}{2} \left(\frac{m}{a}\right) \frac{\rho_f \rho_c}{(\rho_f + \rho_c) |\partial_r \rho_0|_{r_A}} \left[\frac{1}{4} \frac{(\rho_f - \rho_c)^2}{\rho_f \rho_c} + \left(\frac{1}{v_{Af}^2} + \frac{1}{v_{Ac}^2}\right) \frac{\eta_{Cf} \eta_{Cc}}{2} k_z^2 \right] - \frac{1}{2} \frac{(\rho_f \eta_{Cf} + \rho_c \eta_{Cc}) k_z}{\sqrt{(\rho_f + \rho_c) (\rho_f v_{Af}^2 + \rho_c v_{Ac}^2)}}. \quad (6.31)$$

The first term on the right-hand side of Equation (6.31) owes its existence to the term in the dispersion relation related to the TB approximation and represents the contribution of resonant absorption. For long wavelengths, the factor $(1/v_{Af}^2 + 1/v_{Ac}^2) \eta_{Cf} \eta_{Cc} k_z^2 / 2$ can be neglected, so the term related to the resonant damping is independent of the value

6.2. RESONANT ABSORPTION IN A PARTIALLY IONIZED THREAD

of the Cowling's diffusivity and, therefore, of the ionization degree. Then, the term of Equation (6.31) due to the resonant damping takes the same form as in a fully ionized plasma. On the other hand, the second term in the right-hand side of Equation (6.31) is related to the damping by Cowling's diffusion and is also present in the case $l/a = 0$ (see Eq. [5.44]). This term is proportional to k_z , so we also expect it to be of a minor influence in the TT regime.

Next, we take into account that for the present density profile in the transitional layer and $k_z a \ll 1$, $r_A \approx a$ and $|\partial_r \rho_0|_{r_A} \approx \pi (\rho_f - \rho_c) / 2l$. We insert this last expression in Equation (6.31) and use it to give a relation for the ratio of the damping time to the period as

$$\frac{\tau_D}{P} = \mathcal{F} \left[m \left(\frac{l}{a} \right) \left(\frac{\rho_f - \rho_c}{\rho_f + \rho_c} \right) + \frac{2(\rho_f \tilde{\eta}_{Cf} + \rho_c \tilde{\eta}_{Cc}) k_z a}{\sqrt{2\rho_f(\rho_f + \rho_c)}} \right]^{-1}, \quad (6.32)$$

where $\mathcal{F} = 2/\pi$ and both Cowling's diffusivities are expressed in their dimensionless form. To perform a simple application, we compute τ_D/P from Equation (6.32) in the case $m = 1$, $k_z a = 10^{-2}$, and $l/a = 0.2$, resulting in $\tau_D/P \approx 3.18$ for a fully ionized thread ($\tilde{\mu}_f = 0.5$), and $\tau_D/P \approx 3.16$ for an almost neutral thread ($\tilde{\mu}_f = 0.95$). We note that the obtained damping times are consistent with the observations. Furthermore, the ratio τ_D/P depends only very slightly on the ionization degree, suggesting that resonant absorption dominates over Cowling's diffusion. To check this last statement, we compute the ratio of the two terms on the right-hand side of Equation (6.32), which allows us to compare the damping times exclusively due to resonant absorption, $(\tau_D)_{RA}$, and Cowling's diffusion, $(\tau_D)_C$. Thus,

$$\frac{(\tau_D)_{RA}}{(\tau_D)_C} = \sqrt{\frac{2(\rho_f + \rho_c)}{\rho_f}} \left(\frac{\rho_f \tilde{\eta}_{Cf} + \rho_c \tilde{\eta}_{Cc}}{\rho_f - \rho_c} \right) \frac{k_z a}{m(l/a)}. \quad (6.33)$$

This last expression can be further simplified by considering that in filament threads $\rho_f \gg \rho_c$ and $\tilde{\eta}_{Cf} \gg \tilde{\eta}_{Cc}$, so that

$$\frac{(\tau_D)_{RA}}{(\tau_D)_C} \approx \sqrt{2} \tilde{\eta}_{Cf} \frac{k_z a}{m(l/a)}. \quad (6.34)$$

We see that the efficiency of Cowling's diffusion with respect to that of resonant absorption increases with $k_z a$ and $\tilde{\mu}_f$ (through $\tilde{\eta}_{Cf}$). Considering the same parameters as before, one obtains $(\tau_D)_{RA} / (\tau_D)_C \approx 2 \times 10^{-8}$ for $\tilde{\mu}_f = 0.5$, and $(\tau_D)_{RA} / (\tau_D)_C \approx 6 \times 10^{-3}$ for $\tilde{\mu}_f = 0.95$, meaning that resonant absorption is much more efficient than Cowling's diffusion. It is also possible to give an estimation of the wavenumber for which Cowling's diffusion becomes more important than resonant absorption by setting $(\tau_D)_{RA} / (\tau_D)_C \approx 1$ in Equation (6.34). So, one gets

$$k_z a \approx \frac{m(l/a)}{\sqrt{2} \tilde{\eta}_{Cf}}. \quad (6.35)$$

Considering again the same parameters, Equation (6.35) gives $k_z a \approx 5 \times 10^5$ for $\tilde{\mu}_f = 0.5$, and $k_z a \approx 1.7$ for $\tilde{\mu}_f = 0.95$. Since Equation (6.34) is valid only for $k_z a \ll 1$, we expect resonant absorption to be the dominant damping mechanism in the TT regime even for an almost neutral filament plasma.

6.2.3 Numerical computations

The equations solved by PDE2D in the present partially ionized case are,

$$i\omega v_r = -\frac{v_A^2}{B_0} (ik_z B_r - B'_z), \quad (6.36)$$

$$i\omega v_\varphi = \frac{v_A^2}{B_0} \left(i\frac{m}{r} B_z - ik_z B_\varphi \right), \quad (6.37)$$

$$i\omega B_r = -B_0 ik_z v_r + \eta \left(i\frac{m}{r} B'_\varphi + i\frac{m}{r^2} B_\varphi + \frac{m^2}{r^2} B_r \right) \\ + \eta_C (ik_z B'_z + k_z^2 B_r) + \eta_H B_0 \left(k_z^2 B_\varphi - k_z \frac{m}{r} B_z \right), \quad (6.38)$$

$$i\omega B_\varphi = -B_0 ik_z v_\varphi - \eta \left(B''_\varphi + \frac{1}{r} B'_\varphi - \frac{1}{r^2} B_\varphi - i\frac{m}{r} B'_r + i\frac{m}{r^2} B_r \right) \\ - \eta' \left(B'_\varphi + \frac{1}{r} B_\varphi - i\frac{m}{r} B_r \right) - \eta_C \left(k_z \frac{m}{r} B_z - k_z^2 B_\varphi \right) \\ - \eta_H B_0 (k_z^2 B_r + ik_z B'_z), \quad (6.39)$$

$$i\omega B_z = B_0 \left(v'_r + \frac{1}{r} v_r + i\frac{m}{r} v_\varphi \right) \\ - \eta_C \left(B''_z + \frac{1}{r} B'_z - \frac{m^2}{r^2} B_z - ik_z B'_r - ik_z \frac{1}{r} B_r + k_z \frac{m}{r} B_\varphi \right) \\ + \eta'_C (ik_z B_r - B'_z) + \eta_H B_0 \left(ik_z B'_\varphi + ik_z \frac{1}{r} B_\varphi - ik_z \frac{m}{r} B_r \right) \\ + \eta'_H B_0 \left(ik_z B_\varphi - i\frac{m}{r} B_z \right), \quad (6.40)$$

and $v_z = 0$ since no longitudinal displacements are allowed for $\beta = 0$. The numerical procedure is identical to than in the fully ionized case (see Sec. 6.1.3). However, the values of the magnetic diffusivities are not imposed *ad-hoc* here but computed according to the equilibrium physical properties (see Fig. 6.5).

6.2.4 Results

First, we compare the kink mode τ_D/P in the presence of a transitional layer with the value previously obtained in Chapter 5 (Fig. 5.5) for a homogeneous thread. This is done in Figure 6.6a, where we plot the results corresponding to several values of the transitional layer width for a fixed $\tilde{\mu}_f$. Some relevant differences appear with respect to the case $l/a = 0$. First, we see that τ_D/P is dramatically reduced for intermediate values of $k_z a$, including the relevant range. In this region, the ratio τ_D/P becomes smaller as l/a is increased, a behavior consistent with damping by resonant absorption. We confirm this statement by looking at the eigenfunctions of perturbations, which show large-amplitude oscillations at the Alfvén resonance position. We do not include a plot of the eigenfunctions here since they are very similar to those displayed in Figures 6.2 and 6.3 for a fully ionized plasma. Therefore, the presence of diffusion terms due to partial ionization in the induction equation does not suppress the process of resonant absorption. We also see that the ratio τ_D/P for large $k_z a$ is independent of the transitional layer width and coincides with the solution in the absence of transitional layer. The cause

6.2. RESONANT ABSORPTION IN A PARTIALLY IONIZED THREAD

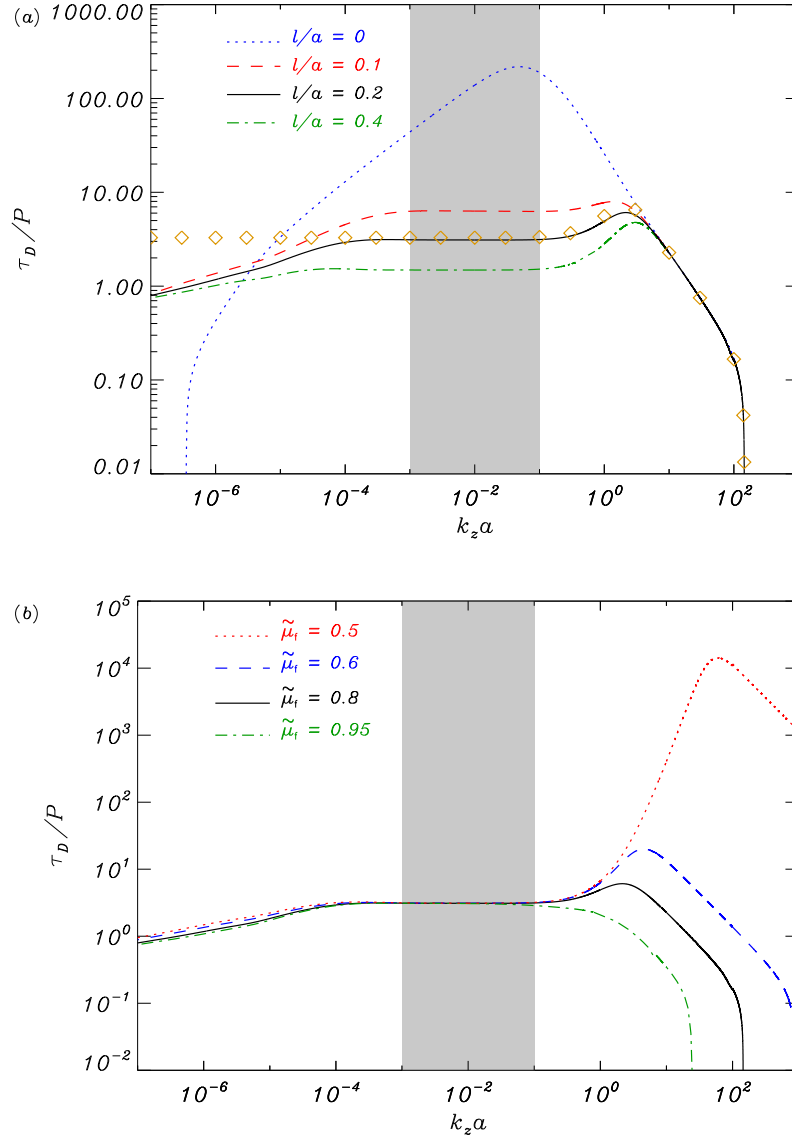


Figure 6.6: τ_D/P of the kink mode in a partially ionized thread as a function of $k_z a$. (a) Results with $\tilde{\mu}_f = 0.8$ for different values of l/a . Symbols are the solution in the TB approximation given by solving Equation (6.29) for $l/a = 0.2$. (b) Results for $l/a = 0.2$ and for different values of $\tilde{\mu}_f$. The different line styles are labeled within the Figure.

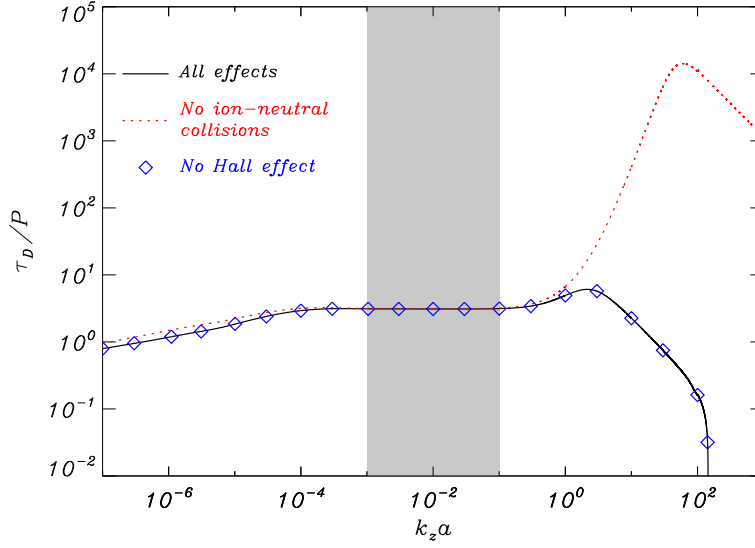


Figure 6.7: τ_D/P of the kink mode in a partially ionized thread as a function of $k_z a$ for $\tilde{\mu}_f = 0.8$ and $l/a = 0.2$. The different line styles represent: the full solution (solid), the solution in the absence of ion-neutral collisions (dotted), and the solution after neglecting Hall's diffusion (symbols).

of this behavior is that perturbations are essentially confined within the homogeneous part of the thread for large $k_z a$, and the kink mode is mainly governed by the internal physical conditions. On the other hand, the solution for very small $k_z a$ is completely different when $l/a \neq 0$. We note that the inclusion of the inhomogeneous transitional layer removes the smaller critical wavenumber, k_z^{c-} , and consequently the kink mode exists for very small values of $k_z a$ (see details regarding the critical wavenumber in Sec. 5.2.2).

Now, we study in Figure 6.6b the dependence of τ_D/P on the ionization degree for a fixed l/a . It turns out that the ionization degree is only relevant for large $k_z a$, for which the ratio τ_D/P significantly depends on $\tilde{\mu}_f$. Figure 6.7 allows us to shed light on this result. Here, we assess the ranges of $k_z a$ where Cowling's and Hall's diffusion dominate. As in the homogeneous thread case, we find that Hall's diffusion is irrelevant in the whole studied range of $k_z a$, while Cowling's diffusion, caused by the presence of neutrals, dominates the damping for large $k_z a$. In the whole range of relevant wavenumbers, resonant absorption is the most efficient damping mechanism, with the damping ratio independent of the ionization degree as predicted by Equation (6.32). On the contrary, we find that ohmic diffusion dominates for very small $k_z a$. It is important noting that although the kink mode is still resonantly coupled to Alfvén continuum modes for very small $k_z a$, the damping time related to Ohm's dissipation becomes smaller than that due to resonant absorption, meaning that the kink wave is mainly damped by ohmic diffusion for very small $k_z a$. Since η is almost independent of the ionization degree, the ratio τ_D/P in the region of very small $k_z a$ slightly depends on the value of $\tilde{\mu}_f$.

Finally, we compare the full numerical solution with that obtained by solving the analytical dispersion relation in the TB approximation (Eq. [6.29]). For the case $l/a =$

0.2, and $\tilde{\mu}_f = 0.8$, we plot by means of symbols in Figure 6.6a the result obtained from Equation (6.29). We can see a very good agreement between the approximation and the numerical result (solid line) for $k_z a \gtrsim 10^{-4}$, while both solutions do not agree for $k_z a \lesssim 10^{-4}$, which corresponds to the range of $k_z a$ for which Ohm's diffusion dominates. Equation (6.29) was derived by taking into account the effect of resonant absorption and Cowling's diffusion, but the influence of Ohm's diffusion on the damping was not included. For this reason, the approximate solution does not correctly describe the kink mode damping for very small $k_z a$, which corresponds to extremely long and unrealistic wavelengths, while it successfully agrees with the full numerical solution for realistic wavelengths and even larger values of $k_z a$.

6.3 Conclusions

In this Chapter, we have studied the role of resonant absorption for the damping of kink MHD modes in fully ionized and partially ionized filament threads. In the fully ionized case, we have investigated the resonant coupling of the kink mode to both Alfvén and slow continuum modes. The obtained damping times are consistent with those reported by the observations. In addition, we have found that, contrary to the Alfvén resonance, the slow resonance is very inefficient in damping the kink mode for typical prominence conditions. Hence, the obtained damping time in the case $\beta \neq 0$ is approximately the same obtained in pressure-less conditions (e.g., Ruderman & Roberts 2002; Goossens et al. 2002; Arregui et al. 2008) and the effect of the slow resonance is not relevant.

Subsequently, we have assessed the combined effect of both resonant absorption and partial ionization on the kink mode damping in a partially ionized filament thread. Focusing on the results within the observationally relevant range of $k_z a$, we have found that resonant absorption entirely dominates the kink mode damping, with τ_D/P in agreement with the value in the fully ionized case. None of the dissipative effects caused and/or enhanced by partial ionization (i.e., Ohm's, Cowling's, and Hall's diffusion) is of special relevance in the observationally important range of wavenumbers. The plasma partial ionization does not affect the mechanism of resonant absorption. The present results reinforce resonant absorption as probably the best candidate for the damping of filament thread transverse oscillations.

Damping of Kink Modes in a Longitudinally Inhomogeneous Prominence Fine Structure*

Early low-resolution observations (e.g., [Simon et al. 1986](#); [Demoulin et al. 1987](#); [Engvold et al. 1987](#)) and theoretical models (e.g., [Ballester & Priest 1989](#); [Schmieder 1992](#); [Rempel et al. 1999](#)), suggested that the dense and cool prominence plasma which forms the fine structure only occupies a part of a much larger magnetic flux tube, while the rest of the magnetic tube is filled with coronal plasma. This idea is also supported by more recent high-resolution observations (e.g., [Okamoto et al. 2007](#); [Lin et al. 2007](#), [2008](#)). In the previous Chapters of this Thesis, we have neglected the variation of the plasma physical conditions along the magnetic tube. This assumption was adopted in order to simplify matters, allowing us to work both analytically and numerically on the problem of the damping of the oscillations. Strictly speaking, this approximation is applicable to waves travelling along a thread and whose wavelength is short compared to the thread length. Here, our aim is to improve the model and to take into account the longitudinal inhomogeneity of the fine structure. Hence, we extend the studies of Chapter 6 about the damping of kink modes by resonant absorption and Cowling's diffusion in a longitudinally homogeneous magnetic tube to the case of a magnetic cylinder only partially filled with the prominence material. This configuration applies to standing waves in a prominence thread.

Section 7.1 contains a description of the model and the mathematical method. The dispersion relation of the transverse kink modes supported by the model is obtained in the thin tube case, and analytical approximations to the frequency and the damping ratio are obtained (Sec. 7.2). A parametric study of the solutions of the dispersion relation is investigated in Section 7.3, while the conclusions of this Chapter are given in Section 7.4.

7.1 Model and basic equations

7.1.1 Equilibrium configuration

The model is schematically plotted in Figure 7.1. We consider a straight and cylindrical flux tube of length L and radius a , whose ends are fixed at two rigid walls representing the solar photosphere. The magnetic tube is only partially filled with the cool and dense prominence material. The magnetic tube is composed of a central and dense region of

*This Chapter is based on the results of R. Soler, R. Oliver, & J. L. Ballester 2010, in preparation

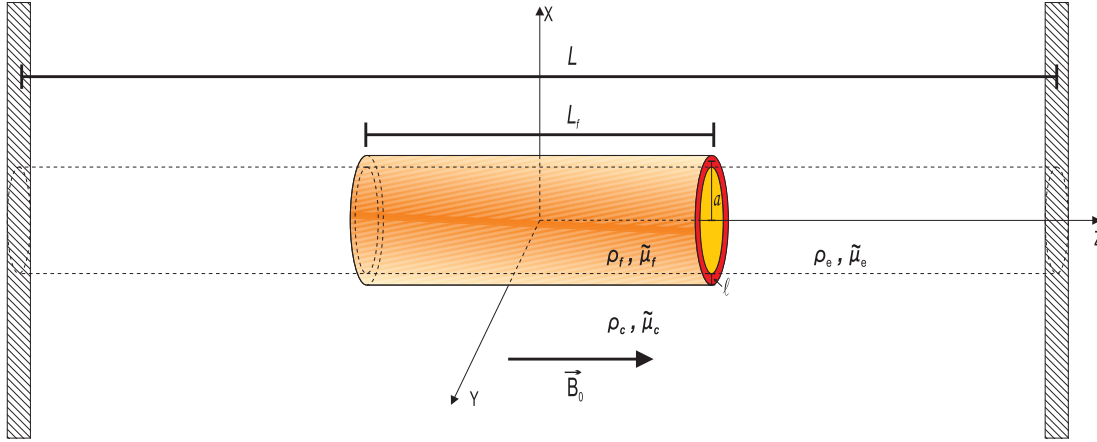


Figure 7.1: Sketch of the filament thread model considered in this Chapter.

length L_f with prominence-like conditions and representing the prominence fibril, surrounded by two much less dense zones representing the evacuated part of the flux tube. For simplicity, both the dense and the evacuated (i.e., coronal) part are taken homogeneous, with uniform densities ρ_f and ρ_e , respectively. The external, coronal medium has density ρ_c , which is also homogeneous. Subscripts f, e, and c denote the dense (fibril) part, the evacuated region, and the corona, respectively. We assume that the evacuated part of the tube has a density similar to the coronal one, so $\rho_e/\rho_c \approx 1$. On the contrary, the density contrast in the dense part is $\rho_f/\rho_c = 200$. In the dense region, we include a transversely inhomogeneous transitional layer of thickness l , that continuously connects the internal region to the external region. A sinusoidal variation of the density is considered in the transitional layer (Eq. [6.1]). For our subsequent analysis, we assume that this transitional layer is thin in comparison to the tube radius, so that the ratio l/a is small. Finally, the magnetic field is taken homogeneous and orientated along the z -direction, namely $\vec{B}_0 = B_0 \hat{e}_z$, with $B_0 = 5$ G everywhere. Thus, for $L_f = L$, i.e, a fully filled tube, the model reduces to the configuration studied in Chapter 6.

The dense plasma is assumed partially ionized with an arbitrary ionization degree $\tilde{\mu}_f$. Both the evacuated part and the corona are taken fully ionized, thus $\tilde{\mu}_e = \tilde{\mu}_c = 0.5$. We consider the effect of Cowling's diffusion in the generalized induction equation (Eq. [5.2]). Provided that ρ_f , ρ_e , and ρ_c are constants, the corresponding Cowling's diffusivities, namely η_{Cf} , η_{Ce} , and η_{Cc} , respectively, are also constants. Since both the corona and the evacuated region are fully ionized and much less dense than the filament plasma, we have $\eta_{Cc} \ll \eta_{Cf}$ and $\eta_{Ce} \ll \eta_{Cf}$. For the sake of simplicity, we set $\eta_{Ce} = \eta_{Cc} = 0$, and the effect of Cowling's diffusion is only considered in the dense and partially ionized part of the thread. If Cowling's diffusion were considered in the evacuated and coronal regions, it would have a very minor influence since Cowling's diffusivities in these regions are much smaller than that in the dense part of the flux tube.

7.1.2 Mathematical method

The general investigation of the ideal MHD transverse oscillations supported by our equilibrium in the case $l/a = 0$ and for $\beta = 0$ was performed by Díaz et al. (2002). These

authors obtained the oscillatory frequencies and eigenfunctions for arbitrary values of L , L_f , and a . Here, we could follow a treatment similar to that of [Díaz et al. \(2002\)](#), but this requires a significant mathematical effort that is beyond the purpose of the present Chapter. Instead, we consider the much simpler approach introduced by [Dymova & Ruderman \(2005\)](#), who studied the same configuration but in the thin tube limit, i.e., for $a/L \ll 1$ and $a/L_f \ll 1$. Note that these two conditions are equivalent to requesting the tube radius being much smaller than both the total tube length and the fibril length. The typical observed transverse width of filament threads is around 100 km, whereas their length is between one and two orders of magnitude larger (see, e.g., [Lin 2004](#)). So, the condition $a/L_f \ll 1$ is easily satisfied. In addition, $L > L_f$ and so the condition $a/L \ll 1$ is also satisfied in prominence fine structures. One can relate L to the typical spatial scale in prominences and filaments, i.e., $L \sim 100,000$ km (see details in [Table 1.2](#)).

Assuming the $\beta = 0$ approximation and a time dependence of the form $\exp(-i\omega t)$, we can define a modified Alfvén speed squared as $\Gamma_A^2 = v_A^2 - i\omega\eta_C$, which contains the effect of Cowling’s diffusion (see details in [Sec. 5.2.1](#)). Thus, the relevant equations for our investigation are

$$\rho_0 \frac{\partial \vec{v}_1}{\partial t} = \frac{1}{\mu} (\nabla \times \vec{B}_1) \times \vec{B}_0, \quad (7.1)$$

$$\frac{\partial \vec{B}_1}{\partial t} = \frac{\Gamma_A^2}{v_A^2} \nabla \times (\vec{v}_1 \times \vec{B}_0). \quad (7.2)$$

Equations (7.1) and (7.2) can be combined to arrive at the following equation for the total pressure perturbation, p_T ,

$$\frac{\partial^2 p_T}{\partial t^2} - \Gamma_A^2 \nabla^2 p_T = 0, \quad (7.3)$$

along with an equation relating the total pressure and radial velocity perturbations as

$$\frac{\partial^2 v_r}{\partial t^2} - \Gamma_A^2 \frac{\partial^2 v_r}{\partial z^2} = -\frac{1}{\rho_0} \frac{\partial^2 p_T}{\partial t \partial r}. \quad (7.4)$$

Now, we write all perturbations proportional to $\exp(-i\omega t + m\varphi)$, and Equation (7.3) becomes

$$\frac{\partial^2 p_T}{\partial z^2} + \frac{1}{r} \frac{\partial}{\partial r} \left(r \frac{\partial p_T}{\partial r} \right) + \left(\frac{\omega^2}{\Gamma_A^2} - \frac{m^2}{r^2} \right) p_T = 0. \quad (7.5)$$

Following [Dymova & Ruderman \(2005\)](#), we can perform a different scaling of Equation (7.5) inside the tube and in the corona. For perturbations inside the tube, the characteristic scale in the r -direction is a , while the characteristic scale in the z -direction is L . Since $a/L \ll 1$, the term with the longitudinal derivative and the term proportional to ω^2 are much smaller than the other terms. In such a case, Equation (7.5) inside the tube reduces to

$$\frac{\partial}{\partial r} \left(r \frac{\partial p_{Ti}}{\partial r} \right) - \frac{m^2}{r^2} p_{Ti} \approx 0, \quad (7.6)$$

with $i = f$ or e . The solution of Equation (7.6) for regular perturbations at $r = 0$ is

$$p_{Ti} \approx A_i(z) \left(\frac{r}{a} \right)^m, \quad (7.7)$$

CHAPTER 7. KINK MODES IN AN INHOMOGENEOUS FINE STRUCTURE

where $A_i(z)$ is an arbitrary function of z .

On the other hand, the characteristic scale of perturbations outside the tube, i.e., in the corona, is L in both the r - and z -directions, so that no terms can be neglected in Equation (7.5). However, we can express the total pressure perturbation in the corona as $p_{\text{Tc}} = A_c(z)F(r)$ and use the technique of separation of variables to obtain the following expressions

$$\frac{d^2 F}{dr^2} + \frac{1}{r} \frac{dF}{dr} - \left(k_n^2 + \frac{m^2}{r^2} \right) F = 0, \quad (7.8)$$

and

$$\frac{d^2 A_c}{dz^2} + \frac{\omega^2}{v_{\text{Ac}}^2} A_c = -k_n^2 A_c, \quad \text{with } A_c = 0 \quad \text{at } z = \pm L/2, \quad (7.9)$$

where k_n is a separation constant, with n accounting for the different radial harmonics. In Equation (7.9) we have taken into account that the Cowling's diffusivity is neglected in the corona, so $\Gamma_{\text{Ac}}^2 = v_{\text{Ac}}^2$. Equation (7.8) is the modified Bessel Equation. Here, we only consider trapped modes and assume $k_n^2 > 0$ ¹. Then, the solution of Equation (7.8) is $F(r) = K_m(k_n r)$, whose asymptotic expansion near the tube boundary allows us to express the total pressure perturbation in the corona as

$$p_{\text{Tc}} \approx A_c(z) \left(\frac{a}{r} \right)^m. \quad (7.10)$$

Boundary conditions

Let us consider now appropriate boundary conditions at the cylinder edge, i.e., $r = a$. In the evacuated part of the tube, we assume $\rho_e = \rho_c$ and so we do not take the transitional layer into account. Hence, the boundary conditions are those given by [Dymova & Ruderman \(2005\)](#) in their Equation (4), namely

$$[[p_{\text{T}}]] = 0, \quad [[v_r]] = 0, \quad \text{at } r = a \quad \text{for } |z| > L_f/2, \quad (7.11)$$

where $[[X]]$ stands for the jump of the quantity X .

On the other hand, in the dense part of the tube we consider the effect of resonant absorption in the transitional layer. We follow the treatment by [Andries et al. \(2005\)](#), who generalize the concept of the jump conditions at the resonance position of [Sakurai et al. \(1991a\)](#) to the case of a longitudinally inhomogeneous tube. [Andries et al. \(2005\)](#) combined the jump conditions with the thin boundary approximation to obtain analytical expressions of the dispersion relation and the frequency for longitudinally stratified tubes. The accuracy of this analytical method was numerically verified by [Arregui et al. \(2005\)](#), who found a good agreement between the expressions of [Andries et al. \(2005\)](#) and their numerical computations. In the thin tube approximation, [Dymova & Ruderman \(2006\)](#) provide equivalent expressions for the jump conditions that can be applied to our perturbations. In our notation, the jump conditions for the total pressure and the radial velocity perturbations provided by [Dymova & Ruderman \(2006\)](#) are

$$[[p_{\text{T}}]] = 0, \quad [[v_r]] = -\pi\omega_{\text{R}} \frac{m^2/a^2}{|\rho_0 \Delta_n|_{r_{\text{A}}}} p_{\text{T}}, \quad \text{at } r = r_{\text{A}} \quad \text{for } |z| < L_f/2, \quad (7.12)$$

¹This condition may not be satisfied for high harmonics but we need not worry about this issue since here we focus our investigation on the fundamental mode, which is non-leaky in the present configuration.

with $\Delta_n = \frac{d}{dr} (\omega_R^2 - \lambda_n^2)$, where λ_n^2 are the eigenvalues of the Sturm-Liouville problem

$$v_A^2(r) \frac{d^2 G}{dz^2} = -\lambda_n^2(r) G, \quad (7.13)$$

with appropriate boundary conditions for G at $z = \pm L_f/2$. Equation (7.13) describes the spectrum of Alfvén modes, with $\lambda_n(r)$ the corresponding frequencies of the Alfvén continuum. In general, it is not straight-forward to deduce these boundary conditions because they are given by the continuity of G at $z = \pm L_f/2$, hence the value of G at $z = \pm L_f/2$ is also determined by the properties of the evacuated region. In a longitudinally homogeneous tube, i.e., for $L_f = L$ and with the Alfvén speed depending on the radial direction only, we simply have that the boundary conditions are $G(\pm L/2) = 0$ and obtain $\lambda_n(r) \equiv \omega_A(r) = \frac{n\pi}{L} v_A(r)$. In such a case, the jump conditions of Equation (7.12) reduce to those provided by Sakurai et al. (1991a).

For our subsequent analysis, we do not need the precise value of $\lambda_n(r)$ but only its functional dependence on the radial direction. For the given sinusoidal density profile, we can express the Alfvén speed squared in the transitional layer as $v_A^2(r) = v_{Af}^2/f(r)$, with

$$f(r) = \frac{1}{2} \left\{ \left(1 + \frac{\rho_c}{\rho_f} \right) - \left(1 - \frac{\rho_c}{\rho_f} \right) \sin \left[\frac{\pi}{l} (r - a) \right] \right\}. \quad (7.14)$$

Hence, Equation (7.13) is rewritten as

$$v_{Af}^2 \frac{d^2 G}{dz^2} = -\lambda_n^2(r) f(r) G. \quad (7.15)$$

With no loss of generality, we can assume that G is only a function of z , i.e., the different magnetic surfaces are not coupled to each other. So, according to Equation (7.15), the quantity $\lambda_n^2(r) f(r)$ corresponds to the Alfvén eigenvalue squared in the dense part of the tube. Since the dense region is homogeneous, its corresponding Alfvén eigenvalue does not depend on r , meaning that the radial contributions of $\lambda_n^2(r)$ and $f(r)$ cancel. Thus, we define $\lambda_{fn}^2 \equiv \lambda_n^2(r) f(r)$, with λ_{fn} a constant corresponding to the Alfvén eigenvalue in the homogeneous dense part of the tube. Therefore, we have

$$\lambda_n^2(r) = \frac{\lambda_{fn}^2}{f(r)}, \quad (7.16)$$

where the radial dependence of $\lambda_n^2(r)$ comes from the function $f(r)$. With the help of Equation (7.16), we obtain that $\Delta_n = \lambda_n^2(r) f'(r)/f(r)$, where the prime denotes a radial derivative. Finally, the factor $|\rho_0 \Delta_n|_{r_A}$ in the jump condition for the radial velocity perturbation (Eq. [7.12]) is

$$|\rho_0 \Delta_n|_{r_A} = \omega_R^2 |\partial_r \rho_0|_{r_A}, \quad (7.17)$$

where we have used the resonant condition, namely $\lambda_n^2(r_A) = \omega_R^2$. Note that we still need the value of r_A , which could be computed from the resonant condition if the eigenvalues $\lambda_n^2(r)$ were *a priori* known. A reasonable assumption in the TT limit is to consider $r_A \approx a$, so that $|\partial_r \rho_0|_{r_A} \approx \pi(\rho_f - \rho_c)/2l$ for our sinusoidal profile.

CHAPTER 7. KINK MODES IN AN INHOMOGENEOUS FINE STRUCTURE

Solution in the evacuated region

Let us consider first the boundary conditions for the evacuated part (Eq. [7.11]). The analysis here is identical to that of [Dymova & Ruderman \(2005\)](#). For the condition on the total pressure perturbation, we obtain $A_e(z) = A_c(z) = A(z)$. Next, we rewrite Equation (7.4) as

$$v_A^2 \frac{\partial^2 v_r}{\partial z^2} + \omega^2 v_r = -\frac{i\omega}{\rho_0} \frac{\partial p_T}{\partial r}. \quad (7.18)$$

We evaluate Equation (7.18) for $r \approx a$ on both sides of the tube boundary. Thus, in the evacuated part,

$$v_{Ae}^2 \frac{\partial^2 v_{re}}{\partial z^2} + \omega^2 v_{re} = -\frac{i\omega}{\rho_e} \frac{m}{a} A(z), \quad \text{for } r \lesssim a, \quad (7.19)$$

whereas in the corona,

$$v_{Ac}^2 \frac{\partial^2 v_{rc}}{\partial z^2} + \omega^2 v_{rc} = \frac{i\omega}{\rho_c} \frac{m}{a} A(z), \quad \text{for } r \gtrsim a. \quad (7.20)$$

According to the boundary condition for v_r given by Equation (7.11), $v_{re} = v_{rc}$. Thus, we combine Equations (7.19) and (7.20) to find the following two expressions

$$\frac{\partial^2 v_r}{\partial z^2} = i\omega \frac{m}{a} \frac{\mu}{B_0^2} \frac{\rho_e - \rho_c}{\rho_e + \rho_c} A(z), \quad (7.21)$$

$$v_r = -i \frac{m}{a} \frac{1}{\omega} \frac{2}{\rho_e - \rho_c} A(z), \quad (7.22)$$

where we have considered that the magnetic field is homogeneous. Now, we differentiate Equation (7.22) with respect to z twice and compare the resulting expression with Equation (7.21). We obtain

$$\frac{d^2 A(z)}{dz^2} + \frac{\omega^2}{c_{ke}^2} A(z) = 0, \quad (7.23)$$

with

$$c_{ke}^2 \equiv \frac{2B_0^2}{\mu(\rho_e + \rho_c)} = \frac{\rho_e v_{Ae}^2 + \rho_c v_{Ac}^2}{\rho_e + \rho_c}. \quad (7.24)$$

The quantity c_{ke} corresponds to the kink speed in the evacuated region.

To solve Equation (7.23), we consider the line-tying condition at the photosphere, i.e., $A(\pm L/2) = 0$. Therefore, the solution in the two evacuated zones is

$$A(z) = \begin{cases} C_1 \sin \left[\frac{\omega}{c_{ke}} (z - L/2) \right], & \text{for } z > L_f/2, \\ C_2 \sin \left[\frac{\omega}{c_{ke}} (z + L/2) \right], & \text{for } z < -L_f/2, \end{cases} \quad (7.25)$$

where C_1 and C_2 are constants.

Solution in the dense region

In the dense region, we adopt the thin boundary approach and use the jump conditions given by Equation (7.12) as our boundary conditions. Again, the condition over the total pressure perturbation gives $A_f(z) = A_c(z) = A(z)$. Near the boundary we express $v_{rc} = v_{rf} + \delta v_r$, where δv_r is the jump of the radial velocity perturbation provided by Equation (7.12), namely

$$\delta v_r = -\pi \omega_R \frac{m^2/a^2}{|\rho_0 \Delta_n|_{r_A}} p_T = -\pi \frac{m^2/a^2}{\omega_R |\partial_r \rho_0|_{r_A}} p_T. \quad (7.26)$$

As before, we evaluate Equation (7.4) on both sides of the tube boundary and, after some algebra, we arrive at the following expressions

$$\begin{aligned} \frac{\partial^2 v_{rf}}{\partial z^2} &= \frac{m}{a} \frac{i\omega}{v_{Ac}^2 - \Gamma_{Af}^2} \frac{\rho_f + \rho_c}{\rho_f \rho_c} A(z) \\ &+ \frac{m^2/a^2}{\omega_R |\partial_r \rho_0|_{r_A}} \frac{\pi}{v_{Ac}^2 - \Gamma_{Af}^2} \left[v_{Ac}^2 \frac{d^2 A(z)}{dz^2} + \omega^2 A(z) \right], \end{aligned} \quad (7.27)$$

$$\begin{aligned} v_{rf} &= -\frac{m}{a} \frac{i}{\omega} \frac{\rho_f \Gamma_{Af}^2 + \rho_c v_{Ac}^2}{\rho_f \rho_c (v_{Ac}^2 - \Gamma_{Af}^2)} A(z) \\ &- \frac{\pi}{\omega^2} \frac{\Gamma_{Af}^2}{v_{Ac}^2 - \Gamma_{Af}^2} \frac{m^2/a^2}{\omega_R |\partial_r \rho_0|_{r_A}} \left[v_{Ac}^2 \frac{d^2 A(z)}{dz^2} + \omega^2 A(z) \right]. \end{aligned} \quad (7.28)$$

Now, we differentiate Equation (7.28) with respect to z twice and compare the resulting expression with Equation (7.27), obtaining

$$\begin{aligned} \frac{d^4 A(z)}{dz^4} &+ \left[\omega^2 \left(\frac{\Gamma_{Af}^2 + v_{Ac}^2}{\Gamma_{Af}^2 v_{Ac}^2} \right) + \frac{i\omega \omega_R |\partial_r \rho_0|_{r_A}}{\pi} \frac{(\rho_f \Gamma_{Af}^2 + \rho_c v_{Ac}^2)}{m/a} \frac{(\rho_f \rho_c \Gamma_{Af}^2 v_{Ac}^2)}{\Gamma_{Af}^2 v_{Ac}^2} \right] \frac{d^2 A(z)}{dz^2} \\ &+ \omega^2 \left[\frac{\omega^2}{\Gamma_{Af}^2 v_{Ac}^2} + \frac{i\omega \omega_R |\partial_r \rho_0|_{r_A}}{\pi} \frac{(\rho_f + \rho_c)}{m/a} \frac{(\rho_f \rho_c \Gamma_{Af}^2 v_{Ac}^2)}{\Gamma_{Af}^2 v_{Ac}^2} \right] A(z) = 0. \end{aligned} \quad (7.29)$$

The general Equation (65) of [Dymova & Ruderman \(2006\)](#) and our Equation (7.29) are equivalent if a constant piecewise density is assumed in the former and Cowling's diffusion is omitted in the latter. Equation (7.29) can be solved by taking a solution of the form $\exp(ik_z z)$ and obtaining the subsequent forth-order polynomial for k_z . Two independent values of k_z are possible, namely k_{z1} and k_{z2} . Thus, the solution of Equation (7.29) is

$$A(z) = D_1 \exp(ik_{z1}z) + D_2 \exp(-ik_{z1}z) + D_3 \exp(ik_{z2}z) + D_4 \exp(-ik_{z2}z), \quad (7.30)$$

with D_1 , D_2 , D_3 , and D_4 constants that are determined by the boundary conditions at $z = \pm L_f/2$. However, to keep this general analysis implies that the following expressions are complicated and require an additional mathematical effort, which is beyond the purpose of the present Chapter. Instead, we choose a more restrictive way to simplify matters.

For our next analysis, Equation (7.29) is rewritten in a convenient form as

$$\frac{b^2}{\omega^2} \frac{d^4 A(z)}{dz^4} + \frac{d^2 A(z)}{dz^2} + \frac{\omega^2}{\tilde{c}_{kf}^2} A(z) = 0, \quad (7.31)$$

CHAPTER 7. KINK MODES IN AN INHOMOGENEOUS FINE STRUCTURE

where \tilde{c}_{kf}^2 and b^2 are defined as

$$\tilde{c}_{kf}^2 = \frac{\frac{\rho_f \Gamma_{Af}^2 + \rho_c v_{Ac}^2}{\rho_f + \rho_c} - i\pi\omega (\Gamma_{Af}^2 + v_{Ac}^2) \left(\frac{\rho_f \rho_c}{\rho_f + \rho_c} \right) \frac{m/a}{\omega_R |\partial_r \rho_0|_{r_A}}}{1 - i\pi\omega \left(\frac{\rho_f \rho_c}{\rho_f + \rho_c} \right) \frac{m/a}{\omega_R |\partial_r \rho_0|_{r_A}}}, \quad (7.32)$$

$$b^2 = -\frac{i\omega\pi\Gamma_{Af}^2 v_{Ac}^2 \left(\frac{\rho_f \rho_c}{\rho_f + \rho_c} \right) \frac{m/a}{\omega_R |\partial_r \rho_0|_{r_A}}}{\frac{\rho_f \Gamma_{Af}^2 + \rho_c v_{Ac}^2}{\rho_f + \rho_c} - i\pi\omega (\Gamma_{Af}^2 + v_{Ac}^2) \left(\frac{\rho_f \rho_c}{\rho_f + \rho_c} \right) \frac{m/a}{\omega_R |\partial_r \rho_0|_{r_A}}}. \quad (7.33)$$

Our definition of the modified kink speed, \tilde{c}_{kf} , takes into account both the effect of Cowling's diffusion (through Γ_{Af}^2) and the effect of resonant absorption. If the terms related to resonant absorption are omitted, one has $b^2 = 0$ and \tilde{c}_{kf}^2 becomes

$$\tilde{c}_{kf}^2 = \frac{\rho_f \Gamma_{Af}^2 + \rho_c v_{Ac}^2}{\rho_f + \rho_c}, \quad (7.34)$$

which reduces to the ideal kink speed when Cowling's diffusion is neglected, i.e., $\Gamma_{Af}^2 = v_{Af}^2$.

In the case of the fundamental mode, one could assume that, when the terms related to Cowling's diffusion and resonant absorption are present, the characteristic scale for the variations of the eigenfunctions in the z -direction is only slightly modified with respect to the ideal case without transitional layer. Therefore, a reasonable approximation is to relate the forth-order derivative of $A(z)$ in Equation (7.31) with the second-order derivative as follows

$$\frac{d^4 A(z)}{dz^4} \sim -\mathcal{K}^2 \frac{d^2 A(z)}{dz^2}, \quad (7.35)$$

where the quantity \mathcal{K} plays the role of the longitudinal wavenumber. We can approximate \mathcal{K} by its expression in the ideal case, namely

$$\mathcal{K}^2 \approx \frac{\omega^2}{c_{kf}^2}, \quad (7.36)$$

with c_{kf}^2 the ideal kink speed. Hence, Equation (7.31) becomes

$$\frac{d^2 A(z)}{dz^2} + \frac{\omega^2}{\tilde{c}_{kf}^2 \left(1 - \frac{b^2}{c_{kf}^2} \right)} A(z) \approx 0, \quad (7.37)$$

which is formally identical to Equation (7.23). It is important recalling that the approximation of the forth-order z -derivative of $A(z)$ may introduce some uncertainty in the solutions of Equation (7.37) in comparison with the solutions of the full Equation (7.29). However, we expect a minor discrepancy in the case of the fundamental mode because its characteristic scale in the z -direction should not be essentially modified when the terms related to Cowling's diffusion and resonant absorption are taken into account in the equations.

7.2. DISPERSION RELATION AND ANALYTICAL APPROXIMATIONS

The solutions of Equation (7.37) can be separated according to their symmetry about $z = 0$. Thus,

$$A(z) = \begin{cases} E_1 \cos\left(\frac{\omega}{\tilde{c}_{kf}\sqrt{1-\frac{b^2}{c_{kf}^2}}}z\right), & \text{for even modes,} \\ E_2 \sin\left(\frac{\omega}{\tilde{c}_{kf}\sqrt{1-\frac{b^2}{c_{kf}^2}}}z\right), & \text{for odd modes,} \end{cases} \quad \text{if } |z| \leq L_f/2, \quad (7.38)$$

with E_1 and E_2 constants.

7.2 Dispersion relation and analytical approximations

Here, we seek a dispersion relation for the fundamental kink mode. This solution corresponds to the even mode with the lowest frequency. In order to match the solution in the dense part (Eq. [7.38]) with that in the evacuated regions (Eq. [7.25]), we impose the boundary conditions

$$[[A]] = 0, \quad \left[\left[\frac{dA}{dz} \right] \right] = 0, \quad \text{at } z = \pm L_f/2, \quad (7.39)$$

corresponding to a contact discontinuity (Goedbloed & Poedts 2004). We finally arrive at the dispersion relation, namely

$$\frac{1}{\tilde{c}_{kf}\sqrt{1-\frac{b^2}{c_{kf}^2}}} \tan\left(\frac{\omega}{\tilde{c}_{kf}\sqrt{1-\frac{b^2}{c_{kf}^2}}} \frac{L_f}{2}\right) - \frac{1}{c_{ke}} \cot\left[\frac{\omega}{c_{ke}} \left(\frac{L-L_f}{2}\right)\right] = 0. \quad (7.40)$$

The fundamental kink mode is given by the first root of Equation (7.40). A first-order Taylor expansion of Equation (7.40) provides us with an approximation to the frequency as

$$\omega^2 \approx \frac{4}{(L-L_f)L_f} \tilde{c}_{kf}^2 \left(1 - \frac{b^2}{c_{kf}^2}\right). \quad (7.41)$$

We can extract two main results from Equation (7.41). First of all, Equation (7.41) only depends on the physical properties of the dense region and the corona through \tilde{c}_{kf} , c_{kf} , and b , and includes no contributions from the evacuated part. And second, the form of Equation (7.41) is similar to the approximation of the kink mode frequency in a homogeneous tube, i.e., $\omega^2 \approx k_z^2 c_{kf}^2$, where k_z is the longitudinal wavenumber. Thus, it seems that the main differences between the expression for the homogeneous tube and that for the partially filled tube are that $4/(L-L_f)L_f$ replaces k_z^2 , and that a redefined kink speed has to be taken into account. This suggests that a similar replacement could be performed in the equations deduced throughout this Thesis to adapt them to the case of a partially filled thread. This approximation of the frequency is similar to that obtained by Joarder & Roberts (1992b) for the *string modes* of their slab configuration. Note that Equation (7.41) fails to represent the kink mode frequency in the limits $L_f/L \approx 1$ and $L_f/L \approx 0$, so one should consider intermediate values of L_f/L

in Equation (7.41). The correct expressions for the fundamental kink mode frequency in these limits are

$$\omega = \frac{\pi}{L} \tilde{c}_{kf} \sqrt{1 - \frac{b^2}{c_{kf}^2}}, \quad \text{for} \quad L_f/L = 1, \quad (7.42)$$

and

$$\omega = \frac{\pi}{L} c_{ke}, \quad \text{for} \quad L_f/L = 0. \quad (7.43)$$

7.2.1 Damping by Cowling's diffusion

Let us consider the case without transverse transitional layer, i.e., $l/a = 0$. Then, \tilde{c}_{kf} is given by Equation (7.34) and $b^2 = 0$ since there is no jump of the radial velocity. Equation (7.41) allows us to obtain the real and imaginary parts of the frequency as

$$\begin{aligned} \omega &= \pm \left[\frac{\rho_f v_{Af}^2 + \rho_c v_{Ac}^2}{\rho_f + \rho_c} - \left(\frac{\rho_f \eta_{Cf}}{\rho_f + \rho_c} \right)^2 \frac{1}{(L - L_f) L_f} \right]^{1/2} \frac{2}{\sqrt{(L - L_f) L_f}} \\ &\quad - i \left(\frac{\rho_f \eta_{Cf}}{\rho_f + \rho_c} \right) \frac{2}{(L - L_f) L_f}. \end{aligned} \quad (7.44)$$

This last expression is formally identical to Equation (5.43) if the replacement of k_z^2 by $4/(L - L_f)L_f$ is done. Note that the second term of the real part of the frequency was neglected in Equation (5.43). Therefore, we see again that the expression for the homogeneous thread can be extended to a partially filled thread by selecting an appropriate value for the longitudinal wavenumber. By setting the real part of Equation (7.44) equal to zero, we obtain two critical values of L_f/L as

$$(L_f/L)_c^\pm = \frac{1}{2} \pm \frac{1}{2} \left[1 - \left(\frac{2\rho_f}{\rho_f + \rho_c} \right) \tilde{\eta}_{Cf}^2 \right]^{1/2}, \quad (7.45)$$

with $\tilde{\eta}_{Cf} = \eta_{Cf}/v_{Af}L$. Hence, the kink mode only exists for $(L_f/L)_c^- < L_f/L < (L_f/L)_c^+$. We cast Equation (7.45) for $\rho_f/\rho_c = 200$ and the extreme case of an almost neutral plasma with $\tilde{\mu}_f = 0.99$, obtaining $(L_f/L)_c^- \approx 10^{-5}$ and $(L_f/L)_c^+ \approx 0.99999$. For smaller values of $\tilde{\mu}_f$, $(L_f/L)_c^-$ decreases and $(L_f/L)_c^+$ increases. Hence, the presence of these critical values is irrelevant for realistic values of L_f/L .

For L_f/L far from the critical values, one can drop the second term in the real part of Equation (7.44). In such a case, the ratio of the damping time to the period is

$$\frac{\tau_D}{P} \approx \frac{1}{2\pi} \left(\frac{\rho_f + \rho_c}{\rho_f} \right)^{1/2} \frac{1}{\tilde{\eta}_{Cf}} \sqrt{2 \left(1 - \frac{L_f}{L} \right) \frac{L_f}{L}}. \quad (7.46)$$

Again, Equation (7.46) is equivalent to Equation (5.44). For $\rho_f/\rho_c = 200$, $L_f/L = 0.1$, and $L = 10^7$ m, Equation (7.46) gives $\tau_D/P \approx 493$ for $\tilde{\mu}_f = 0.8$, and $\tau_D/P \approx 15$ for $\tilde{\mu}_f = 0.99$. These results indicate that, as in a homogeneous thread, we need an almost neutral prominence plasma, i.e., $\tilde{\mu}_f \approx 1$, for the damping due to Cowling's diffusion to be efficient. Such large values of $\tilde{\mu}_f$ are probably unrealistic in the context of prominences.

7.2.2 Damping by resonant absorption

Finally, we study here the general case $l/a \neq 0$. The full expressions of \tilde{c}_{kf} and b^2 given by Equations (7.32) and (7.33) are taken into account. We express the frequency as $\omega = \omega_R + i\omega_I$, and use Equation (7.41) to provide an expression for the ratio ω_I/ω_R after neglecting terms of $\mathcal{O}(\omega_I^2)$ and $\mathcal{O}(\omega_I L^{-2})$. Thus, we obtain

$$\frac{\omega_I}{\omega_R} \approx -\frac{\pi (\rho_f - \rho_c)^2}{8 (\rho_f + \rho_c)} \frac{m/a}{|\partial_r \rho_0|_{r_A}} - \left(\frac{\rho_f}{\rho_f + \rho_c} \right)^{1/2} \frac{\tilde{\eta}_{Cf}}{\sqrt{2 \left(1 - \frac{L_f}{L}\right) \frac{L_f}{L}}}. \quad (7.47)$$

The first term on the right-hand side of Equation (7.47) is caused by resonant absorption and the second term is due to Cowling's diffusion. The term related to Cowling's diffusion was already present in the case $l/a = 0$. The term related to the damping by resonant absorption takes the same form as in a homogeneous tube. Note that this does not mean that the real and imaginary parts of the frequency do not depend on L_f/L , but both quantities are affected in the same way so that their ratio remains unaffected. This important result is consistent with the conclusions of Andries et al. (2005) and Arregui et al. (2005). These authors found that the kink mode damping ratio of a longitudinally stratified tube with mean density ρ_{mean} is the same as that obtained for a homogeneous tube with density ρ_{mean} . Since in our equilibrium the transversely transitional layer is only present in the dense part of the tube and both the evacuated zone and the corona have the same density, resonant absorption only takes place in the dense part of the tube. Therefore, the mean density of the part of the tube where resonant absorption takes place is, obviously, $\rho_{\text{mean}} = \rho_f$. Hence, according to Andries et al. (2005) and Arregui et al. (2005), the kink mode damping ratio in our case must be the same as that of a homogeneous tube with density ρ_f , as our results indicate.

By assuming a sinusoidal variation for the density in the transitional layer and $r_A \approx a$, the expression for τ_D/P according to Equation (7.47) is

$$\frac{\tau_D}{P} \approx \frac{2}{\pi} \left[m \left(\frac{l}{a} \right) \left(\frac{\rho_f - \rho_c}{\rho_f + \rho_c} \right) + \tilde{\eta}_{Cf} \left(\frac{\rho_f}{\rho_f + \rho_c} \right)^{1/2} \frac{4}{\sqrt{2 \left(1 - \frac{L_f}{L}\right) \frac{L_f}{L}}} \right]^{-1}, \quad (7.48)$$

which is equivalent to Equation (6.32) for $\tilde{\eta}_{Cc} = 0$ and $k_z = 2/\sqrt{(L - L_f)L_f}$. As obtained from Equation (6.32), the contribution of resonant absorption to the damping is much more important than that of Cowling's diffusion.

7.3 Results

Here, we numerically solve the dispersion relation (Eq. [7.40]) by means of standard methods and obtain the frequency of the fundamental kink mode for the parameters $\rho_f/\rho_c = 200$, $\rho_e/\rho_c = 1$, and $L = 10^7$ m. We study the dependence of the results with L_f/L .

First, we plot in Figure 7.2 the $A(z)$ function corresponding to the fundamental symmetric kink mode for different values of L_f/L . The $A(z)$ function gives the dependence

of the perturbations in the longitudinal direction. We see that $A(z)$ is mainly confined within the dense part of the flux tube and satisfies the line-tying condition at $z = \pm L/2$. For a homogeneous tube, i.e., $L_f = L$, the $A(z)$ function becomes a cosine function.

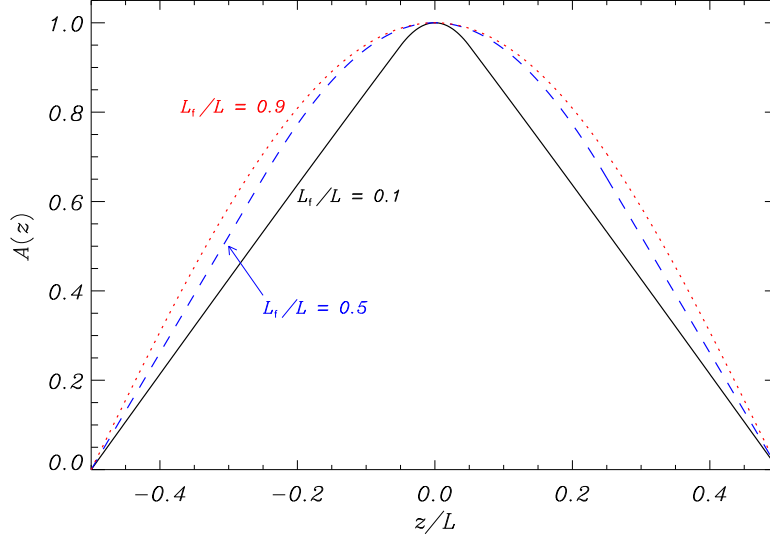


Figure 7.2: $A(z)$ function (in arbitrary units) corresponding to the fundamental kink mode for $L_f/L = 0.1, 0.5,$ and 0.9 . The different line styles are labeled in the Figure.

7.3.1 Case without transverse transitional layer ($l/a = 0$)

Here, we take into account the case without transverse transitional layer, i.e., $l/a = 0$, and so we study the kink mode damping due to Cowling’s diffusion exclusively. Figure 7.3a displays the dimensionless real part of the frequency, $\omega_R \tau_A$, with $\tau_A = L/v_{Af}$ the Alfvén travel time, as a function of L_f/L for different values of the ionization degree in the dense region, whereas Figure 7.3b shows the corresponding values of the absolute value of dimensionless imaginary part of the frequency, $|\omega_I \tau_A|$. We see that ω_R increases as L_f decreases, while its value is independent of the ionization degree. On the contrary, ω_I is strongly dependent on the ionization degree, as expected, and also increases as L_f decreases.

On the other hand, Figure 7.4 displays τ_D/P versus L_f/L . The obtained values of τ_D/P are in agreement with the approximation given by Equation (7.46). The numerical solution shows little dependence on L_f/L , while the analytical approximation diverges from the numerical value in the limits of very small and very large L_f/L . As expected, the analytical expressions derived from Equation (7.41) are not accurate in these limits of L_f/L . Given the large values of τ_D/P , we can conclude in this subsection that the damping due to Cowling’s diffusion in a partially filled flux tube does not increase with respect to the homogeneous tube case of Chapter 5.

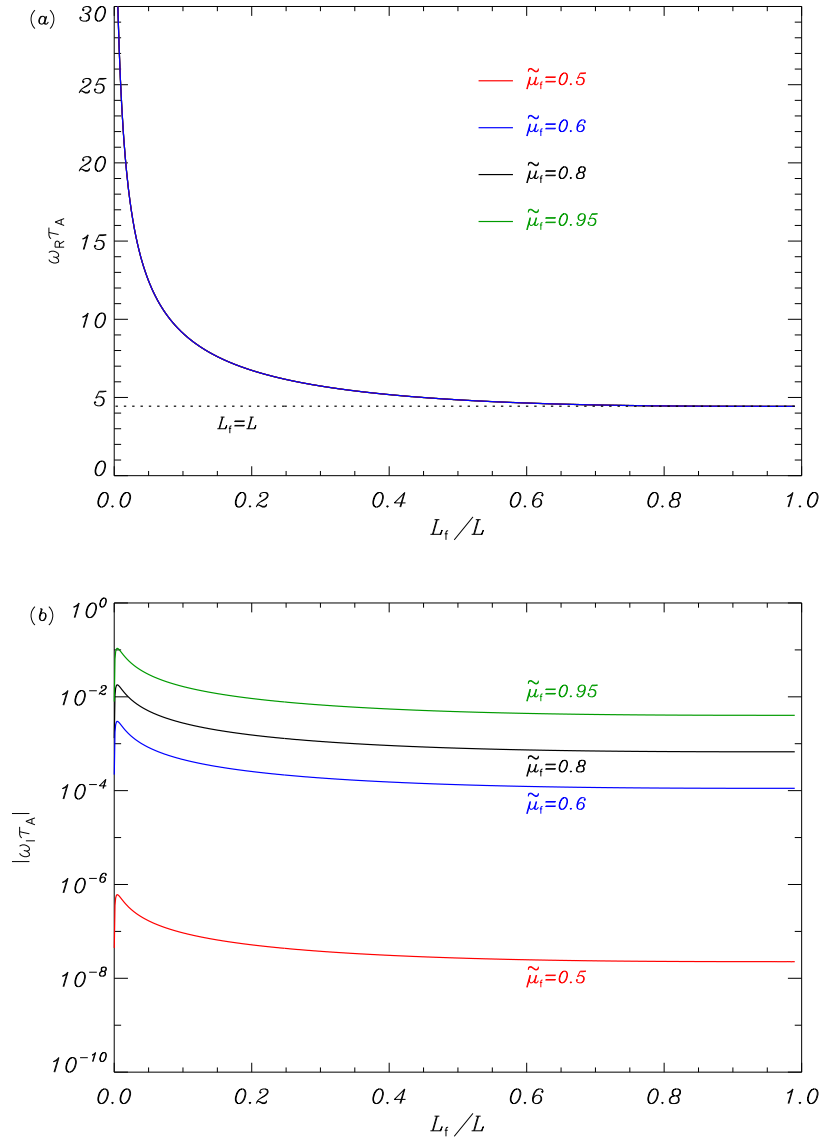


Figure 7.3: Dimensionless (a) real part and (b) absolute value of the imaginary part of the frequency of the fundamental kink mode as a function of L_f/L and in the absence of transverse transitional layer, i.e., $l/a = 0$. The different line styles represent the results for $\tilde{\mu}_f = 0.5, 0.6, 0.8$, and 0.95 . The dotted line in panel (a) corresponds to the frequency of a homogeneous tube with filament conditions, i.e., $L_f = L$. Note that in panel (a) the different solutions are superimposed. The different line styles are labeled in the Figure.

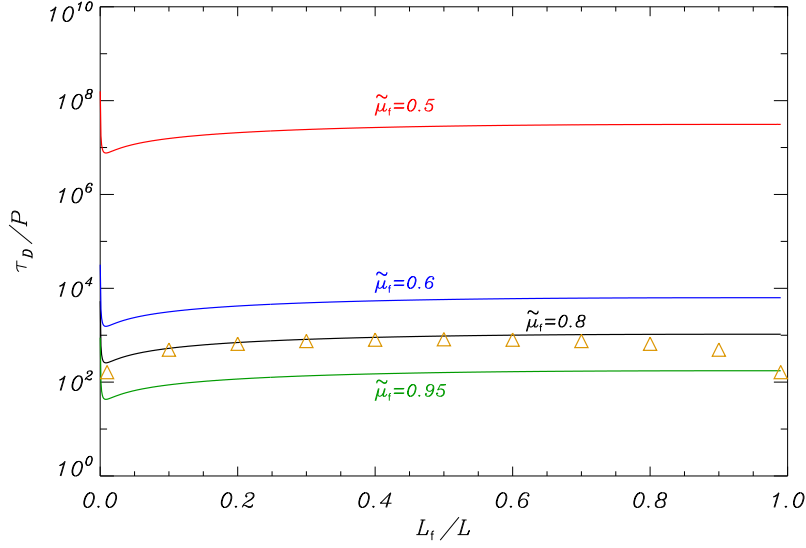


Figure 7.4: τ_D/P of the fundamental kink mode as a function of L_f/L in the absence of transverse transitional layer, i.e., $l/a = 0$, for $\tilde{\mu}_f = 0.5, 0.6, 0.8$, and 0.95 . Symbols are the approximate solution given by Equation (7.46) for $\tilde{\mu}_f = 0.8$. The different line styles are labeled in the Figure.

7.3.2 Case with transverse transitional layer ($l/a \neq 0$)

Now, we take the case $l/a \neq 0$ into account. The kink mode is damped by resonant absorption in the transitional layer. We have computed both the real and imaginary parts of the frequency of the fundamental kink mode as a function of the different parameters, namely $\tilde{\mu}_f$, l/a , and L_f/L . Regarding the real part of the frequency, we find that its value is almost independent of $\tilde{\mu}_f$ and l/a , while its behavior with L_f/L is the same plotted in Figure 7.3a. Therefore, the presence of the transverse transitional layer does not modify the period of the kink oscillations with respect to the case $l/a = 0$, and so we do not plot ω_R again for the sake of simplicity.

On the other hand, Figure 7.5a shows $|\omega_I \tau_A|$ for different values of l/a . These computations correspond to an ionization degree $\tilde{\mu}_f = 0.8$, but equivalent computations for other values of $\tilde{\mu}_f$ provide almost identical results because the effect of Cowling's diffusion is negligible in comparison to that of resonant absorption. As expected, the value of $|\omega_I \tau_A|$ increases with l/a . In order to assess the efficiency of the resonant damping, Figure 7.5b displays the corresponding values of τ_D/P . In comparison to the damping by Cowling's diffusion (see Fig. 7.4), much smaller values of τ_D/P are now obtained. As predicted analytically by Equation (7.48), τ_D/P is almost independent of L_f/L . By comparing Figures 7.3a and 7.5a, we see that both the real and imaginary parts of the frequency have a very similar dependence on L_f/L , so the dependence on L_f/L is canceled when the damping ratio is computed, such as we mentioned at the end of Section 7.2.2. In addition, a very good agreement between the numerical result and the analytical approximation (Eq. [7.48]) is found.

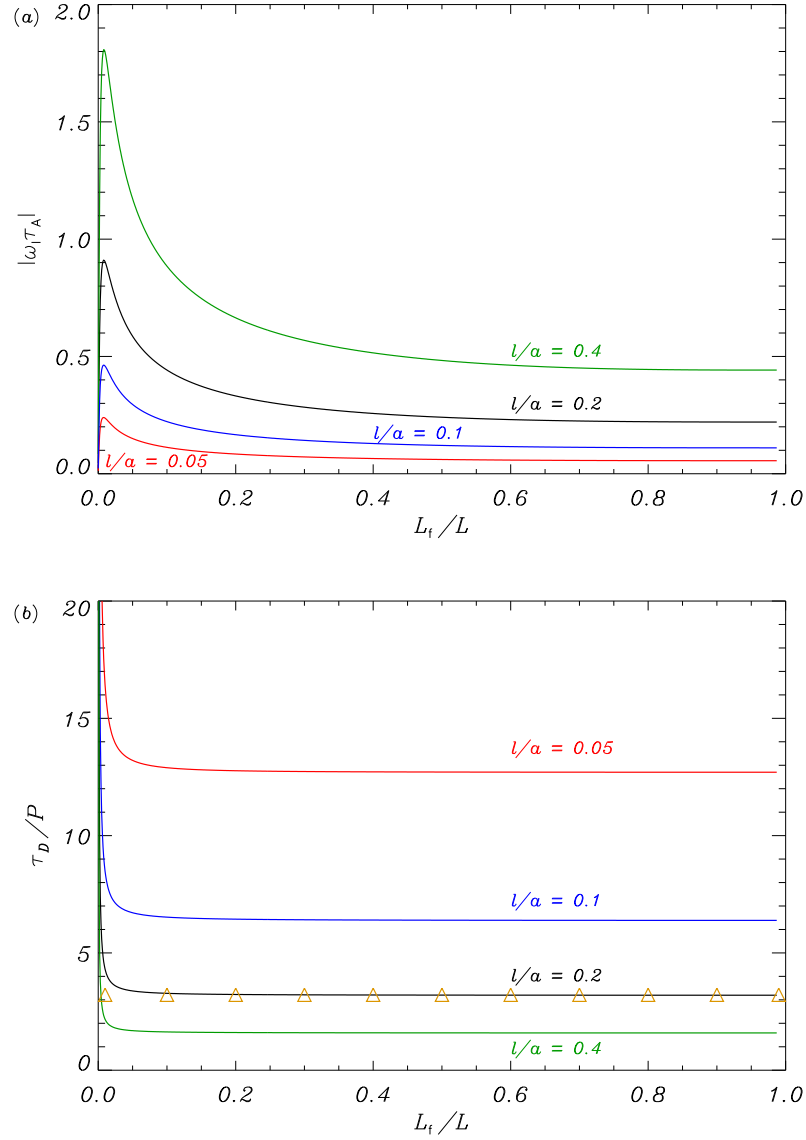


Figure 7.5: (a) Absolute value of the dimensionless imaginary part of the frequency and (b) τ_D/P of the fundamental kink mode as a function of L_f/L . The different line styles represent the results for $l/a = 0.05, 0.1, 0.2,$ and 0.4 . The symbols in panel (b) correspond to the approximate solution given by Equation (7.48) for $l/a = 0.2$. In all computations, $\tilde{\mu}_f = 0.8$.

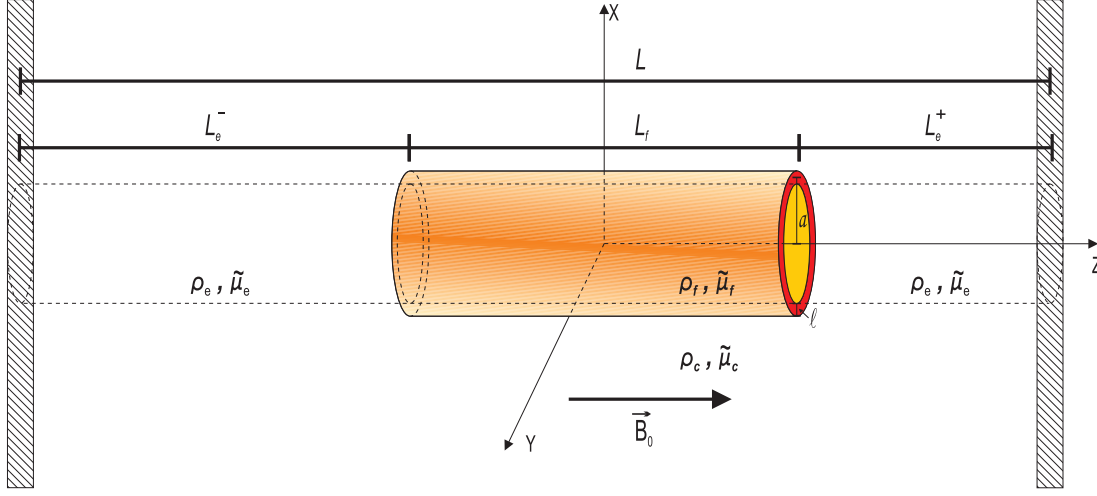


Figure 7.6: Sketch of the filament thread model considered in Section 7.3.3.

7.3.3 Effect of the position of the dense part within the flux tube

In this Section we study the effect of the position of the dense region within the flux tube. The results of the previous Sections correspond to the case in which the dense region is located at the center of the cylinder. Here, we allow the dense region to be displaced from the center of the tube. Figure 7.6 shows a sketch of the present configuration, in which the total length of the magnetic tube and the fibril length are kept as L and L_f , respectively. In this Figure, the length of the evacuated regions to the left and right of the fibril are L_e^- and L_e^+ , respectively. For given L and L_f , we can write $L_e^+ = L - L_e^- - L_f$, hence it is enough to select a value for L_e^- in order to set the length of both evacuated parts. The allowed values of L_e^- are in the range $0 \leq L_e^- \leq L - L_f$. For $L_e^- = 0$, the dense part is totally displaced to the left-hand side end of the flux tube, while the contrary occurs for $L_e^- = L - L_f$. For $L_e^- = L_e^+ = \frac{1}{2}(L - L_f)$ the dense region is located at the center of the tube, i.e., we revert to the configuration studied in the previous Sections of the present Chapter.

A new dispersion relation including this additional ingredient of the model can be analytically derived. However, now we cannot separate the solutions according to their symmetry about $z = 0$, hence the dispersion relation is more complex than Equation (7.40). The dispersion relation is

$$\begin{aligned}
 & \frac{\tilde{c}_{kf} h \cos\left(\frac{\omega}{\tilde{c}_{kf} h} \frac{L_f}{2}\right) \cos\left(\frac{\omega}{c_{ke}} L_e^-\right) - c_{ke} \sin\left(\frac{\omega}{\tilde{c}_{kf} h} \frac{L_f}{2}\right) \sin\left(\frac{\omega}{c_{ke}} L_e^-\right)}{\tilde{c}_{kf} h \sin\left(\frac{\omega}{\tilde{c}_{kf} h} \frac{L_f}{2}\right) \cos\left(\frac{\omega}{c_{ke}} L_e^-\right) + c_{ke} \cos\left(\frac{\omega}{\tilde{c}_{kf} h} \frac{L_f}{2}\right) \sin\left(\frac{\omega}{c_{ke}} L_e^-\right)} \\
 & + \frac{\tilde{c}_{kf} h \cos\left(\frac{\omega}{\tilde{c}_{kf} h} \frac{L_f}{2}\right) \cos\left(\frac{\omega}{c_{ke}} L_e^+\right) - c_{ke} \sin\left(\frac{\omega}{\tilde{c}_{kf} h} \frac{L_f}{2}\right) \sin\left(\frac{\omega}{c_{ke}} L_e^+\right)}{\tilde{c}_{kf} h \sin\left(\frac{\omega}{\tilde{c}_{kf} h} \frac{L_f}{2}\right) \cos\left(\frac{\omega}{c_{ke}} L_e^+\right) + c_{ke} \cos\left(\frac{\omega}{\tilde{c}_{kf} h} \frac{L_f}{2}\right) \sin\left(\frac{\omega}{c_{ke}} L_e^+\right)} = 0, \quad (7.49)
 \end{aligned}$$

with $h = \sqrt{1 - \frac{b^2}{c_{kf}^2}}$. In the case $L_e^- = L_e^+$ and for solutions symmetric about $z = 0$, Equation (7.49) reduces to Equation (7.40).

Next, we obtain the lowest frequency solution, equivalent to the fundamental kink

mode of the case $L_e^- = L_e^+$. To do so, we numerically solve Equation (7.49) for $L_f/L = 0.2$ and $\tilde{\mu}_f = 0.8$, and study the dependence of the result with L_e^-/L . First, we display in Figure 7.7 the $A(z)$ function for different values of L_e^-/L . Since the oscillation is dominated by the physical properties of the dense region, we see that the maximum of $A(z)$ is always in the dense part, regardless of its location within the flux tube.

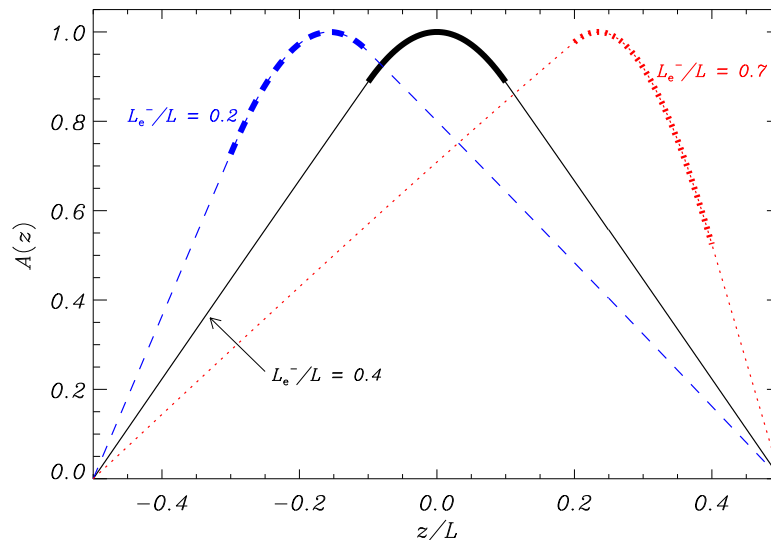


Figure 7.7: $A(z)$ function (in arbitrary units) corresponding to the fundamental kink mode for $L_f/L = 0.2$. The different line styles represent $L_e^-/L = 0.2, 0.4$, and 0.7 . The thick part of the lines corresponds to the location of the fibril within the magnetic tube.

Figure 7.8 displays both the real and imaginary parts of the frequency as a function of L_e^-/L . We obtain that the minimum of ω_R takes place when the dense part is centered within the flux tube, i.e., for $L_e^-/L = \frac{1}{2}(1 - L_f/L) = 0.4$, and ω_R grows symmetrically around $L_e^-/L = 0.4$ when L_e^-/L increases or decreases. The dependence of ω_I on L_e^-/L shows the same behavior than ω_R . Such as happens with the dependence on L_f/L (Fig. 7.5), the dependence on L_e^-/L also cancels out when the damping ratio is computed (see Fig. 7.9). Hence, in our model the value of τ_D/P is independent of both L_f/L and L_e^-/L . We can also see in Figure 7.9 that the approximate τ_D/P given by Equation (7.48) remains valid when the fibril part is not located at the center of the magnetic tube.

7.4 Conclusion

We have adopted a simplified model made of a magnetic cylinder with a dense region with prominence-like conditions, surrounded by two much less dense zones with coronal properties representing the evacuated part of the flux tube. For simplicity, the densities inside these regions are homogeneous (but different), and the thin tube and $\beta = 0$ approximations have been applied following the treatment by Dymova & Ruderman (2005, 2006).

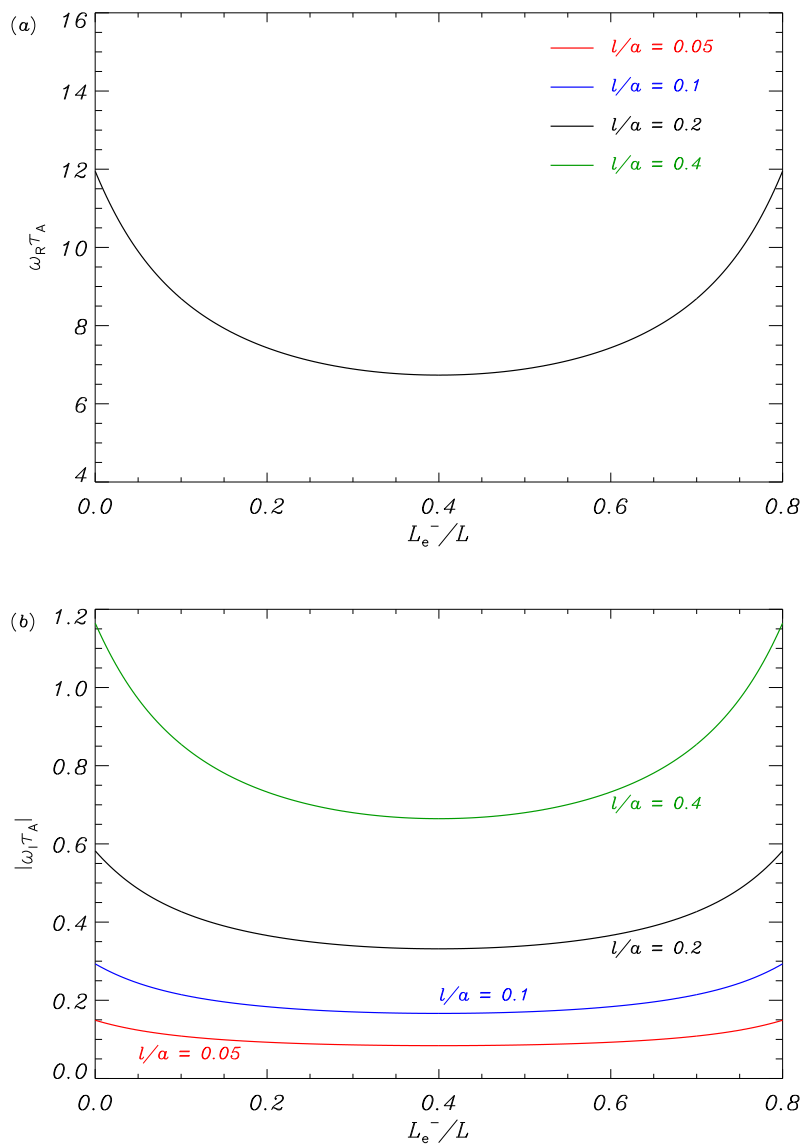


Figure 7.8: Dimensionless (a) real part and (b) absolute value of the imaginary part of the frequency of the fundamental kink mode as a function of L_e^-/L , with $L_f/L = 0.2$ and $\tilde{\mu}_f = 0.8$. The different line styles represent the results for $l/a = 0.05, 0.1, 0.2$, and 0.4 . Note that in panel (a) the different solutions are superimposed.

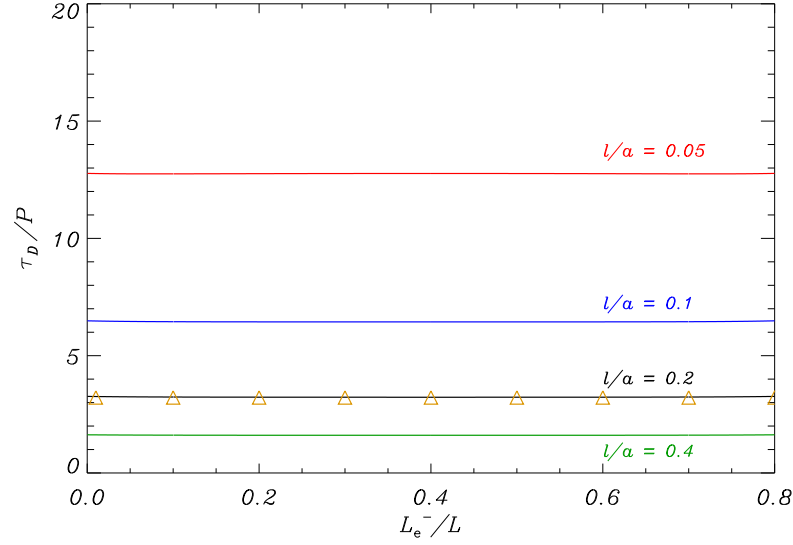


Figure 7.9: τ_D/P of the fundamental kink mode as a function of L_e^-/L , with $L_f/L = 0.2$ and $\tilde{\mu}_f = 0.8$. The different line styles represent the results for $l/a = 0.05, 0.1, 0.2$, and 0.4 . The symbols correspond to the approximate solution given by Equation (7.48) for $l/a = 0.2$.

We have found that the kink mode behavior is mainly governed by the physical properties of the dense, prominence region. The analytical expressions of τ_D/P obtained for a homogeneous thread can be easily generalized to a partially filled flux tube by selecting appropriate values of the longitudinal wavenumber in the formulas of the homogeneous case, given in Chapter 6. In particular, this equivalent longitudinal wavenumber, k_z , depends on the lengths of both the dense region, L_f , and the whole flux tube, L , as $k_z = 2/\sqrt{(L - L_f)L_f}$. In addition, we have obtained that the damping ratio by resonant absorption is independent of the ratios L_f/L and L_e^-/L , which account for the length of the dense region and its position within the magnetic tube, respectively. This result might have important repercussions from a seismological point of view.

The present investigation should be improved in the future by considering a continuous variation of the density in the longitudinal direction as in Andries et al. (2005) and Arregui et al. (2005), instead of our constant piecewise function. Both the period and the damping time may depend on the chosen density profile, but if the transition between the denser part and the evacuated part is narrow, we expect to obtain a small correction to our present results. In addition, one could go beyond the thin tube approximation by using the more general analytical approach of Díaz et al. (2002) or finding the eigenmodes numerically. Moreover, the study of the time-dependent problem by means of both linear and non-linear numerical simulations is also of interest.

Part III

**Collective Oscillations of
Filament Threads**

8

Collective Magnetohydrodynamic Waves in Two Cylindrical Filament Threads with Mass Flows*

In the previous Chapters, we have investigated the individual oscillations of prominence and filament fine structures. Some observations (e.g., [Yi et al. 1991](#); [Lin et al. 2007](#); [Schmieder et al. 2010](#)) suggest that groups of near threads might oscillate coherently, i.e., in phase. Collective oscillations have also been reported in the case of coronal loops ([Schrijver & Brown 2000](#); [Verwichte et al. 2004](#)) and in global motions of two spines within the same prominence ([Ning et al. 2009b](#)). Therefore, the investigation of collective oscillations of groups of threads seems the obvious next step.

As we commented in the Introduction (Chap. 1), a number of works have studied the phenomenon of collective thread oscillations in Cartesian geometry ([Díaz et al. 2005](#); [Díaz & Roberts 2006](#)). In cylindrical geometry, the studies by [Luna et al. \(2009\)](#), who used the analytical T-matrix theory of scattering (e.g., [Twersky 1952](#); [Waterman 1969](#); [Bogdan & Zweibel 1987](#); [Keppens et al. 1994](#)) in the context of pressure-less coronal loops, can also be applied to filament threads. Here, our purpose is to take the method of [Luna et al. \(2009\)](#) into account and to apply it to the context of prominence oscillations. In addition, we extend the formalism of [Luna et al. \(2009\)](#) by considering the case $\beta \neq 0$ and by allowing the presence of flows in the equilibrium. In this Chapter, we present the mathematical method and investigate the ideal MHD modes supported by two filament threads. The study of the damping of these collective modes is relegated to Chapter 9.

Section 8.1 contains a description of the model configuration and the mathematical method. The collective MHD modes of two identical threads are investigated in Section 8.2. In particular, we assess the effect of mass flows along the threads (Sec. 8.2.2). Finally, we extend our investigation to the case of non-identical threads in Section 8.3.

8.1 Model and theory

8.1.1 Equilibrium configuration

Our equilibrium system is made of an arbitrary configuration of N homogeneous and unlimited parallel cylinders, representing prominence threads, embedded in an also homogeneous and unbounded coronal medium. Each thread has its own radius, a_j , effective temperature, \tilde{T}_j , and density, ρ_j , where the subscript $j = 1, 2, \dots, N$ refers to a particular thread. On the other hand, the coronal effective temperature and density are \tilde{T}_c and

*This Chapter is based on the results of R. Soler, R. Oliver, & J. L. Ballester 2009, *Propagation of Nonadiabatic Magnetoacoustic Waves in a Threaded Prominence With Mass Flows*, ApJ, 693, 1601.

ρ_c , respectively. Both the prominence plasma and the coronal medium are assumed to be fully ionized. The cylinder axes are parallel to the z -direction. The magnetic field is uniform and also orientated along the z -direction, $\vec{B}_j = B_j \hat{e}_z$ being the magnetic field in the j -th thread, and $\vec{B}_c = B_c \hat{e}_z$ in the coronal medium. In addition, steady mass flows are assumed along magnetic field lines, with flow velocities and directions that can be different within the threads and in the corona. Thus, $\vec{v}_j = v_j \hat{e}_z$ represents the mass flow in the j -th thread, whereas $\vec{v}_c = v_c \hat{e}_z$ corresponds to the coronal flow. For simplicity, in all the following expressions a subscript 0 indicates local equilibrium values, while subscripts j or c denote quantities explicitly computed in the j -th thread or in the corona, respectively.

8.1.2 Mathematical method

We consider linear and adiabatic perturbations from the equilibrium state. Such as shown in Section 4.1.2, magnetoacoustic waves are governed by

$$\Upsilon^2 [\Upsilon^2 - (c_s^2 + v_A^2) \nabla^2] \Delta + c_s^2 v_A^2 \frac{\partial^2}{\partial z^2} \nabla^2 \Delta = 0, \quad (8.1)$$

where $\Delta = \nabla \cdot \vec{v}_1$ is the divergence of the velocity perturbation, and $\Upsilon = \frac{\partial}{\partial t} + v_0 \frac{\partial}{\partial z}$ is the Doppler-shifted time operator. The quantities in Equation (8.1), as well as in the following expressions, are defined in previous Chapters. Considering cylindrical coordinates, namely r , φ , and z for the radial, azimuthal, and longitudinal coordinates, respectively, we write Δ in the following form,

$$\Delta = \psi(r, \varphi) \exp(ik_z z - i\omega t), \quad (8.2)$$

where the function $\psi(r, \varphi)$ contains the full radial and azimuthal dependence. By inserting this last expression into Equation (8.1), a Helmholtz Equation is obtained, namely

$$\nabla_{r\varphi}^2 \psi(r, \varphi) + m_0^2 \psi(r, \varphi) = 0, \quad (8.3)$$

where $\nabla_{r\varphi}^2$ is the Laplacian operator for the r and φ coordinates, and m_0^2 is the radial wavenumber defined as

$$m_0^2 = \frac{(\Omega_0^2 - k_z^2 v_A^2) (\Omega_0^2 - k_z^2 c_s^2)}{(v_A^2 + c_s^2) (\Omega_0^2 - k_z^2 c_T^2)}, \quad (8.4)$$

with $\Omega_0 = \omega - k_z v_0$ the Doppler-shifted frequency. We investigate non-leaky modes, which are given by $m_c^2 < 0$. We impose no restriction on the wave character within the threads.

To solve Equation (8.3), we consider the technique developed by Luna et al. (2009) based on the study of normal modes of an arbitrary configuration of magnetic cylinders by means of the T-matrix theory of scattering. An alternative approach for a system of two cylinders was adopted by Van Doorselaere et al. (2008), who used bicylindrical coordinates and the thin tube approximation to obtain an analytical dispersion relation. Here, we adopt the more general T-matrix theory of Luna et al. (2009), allowing us to obtain the normal mode frequencies of systems of N cylinders with arbitrary radii. The novelty with respect to the work of Luna et al. (2009) is that the method is applied here to solve a Helmholtz equation for the divergence of the velocity perturbation, whereas

Luna et al. (2009) considered an equation for the total pressure perturbation in the $\beta = 0$ approximation (their Eq. [1]). The present approach allows us to generalize the results of Luna et al. (2009) to the $\beta \neq 0$ case, and therefore slow modes are also described. Mass flows are also included in our formalism. However, the rest of the technique is absolutely equivalent to that of Luna et al. (2009), and the reader is referred to their work for an in-depth explanation of the mathematical technique (see also an equivalent formalism in, e.g., Bogdan & Cattaneo 1989). We give a summary of the method next.

The key point of the T-matrix theory of scattering is that the solution of Equation (8.3) is decomposed in several *fields* with different physical meanings. Following Luna et al. (2009), the internal or transmitted $\psi(r, \varphi)$ field of the j-th thread is

$$\psi_{\text{int}}^j(r, \varphi) = \sum_{m=-\infty}^{\infty} A_m^j J_m(m_j |\vec{r} - \vec{r}_j|) e^{im\varphi_j}, \quad (8.5)$$

where m is the (integer) azimuthal wavenumber, \vec{r}_j and φ_j are the radial vector and the azimuthal angle corresponding to the position of the j-th thread center with respect to the origin of coordinates, respectively, A_m^j are constants accounting for the contribution of each multipole m , and J_m is the Bessel function of the first kind of order m .

On the other hand, the solution in the external medium is more difficult to handle. The external field related to the j-th thread can be generally expressed as

$$\psi_{\text{ext}}^j(r, \varphi) = \sum_{m=-\infty}^{\infty} \psi_m^j(r, \varphi), \quad (8.6)$$

with

$$\psi_m^j(r, \varphi) = \alpha_{1m}^j H_m^{(1)}(m_c |\vec{r} - \vec{r}_j|) e^{im\varphi_j} + \alpha_{2m}^j H_m^{(2)}(m_c |\vec{r} - \vec{r}_j|) e^{im\varphi_j}, \quad (8.7)$$

where the first term of Equation (8.7) corresponds to outgoing waves and the second term to incoming waves, with $H_m^{(1)}$ and $H_m^{(2)}$ the usual Hankel functions, and α_{1m}^j and α_{2m}^j constants. We must now note that $\sum_j \psi_{\text{ext}}^j(r, \varphi)$ does not correspond to the total net external solution since, for example, the outgoing wave of a particular thread contributes to the incoming waves of the other threads. Instead, Bogdan & Cattaneo (1989) express the total net external field as

$$\psi_{\text{ext}}(r, \varphi) = \sum_j^N \psi_{\text{scat}}^j(r, \varphi), \quad (8.8)$$

with ψ_{scat}^j the *scattered field* generated by the j-th thread. Thus, we can define the *exciting field* of the j-th thread as the difference between the total field and its own scattered contribution, i.e., the sum of the scattered field of the other threads, namely

$$\psi_{\text{excit}}^j(r, \varphi) = \psi_{\text{ext}}(r, \varphi) - \psi_{\text{scat}}^j(r, \varphi) = \sum_{n \neq j} \psi_{\text{scat}}^n(r, \varphi). \quad (8.9)$$

While only the scattered fields contribute to the net solution of Equation (8.3), it is conceptually useful to understand the exciting fields as the cross-talk mechanism between the different flux tubes. Waterman (1969) introduces the T-matrix operator of the j-th thread, \mathbf{T}^j , which linearly relates both its scattered and exciting fields as

$$\psi_{\text{scat}}^j(r, \varphi) = \mathbf{T}^j \psi_{\text{excit}}^j(r, \varphi). \quad (8.10)$$

CHAPTER 8. COLLECTIVE MHD WAVES IN TWO FLOWING THREADS

Bogdan & Zweibel (1987) show that, for cylindrical scatterers, the T-matrix is diagonal, while Keppens et al. (1994) give an expression for its elements, namely

$$T_{mm}^j = \frac{1}{2} \left(1 - \frac{\alpha_{1m}^j}{\alpha_{2m}^j} \right), \quad (8.11)$$

with α_{1m}^j and α_{2m}^j the same constants of Equation (8.7). With the help of these last definitions, and after some algebraic manipulations involving Bessel functions properties, we rewrite Equation (8.7) as

$$\psi_m^j(r, \varphi) = 2\alpha_{2m}^j J_m(m_c |\vec{r} - \vec{r}_j|) e^{im\varphi_j} - 2\alpha_{2m}^j T_{mm}^j H_m^{(1)}(m_c |\vec{r} - \vec{r}_j|) e^{im\varphi_j}, \quad (8.12)$$

from which we can identify both the exciting and scattered fields of the j -th thread, namely

$$\psi_{\text{excit}}^j(r, \varphi) = \sum_{m=-\infty}^{\infty} 2\alpha_{2m}^j J_m(m_c |\vec{r} - \vec{r}_j|) e^{im\varphi_j}, \quad (8.13)$$

$$\psi_{\text{scat}}^j(r, \varphi) = - \sum_{m=-\infty}^{\infty} 2\alpha_{2m}^j T_{mm}^j H_m^{(1)}(m_c |\vec{r} - \vec{r}_j|) e^{im\varphi_j}. \quad (8.14)$$

According to Equation (8.8), the total net external field can be finally written as

$$\psi_{\text{ext}}(r, \varphi) = - \sum_j^N \sum_{m=-\infty}^{\infty} 2\alpha_{2m}^j T_{mm}^j H_m^{(1)}(m_c |\vec{r} - \vec{r}_j|) e^{im\varphi_j}. \quad (8.15)$$

Equations (8.5) and (8.15) allow us to construct the spatial distribution of Δ . Subsequently, the rest of perturbations can be obtained. Finally, we obtain from Equation (8.9) that the constants $\alpha_{2,m}^j$ form a homogeneous system of linear algebraic equations, namely

$$\alpha_{2m}^j + \sum_{k \neq j} \sum_{n=-\infty}^{\infty} T_{nn}^k \alpha_{2n}^k H_{n-m}^{(1)}(m_c |\vec{r}_j - \vec{r}_k|) e^{i(n-m)\varphi_{jk}} = 0, \quad \text{for } -\infty < m < \infty. \quad (8.16)$$

Once the sums in both integers m and n are truncated to a finite number of terms, the non-trivial, i.e., non-zero, solution of the system given by Equation (8.16) provides us with a dispersion relation for the oscillatory frequency, ω , which is enclosed in the definitions of m_j and m_c . The dispersion relation is a very transcendental expression, which we solve by standard numerical procedures. To make sure that the number of terms considered in Equation (8.16) is large enough, i.e., that the truncation values of m and n are large enough, we increase the number of terms until we check that a good convergence of the frequency is obtained.

The main difference between our application and that of Luna et al. (2009) is in the definition of the T-matrix elements. These elements are obtained by imposing appropriate boundary conditions at the edge of the threads, i.e., at $|\vec{r} - \vec{r}_j| = a_j$. In our case, these boundary conditions are the continuity of both the total pressure perturbation, p_{T_1} , and

8.2. COLLECTIVE MODES IN TWO IDENTICAL FILAMENT THREADS

the Lagrangian radial displacement, $\xi_r = iv_r/\Omega_0$. Expressions for these quantities as functions of Δ and its derivative are

$$p_{T_1} = -i\rho_0 \frac{(\Omega_0^2 - k_z^2 c_s^2)(\Omega_0^2 - k_z^2 v_A^2)}{\Omega_0^3 m_0^2} \Delta, \quad (8.17)$$

$$\xi_r = -i \frac{(\Omega_0^2 - k_z^2 c_s^2)}{\Omega_0^3 m_0^2} \frac{\partial \Delta}{\partial r}. \quad (8.18)$$

Thus, in our case the T -matrix elements are

$$T_{mm}^j = \frac{m_c \rho_j \left(\Omega_j^2 - k_z^2 v_{A_j}^2 \right) \frac{J'_m(m_c a_j)}{J'_m(m_j a_j)} - m_j \rho_c \left(\Omega_c^2 - k_z^2 v_{A_c}^2 \right) \frac{J_m(m_c a_j)}{J_m(m_j a_j)}}{m_c \rho_j \left(\Omega_j^2 - k_z^2 v_{A_j}^2 \right) \frac{H'_m(m_c a_j)}{J'_m(m_j a_j)} - m_j \rho_c \left(\Omega_c^2 - k_z^2 v_{A_c}^2 \right) \frac{H_m(m_c a_j)}{J_m(m_j a_j)}}, \quad (8.19)$$

where the prime denotes the derivative with respect to the argument of the function. Note that the denominator of T_{mm}^j vanishes at the normal mode frequencies of each individual thread. This can be easily checked by comparing the denominator of Equation (8.19) with the dispersion relation of an isolated thread (see Eq. [3.18]) in which modified Bessel functions are used instead of Hankel functions. The equivalence between both kinds of functions is given in Abramowitz & Stegun (1972).

8.2 Collective modes in two identical filament threads

We apply the method to a configuration of two threads (see Fig. 8.1). We use subscripts 1 and 2 to denote the physical conditions of thread 1, namely T_1 , ρ_1 , and a_1 for the temperature, density, and radius of thread 1, respectively, and T_2 , ρ_2 , and a_2 the equivalent quantities of the thread 2. The distance between centers is d and the magnetic field strength is B_0 everywhere. The flow velocity inside the cylinders is denoted by v_1 and v_2 , respectively, whereas the flow velocity in the coronal medium is v_c .

In this Section, we consider identical threads. We take $\tilde{T}_1 = \tilde{T}_2 = \tilde{T}_f = 10^4$ K and $\rho_1 = \rho_2 = \rho_f = 5 \times 10^{-11}$ kg m⁻³, while the coronal effective temperature and density are $\tilde{T}_c = 2 \times 10^6$ K and $\rho_c = 2.5 \times 10^{-13}$ kg m⁻³, respectively. Their radii are $a_1 = a_2 = a = 100$ km, and the magnetic field strength is $B_0 = 5$ G. With no loss of generality, we assume no flow in the external medium, i.e., $v_c = 0$.

8.2.1 Results in the absence of flows

First, we study the normal modes in the absence of flows, i.e., $v_1 = v_2 = 0$. We fix the longitudinal wavenumber to $k_z a = 10^{-2}$ and the distance between threads to $d = 4a$. We reobtain the four kink modes described by Luna et al. (2008, 2009) in the $\beta = 0$ case, i.e., the S_x , A_x , S_y , and A_y modes, where S or A denote symmetry or antisymmetry of the total pressure perturbation with respect to the yz -plane, and the subscripts refer to the main direction of polarization of motions. Note that in our configuration, the x -axis connects the centers of the cylinders (see Fig. 8.1). These four kink modes are mainly governed by multipoles with $|m| = 1$. It is worth mentioning that an infinite number of other solutions related to larger $|m|$, i.e., fluting-like modes, are also present. Moreover,

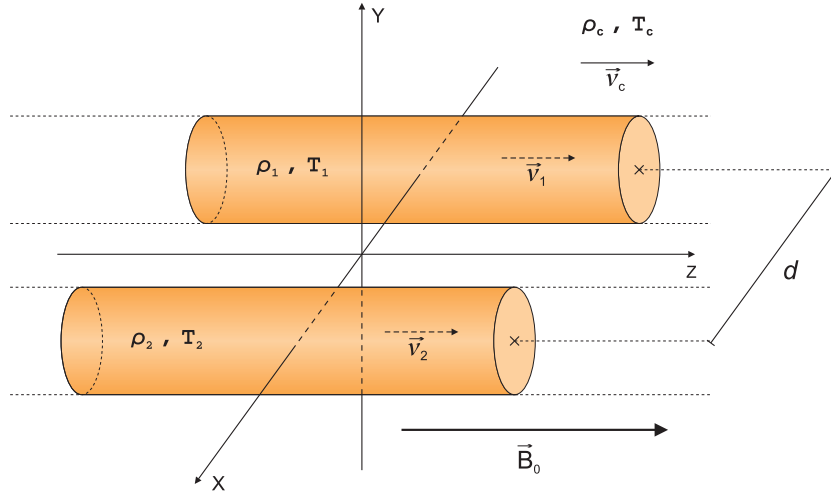


Figure 8.1: Sketch of the configuration of two parallel cylindrical filament threads.

two solutions with $m = 0$ as their dominant multipole, i.e., sausage-like modes, exist, but they are leaky modes for small values of $k_z a$. We focus our investigation on the four kink solutions described before.

In addition, we also find two more fundamental collective wave modes (one symmetric and one antisymmetric) mainly polarized along the z -direction, which we call S_z and A_z modes following the notation of Luna et al. (2008). These new solutions correspond to slow modes, which are absent in the investigations of Luna et al. (2008, 2009) due to their $\beta = 0$ approximation. The S_z and A_z solutions have sausage-like properties, i.e., their dominant multipole is $m = 0$. An infinite number of slow modes, mainly governed by larger values of $|m|$, are also found, but we restrict ourselves to the fundamental S_z and A_z modes.

The total pressure perturbation field, p_{T1} , and the transverse Lagrangian displacement vector-field, $\vec{\xi}_\perp$, corresponding to the six fundamental modes are displayed in Figure 8.2. On the other hand, Figure 8.3 displays a cut of the Cartesian components of the Lagrangian displacement (ξ_x , ξ_y , and ξ_z) at $y = 0$, again for these six solutions. One can see in Figure 8.3 that the amplitude of the longitudinal, i.e., magnetic field aligned, Lagrangian displacement, ξ_z , of the S_z and A_z modes is much larger than the amplitude of transverse displacements, ξ_x and ξ_y , such as corresponds to slow modes in $\beta < 1$ homogeneous media, while the contrary occurs for the S_x , A_x , S_y , and A_y kink solutions.

Such as stated by Luna et al. (2009), a collective wave mode is the result of the coupling between individual modes. So the reader must be aware that here we indistinctly use both expressions, i.e., collective modes and coupled modes, to refer to wave solutions whose perturbations have significant amplitudes in both threads.

Dependence on the distance between threads

Figure 8.4a displays the ratio of the frequency of the four kink solutions to the frequency of the individual kink mode, ω_k , computed from the dispersion relation of an isolated cylinder (Eq. [3.18]), as a function of the distance between the center of cylinders,

8.2. COLLECTIVE MODES IN TWO IDENTICAL FILAMENT THREADS

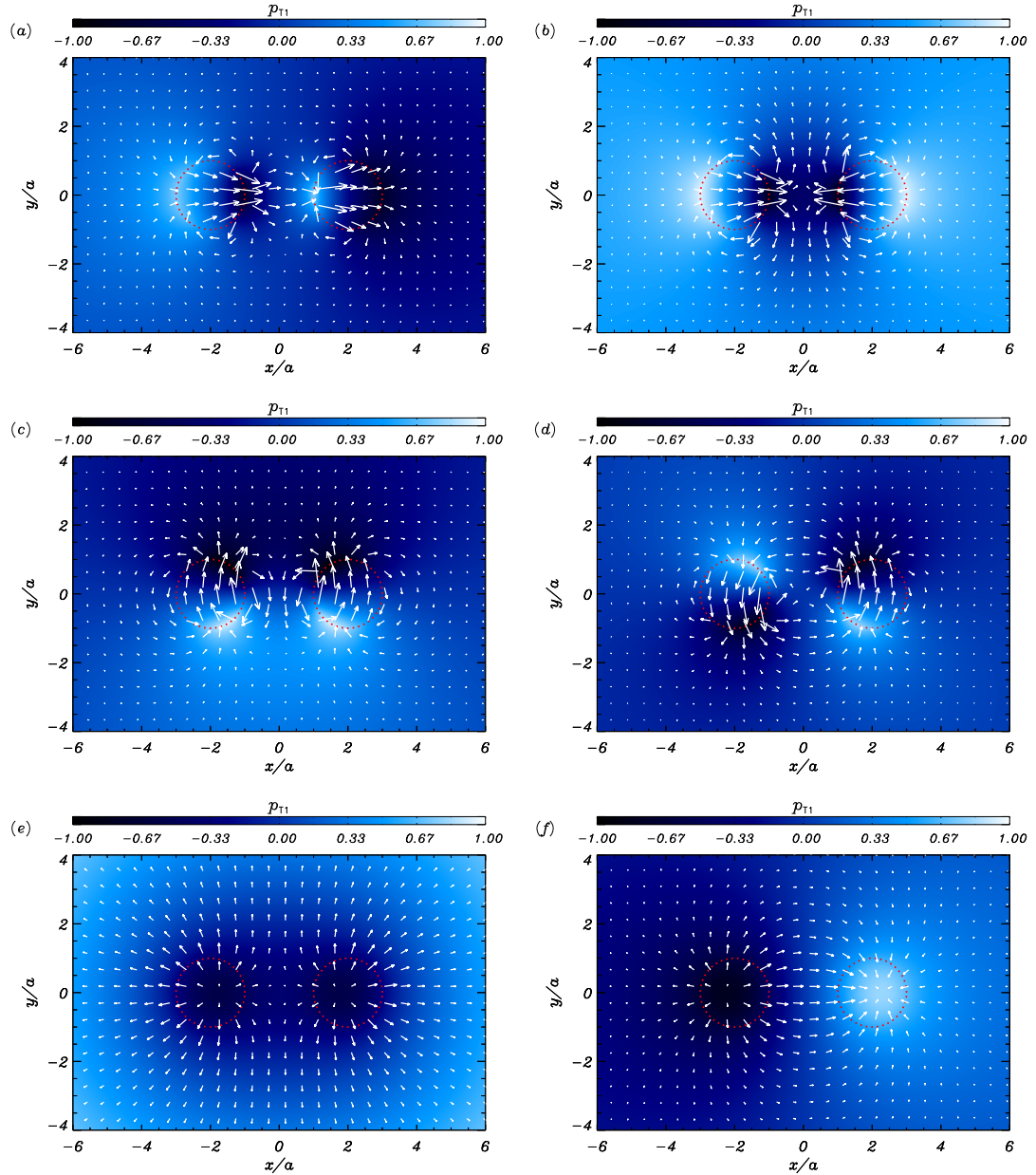


Figure 8.2: Total pressure perturbation field (contour plot in arbitrary units) and transverse Lagrangian displacement (arrows) plotted in the xy -plane corresponding to the wave modes (a) S_x , (b) A_x , (c) S_y , (d) A_y , (e) S_z , and (f) A_z in the absence of flows and for $d = 4a$ and $k_z a = 10^{-2}$. The dotted circles denote the location of the undisturbed threads.

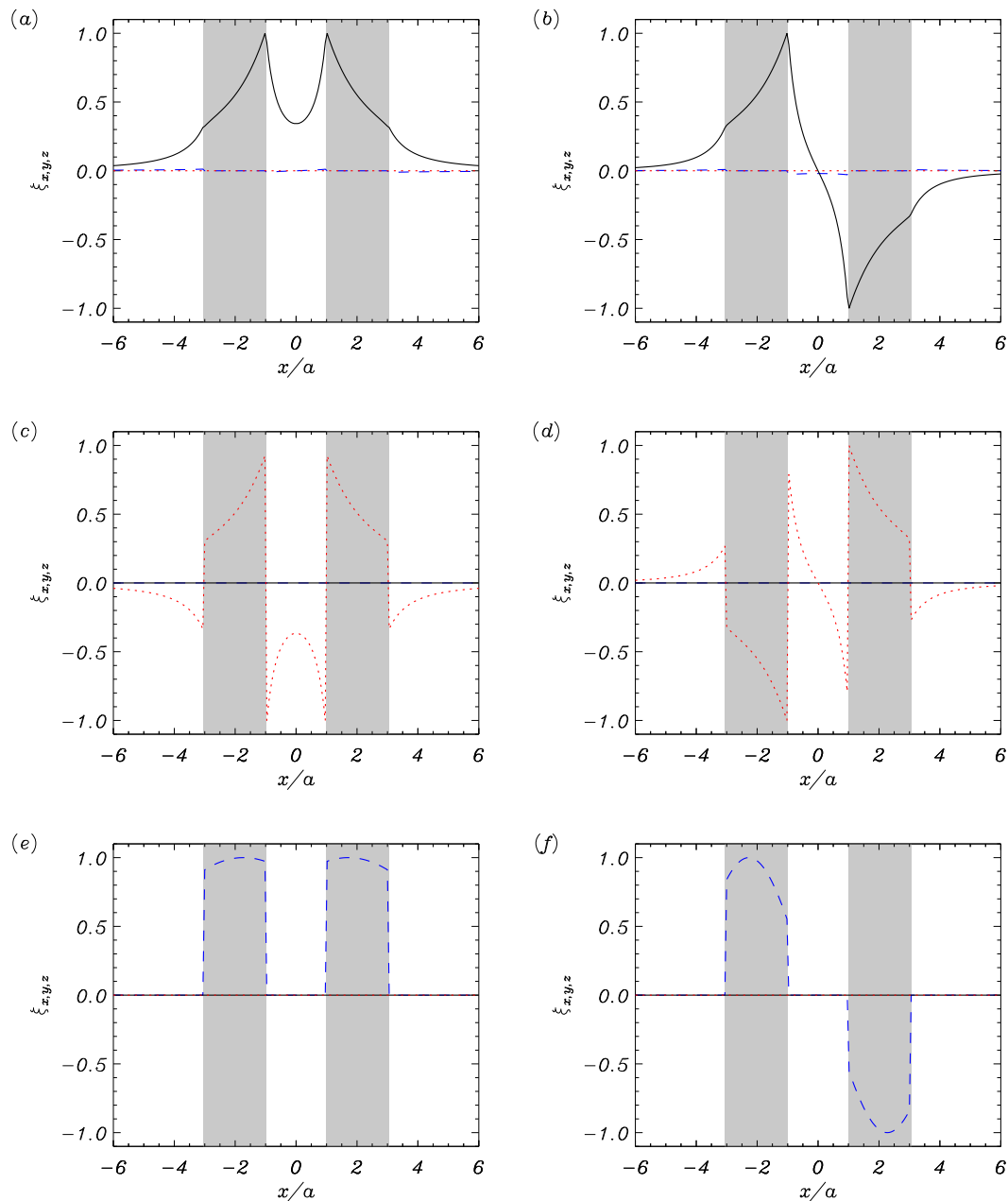


Figure 8.3: Cut at $y = 0$, $z = 0$ of the Cartesian components of the Lagrangian displacement ξ_x (solid), ξ_y (dotted), and ξ_z (dashed) corresponding to the wave modes (a) S_x , (b) A_x , (c) S_y , (d) A_y , (e) S_z , and (f) A_z in the absence of flows and for $d = 4a$ and $k_z a = 10^{-2}$. The shaded zones denote the location of the undisturbed threads. Arbitrary units have been used

8.2. COLLECTIVE MODES IN TWO IDENTICAL FILAMENT THREADS

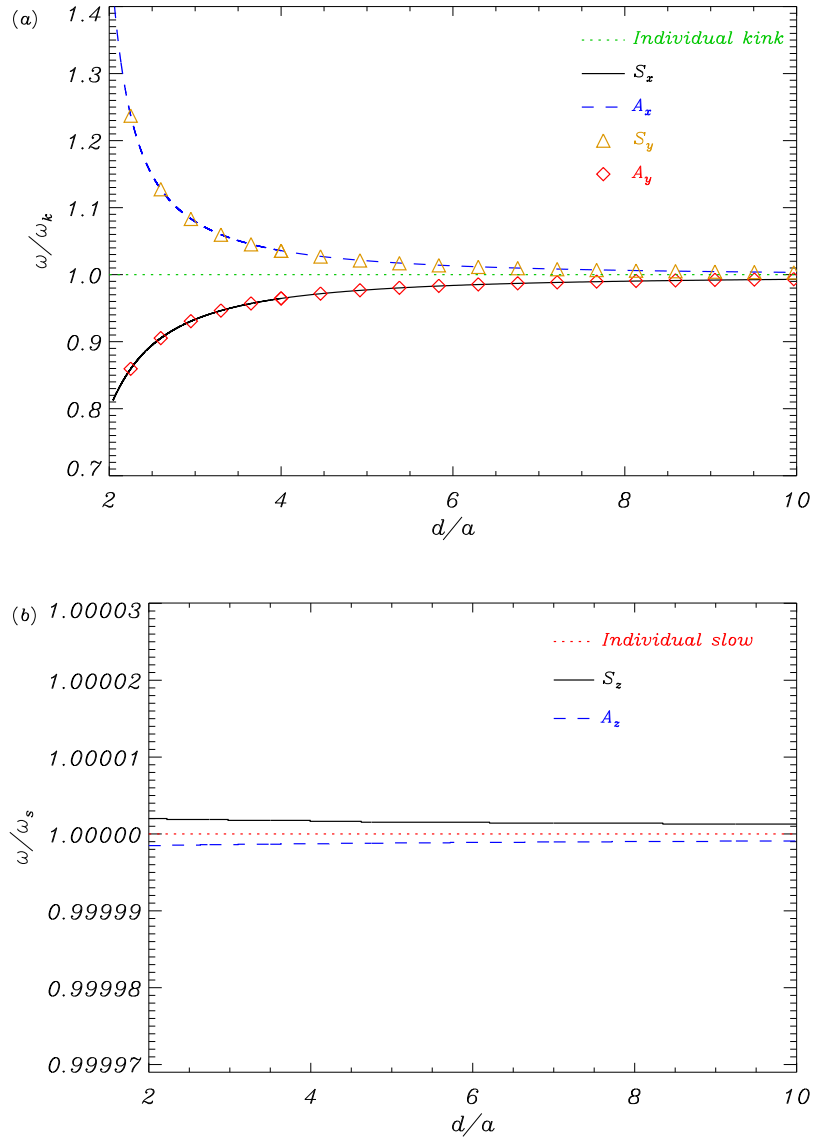


Figure 8.4: *a)* Ratio of the frequency of the collective kink modes to the individual kink mode frequency in the case of identical threads. *(b)* Ratio of the frequency of the collective slow modes to the individual slow mode frequency in the case of identical threads. In both cases $k_z a = 10^{-2}$. The meaning of the different lines is indicated within the Figure.

d. This Figure is equivalent to Figure 3 of Luna et al. (2008) and, in agreement with them, one can see that the smaller the distance between centers, the larger the interaction between threads and so the larger the separation between frequencies. The frequency of the collective kink modes is almost identical to the individual kink frequency for a distance between threads larger than 6 or 7 radii. For larger distances, the interaction between threads is much weaker and we expect oscillations to be almost individual. The collective behavior of oscillations is therefore stronger for smaller distances, as expected. High-resolution observations (e.g., Lin et al. 2007, 2008, 2009) indicate that the separation between neighboring threads is usually of the order of the thread widths. For this reason, we consider hereafter small, realistic distances in order to study the collective behavior of oscillations.

In addition, we see that the kink modes appear in pairs, i.e., the S_x and A_y solutions have an almost identical frequency, and the same applies to the A_x and S_y solutions. Van Doorselaere et al. (2008) showed that for thin tubes (TT), i.e., $k_z a \ll 1$, only two kink modes are present, which were called low- and high-frequency modes, respectively. Van Doorselaere et al. (2008) give an expression for the frequency of their low- and high-frequency kink modes, which in our notation is

$$\omega_{\pm}^2 = \frac{\omega_k^2}{1 \mp \left(\frac{\rho_f - \rho_c}{\rho_f + \rho_c} \right) e^{-2 \operatorname{arccosh}\left(\frac{d}{2a}\right)}}, \quad (8.20)$$

where ω_+ corresponds to the high-frequency solution and ω_- to the low-frequency mode. An accurate approximation to Equation (8.20) for $d/a \gtrsim 4$ is obtained by writing $\operatorname{arccosh}\left(\frac{d}{2a}\right) \approx \ln\left(\frac{d}{a}\right)$. Also note that for typical prominence and coronal densities $\left(\frac{\rho_f - \rho_c}{\rho_f + \rho_c}\right) \approx 1$. So, one gets

$$\omega_{\pm}^2 \approx \frac{\omega_k^2}{1 \mp \left(\frac{a}{d}\right)^2}. \quad (8.21)$$

From Equation (8.21) one clearly see that for $d/a \rightarrow \infty$, $\omega_{\pm} \rightarrow \omega_k$.

For arbitrary $k_z a$, each of the two modes of Van Doorselaere et al. (2008) splits in two different solutions. Thus, the low-frequency mode becomes the S_x and A_y modes, whereas the high-frequency mode corresponds to the A_x and S_y solutions. For $k_z a = 10^{-2}$, the frequencies of the two modes of each pair are still almost degenerated, so Equation (8.20) remains as a good approximation to their frequencies. For the sake of simplicity, we use the notation of Van Doorselaere et al. (2008) if the modes are indiscernible when their frequencies are plotted together for small values of $k_z a$.

Regarding slow modes, Figure 8.4b displays the ratio of the frequency of the S_z and A_z solutions to the frequency of the individual slow mode, ω_s , also computed from Equation (3.18). One can see that the frequencies of the S_z and A_z modes are almost identical to the individual slow mode frequency, and so the strength of the interaction is almost independent of the distance between cylinders. This is consistent with the fact that transverse motions (responsible for the interaction between threads) are not significant for slow-like modes in comparison with their longitudinal motions. Therefore, the S_z and A_z modes essentially behave as individual slow modes, contrary to kink modes, which display a more significant collective behavior.

8.2.2 Effect of mass flows

Luna et al. (2009) studied the effect of considering different densities in each cylinder on the collective modes. They concluded that collective motions are only possible in the case of cylinders with similar densities and so similar individual kink frequencies. The aim of the present Section is to assess the effect of flows on the behavior of the previously described collective modes for identical threads. We vary the flow velocities in both cylinders, namely v_1 and v_2 , between -30 km s^{-1} and 30 km s^{-1} . This range corresponds to the typically observed flow velocities in filament threads (e.g., Lin et al. 2003). These flow velocities are below the critical value that determines the apparition of the Kelvin-Helmholtz instability (see details in Holzwarth et al. 2007, and in Sect. 4.1.4). In our configuration, a positive flow velocity means that the mass is moving towards the positive z -direction, whereas the contrary happens for negative flow velocities. From Chapter 4, we know that the symmetry between waves whose propagation is parallel ($\omega > 0$) or anti-parallel ($\omega < 0$) with respect to magnetic field lines is broken by the presence of flows. Hence, we must take into account the direction of wave propagation in order to perform a correct description of the wave behavior. Following the notation of Chapter 4, we call forward waves those solutions with $\omega > 0$, while backward waves are solutions with $\omega < 0$.

We begin this investigation with transverse modes. First, we fix $v_1 = -20 \text{ km s}^{-1}$ and study the behavior of the oscillatory frequency when v_2 varies (see Fig. 8.5). We restrict ourselves to forward propagation because the following argumentation can be easily extended to backward waves. We use the notation by Van Doorselaere et al. (2004) of low-frequency modes (S_x and A_y) and high-frequency modes (A_x and S_y). To understand the asymptotic behavior of frequencies in Figure 8.5, we define the following Doppler-shifted individual kink frequencies as

$$\Omega_{k1} = \omega_k - v_1 k_z, \tag{8.22}$$

$$\Omega_{k2} = \omega_k - v_2 k_z. \tag{8.23}$$

Since v_1 is fixed, Ω_{k1} is a horizontal line in Figure 8.5, whereas Ω_{k2} is linear in v_2 . Three interesting situations have been pointed by means of small letters from a to c in Figure 8.5. Each of these letters also corresponds to a panel of Figure 8.6 in which the total pressure perturbation field of the S_x mode is plotted. The results for the other modes are equivalent. The three different situations are commented in detail next (remember that in all cases $v_1 = -20 \text{ km s}^{-1}$).

- (a) $v_2 = 10 \text{ km s}^{-1}$ ($v_2 > v_1$). This corresponds to a situation of counter-streaming flows. From Figure 8.5 we see that the frequency of low-frequency modes is close to Ω_{k2} , whereas that of high-frequency solutions is near Ω_{k1} . Thus, these solutions do not interact with each other and low-frequency (high-frequency) solutions are related to individual oscillations of the second (first) thread. This is verified by looking at the total pressure perturbation field in Figure 8.6a, corresponding to the S_x mode, which shows that only the second thread is significantly perturbed. Therefore, for an external observer this situation corresponds in practice to an individual thread oscillation.
- (b) $v_2 = -20 \text{ km s}^{-1}$ ($v_2 = v_1$). The flow velocities and their directions are equal in both threads. In such a situation, low- and high-frequency modes couple. At

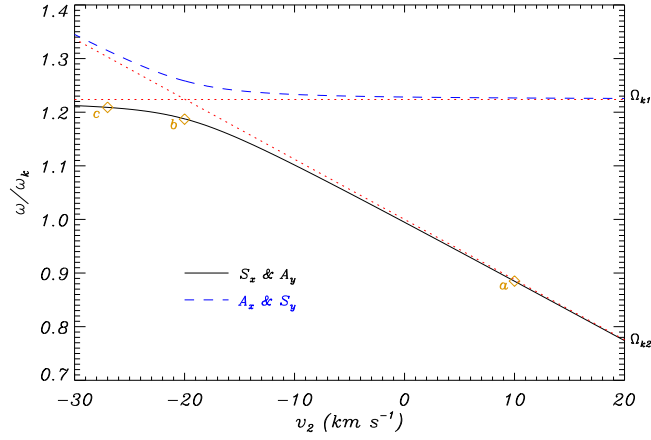


Figure 8.5: Ratio of the frequency of the forward kink modes to the individual kink frequency, ω_k , as a function of v_2 for $v_1 = -20 \text{ km s}^{-1}$. The meaning of the solid and dashed lines is indicated within the Figure. The dotted lines correspond to the Doppler-shifted individual kink frequencies of the threads, Ω_{k1} and Ω_{k2} , respectively, given by Equations (8.22) and (8.23). The symbols and the small letters refer to particular situations studied in the text.

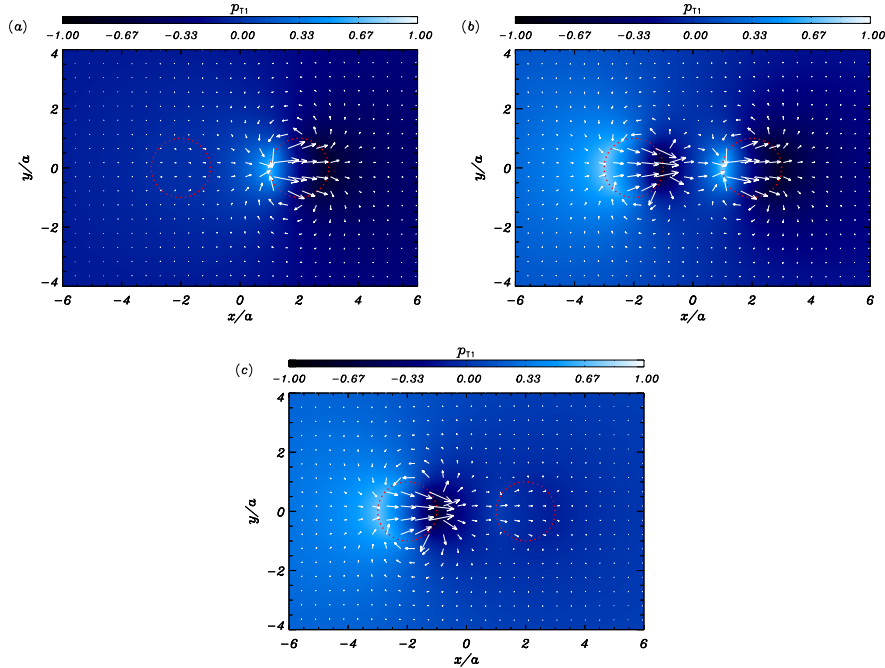


Figure 8.6: Total pressure perturbation field (contour plot in arbitrary units) and transverse Lagrangian displacement (arrows) plotted in the xy -plane corresponding to the forward S_x mode for each particular situation indicated in Figure 8.5, i.e., (a) $v_2 = 10 \text{ km s}^{-1}$, (b) $v_2 = -20 \text{ km s}^{-1}$, and (c) $v_2 = -27 \text{ km s}^{-1}$. In all three cases, $v_1 = -20 \text{ km s}^{-1}$, $d = 4a$, and $k_2 a = 10^{-2}$. The dotted circles denote the location of the undisturbed threads.

8.2. COLLECTIVE MODES IN TWO IDENTICAL FILAMENT THREADS

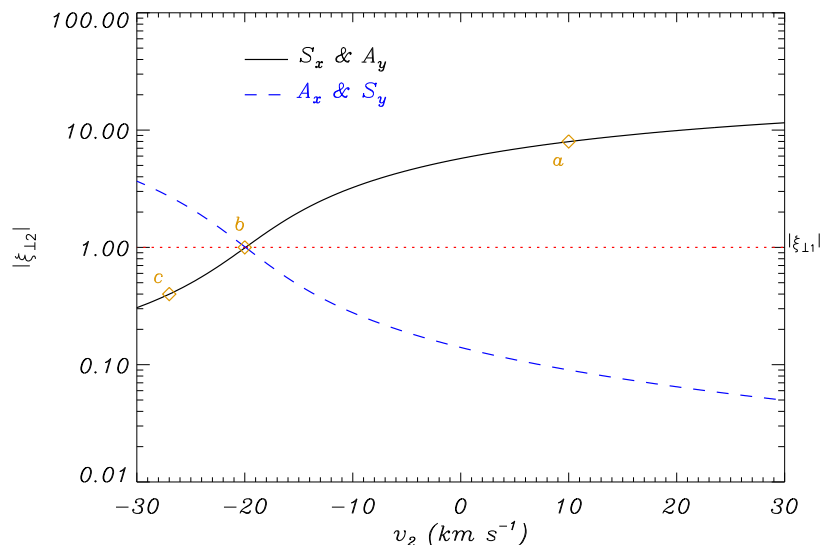


Figure 8.7: Modulus of the transverse Lagrangian displacement of forward kink modes at the center of the second thread, $|\xi_{\perp 2}|$, as a function of v_2 for $v_1 = -20 \text{ km s}^{-1}$. The meaning of the solid and dashed lines is given within the Figure. The dotted line is the displacement at the center of the first thread, namely $|\xi_{\perp 1}|$, which is normalized to unity. The symbols and the small letters refer to particular situations studied in the text.

the coupling, an avoided crossing of the solid and dashed lines is seen in Figure 8.5. Because of this coupling solutions are related no more to oscillations of an individual thread but they are now collective. For this reason, Figure 8.6b shows a significant pressure perturbation and displacement in both threads.

- (c) $v_2 = -27 \text{ km s}^{-1}$ ($v_2 < v_1$). This case is the opposite one to case (a) and corresponds again to an individual thread oscillation.

Figure 8.7 displays the amplitude of the transverse Lagrangian displacement at the center of the second thread, $|\xi_{\perp 2}| = \sqrt{\xi_{x2}^2 + \xi_{y2}^2}$, as a function of v_2 , for forward kink waves. The displacement amplitude at the center of the first thread is always normalized to unity. The three previously commented situations have been pointed again in Figure 8.7. We clearly see that the displacement amplitude is only comparable in both threads, and so their dynamics is collective, when their flow velocities are similar.

Next we turn our attention to slow modes. The behavior of the S_z and A_z modes with respect to the flow is similar to that of low- and high-frequency kink solutions, so we comment them in short. S_z and A_z solutions can only be considered collective when the flow velocity is the same in both threads because, in such a case, the S_z and A_z modes couple. If different flows within the threads are considered, the S_z and A_z slow modes lose their collective aspect. Then, the S_z and A_z solutions behave like individual slow modes, and their frequencies are very close to the Doppler-shifted individual slow frequencies, namely

$$\Omega_{s1} = \omega_s - v_1 k_z, \quad (8.24)$$

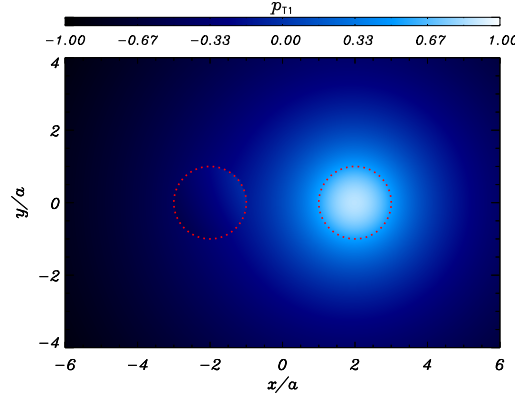


Figure 8.8: Total pressure perturbation field, in arbitrary units, plotted in the xy -plane corresponding to the forward A_z slow mode for $v_1 - v_2 = 10^{-3} \text{ km s}^{-1}$. The dotted circles denote the location of the undisturbed threads.

$$\Omega_{s2} = \omega_s - v_2 k_z. \quad (8.25)$$

The coupling between slow modes is much more sensible to the flow velocities in comparison with kink modes, and the S_z and A_z solutions quickly decouple if v_1 and v_2 slightly differ. An example of this behavior is seen in Figure 8.8, which displays the total pressure perturbation field of the A_z mode for $v_1 - v_2 = 10^{-3} \text{ km s}^{-1}$. Although the difference of the flow velocities is insignificant, the A_z mode essentially behaves as the individual slow mode of the second thread. Equivalently, the S_z solution becomes the individual slow mode of the first thread for this flow configuration.

The main idea behind these results is that kink or slow wave modes with a collective appearance, i.e., modes with a similar displacement amplitude within all threads, are only possible when the Doppler-shifted individual kink (Eqs. [8.22] and [8.23]) or slow (Eqs. [8.24] and [8.25]) frequencies are similar in both threads. In a system of identical threads, this can only be achieved by considering the same flow velocities within all threads, since all of them have the same individual kink and slow frequencies. However, if threads with different physical properties are considered, i.e., with different individual frequencies, the coupling may occur for different flow velocities. This is explored in the next Section.

8.3 Collective modes in two non-identical filament threads

8.3.1 Conditions for collective motions

Now, we consider a system of two non-identical threads. From Section 8.2 we expect that collective kink motions occur when the Doppler-shifted individual kink frequencies of both threads coincide. The relation between flow velocities v_1 and v_2 for which the coupling takes place can be easily estimated from the next expression

$$\omega_{k1} - v_1 k_z \approx \omega_{k2} - v_2 k_z. \quad (8.26)$$

8.3. COLLECTIVE MODES IN TWO NON-IDENTICAL FILAMENT THREADS

Note that, for non-identical threads, the individual kink frequency of each thread is different, i.e., $\omega_{k1} \neq \omega_{k2}$. The relation between flow velocities at the coupling is

$$v_1 - v_2 \approx \frac{\omega_{k1} - \omega_{k2}}{k_z}. \quad (8.27)$$

This last expression can be simplified by considering the kink frequency approximation in the long-wavelength limit and $\rho_c \ll \rho_1, \rho_2$, namely

$$\omega_{kj} \approx \pm \sqrt{\frac{2}{1 + \rho_c/\rho_j}} v_{Aj} k_z \approx \pm \sqrt{2} v_{Aj} k_z, \quad (8.28)$$

for $j = 1, 2$, where the $+$ sign is for forward waves and the $-$ sign is for backward waves. Then, one finally obtains

$$v_1 - v_2 \approx \pm \sqrt{2} (v_{A1} - v_{A2}), \quad (8.29)$$

where the meaning of the $+$ and $-$ signs is the same as before. In the case of identical threads, $v_{A1} = v_{A2}$ and $v_1 - v_2 = 0$. Thus the flow velocity must be the same in both threads to obtain collective motions, as concluded in Section 8.2. An equivalent analysis can be performed for collective slow modes and one obtains that the flow velocities must verify

$$v_1 - v_2 \approx \pm (c_{s1} - c_{s2}). \quad (8.30)$$

In general, the coupling between slow modes occurs for flow velocities different from those giving rise to coupling between kink modes. This makes difficult the simultaneous existence of collective slow and kink solutions in systems of non-identical threads. Unlike the case studied by Luna et al. (2009) of cylinders with different densities, collective normal modes of non-identical tubes are possible when flows are included and the flow velocities have the appropriate values.

8.3.2 Application to a particular configuration

Next, we assume a particular configuration of two non-identical threads to verify the argumentation of Section 8.3.1. The thread radii are $a_1 = 100$ km and $a_2 = 150$ km, whereas their physical properties are $\tilde{T}_1 = 1.5 \times 10^4$ K, $\rho_1 = 3.33 \times 10^{-11}$ kg m $^{-3}$, and $\tilde{T}_2 = 10^4$ K, $\rho_2 = 5 \times 10^{-11}$ kg m $^{-3}$. The coronal conditions are $\tilde{T}_c = 2 \times 10^6$ K and $\rho_c = 2.5 \times 10^{-13}$ kg m $^{-3}$. The magnetic field strength is 5 G everywhere and the distance between the thread centers is $d = 400$ km. We assume $v_1 = 10$ km s $^{-1}$.

For the above parameters, four kink solutions are also present, which are grouped in two almost degenerate couples, i.e., the low- and high-frequency kink solutions of Van Doorselaere et al. (2008). The frequency of the backward kink waves as a function of v_2 is displayed in Figure 8.9. At first sight, we see that solutions couple for a particular value of v_2 , as expected. Applying Equation (8.29), and taking into account that $v_{A1} = 77.29$ km s $^{-1}$ and $v_{A2} = 63.08$ km s $^{-1}$, we obtain $v_1 - v_2 \approx \pm 20.10$ km s $^{-1}$, and since $v_1 = -10$ km s $^{-1}$, we get $v_2 \approx 10.10$ km s $^{-1}$ for backward waves. We see that the approximate value of v_2 obtained from Equation (8.29) is in good agreement with Figure 8.9. In addition, we obtain that, for backward propagation, collective dynamics appear in a situation of counter-streaming, i.e., opposite flows. This result is of special relevance because counter-streaming flows have been detected in prominences

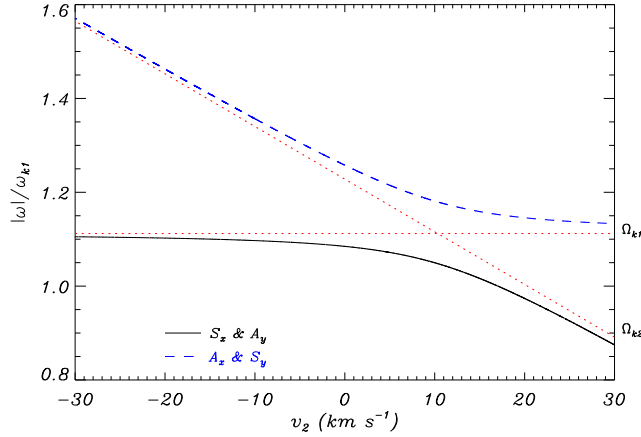


Figure 8.9: Ratio of the frequency of the backward kink modes of non-identical threads to the individual kink frequency of the first thread, ω_{k1} , as a function of v_2 for $v_1 = -10 \text{ km s}^{-1}$. The meaning of the solid and dashed lines is given within the Figure. The dotted lines correspond to the Doppler-shifted individual kink frequencies of the threads, Ω_{k1} and Ω_{k2} , respectively.

(e.g. Zirker et al. 1998; Lin et al. 2003) and might play a crucial role in the collective behavior of oscillations. On the contrary, in the forward propagation case we obtain $v_2 \approx -30.10 \text{ km s}^{-1}$ from Equation (8.29), meaning that both flows are in the same direction and quite a large value of v_2 is obtained in comparison with the backward propagation case.

Regarding slow modes, taking into account that $c_{s1} = 14.40 \text{ km s}^{-1}$ and $c_{s2} = 11.76 \text{ km s}^{-1}$, Equation (8.30) gives $v_2 \approx -12.64 \text{ km s}^{-1}$ for forward slow waves and $v_2 \approx -7.36 \text{ km s}^{-1}$ for backward slow waves. Note that in our particular example the flow velocities needed for the coupling situation are realistic and within the range of typically observed velocities. However, if threads with very different physical properties and, therefore, with very different Alfvén and sound speeds are considered, the coupling flow velocities could be larger than the observed values. This means that the conditions necessary for collective oscillations of systems of threads with very different temperatures and/or densities may not be realistic in the context of solar prominences.

8.4 Conclusion

In this Chapter, we have assessed the effect of mass flows on the collective behavior of slow and kink wave modes in systems of prominence threads. We have seen that the relation between the individual Alfvén (sound) speed of the threads is the relevant parameter which determines whether the behavior of kink (slow) modes is collective or individual. In the absence of flows and when the Alfvén speeds of the threads are similar, kink modes are of collective type. On the contrary, perturbations are confined within an individual thread if the Alfvén speeds differ. In the case of slow modes, the conclusion is equivalent but replacing the Alfvén speeds by the sound speeds of the threads. On the other hand, when flows are present in the equilibrium, one can

find again collective motions even in systems of non-identical threads by considering appropriate flow velocities. These velocities are within the observed values when threads with not too different temperatures and densities are assumed. However, since the flow velocities required for collective oscillations must take very particular values, such a special situation may rarely occur in prominences.

Therefore, if coherent oscillations of groups of threads are observed in prominences (e.g., [Lin et al. 2007](#)), our results allow us to conclude that either the physical properties and flow velocities of all oscillating threads are quite similar or, if they have different properties, that the flow velocities in the threads are the appropriate ones to allow for collective motions. From our point of view, the first option is the most probable one since the flow velocities required in the second case correspond to a very peculiar situation. This conclusion has important repercussions for future prominence seismological applications, because if collective oscillations are observed in large areas of a prominence, the threads in such regions should possess very similar temperatures, densities, and magnetic field strengths.

Here, we have only considered two-thread systems, but the method can be applied to an arbitrary multi-thread configuration similar to that studied by [Luna et al. \(2010\)](#) in the context of multi-stranded coronal loops. [Luna et al. \(2010\)](#) found that in an arbitrary system of several cylinders, the oscillatory frequencies of the collective transverse modes can be always classified into three groups: the low, mid, and high modes. In a two-cylinder configuration, the S_x and A_y solutions are low modes, whereas the A_x and S_y solutions are high modes. The mid modes in a two-cylinder system correspond to the rest of collective transverse modes governed by larger values of m , i.e., fluting modes. Hence, the results obtained here for two threads can be generalized to an arbitrary configuration.

Damping of Collective Magnetohydrodynamic Waves in Two Cylindrical Filament Threads*

Here, we extend the results of Chapter 8 by considering the presence of damping mechanisms. From the studies of wave damping in isolated filament threads performed in the previous Chapters of this thesis, we have determined that non-adiabatic effects for slow modes and resonant absorption for kink modes are the most efficient damping mechanisms. Here, we investigate these two effects on the attenuation of the collective modes of a two-thread configuration.

Section 9.1 contains a description of the model configuration and the expression of the T-matrix elements that apply to the present case. Then, we study the damping of the collective modes of two filament threads by non-adiabatic effects (Sec. 9.2) and resonant absorption (Sec. 9.3). Finally, Section 9.4 contains the main conclusions of this Chapter.

9.1 Model and method

9.1.1 Equilibrium

The present equilibrium configuration is similar to that considered in Chapter 8, i.e., two homogeneous and unlimited parallel cylinders, representing prominence threads, embedded in an also homogeneous and unbounded coronal medium (see Fig 8.1). The meaning of all the quantities and expressions is also the same as in Chapter 8. The difference between the present equilibrium and that of Chapter 8 is that thin transitional layers (TTLs) between the cylindrical threads and the external corona are taken into account. The transitional layers are thin in comparison with the thread mean radius. Figure 9.1 displays a cut of the model at $z = 0$. In addition, here we consider the presence of non-adiabatic terms, i.e, radiative losses and thermal conduction, in the energy equation, using the same formalism as in Chapter 4. Therefore, the reader is referred to that Chapter for a more detailed explanation. For simplicity, and since the effect of flows was assessed in Chapter 8, we consider no flows in the equilibrium.

*This Chapter is based on the results of R. Soler, R. Oliver, & J. L. Ballester 2009, *Propagation of Nonadiabatic Magnetoacoustic Waves in a Threaded Prominence With Mass Flows*, ApJ, 693, 1601, and R. Soler, I. Arregui, R. Oliver, & J. L. Ballester 2010, in preparation

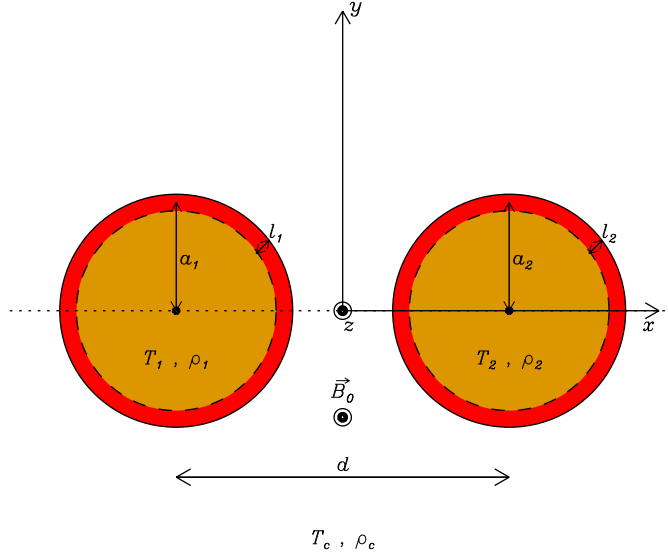


Figure 9.1: Cut in the xy -plane of the configuration of two parallel cylindrical filament threads with thin transitional layers.

9.1.2 Basic equations

To find the normal mode frequencies we consider again the T-matrix theory of scattering. The method is identical to that explained in Section 8.1.2. The only differences are in the definitions of the T-matrix elements, T_{mm}^j , and the radial wavenumbers, m_j and m_c , since now they have to include the effect of the non-adiabatic mechanisms and the resonant absorption at the TTLs. Also note that since there are no flows, the Doppler-shifted frequencies, Ω_j and Ω_c , simply become the oscillatory frequency, ω . Because of the presence of both non-adiabatic effects and resonant absorption, the collective normal mode frequencies are complex quantities, namely $\omega = \omega_R + i\omega_I$. With no loss of generality, we restrict ourselves to modes with $\omega_R > 0$, i.e., forward waves.

As explained in Chapter 4, non-adiabatic effects can be easily included by considering the so-called non-adiabatic sound speed, Λ (see Eq. [4.6]), which replaces the adiabatic sound speed, c_s , in the equations. Hence, the non-adiabatic versions of the radial wavenumbers m_j and m_c , namely \tilde{m}_j and \tilde{m}_c , respectively, are defined as

$$\tilde{m}_j^2 = \frac{(\omega^2 - k_z^2 v_{Aj}^2)(\omega^2 - k_z^2 \Lambda_j^2)}{(v_{Aj}^2 + \Lambda_j^2)(\omega^2 - k_z^2 \tilde{c}_{Tj}^2)}, \quad \tilde{m}_c^2 = \frac{(\omega^2 - k_z^2 v_{Ac}^2)(\omega^2 - k_z^2 \Lambda_c^2)}{(v_{Ac}^2 + \Lambda_c^2)(\omega^2 - k_z^2 \tilde{c}_{Tc}^2)}. \quad (9.1)$$

On the other hand, the effect of resonant absorption at the TTL is incorporated here by combining the jump conditions at the resonance with the thin boundary (TB) approximation. Extensive details about this technique are provided in Chapter 6. In the light of the minor contribution to the attenuation of the slow resonance compared to that of the Alfvén resonance found in Section 6.1, the first one is neglected and only the second one is taken into account. The jump conditions at the Alfvén resonance point for the radial displacement and the total pressure perturbation are given in Equation (6.7).

In the TB approach, these jump conditions replace the boundary conditions, namely $[[\xi_r]] = [[p_{T_1}]] = 0$ at $|\vec{r} - \vec{r}_j| = a_j$, used to compute the T-matrix elements in the case without transitional layers. The T-matrix theory of scattering along with the formalism of the TB has been previously used to investigate resonant absorption in sunspot fibrils with TTLs (Keppens et al. 1994; Keppens 1995, 1996). Thus, the T-matrix elements in the non-adiabatic case with TTLs take the following form,

$$T_{mm}^j = \frac{\tilde{m}_c \rho_j \left(\omega^2 - k_z^2 v_{Aj}^2 \right) \frac{J'_m(\tilde{m}_c a_j)}{J'_m(\tilde{m}_j a_j)} - \tilde{m}_j \rho_c \left(\omega^2 - k_z^2 v_{Ac}^2 \right) \frac{J_m(\tilde{m}_c a_j)}{J_m(\tilde{m}_j a_j)} \dots}{\tilde{m}_c \rho_j \left(\omega^2 - k_z^2 v_{Aj}^2 \right) \frac{H_m^{(1)}(\tilde{m}_c a_j)}{J'_m(\tilde{m}_j a_j)} - \tilde{m}_j \rho_c \left(\omega^2 - k_z^2 v_{Ac}^2 \right) \frac{H_m^{(1)}(\tilde{m}_c a_j)}{J_m(\tilde{m}_j a_j)} \dots} \dots + i\pi \frac{m^2/r_{Aj}}{|\rho_0 \Delta_{Aj}|_{r_{Aj}}} \rho_j \rho_c \left(\omega^2 - k_z^2 v_{Aj}^2 \right) \left(\omega^2 - k_z^2 v_{Ac}^2 \right) \frac{J_m(\tilde{m}_c a_j)}{J'_m(\tilde{m}_j a_j)} \delta_m^j \dots \dots + i\pi \frac{m^2/r_{Aj}}{|\rho_0 \Delta_{Aj}|_{r_{Aj}}} \rho_j \rho_c \left(\omega^2 - k_z^2 v_{Aj}^2 \right) \left(\omega^2 - k_z^2 v_{Ac}^2 \right) \frac{H_m^{(1)}(\tilde{m}_c a_j)}{J'_m(\tilde{m}_j a_j)} \delta_m^j \dots \dots, \quad (9.2)$$

with r_{Aj} the resonant position at the TTL of the j -th thread, $\Delta_{Aj} = \frac{d}{dr} [\omega^2 - \omega_A^2(r)]_j$, and the parameter δ_m^j defined as

$$\delta_m^j = \begin{cases} 1, & \text{if } \omega_{Aj} < \omega_R < \omega_{Ac}, \\ 0, & \text{otherwise.} \end{cases} \quad (9.3)$$

With the parameter δ_m^j we make sure that the term related to the Alfvén resonance does not contribute when the real part of the normal mode frequency is outside the Alfvén continuum of the j -th thread. In addition, by fixing $\delta_m^j = 0$ for a particular value of m , we can omit resonant absorption for that particular multipole. Such as happens with the T-matrix elements of a homogeneous tube (Eq. [8.19]), the denominator of Equation (9.2) corresponds to the dispersion relation of a single tube with a TTL (see, e.g., Van Doorselaere et al. 2004).

Equation (9.2) is a general expression for any given density profile in the transitional layers. For simplicity, we assume that all the TTLs have a sinusoidal density profile (Eq. [6.1]), thus

$$|\rho_0 \Delta_{Aj}|_{r_{Aj}} = \omega_R^2 \left(\frac{\rho_j - \rho_c}{l_j} \right) \frac{\pi}{2} \cos \left[\frac{\pi}{l_j} (r_{Aj} - a_j) \right], \quad (9.4)$$

where l_j is the TTL thickness of the j -th thread, and r_{Aj} is now given by Equation (6.5), which depends on ω_R . The condition of thin layers implies $l_j/a_j \ll 1$. Here, this condition is relaxed since the accuracy of the TB approach is still reasonably good when the restriction $l_j/a_j \ll 1$ is not fully verified but l_j remains smaller than the thread mean radius, i.e., $l_j/a_j < 1$ (Van Doorselaere et al. 2004).

The complex oscillatory frequency is obtained from the non-trivial solution of an algebraic system equivalent to that given by Equation (8.16). However, note that the value of ω_R is previously needed to compute r_{Aj} and δ_m^j . We therefore use a two-step procedure. First, we solve the system in the case without TTLs, i.e., for $\delta_m^j = 0$ for all j and m , and obtain ω_R . We assume that the real part of the frequency is approximately the same when the TTLs are included, allowing us to determine both r_A and δ_m^j . Subsequently, we solve the full system with these parameters, obtaining the actual ω_R and ω_I .

9.2 Damping by non-adiabatic effects

First, we study the damping exclusively due to non-adiabatic mechanisms. Therefore, we do not take into account the presence of the TTLs and fix $\delta_m^1 = \delta_m^2 = 0$ for all values of m . We consider identical threads, with $\tilde{T}_1 = \tilde{T}_2 = 10^4$ K, $\rho_1 = \rho_2 = 5 \times 10^{-11}$ kg m⁻³, and $a_1 = a_2 = a = 100$ km. The coronal effective temperature and density are $\tilde{T}_c = 10^6$ K and $\rho_c = 2.5 \times 10^{-13}$ kg m⁻³, respectively, while the magnetic field strength is $B_0 = 5$ G. We assume the Prominence (2) radiation regime for the prominence plasma (see Table 2.1), while the corona is assumed to be optically thin. The results for other prominence radiation regimes are not included here because all of them show a similar behavior. A constant heating per unit volume is included.

Figure 9.2a shows the ratio of the damping time to the period, τ_D/P , of the collective S_x , A_x , S_y , and A_y kink modes as a function of the distance between threads, d/a , for $k_z a = 10^{-2}$. We see that the damping times are between 5 and 7 orders of magnitude larger than their corresponding periods. Hence, as in the case of individual kink modes (see Chap. 4), dissipation by non-adiabatic mechanisms is not efficient enough to obtain realistic values of τ_D/P of transverse thread oscillations. To shed light on the behavior of the kink modes damping ratio with the separation between threads, we plot in Figure 9.3 the dimensionless imaginary part of the frequency, $\omega_I \tau_A$, with $\tau_A = a/v_{Af}$ the internal Alfvén travel time, versus d/a . The equivalent values of ω_R are not displayed for the sake of simplicity, because they are almost the same shown in Figure 8.4a for the adiabatic case. A comparison between Figures 9.2a and 9.3 shows that the behavior of the damping ratio is mainly governed by the imaginary part of the frequency.

Regarding slow modes, Figure 9.2b shows τ_D/P corresponding to the S_z and A_z solutions versus d/a . One can see that both collective slow modes are efficiently attenuated by non-adiabatic mechanisms, with $\tau_D/P \approx 5$, which is comparable to the results of individual slow modes. Both the real and imaginary parts of the frequency (not displayed here) show very little dependence on the distance between threads, and so the slow modes damping ratio is almost independent of d/a .

We have checked that the dependence of the damping time with $k_z a$ is equivalent to that shown in Figures 4.4b and 4.5a for individual oscillations, i.e., radiative losses from the prominence plasma in the case of slow modes and coronal thermal conduction in the case of kink modes dominate the damping for relevant values of $k_z a$. We have also performed similar computations but considering non-identical threads. In such a case, the collective normal modes become, in practice, individual modes of one of the two threads. Then, the damping times are the same obtained in Chapter 4 for oscillations of individual threads. We therefore conclude that the efficiency of non-adiabatic effects as damping mechanisms for collective modes is not substantially modified in comparison with the individual oscillations for neither identical nor non-identical threads.

9.3 Damping by resonant absorption

Here, we consider the presence of the TTLs between the filament threads and the corona. Also, the presence of non-adiabatic effects is retained in the equations. Now, kink modes are damped by resonant absorption in the Alfvén continuum. On the contrary, the frequencies of both the S_z and A_z slow modes are outside the Alfvén continua,

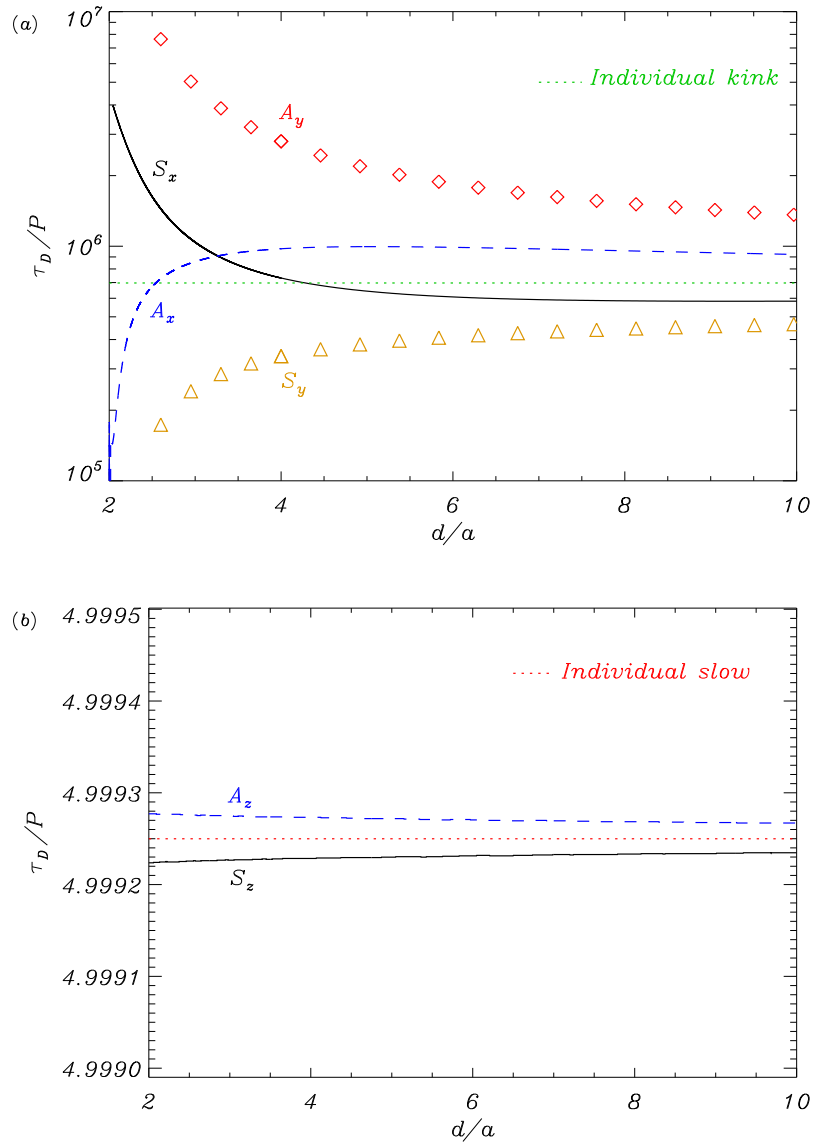


Figure 9.2: Results of the damping by non-adiabatic effects in the case of identical threads. Ratio of the damping time to the period, τ_D/P , of the collective (a) kink modes and (b) slow modes versus the normalized distance between threads, d/a . In both cases $k_z a = 10^{-2}$. The different lines are labeled within the Figure.

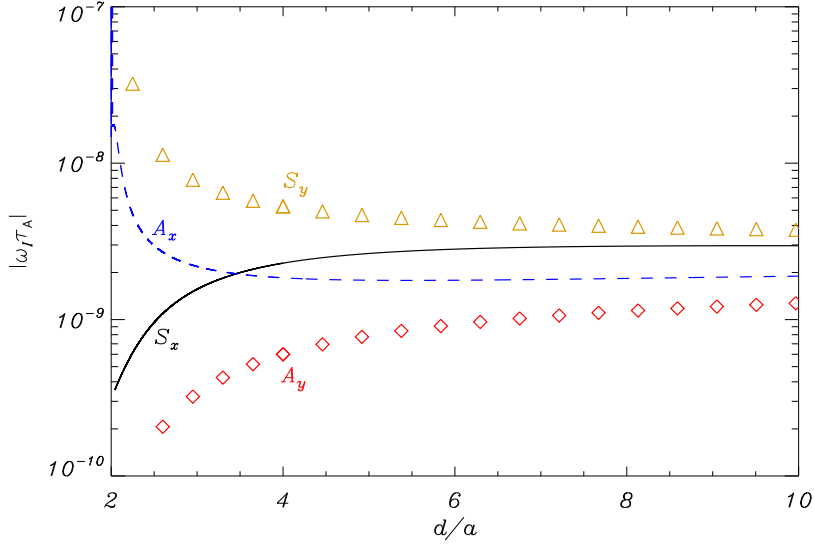


Figure 9.3: Absolute value of the dimensionless imaginary part of the frequency, $\omega_I \tau_A$, of the non-adiabatic collective kink modes versus the normalized distance between threads, d/a , with $k_z a = 10^{-2}$. The different line styles and symbols are labeled within the Figure.

meaning that these modes are not resonantly coupled to Alfvén continuum modes and, therefore, not damped by resonant absorption. The slow modes damping times in the presence of TTLs are the same as those obtained for homogeneous tubes, i.e., the damping is exclusively due to non-adiabatic effects. For this reason, we focus our next study on kink modes.

In this Section we consider the value $k_z a = 10^{-1}$ of the dimensionless longitudinal wavenumber. We use a larger value of $k_z a$ with respect to the previous Sections because the numerical method used to solve the system given by Equation (8.16) does not provide a good convergence of the solution when the full expression of the T-matrix elements is taken into account (Eq. [9.2]) and the longitudinal wavenumber is very small. We have to take a large number of terms in Equation (8.16), i.e., a very large truncation number, to obtain an accurate enough frequency when $k_z a < 10^{-1}$, which significantly increases the computational effort. For this reason, we take a larger $k_z a$ and so a smaller number of terms in Equation (8.16). To make sure that the results for $k_z a = 10^{-1}$ can be compared to those of the previous Sections, we have studied the dependence of the results on $k_z a$ for a particular set of parameters (see further details in Figure 9.6a), and have obtained that τ_D/P becomes independent of $k_z a$ for $k_z a < 10^{-1}$.

9.3.1 Identical threads

First, we take into account the case of two identical threads. The physical conditions are the same considered in Section 9.2. Figure 9.4a displays the dimensionless imaginary part of the frequency of the collective kink modes as a function of the distance between the filament threads, while Figure 9.4b shows the corresponding ratio of the damping

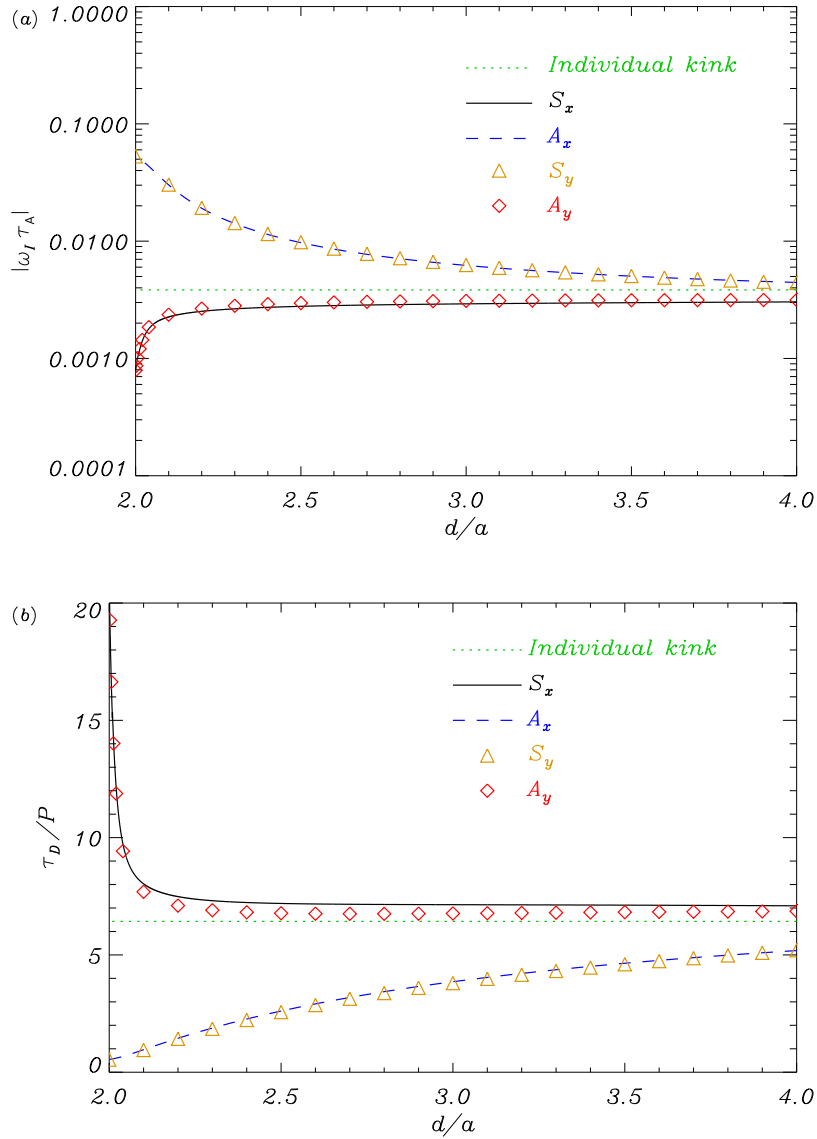


Figure 9.4: Damping of the collective kink modes by resonant absorption in the case of identical threads. (a) Absolute value of the dimensionless imaginary part of the frequency, $\omega_I \tau_A$, versus the normalized distance between threads, d/a , for $l/a = 0.1$. (b) Corresponding ratio of the damping time to the period, τ_D/P . In both cases $k_z a = 10^{-1}$. The different line styles and symbols are labeled within the Figure.

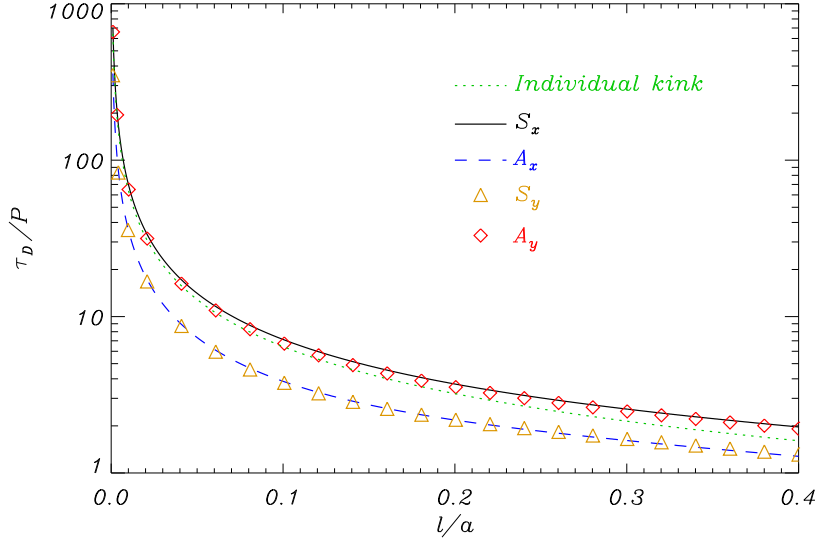


Figure 9.5: Ratio of the damping time to the period, τ_D/P , versus the transitional layer thickness, l/a , for two identical threads with $d/a = 3$ and $k_z a = 10^{-1}$. The different line styles and symbols are labeled within the Figure.

time to the period. The dependence of the real part of the frequency with the distance between threads is the same as in the case $l/a = 0$ (see Fig. 8.4a) and, again for simplicity, is not displayed here. The dependence of ω_I with the separation between threads is stronger than the dependence of ω_R , so that the behavior of τ_D/P with the separation is mainly governed by ω_I . By comparing the vertical axes of Figures 9.4b and Figure 9.2b, one can see the expected result that resonant absorption is much more efficient than non-adiabatic mechanisms for the damping of kink modes. The value of τ_D/P of the four kink solutions tends to the value of an isolated cylinder when the distance between their axes is large. For intermediate separations, the damping ratio of low-frequency (S_x and A_y) kink modes is almost independent of d and close to the value of individual kink oscillations, while τ_D/P increases for very small separations. In the case of high-frequency (A_x and S_y) kink modes, their τ_D/P continuously decreases as the two threads become closer. Note the very efficient attenuation of these solutions for small separations, with the damping ratio of the A_x and S_y modes almost an order of magnitude smaller than that of the S_x and A_y solutions.

In Figure 9.5 we see the dependence of τ_D/P on the transitional layer thickness. As expected, the value of τ_D/P of the four kink solutions decreases as l/a grows. This behavior is identical to that of the individual kink oscillation and fully consistent with a damping by resonant absorption.

Next, Figure 9.6a displays the dependence of τ_D/P on $k_z a$. It is interesting to compare Figure 9.6a with Figure 6.4a, corresponding to the individual kink mode. For small and realistic values of $k_z a$, i.e., $k_z a < 10^{-1}$, the damping ratio of the four kink solutions is independent of $k_z a$. As $k_z a$ is increased, the damping ratio of both the S_x and A_y solutions increases, following a similar behavior to that of the individual kink mode (Fig. 6.4a). On the contrary, the damping ratio of the A_x and S_y modes first

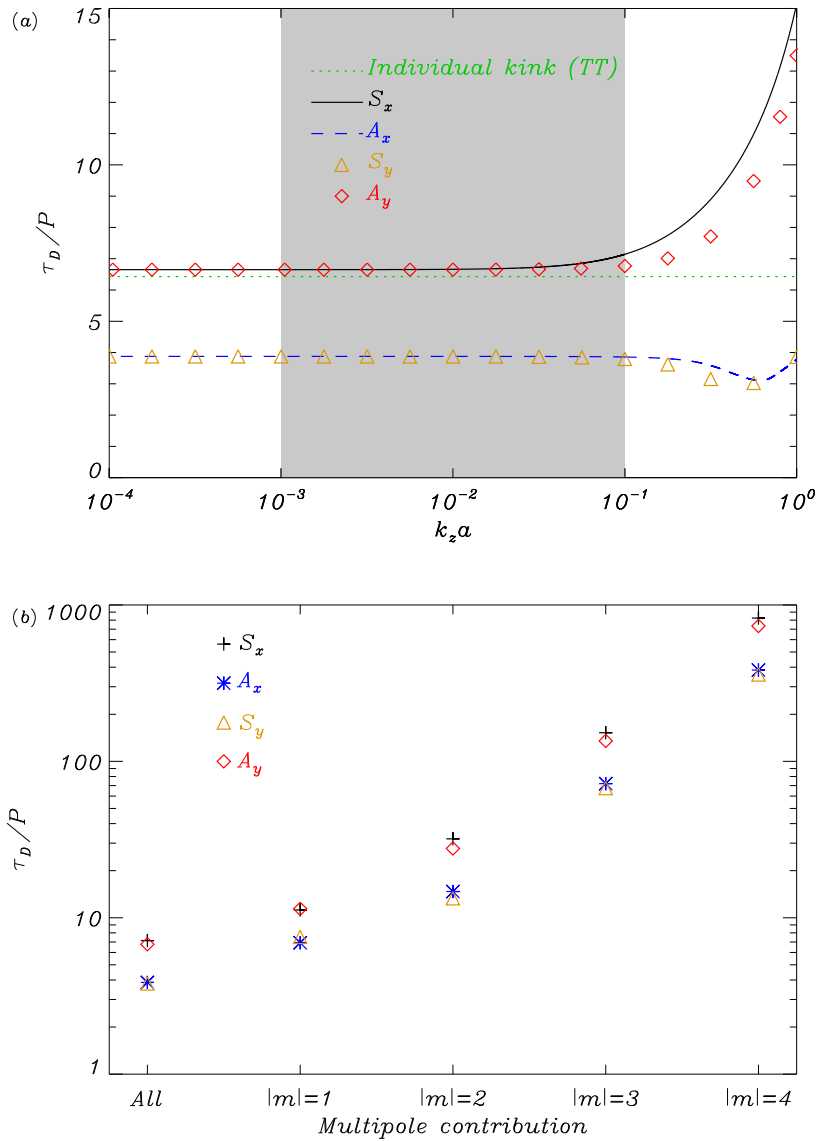


Figure 9.6: Damping of the collective kink modes by resonant absorption in the case of two identical threads. (a) Ratio of the damping time to the period, τ_D/P , versus $k_z a$ for $l/a = 0.1$ and $d/a = 3$. (b) Particular contribution of the first multipoles m to τ_D/P for $l/a = 0.1$, $d/a = 3$, and $k_z a = 10^{-1}$. The different line styles and symbols are labeled within the Figure. The grey area in panel (a) corresponds to the range of realistic values of the parameter $k_z a$.

CHAPTER 9. DAMPING OF MHD WAVES IN TWO CYLINDRICAL THREADS

slightly decreases and later increases again as $k_z a$ becomes larger. We can also see that, such as happens for the real part of the frequency (see [Van Doorselaere et al. 2008](#)), the S_x and A_y modes have an almost identical τ_D/P for $k_z a \ll 1$, whereas the same applies for the A_x and S_y solutions. Far from the thin tube limit, the four solutions have different damping ratios.

The present results indicate that, regarding the damping by resonant absorption, the low-frequency (S_x and A_y) modes behave more similarly to the individual kink mode than the high-frequency (A_x and S_y) solutions. To shed light on this result, let us consider the particular contribution of each multipole m to the resonant damping. To do so, we fix $\delta_m^i = 0$ except for those m whose particular contribution we want to assess, and compute the damping ratio in each case. Figure 9.6b shows the result of these computations. As expected for kink-like oscillations, the dominant multipole for all solutions is $|m| = 1$. We can see that, when a particular m is selected, the damping ratio of the A_x and S_y modes is smaller than that of the S_x and A_y modes. For this reason, the total damping ratio of the former is smaller than that of the latter.

To explain the reason that makes the A_x and S_y modes more damped than the S_x and A_y modes let us take into account the results by [Arregui et al. \(2007b\)](#). These authors numerically studied the damping of the transverse fundamental (symmetric) mode of two slabs with transitional layers in Cartesian geometry. They found that, although both the real and imaginary parts of the frequency are affected by the separation between the two slabs, this parameter has little effect on the damping ratio. In particular, [Arregui et al. \(2007b\)](#) related the efficiency of the attenuation to the magnitude of the total pressure perturbation within the transitional layers. According to [Andries et al. \(2000\)](#), the efficiency of the resonant coupling between the global transverse mode and Alfvén continuum modes is given by the jump of the radial energy flux across the dissipative layer. In the case of an isolated cylinder, [Andries et al. \(2000\)](#) provide an approximate expression for the jump of the radial energy flux, $[[\mathcal{S}_r]]$, which in our present notation is

$$[[\mathcal{S}_r]] \approx \frac{\pi}{2} e^{2\omega_I t} \omega_R \frac{m^2/a^2}{|\rho_0 \Delta_A|_{r_A}} p_{T_1}^2, \quad \text{at } r = r_A. \quad (9.5)$$

The larger $[[\mathcal{S}_r]]$, the more energy from the global mode is deposited in the dissipative layer, and so the more damped is the global mode. When a system of several cylinders is taken into account, we expect that the dependence of $[[\mathcal{S}_r]]$ with p_{T_1} in the resonant layer of each cylinder is similar to that given by Equation (9.5). Thus, one can reasonably assume that the efficiency of resonant absorption for the damping of a collective mode is proportional to $[[\mathcal{S}_r]]$, and so proportional to $p_{T_1}^2$ at the resonance positions, meaning that the larger the total pressure perturbation in the dissipative layers, the more efficient resonant absorption. In order to check this last statement, we plot in Figure 9.7 the normalized value of $p_{T_1}^2$ in the xy -plane corresponding to the S_x (panel a) and A_x (panel b) modes. These results correspond to the case $l/a = 0$ because the TB approach only provides us with information about the frequency, but the form of the perturbations in the inhomogeneous layer cannot be obtained with this formalism. A numerical integration of the resistive MHD equations is needed to obtain the perturbations in the transitional layers. However, since the total pressure perturbation is constant across the dissipative layer, we expect $p_{T_1}^2$ to be approximately the same when $l/a \neq 0$. To better compare the two panels of Figure 9.7, we display in Figure 9.8 a cut of $p_{T_1}^2$ along the direction

that connects the axes of the two cylinders. For the two modes, the maximum value of $p_{T_1}^2$ takes place in this cut. We see that $p_{T_1}^2$ of the A_x mode reaches a larger value in the transitional layers than that of the S_x solution. This result qualitatively explains why the A_x mode is more damped than the S_x solution. Equivalently, a similar conclusion allows us to understand the different attenuation of the S_y and A_y solutions. An in-depth study of the process of resonant absorption in two-dimensional configurations (see [Russell & Wright 2010](#)) is needed for a more robust explanation of the different damping rates of the four kink solutions.

Finally, Figure 9.9 allows us to study in-depth the dependence on the thickness of the transitional layers. Figure 9.9 shows τ_D/P versus l_2/a when $l_1/a = 0.1$. We see that even when $l_2/a = 0$, so that there is no Alfvén resonance in the second thread, we obtain quite an efficient damping of the four kink solutions. By comparing Figures 9.5 and 9.9 we see that the values of τ_D/P obtained when $l_2/a = 0$ are not substantially larger than those of the case $l_1/a = l_2/a$. In particular, there is a factor 2, approximately, between the value of τ_D/P in the case $l_1/a = 0.1$ and $l_2/a = 0$, and that in the case $l_1/a = l_2/a = 0.1$. This means that a resonance in the transitional layer of one of the two threads is enough to efficiently damp a collective mode.

9.3.2 Non-identical threads

Here, we consider the case of two non-identical threads. We perform a parametric study based on the values of the densities and the thickness of the transitional layers. We assume $k_z a = 10^{-1}$ in the following computations, and the radii of both threads are set equal for simplicity, i.e., $a_1 = a_2 = a$. As pointed out by [Luna et al. \(2009\)](#), the use of S_x , A_x , S_y , and A_y to denote the four kink modes in a system of two non-identical cylinders is not strictly correct since, in such a case, the total pressure and velocity perturbations can be significantly different in both cylinders. However, we keep here this notation for the sake of simplicity and denote the four solutions according to their behavior in a system with identical densities.

First, we fix $\rho_1 = 5 \times 10^{-11} \text{ kg m}^{-3}$ and study the dependence of the frequency on ρ_2 . For this computation we consider $l_1/a = l_2/a = 0.1$. Figure 9.10a shows the real part of the frequency of the four kink modes as a function of ρ_2 . This result is equivalent to that of [Luna et al. \(2009\)](#), i.e., the collective modes become the individual modes of each thread when different densities are considered. In particular, for $\rho_2 < \rho_1$ the S_x and A_y modes are related to the kink oscillations of the first thread because the real part of their frequency coincides with the kink frequency of the first thread. On the contrary, the A_x and S_y solutions correspond to kink motions of the second thread. This behavior is the opposite one for $\rho_2 > \rho_1$. It is also worth noting that the low-frequency (S_x and A_y) modes can be below the internal cut-off frequencies of one of the two threads. By approximating $\omega_{kj}^2 \approx 2\omega_{Aj}^2$, one easily obtains that the low-frequency solutions are below ω_{A2} for $\rho_2/\rho_1 \lesssim 1/2$, whereas they are below ω_{A1} for $\rho_2/\rho_1 \gtrsim 2$. This means that the frequency of the S_x and A_y modes is only within the Alfvén continua of both threads for $1/2 \lesssim \rho_2/\rho_1 \lesssim 2$. On the contrary, the high-frequency (A_x and S_y) solutions are always within both continua.

On the other hand, Figure 9.10b displays the corresponding values of τ_D/P . We see that the value of τ_D/P of the S_x and A_y modes shows little dependence on ρ_2/ρ_1 . Even when the frequency of these modes falls outside one of the two continua, the value of

CHAPTER 9. DAMPING OF MHD WAVES IN TWO CYLINDRICAL THREADS

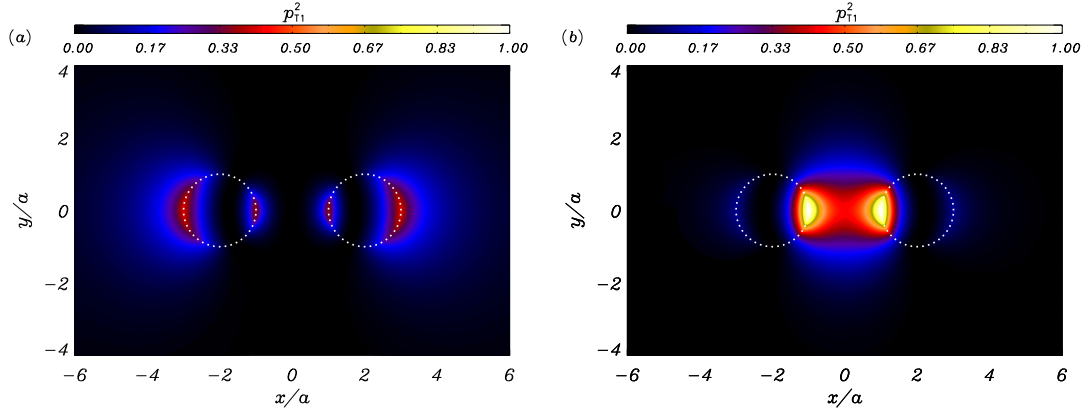


Figure 9.7: Total pressure perturbation squared (contour plot) plotted in the xy -plane corresponding to the wave modes (a) S_x and (b) A_x for $d = 4a$ and $k_z a = 10^{-1}$. The dotted circles denote the location of the undisturbed threads. Normalized arbitrary units have been used and the maximum of p_{T1}^2 of the A_x mode has been set as reference (unity).

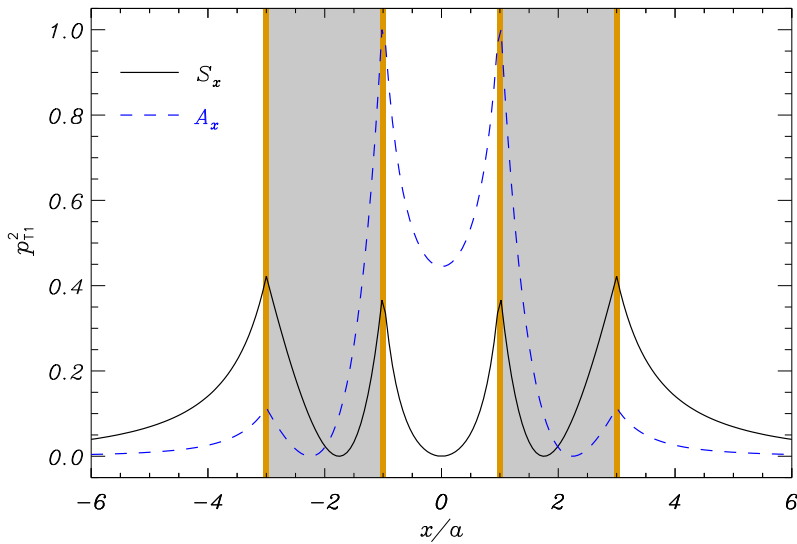


Figure 9.8: Cut at $y = 0$, $z = 0$ of the total pressure perturbation squared, p_{T1}^2 , displayed in Figure 9.7. The grey zones denote the location of the homogeneous part of the threads, while the brown regions correspond to the transitional layers. Normalized arbitrary units have been used and the maximum of p_{T1}^2 of the A_x mode has been set as reference (unity).

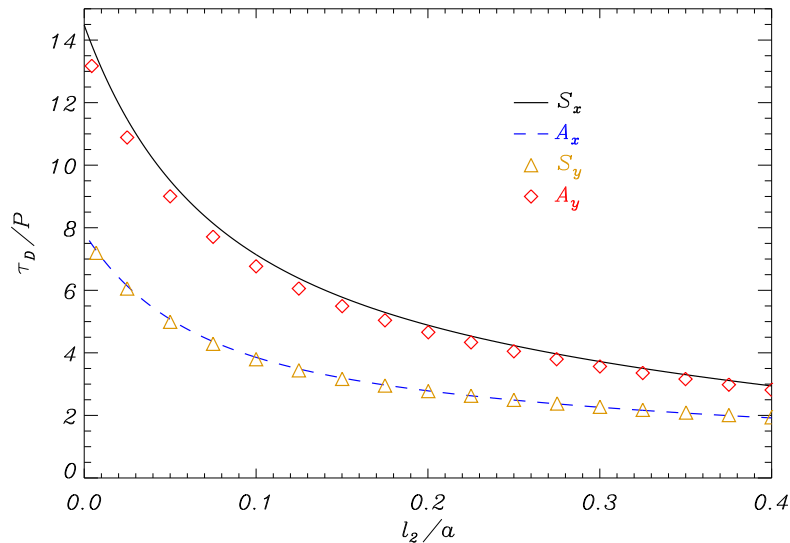


Figure 9.9: Ratio of the damping time to the period, τ_D/P , of the collective kink modes versus l_2/a . In all computations, $l_1/a = 0.1$, $d/a = 3$, $k_z a = 10^{-1}$ and $\rho_1/\rho_c = \rho_2/\rho_c = 200$. The different line styles are labeled within the Figure.

τ_D/P is not substantially modified. Regarding the A_x and S_y modes, we can see that their τ_D/P is more affected by the value of ρ_2/ρ_1 . For these two modes, the minimum of τ_D/P occurs for $\rho_2/\rho_1 \approx 1$. The real part of the frequency of the A_x and S_y modes is always within the Alfvén continua of both threads for all values of ρ_2/ρ_1 , so both resonances contribute to the damping of these solutions.

9.4 Conclusions

In this Chapter, we have studied the damping of collective modes in a system of two cylindrical filament threads. Non-adiabatic effects and resonant absorption have been considered as damping mechanisms. In agreement with previous studies on the damping of individual modes, we have obtained that collective slow modes are efficiently damped by non-adiabatic effects, in particular by radiative losses, and collective kink modes are strongly attenuated by resonant absorption in the Alfvén continuum. In both cases, the computed τ_D/P are consistent with the values reported in the literature.

For slow modes, the values of the damping times of the collective modes are very similar to those of the individual modes, meaning that the collective character of the oscillation does not have, in general, a strong influence on the attenuation by non-adiabatic effects. In the case of kink modes, the interaction between neighboring threads causes a shift of the value of τ_D/P in comparison with the individual kink oscillation of an isolated thread damped by resonant absorption. This is specially noticeable for the A_x and S_y solutions, which are more strongly damped than the other collective kink modes and than the individual kink oscillation. An interesting result is that an efficient damping of the collective kink modes is still obtained if the collective mode is resonantly

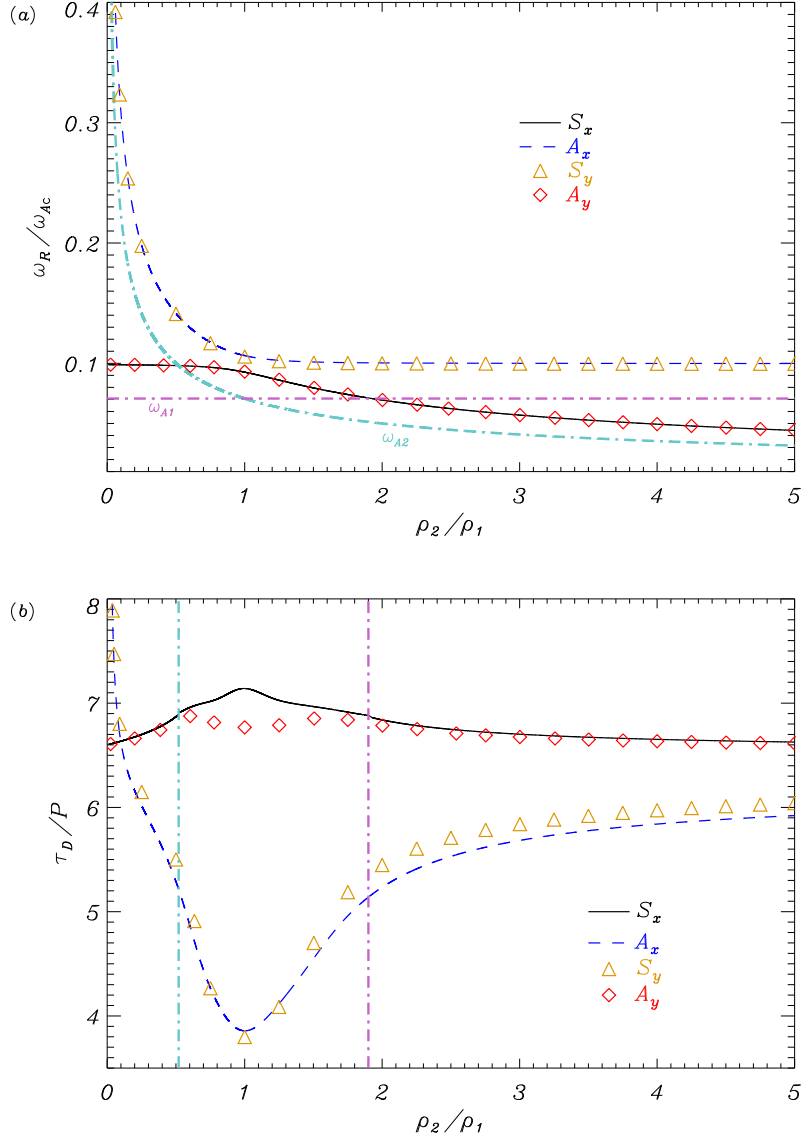


Figure 9.10: Collective kink modes in the case of two non-identical threads. (a) Real part of the frequency, in terms of the external Alfvén frequency, versus ρ_2/ρ_1 . (b) Ratio of the damping time to the period, τ_D/P , versus ρ_2/ρ_1 . The vertical dot-dashed lines in panel b correspond to the values of ρ_2/ρ_1 in which the internal cut-off frequencies of the threads are reached. In all computations, $l_1/a = l_2/a = 0.1$, $d/a = 3$, $k_z a = 10^{-1}$, and $\rho_1/\rho_c = 200$. The different line styles are labeled within the Figure. ω_{A1} and ω_{A2} correspond to the internal Alfvén frequencies of the first and second threads, respectively.

coupled to Alfvén continuum modes of one thread only. This situation can take place when the collective mode frequency is within the Alfvén continuum of one thread only but the frequency is outside the Alfvén continuum of the other thread, or when the transitional layer of one specific thread is absent.

Extending our results to an arbitrary system of many threads, we expect the high modes (according to the notation by [Luna et al. 2010](#)) to be very efficiently attenuated, whereas the low modes may have damping times more similar to that of the individual kink oscillation. This might cause the contribution of the high modes to the collective motion of an ensemble of threads to be less important than the contribution of the low modes, since high modes would probably be quickly damped much before than the low modes. A detailed study of this issue in future investigations is needed in the context of both coronal loops and prominence threads.

Concluding Remarks and Future Work

Concluding remarks

In this thesis, we have investigated some physical mechanisms that may be of relevance for the damping of oscillations in prominence fine structures. Among the effects studied here, resonant absorption for kink modes and the combined effect of radiation losses and ion-neutral collisions for slow modes can provide values of the ratio of the damping time to the period, τ_D/P , compatible with those observed. On the other hand, magnetic diffusion and thermal conduction turn out to be irrelevant for the damping of both transverse and longitudinal thread oscillations. The efficiency of other possible dissipative mechanisms not studied here as, e.g., viscosity, can be easily estimated by means of order-of-magnitude calculations (see [Ballai 2003](#)). One obtains that, in prominence conditions, viscosity is much less efficient than any other mechanism studied here.

On the other hand, some additional effects have also been investigated as, e.g., the influence of mass flows, the collective behavior of groups of oscillating threads, and the effect of the longitudinal inhomogeneity of the fine structure. In the case of individual oscillations, we find that the main influence of mass flows is to shift the value of the real part of the frequency, and so only the period is affected. For realistic flow velocities, this effect can be of importance for slow waves, since they are forced to propagate in the flow direction. Regarding collective oscillations, we obtain that the dominant damping mechanisms are the same as for individual thread oscillations, meaning that the collective behavior of motions does not affect the damping of the oscillations. However, the presence of flows is very relevant for the collective behavior of the oscillations, since only particular values of the flow velocities allow for collective motions, i.e., those velocities that cause the individual Doppler shifted frequencies of the threads to be the same. Finally, the observational evidence that in a fine structure the prominence material only occupies a part of the whole magnetic flux tube has also been taken into account. In the case of the kink mode damping by resonant absorption and ion-neutral collisions, we find that the main conclusions obtained for a homogeneous magnetic cylinder remain valid in the case of a partially filled tube because the kink mode behavior is mainly governed by the physical conditions of the dense part of the tube.

Future work

We are aware that the filament thread models assumed here are simple and may be subjected to some criticism. For example, we have studied perturbations from an equilibrium whose properties are constant in time. Observations from the Hinode spacecraft (e.g., [Okamoto et al. 2007](#); [Berger et al. 2008](#)) show a highly dynamic prominence medium, and it is likely that the properties of the threads may vary in time-scales comparable to the oscillatory periods. For this reason, studies similar to those of [Aschwanden & Terradas \(2008\)](#), [Erdélyi et al. \(2008\)](#), and [Morton & Erdélyi \(2009\)](#), which take into account a changing background medium in the context of coronal loops, should be extended to prominences in the near future.

In addition, the effect of gravity has been also ignored in our investigation. The inclusion of gravity would complicate matters significantly, since a new equilibrium

CONCLUDING REMARKS AND FUTURE WORK

between the gravity force and the magnetic and pressure forces should be found. To our knowledge, there are no consistent models of filament threads which include the effect of gravity. To construct such a model is definitely beyond the purpose and scope of the present thesis. However, on the basis of the results of [McEwan & Díaz \(2007\)](#), who studied the effect of gravity in a coronal slab by ignoring its influence on the equilibrium and only considering its effect on the perturbations, we might anticipate that gravity would have a very minor influence on the periods of an oscillating thread.

There is still much work to do in the field of prominence oscillations and their damping. Our contribution in this thesis has been to identify the important mechanisms and effects that must be investigated in more detail in the future. For example, we could go beyond the normal mode analysis and study the time-dependent problem of impulsively generated oscillations in both isolated threads and bundles of threads. Another issue of special interest is to take into account the effect of ionization and recombination of the plasma species, which could affect the time evolution of the plasma ionization degree. On the other hand, the coupling and interaction between photospheric/chromospheric oscillations and prominence oscillations might be the subject of forthcoming investigations. Finally, the construction of complex three-dimensional models of prominences and their fine structures and the study of their stability properties are also issues of great interest.

Bibliography

- Abdelatif, T. E. 1988, ApJ, 333, 395
- Abramowitz, M., & Stegun, I. A. 1972, Handbook of Mathematical Functions, Dover Publications
- Alfvén, H. 1942, Nature, 150, 405
- An, C.-H. 1984, ApJ, 276, 755
- Andries, J., Tirry, W. J., & Goossens, M. 2000, ApJ, 531, 561
- Andries, J., Goossens, M., Hollweg, J. V., Arregui, I., Van Doorselaere, T. 2005, A&A, 430, 1109
- Arber, T. D., Haynes, M., & Leake, J. E. 2007, ApJ, 666, 541
- Arregui, I., Van Doorselaere, T., Andries, J., Goossens, M., & Kimpe, D. 2005, A&A, 441, 361
- Arregui, I., Andries, J., Van Doorselaere, T., Goossens, M., & Poedts, S. 2007, A&A, 463, 333
- Arregui, I., Terradas, J., Oliver, R., & Ballester, M. 2007, A&A, 466, 1145
- Arregui, I., Ballester, J. L., & Goossens, M. 2008, ApJ, 676, L77
- Arregui, I., Terradas, J., Oliver, R., & Ballester, J. L. 2008, ApJ, 682, L141
- Arregui, I., & Ballester, J. L. 2010, Space Sci. Rev., in press
- Aschwanden, M. 2004, Physics of the solar corona. An introduction (2nd edition), Springer
- Aschwanden, M., & Terradas, J. 2008, ApJ, 686, L127
- Ballester, J. L., & Priest, E. R. 1989, A&A, 225, 213
- Ballester, J. L. 2006, Phil. Trans. R. Soc. A, 364, 405
- Ballai, I. 2003, A&A, 410, L17
- Banerjee, D., Erdélyi, R., Oliver R., & O'Shea, E. 2007, Sol. Phys., 246, 3
- Balsara, D. S. 1996, ApJ, 465, 775
- Balthasar, H., Wiehr, E., Schleicher, H., & Wöhl, H. 1993, A&A, 277, 635
- Berger et al. 2008, ApJ, 676, L89
- Bogdan, T. J., & Zweibel, E. G. 1987, ApJ, 312, 444
- Bogdan, T. J., & Cattaneo, F. 1989, ApJ, 342, 545
- Braginskii, S. I. 1965, Rev. Plasma Phys., 1, 205
- Čadež, V. M., Csík, Á., Erdélyi, R., & Goossens, M. 1997, A&A, 326, 1241
- Cally, P. S. 1986, Sol. Phys., 103, 277
- Cally, P. S. 2003, Sol. Phys., 217, 95
- Cally, P. S. 2006, Sol. Phys., 233, 79
- Carbonell, M., Oliver, R., & Ballester, J. L. 2004, A&A, 415, 739
- Carbonell, M., Terradas, J., Oliver, R., & Ballester, J. L. 2006, A&A, 460, 573
- Carbonell, M., Oliver, R., & Ballester, J. L. 2009, NewA, 14, 277

BIBLIOGRAPHY

- Carbonell, M., Forteza, P., Oliver, R., & Ballester, J. L. 2010, *A&A*, in press
- Chae, J., Ahn, K., Lim, E.-K., Choe, G. S., & Sakurai, T. 2008, *ApJ*, 689, L73
- Chen, F. F. 1984, *Introduction to plasma physics and controlled fusion* (Vol. 1), Plenum Press
- Cirigliano, D., Vial, J.-C., Rovira, M. 2004, *Sol. Phys.*, 223, 95
- Copil, P., Voitenko, Y., & Goossens, M. 2008, *A&A*, 478, 921
- Cox, D. P., & Tucker, W. H. 1969, *ApJ*, 157, 1157
- Dahlburg, R. B., & Mariska, J. T. 1988, *Sol. Phys.*, 117, 51
- Demoulin, P., Raadu, M. A., Malherbe, J. M., & Schmieder, B., 1987, *A&A*, 183, 142
- De Moortel, I. & Hood, A. W. 2004, *A&A*, 415, 705
- De Pontieu, & Haerendel, G. 1998, *A&A*, 338, 729
- De Pontieu, B. 1999, *A&A*, 347, 696
- De Pontieu, B., Martens, P. C. H., & Hudson, H. S. 2001, *ApJ*, 558, 859
- Desch, S. J. 2004, *ApJ*, 608, 509
- Díaz, A J., Oliver R., Erdélyi, R., & Ballester, J. L. 2001, *A&A*, 379, 1083
- Díaz, A J., Oliver R., & Ballester, J. L. 2002, *ApJ*, 580, 550
- Díaz, A J., Oliver R., & Ballester, J. L. 2003, *A&A*, 402, 781
- Díaz, A J., Oliver R., Ballester, J. L., & Roberts, B. 2004, *A&A*, 424, 1055
- Díaz, A J., Oliver R., & Ballester, J. L. 2005, *A&A*, 440, 1167
- Díaz, A. J., & Roberts, B. 2006, *Sol. Phys.*, 236, 111
- Dymova, M. V., & Ruderman, M. S. 2005, *Sol. Phys.*, 229, 79
- Dymova, M. V., & Ruderman, M. S. 2006, *A&A*, 457, 1059
- Edwin, P. M., & Roberts, B. 1982, *Sol. Phys.*, 76, 239
- Edwin, P. M., & Roberts, B. 1983, *Sol. Phys.*, 88, 179
- Engvold, O., Kjeldseth-Moe, O., Bartoe, J. D. F., & Brueckner, G., 1987, in *Proceedings of 21st ESLAB Symposium*, ESA SP-275, 21
- Engvold, O. 2008, in *IAU Symp. 247, Waves & Oscillations in the Solar Atmosphere: Heating and Magneto-Seismology*, ed. R. Erdélyi & C. A. Mendoza-Briceño (Cambridge: Cambridge Univ. Press), 152
- Erdélyi, R., Goossens, M., & Ruderman, M. S. 1995, *Sol. Phys.*, 161, 123
- Erdélyi, R., Ballai, I., Goossens, M. 2001, *A&A*, 368, 662
- Erdélyi, R., Luna-Cardozo, M., Mendoza-Briceño, C. A. 2008, *Sol. Phys.*, 252, 305
- Erdélyi, R., & Fedun, V. 2007, *Science*, 318, 1572
- Ferraro, V. C. A. & Plumpton, C. 1961, *An Introduction to Magneto-Fluid Mechanics*, Oxford University Press

- Field, G. B. 1965, *ApJ*, 142, 531
- Forteza, P., Oliver, R., Ballester, J. L., & Khodachenko, M. L. 2007, *A&A*, 461, 731
- Forteza, P., Oliver, R., & Ballester, J. L. 2008, *A&A*, 492, 223
- Foullon, C., Verwichte, E., & Nakariakov, V. M. 2004, *A&A*, 427, L5
- Foullon, C., Verwichte, E., & Nakariakov, V. M. 2009, *ApJ*, 700, 1658
- Goedbloed, H., & Poedts, S. 2004, *Principles of magnetohydrodynamics*, Cambridge University Press
- Goossens, M., Hollweg, J. V., & Sakurai, T. 1992, *Sol. Phys.*, 138, 233
- Goossens, M., Ruderman, M. S., & Hollweg, J. V. 1995, *Sol. Phys.*, 157, 75
- Goossens, M., Andries, J., & Aschwanden, M. J. 2002, *A&A*, 394, L39
- Goossens, M. 2003, *An introduction to plasma astrophysics and magnetohydrodynamics*, Kluwer Academic Publishers
- Goossens, M., Arregui, I., Ballester, J. L., & Wang, T. J. 2008, *A&A*, 484, 851
- Goossens, M., Terradas, J., Andries, J., Arregui, I., & Ballester, J. L. 2009, *A&A*, 503, 213
- Goossens, M., Andries, J., & Arregui, I. 2006, *Phil. Trans. R. Soc. A*, 364, 433
- Goossens, M. 2008, in *IAU Symp. 247, Waves & Oscillations in the Solar Atmosphere: Heating and Magneto-Seismology*, ed. R. Erdélyi & C. A. Mendoza-Briceño (Cambridge: Cambridge Univ. Press), 228
- Gouttebroze, P., & Labrosse, N. 2009, *A&A*, 503, 663
- Harvey, J. 1969, PhD Thesis, University of Colorado, USA
- Haerendel, G. 1992, *Nature*, 360, 241
- Hildner, E. 1974, *Sol. Phys.*, 35, 123
- Holzwarth, V., Schmitt, D., & Schüssler, M. 2007, *A&A*, 469, 11
- Hood, A. W., & Anzer, U. 1990, *Sol. Phys.*, 126, 117
- Ireland, R. C., van der Linden, R. A. M., & Hood, A. W. 1993, *Sol. Phys.*, 179, 155
- Joarder, P. S., & Roberts, B. 1992a, *A&A*, 256, 264
- Joarder, P. S., & Roberts, B. 1992b, *A&A*, 261, 625
- Joarder, P. S., & Roberts, B. 1993a, *A&A*, 273, 642
- Joarder, P. S., & Roberts, B. 1993b, *A&A*, 277, 225
- Joarder, P. S., Nakariakov, V. M., & Roberts, B. 1997, *Sol. Phys.*, 173, 81
- Keppens, R., Bogdan, T. J., & Goossens, M. 1994, *ApJ*, 436, 372
- Keppens, R. 1995, *Sol. Phys.*, 161, 251
- Keppens, R. 1996, *ApJ*, 468, 907
- Kippenhahn, R., & Schlüter, A. 1957, *Z. Astrophys.*, 43, 36
- Khodachenko, M. L., Arber, T. D., Rucker, H. O., & Hanslmeier, A. 2004, *A&A*, 422, 1073

BIBLIOGRAPHY

- Krishan, V., & Varghese, B. A. 2008, *Sol. Phys.*, 247, 343
- Kulsrud, R., & Pearce, W. P. 1969, *ApJ*, 156, 445
- Kumar, N., Roberts, B. 2003, *Sol. Phys.*, 214, 241
- Kuperus, M., & Raadu, M. A. 1974, *A&A*, 31, 189
- Labrosse, N., Heinzel, P., Vial, J.-C., Kucera, T., Parenti, S., Gunár, S., Schmieder, B., & Kilper, G. 2010, *Space Sci. Rev.*, in press
- Landman, D. A., Edberg, S. J., & Laney, C. D. 1977, *ApJ*, 218, 888
- Leake, J. E., Arber, T. D., & Khodachenko, M. L. 2005, *A&A*, 442, 1091
- Lighthill, M. J. 1960, *Phil. Trans. R. Soc. A*, 252, 397
- Lin, Y. 2004, PhD Thesis, University of Oslo, Norway
- Lin, Y., Engvold, O., & Wiik, J. E. 2003, *Sol. Phys.*, 216, 109
- Lin, Y., Engvold, O., Rouppe van der Voort, L. H. M., Wiik, J. E., & Berger, T. E. 2005, *Sol. Phys.*, 226, 239
- Lin, Y., Engvold, O., Rouppe van der Voort, L. H. M., & van Noort, M. 2007, *Sol. Phys.*, 246, 65
- Lin, Y., Martin, S. F., & Engvold, O. 2008, in *ASP Conf. Ser. 383, Subsurface and Atmospheric Influences on Solar Activity*, ed. R. Howe, R. W. Komm, K. S. Balasubramaniam, & G. J. D. Petrie (San Francisco: ASP), 235
- Lin, Y., Soler, R., Engvold, O., Ballester, J. L., Langangen, Ø., Oliver, R., & Rouppe van der Voort, L. H. M. 2009, *ApJ*, 704, 870
- Luna, M., Terradas, J., Oliver, R., & Ballester, J. L. 2008, *ApJ*, 676, 717
- Luna, M., Terradas, J., Oliver, R., & Ballester, J. L. 2009, *ApJ*, 692, 1582
- Luna, M., Terradas, J., Oliver, R., & Ballester, J. L. 2010, *ApJ*, in press
- Mackay, D. H., Karpen, J. T., Ballester, J. L., Schmieder, B., & Aulanier, G. 2010, *Space Sci. Rev.*, in press
- Mashnich, G. P., Bashkirtsev, V. S., & Khlystova, A. I. 2009, *Astronomy Letters*, 35, 253
- McEwan, M. P., & Díaz, A. J. 2007, *Sol. Phys.*, 246, 243
- Menzel, D. H. 1951, *Proc. Con. on Dyn. of Ionised Media*, UCL, London
- Milne, A. M., Priest, E. R., & Roberts, B. 1979, *ApJ*, 232, 304
- Miteva, R., Zhelyazkov, I., & Erdélyi, R. 2003, *Phys. Plasmas*, 10, 4463
- Molowny-Horas, R., Oliver, R., Ballester, J. L., & Baudin, F. 1997, *Sol. Phys.*, 172, 181
- Molowny-Horas, R., Wiehr, E., Balthasar, H., Oliver, R., & Ballester, J. L. 1999, *JOSO Annual Report 1998*, Astronomical Institute Tatranska Lomnica, 126
- Moreton, G. E. 1960, *Astron. J.*, 65, 494
- Morton, R. J., & Erdélyi, R. 2008, *ApJ*, 707, 750.
- Nakariakov, V. M., & Roberts, B. 1995, *Sol. Phys.*, 159, 213

- Nakariakov, V. M., & Ofman, L. 2001, *A&A*, 372, L53
- Ning, Z., Cao, W., Okamoto, T. J., Ichimoto, K., & Qu, Z. Q. 2009a, *A&A*, 499, 595
- Ning, Z., Cao, & Goode, P. R. 2009b, *ApJ*, 707, 1124
- Okamoto, T. J., et al. 2007, *Science*, 318, 1557
- Oliver, R., Ballester, J. L., Hood, A. W., & Priest, E. R. 1992, *ApJ*, 400, 369
- Oliver, R., Ballester, J. L., Hood, A. W., & Priest, E. R. 1993, *ApJ*, 409, 809
- Oliver, R., & Ballester, J. L. 1995, *ApJ*, 448, 444
- Oliver, R., & Ballester, J. L. 1996, *ApJ*, 456, 393
- Oliver, R., & Ballester, J. L. 2002, *Sol. Phys.*, 206, 45
- Oliver, R. 2009, *Space Sci. Rev.*, 149, 175
- Pandey, B. P., & Wardle, M. 2008, *Mon. Not. R. Astron. Soc.*, 385, 2269
- Parker, E. N. 1953, *ApJ*, 117, 431
- Patsourakos, S., & Vial, J.-C. 2002, *Sol. Phys.*, 208, 253
- Pinto, C., Galli, D., & Bacciotti, F. 2008, *A&A*, 484, 1
- Poland, A., & Anzer, U. 1971, *Sol. Phys.*, 19, 401
- Porter, L. J., Klimchuk, J. A., & Sturrock, P. A. 1994, *ApJ*, 435, 482
- Pouget, G., Bocchialini, K., & Solomon, J. 2006, *A&A*, 450, 1189
- Priest, E. R. 1982, *Solar magnetohydrodynamics*, D. Reitel Publishing Company
- Ramsey, H. E., & Smith, S. F. 1966, *Astron. J.*, 71, 197
- Rempel, M., Schmitt, D., & Glatzel, W. 1999, *A&A*, 343, 615
- Roberts, B., Edwin, P. M., & Benz, A. O. 1984, *ApJ*, 279, 857
- Rosner, R., Tucker, W. H. & Vaiana, G. S. 1978, *ApJ*, 220, 643
- Ruderman, M., & Roberts, B. 2002, *ApJ*, 577, 475
- Ruderman, M. S., & Roberts, B. 2006a, *J. Plasma Phys.*, 72, 285
- Ruderman, M. S., & Roberts, B. 2006b, *Sol. Phys.*, 237, 119
- Ruderman, M., & Erdélyi, R. 2009, *Space Sci. Rev.*, 149, 199
- Russell, A. J. B., & Wright, A. N. 2010, *A&A*, 511, A17
- Sakurai, T., Goossens, M., & Hollweg, J. V. 1991a, *Sol. Phys.*, 133, 227
- Sakurai, T., Goossens, M., & Hollweg, J. V. 1991b, *Sol. Phys.*, 133, 247
- Schmieder, B. 1992, *Sol. Phys.*, 141, 275
- Schmieder, B., Chandra, R., Berlicki, A., & Mein, P. 2010, *A&A*, in press
- Schrijver, C. J., & Brown, D. S. 2000, *ApJ*, 537, L69

BIBLIOGRAPHY

- Schutgens, N. A. J. 1997a, *A&A*, 323, 969
- Schutgens, N. A. J. 1997b, *A&A*, 325, 352
- Schutgens, N. A. J., & Tóth, G. 1999, *A&A*, 345, 1038
- Sewell, G. 2005, *The Numerical Solution of Ordinary and Partial Differential Equations*, Wiley & Sons
- Simon, G., Schmieder, B., Demoulin, P., & Poland, A. I. 1986, *A&A*, 166, 319
- Soler, R., Oliver, R., & Ballester, J. L. 2007a, *Sol. Phys.*, 246, 73
- Soler, R., Oliver, R., & Ballester, J. L. 2007b, *A&A*, 471, 1023
- Soler, R., Oliver, R., & Ballester, J. L. 2008, *ApJ*, 684, 725
- Soler, R., Oliver, R., & Ballester, J. L. 2009a, *NewA*, 14, 238
- Soler, R., Oliver, R., & Ballester, J. L. 2009b, *ApJ*, 693, 1601
- Soler, R., Oliver, R., Ballester, J. L., & Goossens, M. 2009c, *ApJ*, 695, L166
- Soler, R., Oliver, R., & Ballester, J. L. 2009d, *ApJ*, 699, 1553
- Soler, R., Oliver, R., & Ballester, J. L. 2009e, *ApJ*, 707, 662
- Soler, R., Oliver, R., & Ballester, J. L. 2010a, *A&A*, 512, A28
- Soler, R., Oliver, R., & Ballester, J. L. 2010b, in preparation
- Soler, R., Arregui, I., Oliver, R., & Ballester, J. L. 2010c, in preparation
- Spitzer, L. 1962, *Physics of fully ionized gases*, Interscience
- Spruit, H. C. 1982, *Sol. Phys.*, 75, 3
- Stenuit, H., Keppens, R., & Goossens, M. 1998, *A&A*, 313, 392
- Stenuit, H., Tirry, W. J., Keppens, R., & Goossens, M. 1999, *A&A*, 342, 863
- Sy, W. N.-C. 1984, *Plasma Phys. and Controlled Fusion*, 26, 915
- Tanenbaum, B. S. 1961, *Phys. Fluids*, 4, 1262
- Tanenbaum, B. S., & Mintzer, D. 1962, *Phys. Fluids*, 5, 1226
- Terra-Homem, M., Erdélyi, R., & Ballai, I. 2003, *Sol. Phys.*, 217, 199
- Terradas, J., Oliver, R., & Ballester, J. L. 2001, *A&A*, 378, 635
- Terradas, J., Molowny-Horas, R., Wiehr, E., Balthasar, H., Oliver, R., & Ballester, J. L. 2002, *A&A*, 393, 637
- Terradas, J., Carbonell, M., Oliver, R., & Ballester, J. L. 2005, *A&A*, 434, 741
- Terradas, J., Oliver, R., & Ballester, J. L. 2006, *ApJ*, 642, 533
- Terradas, J., Andries, J., & Goossens, M. 2007, *Sol. Phys.*, 246, 231
- Terradas, J., Arregui, I., Oliver, R., & Ballester, J. L. 2008, *ApJ*, 678, L153
- Terradas, J., Goossens, M., & Ballai, I. 2010, *A&A*, in press
- Tirry, W. J., & Goossens, M. *ApJ*, 471, 501

- Tomimura, A. 1990, *Phys. Scripta*, 42, 628
- Tripathi, D., Isobe, H., & Jain, R. 2009, *Space Sci. Rev.*, 149, 283
- Twersky, V. 1952, *ASAJ*, 24, 42
- Tsubaki, T., & Takeuchi, A. 1986, *Sol. Phys.*, 104, 313
- van der Linden, R. A. M., & Goossens, M. 1991, *Sol. Phys.*, 131, 79
- van der Linden, R. A. M. 1993, *Geophys. Astrophys. Fluid Dyn.*, 69, 183
- Van Doorselaere, T., Andries, J., Poedts, S., & Goossens, M. 2004, *ApJ*, 606, 1223
- Van Doorselaere, T., Ruderman, M. S., & Robertson, B. 2008, *A&A*, 485, 849
- Vernazza, J. E., Avrett, E. H., & Loeser, R. 1981, *ApJS*, 45, 635
- Verwichte, E., Nakariakov, V. M., Ofman, L., & Deluca, E.E. 2004, *Sol. Phys.*, 223, 77
- Watanabe, T. 1961a, *Can. J. Phys.*, 39, 1044
- Watanabe, T. 1961b, *Can. J. Phys.*, 39, 1197
- Waterman, P. C. 1969, *ASAJ*, 45, 1417
- Watts, C., & Hanna, J. 2004, *Phys. Plasmas*, 11, 1358
- Wentzel, D. G. 1979, *A&A*, 76, 20
- Wiehr, E. 2004, *Proc. SOHO 13*, ESA SP-547, 185
- Wilson, P. R. 1979, *A&A*, 71, 9
- Wilson, P. R. 1980, *A&A*, 87, 121
- Wilson, P. R. 1981, *ApJ*, 251, 765
- Woods, L. C. 1962, *J. Fluid Mechanics*, 13, 570
- Yi, Z., Engvold, O., & Kiel, S. L. 1991, *Sol. Phys.*, 132, 63
- Yi, Z., & Engvold, O. 1991, *Sol. Phys.*, 134, 275
- Yousif, H. A., & Melka, R. 1997, *Comp. Phys. Com.*, 106, 199
- Zhelyazkov, I., Debosscher, A., & Goossens, M. 1996, *Phys. Plasmas*, 3, 4346
- Zirker, J. B., Engvold, O., & Yi, Z. 1994, *Sol. Phys.*, 150, 81
- Zirker, J. B., Engvold, O., & Martin, S. F. 1998, *Nature*, 396, 440